Experiments on Multi-Level Superconducting Qubits and Coaxial Circuit QED

Michael J. Peterer

Wolfson College, Oxford

A thesis submitted for the degree of

Doctor of Philosophy

Trinity Term 2016

Supervised by Dr. Peter Leek

Clarendon Laboratory

University of Oxford

Experiments on Multi-Level Superconducting Qubits and Coaxial Circuit QED

Michael J. Peterer, Wolfson College, University of Oxford

Trinity Term 2016

Abstract of thesis submitted for the degree of Doctor of Philosophy

Superconducting qubits are a promising technology for building a scalable quantum computer. An important architecture employed in the field is called Circuit Quantum Electrodynamics (circuit QED), where such qubits are combined with high quality microwave cavities to study the interaction between artificial atoms and single microwave photons. The ultra-strong coupling achieved in these systems allows for control and readout of the quantum state of qubits to perform quantum information processing. The work on circuit QED performed in this thesis consisted of realizing an experimental setup for qubit experiments in a new laboratory, investigating the coherence and decay of higher energy levels of superconducting transmon qubits and finally demonstrating a novel coaxial form of circuit QED.

Designing and building a 3D circuit QED setup involved the following main accomplishments: producing high quality 3D cavities; designing and installing the cryogenic microwave setup as well as the room temperature amplification and data acquisition circuitry; successfully developing a recipe for the fabrication of Josephson junctions; controlling and measuring superconducting 3D transmon qubits at 10 mK. Several qubits were fully characterised and have shown coherence times of several microseconds and relaxation times up to 25 μs.

Superconducting qubits in fact possess higher energy levels that can provide significant computational advantages in quantum information applications. In experiments performed at MIT, preparation and control of the five lowest states of a transmon qubit was demonstrated, followed by an investigation of the phase coherence and decay dynamics of these higher energy levels. The decay was found to proceed mainly sequentially with relaxation times in excess of 20 μs for all transitions. This experiment was also reproduced on a 3D transmon fabricated and measured in Oxford, where due to a higher effective qubit temperature a multi-level decay model including thermal excitations was developed to explain the observed relaxation dynamics.

Finally, a coaxial transmon, which we name the coaxmon, is presented and measured with a coaxial LC readout resonator and input/output coupling ports placed inline along the third dimension. This novel coaxial circuit QED architecture holds great promise for developing a scalable planar grid of qubits to build a quantum computer.

Je dédie cette thèse à Karen, une fille fantastique
die mir immer Unterstützig und Liebi geh hät,
and who showed immense patience for my dissident and eccentric state of mind...

Acknowledgements

Dr Peter Leek, I foremost thank you for giving me the opportunity to build up a new circuit QED lab in Oxford with you. It was a great experience, you taught me everything from fabricating Josephson junctions, wiring a dilution fridge, measuring superconducting qubits, analyzing data rigorously, and it goes on. I enjoyed every bit of it, even our emergency intervention mission for the fridge on a Saturday night at 3am. You continue to impress me with your innovative ideas and quick intuition of experimental results, and I wish the LeekLab much success in the future.

Einar Magnusson and Mike Kohlhoff, thank you for being my best friends throughout these years in Oxford. It is clear, the Oxford experience would not have been as empowering without you two. Einar, you gave me a taste for the entrepreneurial spirit, podcasts, and craft beer. Mike, thank you for providing such sharp intellectual sparring during our fervent discussions on politics, economics, and social issues during all those countless nights at the Wolfson Bar and the Kings Arms. Dismaland, Reading, Herrentag, Paris, On a Boat ... the memories will never fade!

Dear great friends in Oxford, thank you for making my time here so much fun. Chris Irons, your poems and worldliness. Damien Storey, your philosophical mind and progressive character. Max Hoerantner, your hacking and challenge spirit. Maryam Aslani, your prodigious intellect and your deep insights into Iranian and Indian sociopolitical issues.

Riccardo Manenti, I will miss our days and nights in the cleanroom and closing the fridge together on friday evenings. Thank you for your friendship and all the help.

Andrew Patterson, the superstar coder, I am indebted to you for all the crucial work you have done to enable my measurements of qubits by programming the e-beam evaporator and coding the FPGA. Thank you.

My lab and office mates, Ani, Joseph, Arjan, Francesca, Alex, Tanja, Peter, thanks for all the interesting discussions, help with research, and great friendships.

Prof William Oliver, thank you for giving me the opportunity to come to MIT and work on such an interesting project, it was a truly enriching experience.

Dr Simon Gustavsson, I don't even know how to start to thank you. You had the patience and showed me how to measure a 3D transmon qubit, and then you let me write the article on the experiment we performed together. I enjoyed our many long skype sessions across the atlantic to figure out the data analysis and the writing of the paper. Finally, thank you for letting us beta-test your Labber software from the beginning on, this was a tremendous help for our experiments in Oxford.

In the context of my research at MIT and the article published, I would like to thank Samuel Bader for developing and running the numerical simulation of the qubit and his crucial contribution to the data analysis and writing of the article.

I acknowledge funding from the EPSRC for my Project Studentship, and I am grateful to Wolfson College for enabling interactions within such a diverse and international community, and for letting me organise the 2015 Wolfson Winter Ball.

A shout out to all my shizzls Robin, Pascal, Benoît, Fred, Hervé, Roman, Claudio, Andri, Patrick, Jannick, Barbara, Torben, Vincent, Romain, and Julian for being my long-time friends, and for not only visiting me on the island but also hosting me regularly for breaks from it in less flat territory.

My folks Claudia and Bruno Peterer, I am proud to have such awesome parents, thank you for having always supported and encouraged me throughout all my life. And my three brothers Dom, André, and Sam, thanks for always being my bros.

Karen, ma boys Jaxson and Minimic2, we had so much fun living together in Oxford. Thank you for sharing this great adventure with me, it will not be the last one...believe me.

Contents

Chapter 1

Introduction

> *"Everybody really knows if you are ever going to make a real quantum computer, it must be solid state."*
>
> — Benjamin Schumacher
>
> Live Science, Sept. 14, 2013, 'Beam Me Up: Bits of Information Teleported Across Computer Chip'

1.1 Quantum Computing

The rise of the digital revolution in the course of the 20th century has deeply transformed all aspects of human society through the development of digital computers and communications technology. This "information age" now dominates our personal lives, defines what drives the economy, and has become the basis for most scientific progress. This has created the need for ever more power to process information and large amounts of data, which has led to a tremendous amount of investments to build gigantic supercomputers consuming vast amounts of energy. Notwithstanding these impressive engineering developments, many problems are still too hard to solve for the likes of any of modern computers, no matter how powerful. Moreover, the computer industry's focus on improving the processing speed and power by crunching ever smaller and ever more transistors (currently 10^{14} and multiple cores) onto a chip is hitting a physical limit. As the physical size of transistors reaches atomic dimensions, the features of quantum physics take effect. Moore's law, an observation made in 1965 which states that the number of transistors in a computer of a given price has been doubling every two years until today, is reaching saturation now because transistors have reached a width of less than 10 nm. Since technological change, productivity, and economic growth have been driven by what Moore's law describes, it is of great interest to find an alternative to conventional information processing: quantum information processing.

Quantum mechanics, which was developed at the beginning of the 20th century, is essentially the theory of nature at small scales, and has arguably been the most successful scientific theory in history. It studies the fundamental interaction of matter and light. In the second half of the 20th century, physicists were no longer content by simply studying and understanding quantum systems as given by nature, but wanted to try designing and manipulating the systems. It was Richard Feynman that proposed in 1981 how to use quantum systems to efficiently solve problems by using quantum systems to simulate other quantum systems [66, 114]. In 1985 at the University of Oxford, David Deutsch formulated the description of a quantum Turing machine [180], i.e. a model of a universal quantum computer [50], and in 1992 presented the first quantum algorithm as the Deutsch-Josza algorithm [51]. Although it has little practical relevance, it describes and demonstrates for the first time a problem that “can be solved exponentially faster by a quantum algorithm than by any possible deterministic classical algorithm”. The discovery that really fuelled interest in quantum computing is Peter Shor's algorithm in 1994 [172] which for the first time demonstrated the power of a quantum computer in an application of high relevance. It allows the factorisation into prime factors of large integer numbers in polynomial time as opposed to exponential time on a classical machine. This is enormously relevant to modern day encryption and secure communication since common"public-key" cryptography (RSA encryption) is based on the fact that the factorisation problem is too hard for any classical computer to solve. A second practical quantum algorithm, discovered by Grover [74], allows for efficient search of database entries. This is an example of an application that has real practical relevance today in light of the rise of Big Data, i.e. an explosion in the amounts of data stored and processed by scientists, businesses and governments worldwide for such uses as predictive analytics. Numerous quantum algorithms have since been discovered [3, 80]. Potential applications for a quantum computer include quantum simulation, which would allow to simulate entire molecules (impossible with classical computers) and would lead to the ability to design new materials or new drugs. Quantum chemistry could lead to the discovery of a catalyst to sequester CO_2. Furthermore, quantum computing could enable efficient machine learning [115] and pattern recognition, and finally cryptography and secure quantum encrypted communication. Just as today's numerous applications of computers were not imagined when computers were developed in the 1950's, the potential applications for quantum computers too, are to be expected to reach beyond our wildest imagination.

The essence of a quantum computer is to take advantage of the quantum coherence inherent in its building blocks. Similar to a classical computer, it stores information in sequences of bits of states 0 or 1. As opposed to a classical bit though, the quantum computer's bits (qubits) are physically realized by a quantum system, and hence the two bit states 0 and 1 can be in a quantum superposition state. This fundamentally different nature of quantum information gives quantum computing advantages like a natural massive parallelism and entanglement, leading to the possibilities of implementing quantum algorithms and performing quantum simulations.

1.2 Realizations of a quantum computer

The field of quantum information and quantum computation is comprehensively presented in the influential book by Nielson and Chuang [141], which gives an overview of the theory and possible implementations of quantum bits. Current candidate physical systems for realizing a quantum computer include quantum dots, solid-state NMR, trapped ions, photonics systems, NV centres, and superconducting circuits. Any candidate quantum system needs to be sufficiently isolated from the environment in order to preserve the coherence of its quantum state, but at the same time it must allow for coherent control on short timescales and with high precision. The difficulty for any candidate system lies in the balancing of the various factors: coherence, control, and connectivity.

Quantum dots use single electron spins [117, 69, 151] and solid-state NMR use the nuclear spin state of phosphorous donors in silicon as qubits [97, 152, 168, 109]. Liquid-state NMR systems are realised by the nuclear spin state in liquid molecules [72, 46, 42, 102, 185, 184, 167]. Ions traps systems use the electronic states of trapped ions [129, 75, 76, 14, 13, 61, 130, 142, 81], and photonic systems use linear optics and the polarized states of a photon [43, 177, 105, 86]. Diamond NV centers [132, 197, 181] use point defects in diamond as qubits. Each of these implementations has its own strong and weak points. Quantum dots, NMR, ion traps, and NV centers obtain very long qubit coherence times (on the order of seconds to hours) and gates with very high fidelity [8], but have difficulty achieving strong enough coupling between qubits to perform multi-qubit logic gates, and thereby scaling-up becomes very hard. On the contrary, superconducting circuits have shorter lifetimes but are highly scalable [44]. Strong coupling between superconducting qubits is achieved and they can be controlled and interconnected by circuit design, for example, using transmission lines and resonators. All elements and properties in superconducting circuits can be designed, engineered, and fabricated with well-established and reliable microfabrication technologies known from conventional integrated circuits that make the devices scalable to a large number of qubits. Moreover, since the superconducting qubits are operated in the microwave frequency range 5 to 15 GHz, the control technology in experiments is readily available from microwave applications in radar systems and the telecommunications industry. It is the coherence times of superconducting qubits that have posed the greatest challenge to considering them as serious candidates for a quantum computer. However, since 2014 their lifetimes have reached the threshold for fault tolerance with quantum error correction [9], and in 2015 quantum error correction codes have been experimentally demonstrated in various forms [160, 165, 164, 98, 45, 99, 196, 144], which preserves the qubit states from decoherence. Considering these tremendous advances it has now become clear that superconducting circuits are one of the most promising implementations for a scalable fault-tolerant quantum computer.

The initial experiment that opened the possibility to use the macroscopic quantum states in a Josephson-junction based superconducting circuit was the discovery that the phase difference across a Josephson junction is subject to Macroscopic Quantum Tunnelling (MQT) [188, 54]. Subsequently, it was shown that the energy levels of a current-biased Josephson junction are quantized at milli-Kelvin temperatures [125]. The superposition of Cooper pair states was achieved in 1997 [137], and in 1999 the coherent manipulation of those states was performed in a Cooper pair box on a nanosecond timescale [138]. The following years gave birth to the flux qubit [146, 131], the charge qubit “quantronium” [187], and the phase qubit [124].

The great challenge is to improve the coherence times and quality factors of the qubits. The decoherence is caused by interactions with the environment and noise in the control parameters. Extended efforts in several labs are made to identify the sources of decoherence and describe the microscopic mechanisms leading to the energy relaxation (T_1 time) and dephasing (T_2 time) of the qubit state. The developed qubits had very short lifetimes on the order of a few nanoseconds in 2002. Since then, there has been remarkable progress: the lifetime of a single qubit has increased by five orders of magnitude [53], see Fig. 1.1. An important step in this development was the introduction of circuit Quantum Electrodynamics (*circuit QED*) [22, 190]. The idea of cavity QED [79], where an atom is strongly coupled to a cavity, is adopted and applied to superconducting qubits by coupling them to microwave resonators, i.e. artificial atoms coherently interact with light on a single microchip. This not only suppresses limiting spontaneous decay mechanisms but also enabled preciser control and more effective readout of the qubit states, two essential criteria for a quantum computer. The discovery of the transmon [103, 84] played a major role in increasing the coherence times into the microseconds, because it allowed the qubit to become insensitive to charge noise. This led to many experiments with transmons: demonstrating readout schemes [18, 158]; demonstration of two-qubit and three-qubit entanglements and algorithms [119, 55, 56, 111, 139, 10]; and implementation of a Toffoli gate with simple quantum error correction codes [10, 65, 160, 122]. Superconducting qubits have also led to many novel and profound quantum optics experiments due to the strong coupling they achieve as artificial atoms. A few examples include: demonstration of a single microwave-photon source [85]; generation of Fock states [82]; observation of two-mode squeezing [63]; quantum teleportation [175]; photon-mediated interactions between distant artificial atoms [183]; a superconducting switch for fast on-chip routing of quantum microwave fields [149]; and an on chip single photon router [83].

1.3 State of the art circuit QED

Since the year 2010, a cohort of single qubit and two-qubit gates were invented for circuit QED. These include: the direct-resonant iSWAP (DRi) [17], the second-order resonator sideband induced iSWAP (RSi) [112], the cross-resonance gate (CR) [38], the Bell-Rabi single-step entanglement gate (BR) [153], the microwave-activated c-Phase gate (MAP) [40], and resonator-induced phase gate (RIP) [147].

In 2011 the group at Yale introduced a new architecture called 3D circuit QED [148] where they placed the transmon qubit on a sapphire chip suspended in a 3D cavity. This tremendously improved energy relaxation times ($T_1 = 20 - 60\,\mu$s) and dephasing times ($T_2 = 5 - 20\,\mu$s). The T_1 is thought to improve in 3D because the electric field of the qubit is more spread out in space, so that the field strength is smaller, and it couples less strongly to defects in the substrate. Furthermore, the transmon in a 3D cavity typically has a single Josephson junction instead of a SQUID with two junctions, while this deprives it of tuneability, it also removes the effects of 1/f flux noise, thereby improving T_2. Coherence times of 3D transmons were improved to today's state of the art range $T_1 = 30 - 140\,\mu$s [163, 192]. In Chapter 7 we use a 3D transmon qubit [150] at MIT with a coherence time of $T_1 = 85\,\mu$s and $T_2 = 90\,\mu$s to investigate the coherence and decay of the higher energy levels with the objective of further understanding decoherence mechanisms. With the improvement of quality factors (see Chapter 5) of coherent planar resonators over 10^6 [126], 2D transmons have also been able to achieve higher lifetimes of up to $T_1 = 44\,\mu$s and $T_2 = 20\,\mu$s [9, 100]. The exponential scaling in performance during the past 15 years has been so immense that it now resembles a "quantum Moore's law", shown in Fig. 1.1, where the qubit relaxation and decoherence times double every three years, and no ultimate limit seems to have been hit yet.

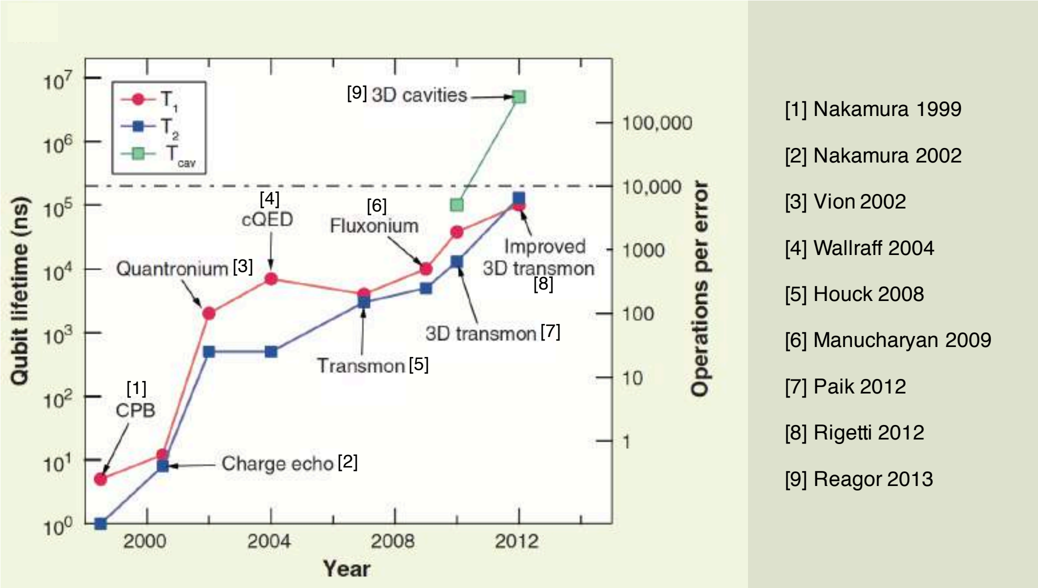

Figure 1.1: Schoelkopf's law illustrating the exponential scaling in performance of superconducting qubits during the past 15 years for qubit relaxation, qubit decoherence, and cavity lifetimes. Figure taken directly from [53].

There has been a strong focus on improving qubit lifetimes, including the most recent breakthrough demonstrating suspended superconducting qubits by silicon micromachining [41]. But since lifetimes have reached the threshold for quantum error correction codes, the past three years have shown tremendous progress in scaling up through new types of circuit QED architectures suitable for scaling up and implementing quantum error correction schemes. Some recent innovations include: a multilayer microwave integrated quantum circuits architecture for scalable quantum computing [27]; a quantum memory made from a coaxial 3D cavity with near-millisecond coherence [157], and a corresponding coaxial line architecture for integrating and scaling 3D cQED systems [6]; and an architecture called planar multilayer circuit quantum electrodynamics taking advantage of both 2D and 3D platforms [128].

The scaling up is accomplished by making a planar grid of qubits with nearest neighbour coupling to implement the surface code [57], with control lines and readout lines available for each qubit independently. The difficulty lies in the dense wiring necessary for the control and readout of many qubits on a planar structure. For this reason it is desirable to have the wiring access the qubits in the third dimension. In this context, we present our own work towards achieving a scalable architecture in Chapter 8. We propose and demonstrate a novel architecture based on planar transmons and resonators with a coaxial geometry which naturally couples to coaxial microwave lines in the third dimension. A transmon with a coaxial geometry has been presented in [26] (they call it a concentric transmon), but it is coupled to an on chip microstrip line for readout, which is a different approach from ours. Our novel coupled coaxial transmon (coaxmon) - coaxial resonator (coaxLC) architecture with input/output control lines in the third dimension is an innovation which could lead to a fully controllable and scalable grid of qubits.

Outline of the Thesis

This thesis presents my work carried out from October 2012 to May 2016 at the University of Oxford in the newly established LeekLab - *Superconducting Quantum Devices*. I performed the work in Chapter 7 as part of a three-months research visit from October to December 2013 in the Superconducting Circuits and Quantum Computing Group at the Massachusetts Institute of Technology (MIT).

In Chapter 2 I first introduce the basic concepts of quantum information and the theory on Josephson junctions and how they are used in superconducting quantum circuits to realize quantum bits in the form of a transmon. The generalized Jaynes-Cummings Hamiltonian describes the interaction between the qubit and the electromagnetic modes in a cavity, and I discuss how it is applied in circuit QED to control and readout qubits. Most of the work in the first year of this D.Phil consisted of designing and building the microwave setup to control and measure a circuit QED system, which is the topic of Chapter 3. A significant part of my work was then to design and fabricate these superconducting circuits, the subject matter of Chapter 4, for which I developed from scratch a fabrication recipe for Josephson junctions. In Chapter 5 I discusses the theory on resonators and 3D cavities, and describe the making and measuring of high quality 3D cavities which are then used to embed the superconducting qubit in the circuit QED setup. In Chapter 6 I perform a complete standard 3D circuit QED experiment by measuring and fully characterising a 3D transmon. The experiment performed at MIT investigates the coherence and decay of higher energy levels of a transmon, and I describe these results in Chapter 7 and compare them to an analogue experiment I performed on a transmon in Oxford. Finally, in Chapter 8 I present our novel coaxial transmon and resonator.

Chapter 2

Theory of superconducting qubits

This chapter introduces the basic concepts of quantum information and the theory on superconducting qubits in circuit QED. The first section presents the quantum bits and the mechanisms of decoherence. The second section describes the Josephson junction, and the third presents how it is used to build an anharmonic two-level system to form a qubit that can be operated it in the transmon regime. The fourth section introduces the generalized Jaynes-Cummings Hamiltonian and how it can be realised with superconducting electrical circuits to achieve circuit QED. In the last section the dispersive regime is derived to discuss the qubit readout mechanism.

2.1 Quantum bit

The smallest unit of classical information is a binary digit, or *bit*, which has the single property of being in one of exactly two states: 0 or 1. Classical computers are based on sequences of bits, each bit physically realised by a solid-state transistor. Similarly, the quantum bit, or *qubit*, is the smallest unit of quantum information. It can take on the state $|0\rangle$ or $|1\rangle$, but due to its quantum mechanical nature can also be in a linear superposition state of both

$$|\psi\rangle = \alpha|0\rangle + \beta|1\rangle\,. \tag{2.1}$$

The numbers α and β are complex numbers, and the states $|0\rangle$ and $|1\rangle$ are vectors living in a two-dimensional complex Hilbert space H. When a qubit in a superposition of states is measured, the wavefunction $|\psi\rangle$ collapses and the outcome reduces to either $|0\rangle$ or $|1\rangle$, with probability $P_{|0\rangle} = |\alpha|^2$ and $P_{|1\rangle} = |\beta|^2$ and normalization

$$|\alpha|^2 + |\beta|^2 = 1\,.$$

2.1.1 Bloch sphere representation

The Bloch sphere representation is a useful concept for geometrically visualising the dynamics and manipulation of any qubit superposition state. From Eq. 2.1 together with the normalization equation and the fact that the global phase of a quantum state has no physical relevance, the wavefunction can be rewritten in the form

$$|\psi\rangle = \cos\frac{\theta}{2}|0\rangle + e^{i\varphi}\sin\frac{\theta}{2}|1\rangle\,. \tag{2.2}$$

The polar angle θ and the azimuth angle φ create the unit three-dimensional *Bloch sphere*, shown in Fig. 2.1. The ground state $|0\rangle$ corresponds to a vector pointing to the north pole, and the excited state $|1\rangle$ to a vector pointing to the south pole, thereby forming a vector basis. Equal superposition states on the sphere point to the equator and form the basis states

$$\{|+\rangle, |-\rangle\} = \{\frac{1}{\sqrt{2}}(|0\rangle + |1\rangle), \frac{1}{\sqrt{2}}(|0\rangle - |1\rangle)\}\,, \tag{2.3}$$

$$\{|i\rangle, |-i\rangle\} = \{\frac{1}{\sqrt{2}}(|0\rangle + i|1\rangle), \frac{1}{\sqrt{2}}(|0\rangle - i|1\rangle)\} \tag{2.4}$$

on the x-axis and y-axis respectively.

Following the description in [141] closely, the Bloch sphere picture describes a fictitious spin-1/2 particle in an effective static magnetic field (defined in the z-axis

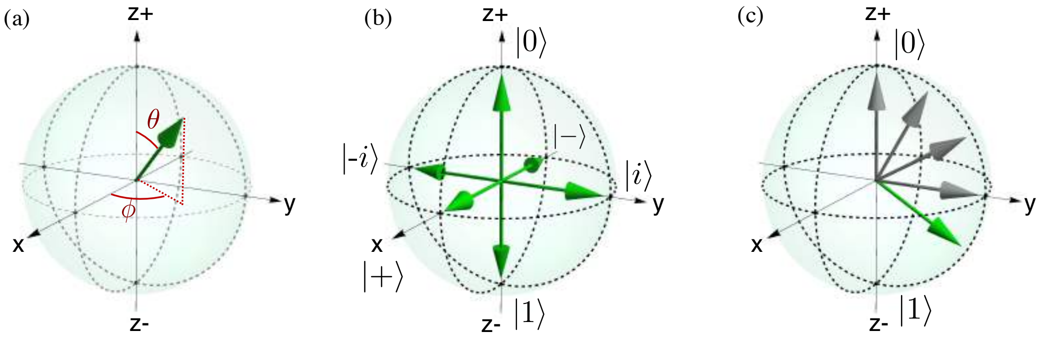

Figure 2.1: Bloch sphere representation. (a) A single qubit state $|\psi\rangle$. (b) The six standard basis states $|0\rangle, |1\rangle, |+\rangle, |-\rangle, |i\rangle$, and$|-i\rangle$. (c) Manipulation of a single qubit state, i.e. driving transitions, is represented as a rotation on the Bloch sphere around the x- or y-axis, here the x-axis.

direction) with a time evolution $\hat{U} = e^{-\hat{H}t/\hbar}$ given by the Hamiltonian

$$\hat{H} = \frac{1}{2}\hbar\omega_{01}\hat{\sigma}_z = \frac{1}{2}\hbar\omega_{01}\begin{pmatrix}1 & 0\\ 0 & -1\end{pmatrix}\,. \tag{2.5}$$

The energy difference between the ground and excited states is $\hbar\omega_{01}$ and $\hat{\sigma}_z$ is the Pauli z-matrix. The magnetic field causes the state vector to precess around the z-axis with the Larmor frequency $\omega_{01}/2\pi$. For quantum control over the qubit state, we are mostly interested in rotations around the x- or y-axis rather than the z-axis, as shown in Fig. 2.1c, since these are the operations that drive qubit transitions between $|0\rangle$ and $|1\rangle$ and any superposition state, see Section 6.4.1. For mathematical convenience it is then common to consider the rotating frame picture, where the coordinate system rotates with the Larmor frequency precession rendering the state vector stationary in this frame.

2.1.2 Decoherence

The greatest challenge with the physical realization of quantum bits is suppressing decoherence mechanisms [88]. The qubit is naturally coupled to the environment and therefore undergoes entanglement with it. The quantum entanglement causes the qubit to loose its defined quantum state over time, resulting in decoherence which can be categorised into two forms: energy relaxation and dephasing.

Energy relaxation is the longitudinal relaxation from the excited state to the ground state (the Bloch vector gradually falls from the south pole $|1\rangle$ to the north pole $|0\rangle$) due to the interaction of noise from the environment that couples at frequencies close to that of the qubit transition frequency, e.g. thermal noise that couples to the qubit. Decay sources include coupling to equilibrium and non-equilibrium quasiparticles [33, 176], trapped vortices [193], and two-level fluctuators [134], among others. The decay time into the ground state $T_1 = 1/\Gamma_1$ is the inverse of the relaxation rate Γ_1. Perfectly isolating our quantum system from the environment would avoid energy relaxation, but for quantum computing some coupling to the system is required to manipulate and readout the state.

The pure dephasing, the transverse relaxation, is the dual of the qubit energy relaxation, and it represents the loss of knowledge about the phase of the quantum state. On the Bloch sphere this is visualized as the azimuthal angle of the state getting randomized. It arises due to random variation of the qubit frequency induced by various noise sources, such as 1/f noise [15], magnetic flux noise and charge dispersion with charge noise [103, 169], fluctuating cavity photon number [16], etc. Phase coherence is not only limited by just the pure dephasing T_ϕ processes, but by the dissipation T_1 effects as well, leading to an overall dephasing T_2 given by

$$\frac{1}{T_2} = \frac{1}{2T_1} + \frac{1}{T_\phi} \tag{2.6}$$

2.2 Superconducting quantum circuits

A qubit in theory is just a mathematical object describing any two-level quantum system. In the physical world, this mathematical object can be realised in many different systems that display quantum mechanical behaviour, see Chapter 1. We use superconducting quantum circuits to fabricate a quantum bit. In quantum mechanics, macroscopic objects typically do not present coherent quantum mechanical behaviour, only microscopic systems like electrons and atoms do. It is therefore startling to consider that an electrical circuit of size of the order of a millimetre and clearly visible to the eye can behave quantum mechanically. Nevertheless, this is possible when the system's collective degrees of freedom are robustly isolated and decoupled from the environment, which requires careful design and engineering of the circuit, and energy dissipation is sufficiently suppressed [52].

At this point we can introduce the most simple quantum circuit, the quantum LC oscillator, shown schematically in Fig. 2.2a, which we will quantize using circuit quantization, closely following [52].

To start, Kirchoff's current law states that the sum of the currents across the inductance and capacitance must be zero, since there are no current sources. The constitutive relations for the inductor are $V(t) = L\,dI/dt$ and $V(t) = d\,\Phi/dt$, and for the capacitor are $I(t) = CdV/dt$. This gives us the relation

$$I_{capacitor} + I_{inductor} = C\frac{d^2\Phi}{dt^2} + \frac{\Phi}{L} = 0\,. \tag{2.7}$$

The general equation of motion describing the dynamics of a system with Lagrangian $\mathcal{L}(q,\dot{q})$ is the Euler-Lagrange equation

$$\frac{d}{dt}\left(\frac{\partial\mathcal{L}(q,\dot{q})}{\partial q}\right) - \frac{\partial\mathcal{L}(q,\dot{q})}{\partial q} = 0\,. \tag{2.8}$$

The Lagrangian satisfying the Eq. 2.8 to obtain Eq. 2.7 is

$$\mathcal{L}(\Phi, \dot{\Phi}) = \frac{1}{2}C\dot{\Phi}^2 - \frac{1}{2}\frac{\Phi^2}{L}\,, \tag{2.9}$$

thereby expressing the difference between the inductive and capacitive energies. To obtain the corresponding Hamiltonian we first compute the generalized canonical momentum conjugate Q to the canonical position Φ as

$$Q = \frac{\partial \mathcal{L}}{\partial \dot{\Phi}} = C\dot{\Phi}\,, \tag{2.10}$$

where the conjugate Q expresses the total charge on the capacitor. The standard Legendre transformation associated with Eq. 2.8 is $H(q,p) = p\dot{q} - \mathcal{L}(q,\dot{q})$ and yields the Hamiltonian for our LC circuit as

$$H(Q,\Phi) = \frac{Q^2}{2C} + \frac{\Phi^2}{2L} = \frac{Q^2}{2C} + \frac{1}{2}C\omega_0^2\Phi^2\,, \tag{2.11}$$

where we defined $\omega_0 = 1/\sqrt{LC}$. This electrical oscillator Hamiltonian Eq. 2.11 has the same form as that of the mechanical harmonic oscillator $\hat{H}_{mech} = \hat{p}^2/2m + m\omega_0^2\hat{x}^2/2$ that describes a particle of mass m with momentum p moving along the x direction in a harmonic quadratic potential $V(x) = 1/2kx^2$ with spring constant k and resonance frequency $\omega_0 = \sqrt{k/m}$. The mapping $p \to Q$, $x \to \Phi$, and $\omega_0 \to 1/\sqrt{LC}$, with the capacitor C representing the mass m, and $1/L$ the mechanical spring constant k, completes the equivalence picture between the electrical oscillator Eq. 2.11 and the mechanical oscillator $\hat{H}_{mech}$. The last step is to quantize the classical variables Φ and Q by replacing them with their quantum versions

$$\Phi \to \hat{\Phi} \qquad\qquad Q \to \hat{Q}\,. \tag{2.12}$$

The quantum mechanical operators $\hat{\Phi}$ and $\hat{Q}$ are Hermitian and satisfy the commutation relation $[\hat{\Phi}, \hat{Q}] = i\hbar$, which allows us to write them as

$$\hat{\Phi} = -i\hbar\frac{\partial}{\partial Q} \qquad\qquad \hat{Q} = i\hbar\frac{\partial}{\partial \Phi}\,. \tag{2.13}$$

From the analogy to the mechanical oscillator, we define the quantum mechanical creation and annihilation operators $\hat{a}$ and $\hat{a}^\dagger$ as

$$\hat{\Phi} = \sqrt{\frac{\hbar Z_0}{2}}(\hat{a} + \hat{a}^\dagger) \qquad \hat{Q} = -i\sqrt{\frac{\hbar}{2Z_0}}(\hat{a} - \hat{a}^\dagger) \tag{2.14}$$

with $Z_0 = \sqrt{L/C}$ defined as the characteristic impedance of the oscillator. The commutation relation becomes $[\hat{a}, \hat{a}^\dagger] = 1$, and the quantized Hamiltonian operator Eq. 2.11 can be expressed in terms of the dimensionless operators as

$$\hat{H} = \hbar\omega_0 \left(\hat{a}^\dagger\hat{a} + \frac{1}{2}\right) . \tag{2.15}$$

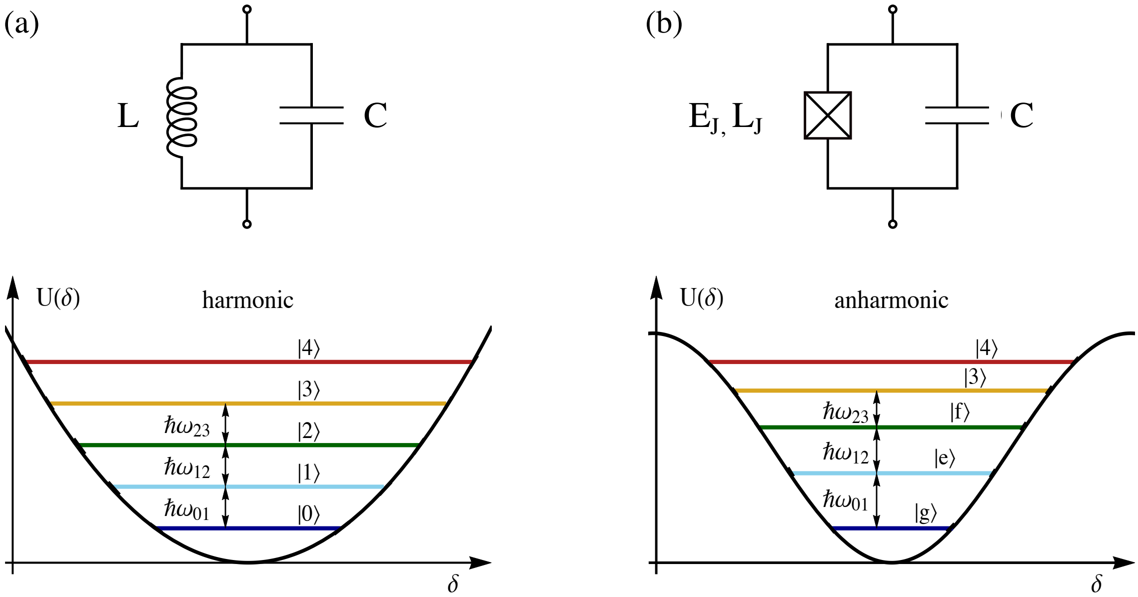

Figure 2.2: (a) Circuit diagram of a parallel LC oscillator and the associated quantum equidistant energy levels. (b) Circuit diagram of a parallel LC resonator with the inductor replaced by a Josephson junction. The quantum oscillator becomes anharmonic, i.e. non-equidistant energy levels, due to the non-linearity of the Josephson inductance.

The energy levels of this oscillator shape a harmonic spectrum, i.e. the levels are equally spaced by $\hbar\omega_n - \hbar\omega_{n-1} = \hbar\omega_0$, as seen in Fig. 2.2a. The idea of superconducting qubits is to use the first two energy levels to implement a quantum bit, using them as the ground $|g\rangle$ and excited $|e\rangle$ states. To build a system as a qubit, however, the superconducting quantum electrical circuit needs to be engineered to act as an anharmonic quantum oscillator, where the energy levels are non-equidistant, see Fig. 2.2b. The anharmonicity is crucially necessary in order to isolate and selectively address the lowest two energy levels $|g\rangle$ and $|e\rangle$ without exciting higher levels. In summary, the two crucial features of the oscillator are that it be *quantum* and *anharmonic*. The only known lossless electrical element that can fulfil the two requirements simultaneously is a Josephson junction. The only other basic conductor building blocks for circuits are the resistor, capacitor, and inductor, which are all linear elements. Indeed, the Josephson junction is a non-dissipative (due to superconductivity) and non-linear inductor (due to the Josephson effect). Building an LC oscillator where the inductor L is a Josephson junction gives us a quantum anharmonic oscillator as desired, ergo the Josephson junction constitutes our essential building block to realise a qubit. Since the junction must be superconducting, the qubit must be operated at a temperature below the critical superconducting temperature $T < T_c$ of the device. The next section introduces the basic theory on the Josephson effect and Josephson junctions.

2.3 Theory of Josephson junctions

2.3.1 Macroscopic quantum phase

Macroscopic systems do not display quantum mechanical behaviour due to the fact that the individual particles have a distribution of microscopic states whereby their quantum properties are averaged out, preventing macroscopic quantities such as current and voltage from displaying quantum superposition. In a superconductor however, BCS theory [179] states that in the vicinity of the Fermi energy mobile electrons condense into Cooper pairs, forming a condensate where all the pairs have the same energy in the ground state and therefore have identically evolving phases, endowing the condensate with a general phase coherence. The ensemble of all particles is then described by the same quantum mechanical wavefunction $\Psi(\vec{r}, t)$

$$\Psi(\vec{r}, t) = \sqrt{n^{CP}(\vec{r}, t)}e^{i\delta(\vec{r}, t)} , \tag{2.16}$$

where n^{CP} is the local Cooper pair density and δ the global phase. The superconductor has a macroscopic quantum current density

$$\vec{J}(\vec{r}, t) = q_s\, n^{CP}(\vec{r}, t) \left(\frac{\hbar}{m} \vec{\nabla} \delta(\vec{r}, t) - \frac{q}{m} \vec{A} \right) , \tag{2.17}$$

with $q_s = 2e$ the charge of a Cooper pair, m its effective mass, and $\vec{A}$ the vector potential. This equation is very important because it effectively states that currents and voltage arise in a superconductor when there are phase gradients and magnetic fields. *Flux quantization* [60, 116, 48] and the *Josephson effect* [94, 95, 5] are two coherent macroscopic effects that arise from Eq. 2.17. This led to the first observations of macroscopic quantum tunnelling in the 1980's in Josephson junctions [188, 54] and energy level quantization [125], which are the fundamental quantum experiments that paved the way for building superconducting qubits based on Josephson junctions.

2.3.2 Josephson relations

In the early twentieth century, quantum mechanics revealed the quantum tunnelling effect of single electrons flowing through an insulating barrier. It was not until 1962 that Brian David Josephson [94] discovered the tunnelling of superconducting Cooper pairs across a weak link, for which he received the Nobel Prize in 1973. As illustrated in Fig. 2.3a, the weak link consists of two coupled superconductors separated by a thin insulating layer, creating a superconductor-insulator-superconductor (SIS) interface commonly called a *Josephson junction.*

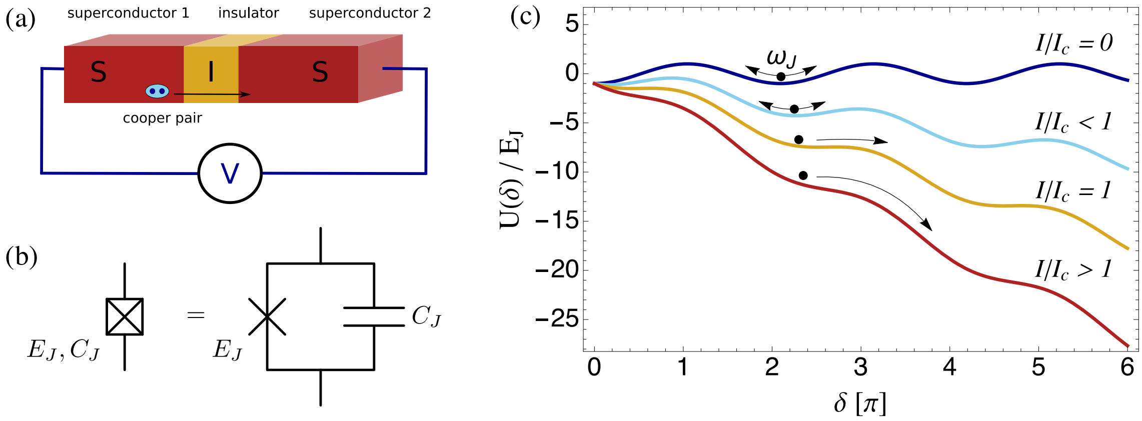

Figure 2.3: (a) A schematic of a Superconductor-Insulator-Superconductor (SIS) junction, called a Josephson junction. (b) Circuit diagram of a Josephson junction element. (c) The washboard potential $U(\delta)$ for the phase difference δ in different current regimes I/I_c.

Following the picture presented in Section 2.3.1, each superconductor is fully described by its condensate wave function $\Psi_i = \sqrt{n_i^{CP}} e^{i\delta_i}$, with $i = 1, 2$ labelling the two superconductors, and $\delta = \delta_1 - \delta_2$ the phase difference across the junction. The Cooper pair tunnelling current is characterised by two main Josephson effects: the DC effect and the AC effect.

DC Josephson effect

The first effect is given by the *Josephson or weak-link current-phase relation*

$$I = I_c \sin \delta. \tag{2.18}$$

It postulates that even without a voltage, the phase difference across the junction creates a supercurrent I. Vice-versa, a DC current flowing across the junction due to tunnelling or a bias current creates a linear phase difference and a voltage drop across the tunnel barrier with a sinusoidal dependence. The constant I_c is the *critical current* giving the maximal supercurrent that the junction can support.

AC Josephson effect

This second effect is given by the *superconducting phase evolution equation*

$$\frac{d\delta}{dt} = \frac{2\pi V}{\Phi_0}\,, \tag{2.19}$$

where the physical constant $\Phi_0 = h/2e$ is the magnetic flux quantum. It postulates that when a voltage V is applied across the junction, then a phase will start to wind up and evolve in time in a linear fashion, and the phase endlessly continues to augment over time with a slope $2e/\hbar$. Since with this effect a DC voltage creates an AC oscillating current, it can turn a voltage into a frequency and generate microwaves.

Neglecting integration constants, this leads to

$$\delta = \frac{2\pi V}{\Phi_0} t\,, \tag{2.20}$$

and substituting this into Eq. 2.18 gives

$$I(t) = I_c \sin\left(\frac{2\pi V}{\Phi_0} t\right). \tag{2.21}$$

Thus the current I becomes an AC current with amplitude I_c and angular frequency $2\pi V/\Phi_0$. The Josephson effect involves only fundamental physical constants, which is why it is used for voltage standards [178].

The potential energy stored in the junction due to the voltage applied (inducing a supercurrent flowing through it) is given by

$$\begin{aligned} E &= \int IV \mathrm{d}t = \int I_c \sin\delta \,\frac{\Phi_0}{2\pi}\frac{\partial\delta}{\partial t}\,\mathrm{d}t = \frac{\Phi_0}{2\pi} I_c \int \sin\delta \,\mathrm{d}\delta = \frac{\Phi_0 I_c}{2\pi} \cos\delta \\ &= E_J \cos\delta\,, \end{aligned} \tag{2.22}$$

where the quantity $E_J = \Phi_0 I_c/2\pi$ is called the *Josephson coupling energy.*

In addition, the total charging energy stored in the junction due to the N excessive Cooper pairs on one side is given by

$$U = \frac{1}{2}C_J V^2 = \frac{1}{2}C_J\left(\frac{N(2e)}{C_J}\right)^2 = 4\frac{e^2}{2C_J}N^2 = 4E_C\,N^2, \tag{2.23}$$

where C_J is the total capacitance of the junction. The quantity $E_C = e^2/2C_J$ is called the *charging energy*, and it represents the electrostatic energy needed to transfer one Cooper pair across the junction.

In a traditional circuit diagram, a real Josephson junction is represented by a crossed square, see Fig. 2.3, and it is modelled by putting in parallel an ideal Josephson junction (a cross) characterised by its Josephson energy E_J and a capacitor C_J. The parameters E_J and C_J can be specified in the fabrication process by choosing the appropriate thickness and overlap area of the thin insulating layer of the junction, see Chapter 4.

Taking now the derivative of the first Josephson relation Eq. 2.18 we obtain $\dot{I} = I_c \cos\delta\, \dot{\delta}$ and inserting this into the second Josephson relation Eq. 2.19 gives

$$V = \frac{\Phi_0}{2\pi I_c} \frac{1}{\cos\delta} \dot{I} = L_J \dot{I}, \tag{2.24}$$

where we defined the Josephson inductance $L_J = L_0/\cos\delta$ with the constant $L_0 = \Phi_0/(2\pi I_c)$. Thus the Josephson junction behaves like a non-linear inductor thanks to the Josephson inductance L_J which accumulates energy when a supercurrent passes through it. However, the accumulated energy is not in the form of a magnetic field, but rather in the form of Josephson energy hidden inside the junction.

2.3.2.1 RCSJ model

The Josephson junction is modelled in the current source RCSJ (Resistively and Capacitively Shunted Josephson Junction) model shown in Fig. 2.3b, which is a parallel circuit consisting of a resistor R, capacitor C_J, and Josephson junction E_J. From Kirchhoff's current law we can write the circuit's differential equation for the bias current I as

$$I = I_c \sin\delta + \frac{V}{R} + C_J \frac{dV}{dt}\,. \tag{2.25}$$

Using Eq. 2.19 leads to the equation of motion for the dynamics of the phase δ as

$$C_J \frac{\Phi_0}{2\pi}\frac{d^2\delta}{dt^2} + \frac{1}{R}\frac{\Phi_0}{2\pi}\frac{d\delta}{dt} = I - I_C \sin\delta\,. \tag{2.26}$$

This describes a damped non-linear oscillator, and when rewriting it as

$$C_J \frac{\Phi_0}{2\pi}\frac{d^2 d}{dt^2} + \frac{1}{R}\frac{\Phi_0}{2\pi}\frac{d\delta}{dt} + \frac{d}{dt}[E_J(1 - \cos\delta - \frac{I}{I_c}\delta)] = 0\,, \tag{2.27}$$

it takes the form $Md^2X/dt^2 + \eta\, dX/dt + \nabla U = 0$, which describes the dynamics of a particle with mass $M = (\Phi_0/2\pi)^2 C$ moving along $X = \delta$ with damping η in an effective potential

$$U(\delta) = E_J(1 - \cos\delta - \frac{I}{I_c}\delta)\,. \tag{2.28}$$

This potential is plotted in Fig. 2.3c and is called the tilted washboard potential. The potential function Eq. 2.28 gives rise to several cases for the current to critical current ratio. For the case of no bias current $I = 0$, the washboard potential is an untilted sine function with local minima. The phase particle is trapped in such a minimum with an approximate harmonic oscillator potential of resonance frequency $\omega_J = \sqrt{2\pi I_c/\Phi_0 C_J}$, referred to as the junction's *plasma frequency*. For the case $I < I_c$, the washboard potential starts to tilt, but not sufficiently to let the phase particle escape the potential well. When the bias current reaches $I > I_c$, the washboard gets sufficiently tilted and the particle escapes its local minimum. It continuously rolls down the washboard, which means the phase continuously changes, i.e. $d\delta/dt > 0$ is finite, thereby creating a voltage drop V across the junction. This is called the running state. The anharmonicity of the potential $U(\delta)$ due to the non-linearity of the Josephson junction, and the tilting of the potential due to a bias current are the two fundamental phenomena that enable the physics of superconducting qubits for quantum information processing.

2.4 The Cooper pair box and the transmon

As mentioned in Section 2.2, a quantized electrical circuit uses a Josephson junction to create the anharmonicity required for use as a qubit. Several types of superconducting circuits have been developed using various combinations of Josephson junctions, capacitors, and inductors. These can be categorized into three types [44]: the charge qubit, phase qubit, and flux qubit. The first charge qubit, known as the Cooper pair box, was born when the superposition of macroscopic quantum states was observed for states holding different number of Cooper pairs on a superconducting island [137]. The flux qubit [70, 182] is based on one or three Josephson junctions connected in series as a loop, creating a flux pointing up or down, and the qubit states relate to the current flowing clockwise or anti-clockwise in the loop. The phase qubit contains a single Josephson junction and is based on qubit states formed within a potential well in the tilted washboard potential Eq. 2.28 as a function of the phase difference δ [124], and the bias current is used to tilt the potential into the running state for the readout of the qubit. In this section we present the theory on superconducting charge qubits, starting with an introduction to the Cooper pair box followed by a discussion on the transmon regime.

2.4.1 The Cooper pair box

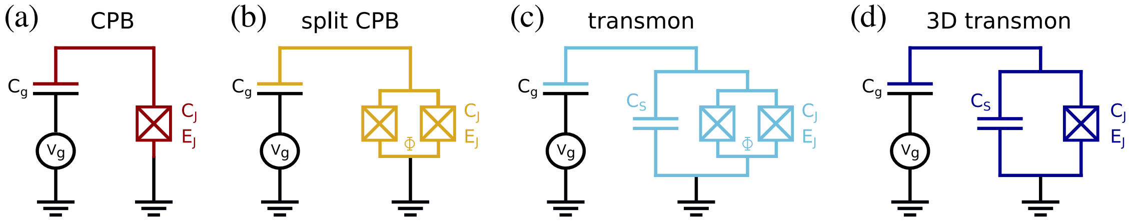

Figure 2.4: Types of charge qubits. (a) a Cooper Pair Box (CPB). (b) A split CPB with tunable Josephson energy. (c) A tunable transmon with split junction. (d) A non-tunable single junction transmon used as a 3D transmon.

A Cooper Pair Box (CPB) is a simple Josephson junction based quantum circuit used as a charge qubit [24, 137, 138, 187]. A small superconducting island is connected on one side via a Josephson junction to a superconducting reservoir, and on the other side coupled to a control gate voltage V_g via a gate capacitor C_g, as shown in Fig. 2.4a. Following [195], the Hamiltonian is obtained from the Lagrangian, which is built with the kinetic energy associated with the capacitor, and with the potential energy determined by the Josephson energy $U(\delta) = E_J(1 - \cos\delta)$. It reads

$$H_{CPB} = 4E_C\left(\hat{N} - n_g\right)^2 - E_J\cos\hat{\delta}\,. \tag{2.29}$$

Here, the first term is the electrostatic energy of the CPB, where $E_C = e^2/2C_\Sigma$ is the charging energy, i.e. the energy needed to add one additional Cooper pair onto the island, the number operator $\hat{N}$ gives the number of excess Cooper pairs on the island, $n_g = C_gV_g/2e$ is the gate induced charge, and $C_\Sigma = C_g + C_J$ is the total capacitance of the CPB to ground given by the sum of the geometric capacitance C_g and the capacitance of the Josephson junction itself C_J. The second term is the energy stored in the Josephson junction which is responsible for the tunnelling of Cooper pairs, with the phase operator $\hat{\delta}$ giving the phase difference across the junction.

Energy levels

The energy eigenstates $|m\rangle$ of this CPB Hamiltonian are obtained by solving

$$\hat{H}_{CPB}|m\rangle = E_m|m\rangle\,. \tag{2.30}$$

The only degree of freedom in the system is the number of excess or deficit Cooper pairs N on the island and it is treated quantum mechanically as the operator $\hat{N}$. The phase operator $\hat{\delta}$ is then defined as the conjugate variable through the commutation relation $[\hat{\delta}, \hat{N}] = i$. The eigenstates and eigenvalues in each basis are given by

$$\hat{\delta}|\delta\rangle = \delta|\delta\rangle \qquad \hat{N}|N\rangle = N|N\rangle\,. \tag{2.31}$$

The respective eigenstates form complete orthonormal bases $\{|\delta\rangle, \delta \in [2\pi]\}$ and $\{|N\rangle, N \in \mathbb{Z}\}$, with the completeness relation $\sum_{N\in\mathbb{Z}} |N\rangle\langle N| = |0\rangle\langle 0| + |1\rangle\langle 1| + |-1\rangle\langle -1| + ... = I$. Through this quantization, the phase operator $\hat{\delta}$ and the number operator $\hat{N}$ can each be written in each other's basis as

$$\hat{\delta}|\hat{N}\rangle = i\frac{\partial}{\partial\hat{N}}|\hat{N}\rangle \qquad \hat{N}|\hat{\delta}\rangle = -i\frac{\partial}{\partial\delta}|\hat{\delta}\rangle\,. \tag{2.32}$$

In the phase basis $|\delta\rangle$ representation the equation Eq. 2.30 can be solved analytically and exactly by using Mathieu functions, see [47, 103] for a detailed discussion. The resulting wavefunctions and eigenenergies E_m are given in terms of the Mathieu functions as

$$E_m(n_g) = E_C a_{2[n_g+k(m,n_g)]}(-E_J/2E_C)\,, \tag{2.33}$$

where $a_r(x)$ is the Mathieu's characteristic value and $k(m, n_g)$ is a function appropriately sorting the eigenvalues. Fig. 2.5 shows a plot of the resulting eigenergies E_m for the first three levels $m = 0, 1, 2$. The Schrödinger equation (2.30) could be equivalently solved in the charge basis $|N\rangle$ representation, albeit is then not analytically solvable. Nevertheless, the charge representation is very useful to gain a more intuitive understanding of the eigentstates E_m level diagram shown in Fig. 2.5, and we therefore discuss it next.

Charge representation

The commutation relation $[\hat{\delta}, \hat{N}] = i$ relates the number states $|N\rangle$ to the phase states $|\delta\rangle$ via the Fourier transform

$$|N\rangle = \frac{1}{2\pi}\int_0^{2\pi} e^{-iN\delta}|\delta\rangle d\delta \qquad |\delta\rangle = \frac{1}{2\pi}\sum_{N\in\mathbb{Z}} e^{iN\delta}|N\rangle \tag{2.34}$$

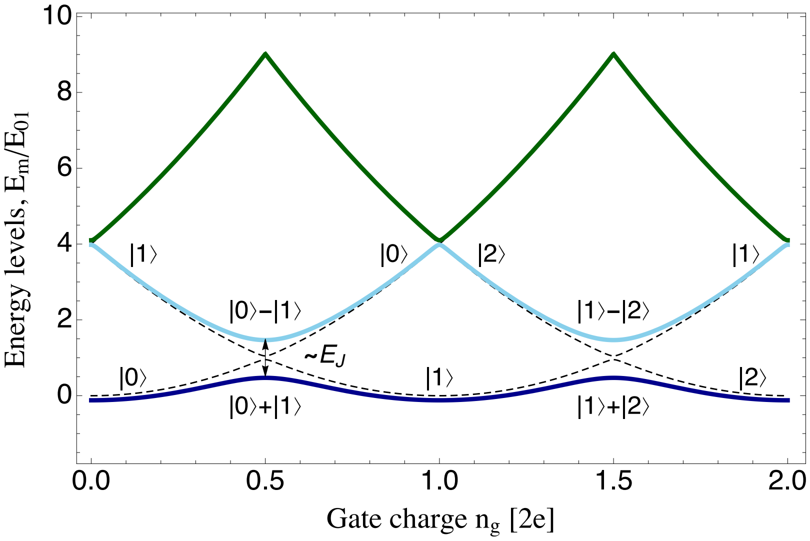

Figure 2.5: Energy level diagram of the Cooper Pair Box showing the eigenergies E_m for the first three levels $m = 0, 1, 2$, as a function of the gate charge n_g, and given in units of the transition energy E_{01} evaluated at the degeneracy point $n_g = 1/2$. The blue, light-blue, and green levels are the ground, first excited, and second excited states respectively. The dashed parabolas show the electrostatic energies of the charge states with a different number of excess Cooper pairs N on the island up to two. The degeneracies of the energies occurring at $n_g = 1/2, 3/2, ...$ are lifted by the Josephson coupling E_J. Here $E_J/E_C = 1$.

The phase operator $\hat{\delta}$ then directly operates on a any number state $|M\rangle$ by lowering or raising the number of Cooper pairs M on the island by one

$$e^{\pm i\hat{\delta}}|M\rangle = |M \mp 1\rangle \,.$$

The operator $e^{i\hat{\delta}}$ has the same effect on a generic state $|M\rangle$ as the operator $\sum_{N\in\mathbb{Z}} |N+1\rangle\langle N|$ would, and therefore we can write

$$e^{i\hat{\delta}} = \sum_{N\in\mathbb{Z}} |N+1\rangle\langle N| \,.$$

With the help of the relation

$$\cos\hat{\delta} = \frac{1}{2}\left(e^{i\hat{\delta}} + e^{-i\hat{\delta}}\right) \,,$$

the Hamiltonian of the CPB is now given in the charge representation as

$$\hat{H}_{CPB} = \sum_{N} [\, 4E_C(\hat{N} - n_g)^2 \, |N\rangle\langle N| \; - \; \frac{E_J}{2} \, (\, |N\rangle\langle N+1| + |N+1\rangle\langle N| \,) \,]. \qquad (2.35)$$

The first term represents the charging energy associated with the number of excess Cooper pairs on the capacitor. The second term describes a Cooper pair tunnelling across the junction in one or the other direction at a rate $E_J/\hbar$. The energy level diagram in Fig. 2.5 is now easier to understand when considering this Hamiltonian. When there is no Josephson coupling $E_J = 0$, we obtain the dashed parabolas (labeled by $|N\rangle$) as the result of the quadratic electrostatic Hamiltonian with a fixed number of Cooper pairs N on the island, each one being shifted on the x-axis by N. Near the crossing of the parabolas, which happens at $n_g = 1/2, 3/2, ...$, the two neighbouring charge states are degenerate. When a Josephson coupling is turned on $E_J > 0$, the coupling between the charge states $|N\rangle$ and $|N+1\rangle$ present in the Hamiltonian mixes the two states, lifting the degeneracy, and thereby leading to an avoided crossing that modifies the energy eigenstates to give new eigenstates with lowest energy $(|0\rangle \pm |1\rangle)/\sqrt{2}$. We define these new symmetric and anti-symmetric superposition states with eigenenergies separated by E_J as the new ground and first excited states $|g\rangle$ and $|e\rangle$. Since in vicinity of such degeneracy points $0 \ll n_g \ll 1$, the coupling energy E_J is only relevant for the new ground and first excited states $|g\rangle$ and $|e\rangle$, higher energy levels are well separated from these first two levels (the anharmonicity is very large), and therefore the system effectively reduces to a two-level quantum system, constituting an effective qubit. This is known as the two-level approximation, which we formally describe next.

Two-level approximation

We consider the CPB Hamiltonian Eq. 2.35 in the charge basis tuned to the sweet spot $n_g = 1/2$ (the tuning is done by controlling the gate voltage V_g). Taking the Hamiltonian for the two lowest energy states only, and performing a Taylor expansion, we obtain

$$\hat{H}_{n_g\approx\frac{1}{2}} = -\frac{\epsilon}{2}(|0\rangle\langle 0| - |1\rangle\langle 1|) - \frac{E_J}{2}(|0\rangle\langle 1| + |1\rangle\langle 0|)\,, \tag{2.36}$$

with $\epsilon = 4E_C(1-2n_g)$, where a constant energy term was subtracted to make ϵ zero at the degeneracy point. Writing the operators $|i\rangle\langle i|$ and $|i\rangle\langle j|$ in terms of Pauli matrices we get

$$H_{n_g\approx\frac{1}{2}} = -\frac{1}{2}(\epsilon\hat{\sigma}_z + E_J\hat{\sigma}_x) = \begin{pmatrix} -\frac{1}{2}\epsilon & -\frac{1}{2}E_J \\ -\frac{1}{2}E_J & \frac{1}{2}\epsilon \end{pmatrix}. \tag{2.37}$$

At the degeneracy point $n_g = 1/2$, the energy difference between the two levels reduces to E_J. This Hamiltonian describes the dynamics of the CPB in the laboratory frame. Since a generic operator $\hat{A}$ can be expanded to $\hat{A} = Tr\hat{A} + \frac{1}{2}\vec{a}\cdot\vec{\sigma}$ with $\vec{a}\cdot\vec{\sigma} = a_x\sigma_x + a_y\sigma_y + a_z\sigma_z$, the CPB Hamiltonian Eq. 2.37 can be visualized as a Bloch vector $\vec{B}$ on the Bloch sphere consisting of the sum of two vectors on the x- and z-axis

$$\hat{H}_{n_g\approx\frac{1}{2}} = \frac{1}{2}\vec{B}\cdot\vec{\sigma}\,, \qquad \text{where} \quad \vec{B} = (-E_J, 0, -\epsilon)\,. \tag{2.38}$$

This simple Hamiltonian can be diagonalised to obtain a new basis where it can be visualized instead as a single vector on the z-axis. The eigenstates and eigenenergies are found to be

$$|g\rangle = \cos\frac{\theta}{2}|0\rangle + \sin\frac{\theta}{2}|1\rangle \tag{2.39}$$

$$|e\rangle = \cos\frac{\theta}{2}|0\rangle - \sin\frac{\theta}{2}|1\rangle \tag{2.40}$$

$$E_{g,e} = \mp\frac{1}{2}\sqrt{\epsilon^2 + E_J^2}\,, \tag{2.41}$$

where $\theta = \arctan(E_J/\epsilon)$ is the mixing angle. This eigenbasis $\{|g\rangle, |e\rangle\}$ is the computational basis used to perform quantum gates. This eigenbasis creates the qubit frame where the qubit Hamiltonian is diagonal and takes on the Hamiltonian of a fictitious spin-1/2 particle in a magnetic field as presented in Section 2.1.1

$$\hat{H} = \frac{1}{2}\hbar\omega_{01}\hat{\sigma}_z \,, \tag{2.42}$$

with energy difference $\hbar\omega_{01} = E_e - E_g = \sqrt{\epsilon^2 + E_J^2}$ between the qubit ground and excited state. In summary, this section demonstrated that a CPB is an effective two-level system that can be implemented as a charge qubit.

2.4.2 The transmon

When biasing the gate voltage to the degeneracy point $n_g = 1/2$, the CPB becomes insensitive to first-order fluctuations of the gate charge and thereby coherence times are much improved [187]. This comes from the fact that the slope of the charge dispersion $\partial E_{01}/\partial n_g$ at that point is null, hence the name "sweet spot". The charge dispersion between neighbouring energy levels is defined as the maximum spread in transition energy

$$\epsilon_{ij} = E_{ij}(n_g = 1/2) - E_{ij}(n_g = 0) \,, \tag{2.43}$$

which quantifies the sensitivity to charge noise, and $E_{ij} = E_j - E_i$ is the energy difference between energy levels i and j.

For the sake of quantum computing however, qubits need long coherence times. As the energy diagram shows a large charge dispersion, the device is highly sensitive to jumps and drifts in the offset charge induced by the environment (charge noise), which changes the qubit transition frequency and thereby causes decoherence. As explained above, operating at the sweet spot reduces this effect substantially to first-order, but the coherence time of the CPB in the charge regime $E_C/E_J \gtrsim 1$ is still limited by the higher-order effects [88], and in practice it requires constant resetting of the gate voltage. The question arises, what values of E_C and E_J allow the longest coherence times? This question was addressed in [103], which suggested operating qubits in the large E_J/E_C limit, for the following reasons. The eigenenergies can be shown to become less sensitive to charge noise for increasing E_J/E_C, as shown in Fig. 2.6. In the limit of large E_J/E_C we obtain

$$\frac{\partial E_{ij}}{\partial n_g} \propto \epsilon_{ij} \sin(2\pi n_g)\,, \tag{2.44}$$

where the charge dispersion decreases exponentially fast with increasing ratio E_J/E_C as

$$\epsilon_{ij} \propto e^{-\sqrt{8E_J/E_C}}\,. \tag{2.45}$$

In other words, energy levels exponentially flatten out and become immune to the change in gate charge n_g. A Cooper pair box operated in this charge insensitive regime $E_J/E_C \gg 1$ has become known as a *transmon* [103]. Physically, the ratio E_J/E_C is increased by increasing the total capacitance $C_\Sigma \propto 1/E_C$ of the transmon. This is achieved by adding a large shunt capacitor C_S [see Fig. 2.4 and Fig. 2.7b) c)] giving a new total capacitance $C_\Sigma = C_J + C_S + C_g$.

The tradeoff for a lower charge noise sensitivity is a decrease in the anharmonicity

$$\alpha = (E_{12} - E_{01})/\hbar\,, \tag{2.46}$$

which leads to a more harmonic oscillator. While the charge dispersion decreases exponentially with E_J/E_C, the anharmonicity only decreases with a weak power law $\alpha =\simeq -(8E_J/E_C)^{-1/2}E_{01}$ [103]. More precisely, the anharmonicity first decreases with increasing E_J/E_C and changes sign at $E_J/E_C \approx 9$, and from thereon the transition E_{12} becomes smaller than E_{01}. Asymptotically, it approaches $\alpha/\hbar \simeq -E_C$ for $E_J/E_C \to \infty$. In this limit, the eigenenergies of the transmon can also be approximated to

$$E_m(n_g) \simeq -E_J + \sqrt{8E_JE_C}\left(m + \frac{1}{2}\right) - \frac{E_C}{12}\left(6m^2 + 6m + 3\right)\,, \tag{2.47}$$

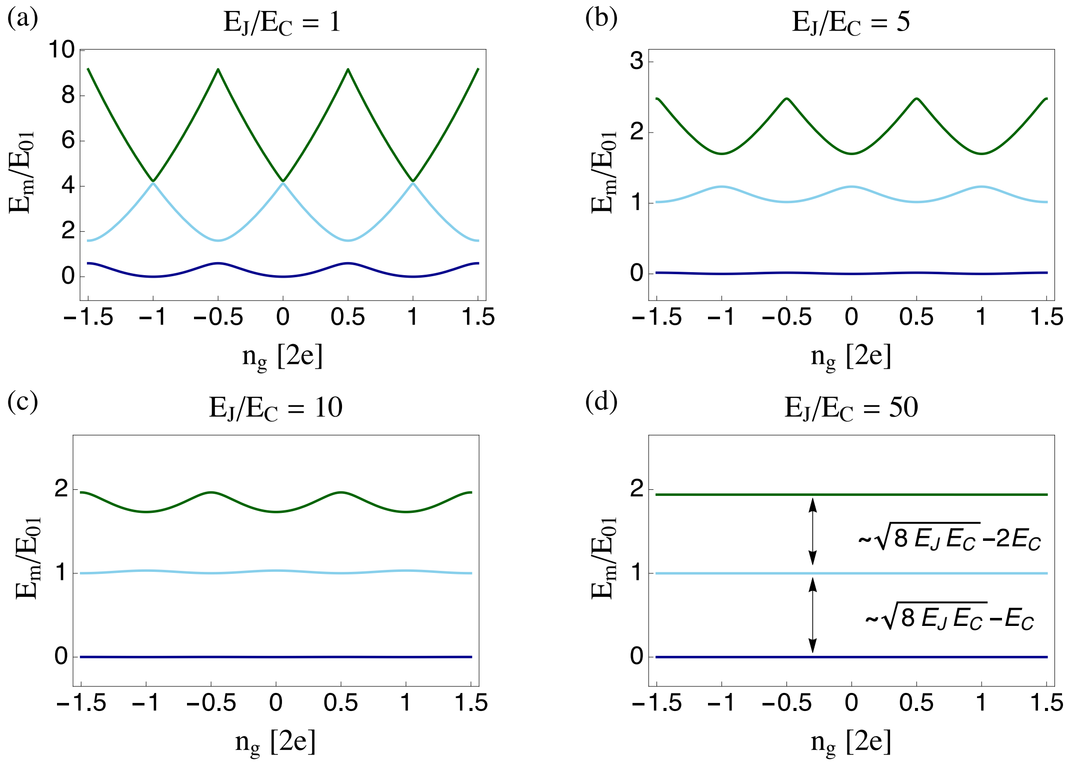

Figure 2.6: Energy diagram of the first three eigenenergies of the qubit Hamiltonian, expressed in units of the transition energy E_{01}, as a function of the gate charge n_g, for different ratios of E_J/E_C. (a) $E_J/E_C = 1$, a Cooper pair box. (b) $E_J/E_C = 5$, the energy levels become flatter. (c) $E_J/E_C = 10$. (d) $E_J/E_C = 50$, the energy levels become entirely flat, setting the CPB in the transmon regime, where it is insensitive to charge noise. Figure reproduced from [103].

with m representing the energy level, and the transition frequencies for the lowest two transitions become

$$E_{01} = \hbar\omega_{01} = E_1 - E_0 \approx \sqrt{8E_CE_J} - E_C \tag{2.48}$$

$$E_{12} = \hbar\omega_{12} = E_2 - E_1 \approx \sqrt{8E_CE_J} - 2E_C. \tag{2.49}$$

Even though the energy level structure of the transmon is only weakly anharmonic, the crucial feature for using it as a qubit is that transitions can be selectively addressed in relative short times ($\sim 4\,\mathrm{ns}$ for our typical $\alpha = 250\,\mathrm{MHz}$). Nonetheless, including sufficiently many energy levels in the models is required to minimise leakage into higher levels [67, 37, 133]. The transition frequency in Eq. 2.48 depends only on the characteristic parameters E_C and E_J, which are initially engineered in the fabrication process. The E_C is fixed, but the E_J can then be tuned in the experiment with a magnetic flux if the Josephson junction is replaced by two Josephson junctions to form a superconducting loop. This tuneability is discussed in the next section.

Tuning the transition frequency

For quantum information processing one may wish to tune the Josephson energy E_J to control the transition frequency of the qubit $\omega_{01} = E_{01}/\hbar$. This is achieved by splitting the Josephson junction into two equal junctions with characteristic Josephson energies ($E_{J,1}$, $E_{J,2}$) and phases ($\hat{\delta}_1, \hat{\delta}_2$), as shown in Fig. 2.4b)c) for a split CPB and a transmon, respectively. An external magnetic flux can be applied through the superconducting loop. Flux quantization sets the relation between the phase difference of the two junctions and the magnetic flux Φ through the loop $\hat{\delta}_1 - \hat{\delta}_2 = 2\pi\Phi/\Phi_0$ [170]. The two junctions being symmetric, the single-junction Hamiltonian Eq. 2.5.2 has an effective Josephson energy $E_J = (E_{J,1} + E_{J,2})\cos(\pi\Phi/\Phi_0)$, which is tunable in Φ, and hence controls the transition frequency Eq. 2.48. Applying a magnetic flux to control the qubit is easily done in 2D circuit QED systems by simply placing a magnetic coil underneath the resonator, or fabricating on-chip flux lines. Unfortunately, it is very difficult to apply a flux in a superconducting 3D cavity without destroying the quality factor of the cavity. If the cavity is made of copper, which is not superconducting, then a coil can be placed underneath the cavity to tune the qubit, at the cost of lower quality factors. Nevertheless, flux tunable aluminium superconducting 3D architectures have been shown with flux bias lines [161] and via a hybrid 3D cavity with a coil [162]. For the purpose of our experiments however, only single junction qubits are used, as depicted in Fig. 2.4d. Since a flux tunable qubit is inherently sensitive to flux noise (external magnetic fields) which leads to decoherence, our single junction qubits have the natural advantage of not being subjected to flux-induced decoherence.

2.5 Circuit Quantum Electrodynamics (cQED)

2.5.1 Cavity QED: matter - light coupling

For quantum computing we need to manipulate and readout the states of qubits using some form of physical interaction. Since the transmon is a two-level system that behaves like a single artificial atom, one can use cavity Quantum Electrodynamics (cavity QED), which studies the interaction between photons and atoms in a cavity. Optical or microwave photons are sent through a highly reflective cavity where they get confined and form quantized electromagnetic modes. Due to the enhancement of the electric field strength in the cavity, a high coupling strength for the electric dipole interaction is achieved even with just a single photon in the cavity. The photon modes can be described as excitations of a quantized harmonic oscillator, which then interact with the two-level system (the qubit), illustrated in Fig. 2.7a. The interactions of this system are described by the Jaynes-Cummings Hamiltonian [91, 22]

$$H = \hbar\omega_c(\hat{a}^\dagger\hat{a} + \frac{1}{2}) + \frac{1}{2}\hbar\omega_{01}\hat{\sigma}_z + \hbar g(|0\rangle\langle 1| + |1\rangle\langle 0|)(\hat{a}^\dagger + \hat{a}) + H_\kappa + H_\gamma. \tag{2.50}$$

The first three terms describe the coherent dynamics of the photon-atom system, whereas the two last terms describe decoherence effects of the system. The first term is the usual energy of a quantum harmonic oscillator describing the single mode of the electromagnetic field in the cavity with resonance frequency ω_c, where the energy of each photon in the cavity is $\hbar\omega_c$. The operators $\hat{a}^\dagger$ and $\hat{a}$ are the photon creation and annihilation operators. The second term describes the energy of the atom as a two-level system with transition energy $\hbar\omega_{01}$, with spin eigenstates measured along the z-axis by the Pauli z-operator $\sigma_z = (|1\rangle\langle 1| - |0\rangle\langle 0|)$. The third term describes the interaction between the photons and the atom. It contains the coupling strength g which expresses the rate at which the atom absorbs photons via $\hat{a}|1\rangle\langle 0|$ and emits photons via $\hat{a}^\dagger|0\rangle\langle 1|$. The interaction terms describing simultaneous excitation (de-excitation) of both the atom and the resonator field mode (they do not conserve energy) can be dropped by using the rotating wave approximation. This approximation [91] arises by moving from the Schrödinger picture to the Heisenberg picture (rotating frame) where the fast oscillating counter-rotating terms can be ignored in the regime where $g \ll \omega_c, \omega_{01}$ and $|\Delta_0| = |\omega_{01} - \omega_c| \ll \omega_{01} + \omega_c$. The Hamiltonian then reduces to

$$H = \hbar\omega_c \hat{a}^\dagger \hat{a} + \frac{1}{2}\hbar\omega_{01}\hat{\sigma}_z + \hbar g(|0\rangle\langle 1|\hat{a}^\dagger + |1\rangle\langle 0|\hat{a}) + H_\kappa + H_\gamma. \tag{2.51}$$

Here the vacuum field energy $\hbar\omega_c/2$ was set to zero. This Hamiltonian for a coupled two-level system is analytically diagonalisable after the rotating wave approximation, which allows us to find the eigenstates in Section 2.5.4. Furthermore, the term H_κ expresses the dissipative loss since the cavity is coupled to the environment. There is a photon decay rate κ which is determined by the ratio of the resonance frequency and the quality factor of the cavity $\kappa = \omega_c/Q$. The last term expresses the coupling of the atom to modes other than the cavity mode which cause the excited state to decay at rate γ. Reducing the decay times by engineering a high quality cavity allows for the strong coupling regime $g \gg \kappa, \gamma$ and vacuum Rabi oscillations [22, 190], where the atom constantly absorbs and reemits a photon at the Rabi frequency g/π.

As discussed in Section 2.2, Fig. 2.2, and Section 2.4.1 the transmon has anharmonic energy levels and therefore the first two states can be isolated and selectively addressed for use as a qubit, i.e. as an artificial atom for cavity QED, leading to so-called circuit QED (cQED). Due to the small anharmonicity $\alpha \approx E_C$ of the transmon,

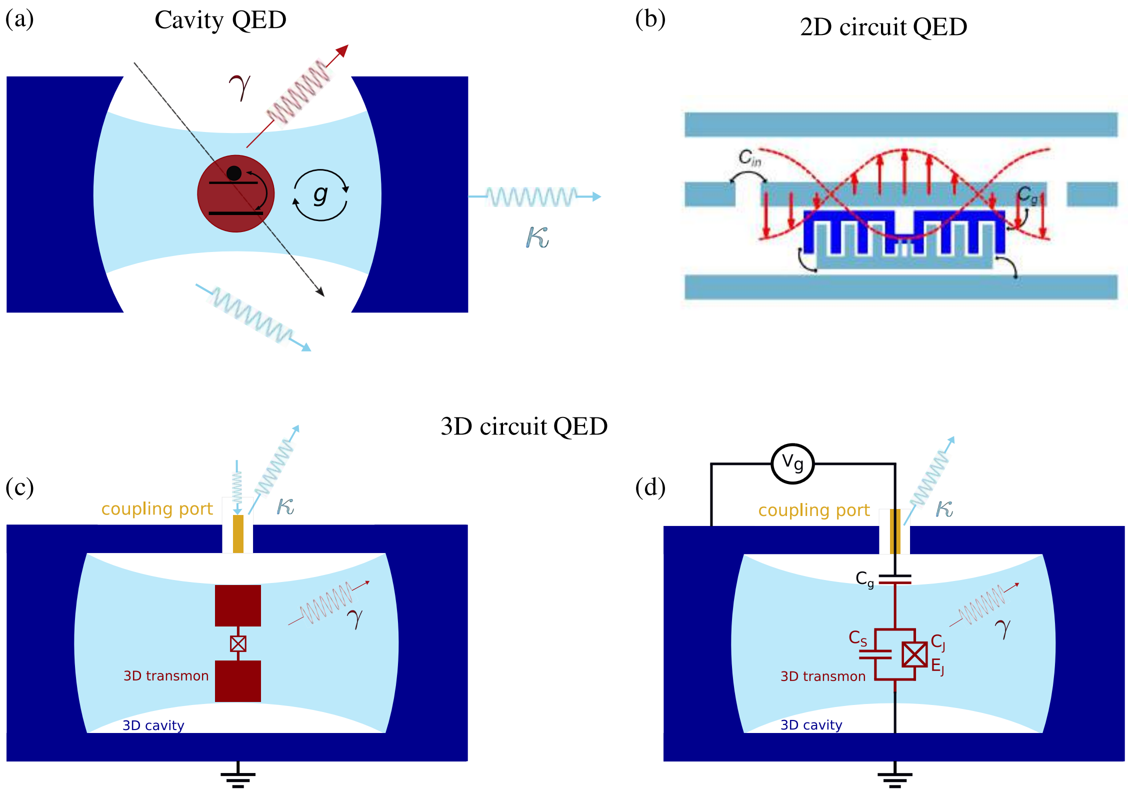

Figure 2.7: (a) A schematic representation of cavity QED. Strong coupling is achieved when the coupling strength g is much larger than the decay rates γ, κ of the cavity and atom. (b) Schematic of 2D on-chip circuit QED, taken from [103], showing the CPW resonator and the coupled transmon. (c) 3D circuit QED. The atom is replaced by a superconducting circuit (transmon) in a closed 3D cavity. (d) Schematic with circuit diagram of (c).

however, (which can be 100-400 MHz), leakage to higher states is significant, and we must consider the couplings to higher levels of the transmon, and the system will therefore be described by the generalized Jaynes-Cummings Hamiltonian presented in Section 2.5.3.

2.5.2 Circuit QED : transmon - photon coupling

The transmon has a large dipole moment due to its large physical size, and this significantly enhances the coupling strength to a photon in a cavity compared to that of an atom described in Section 2.5.1. Indeed the dipole moment of a 3D transmon is given by $d = 2el$ where l is the average distance that separates Cooper pairs $2e$ on the two islands (electrodes of the transmon, see Fig. 2.7c). A typical transmon has $l \simeq 1\,\mathrm{mm}$ and hence a dipole moment of $d \simeq 10^8$ Debye. This beats the dipole moments reached for Rydberg atoms by four orders of magnitude [23]. The transmon's strong coupling to light comes with the drawback of faster spontaneous decay in vacuum. The associated lifetime is given by $\gamma = \hbar\omega_{01}/P_d = 12\hbar\pi c/(\mu_0\omega_{01}^3 d^2)$, where P_d is the power radiated by an oscillating dipole d. Taking the typical transition frequency of the transmon $\omega_{01}/2\pi = 6\,\mathrm{GHz}$ gives it a spontaneous decay lifetime of $\gamma = 17\,\mu\mathrm{s}$. This spontaneous emission can be suppressed by placing the transmon in a resonant circuit or cavity (Purcell effect, see Section 2.5.5), as the density of states available for the emitted photons is reduced.

Realising a cavity QED system with superconducting electrical circuits (cQED) was proposed in [22], and it was first realized in [190]. A good overview is given in [170]. In circuit QED, the transmon plays the role of the atom from cavity QED, and an electrical resonator plays the role of the cavity. The electric field of the standing waves trapped in the resonator couple to the qubit. For traditional 2D circuit QED it is a 1D transmission line resonator, which is capacitively coupled to input and output lines. The transmission line is modelled with the distributed element model [121], because microwaves are high-frequency waves and have wavelengths which approach the physical dimensions of the circuit, making thus the lumped element model inaccurate. The 1D transmission line resonator is physically realised with a coplanar waveguide (CPW) resonator, depicted in Fig. 2.7b. It resembles the cross section of a coaxial cable in two-dimensions. The fact that the resonator is one dimensional constrains the electromagnetic field into a very mall volume, thereby rendering a higher field intensity and very strong coupling.

We use instead the proposed three-dimensional architecture [148], shown in Fig. 2.7 c)d), using a rectangular waveguide cavity machined from superconducting aluminium (see Chapter 5). The two main reasons for this choice are that a high quality factor ($> 10^6$) can more easily be reached when making a 3D cavity, and the electric field strength of the 3D cavity mode and qubit are lower, which leads to a reduced coupling to defects in the qubit substrate that causes decoherence. Our transmon is engineered with a larger shunting capacitance, making its dipole moment larger than conventional 2D qubits. This will not only compensate for the reduced electric field of the photon in the 3D cavity, but also reduce the qubit charging energy E_C, and hence the sensitivity to the dielectric losses. Superconducting qubits in 3D cavities have demonstrated the longest coherence times to date for Josephson junction based qubits, with energy relaxation times over $T_1 > 70\,\mu$s and dephasing times $T_2 > 90\,\mu$s [163, 53].

We can estimate the coupling strength achieved for such a 3D transmon-cavity system by defining the *rms* electric field strength in the cavity as $E_{rms} = \sqrt{\hbar\omega_c/\epsilon_0 V_c}$, where V_c is the volume of the cavity and ϵ_0 the dielectric vacuum constant. Then the coupling strength g is given by $g = 2elE_{rms}\hbar$. Our cavity has a typical dimension of $1.2\,\mathrm{cm}^3$, resonance frequency $\omega_c/2\pi = 10.5\,\mathrm{GHz}$, and the transmon is an electric dipole of dimension of $l = 950\,\mu\mathrm{m}$, which leads to a strong estimated coupling strength of $g/2\pi \simeq 360\,\mathrm{MHz}$.

As discussed in Section 2.4.2, the transmon is insensitive to DC voltage, but it still couples to an AC voltage oscillating close to its transition frequency [104]. The superconducting qubit is subjected to the oscillating electric field of the cavity mode (photon), which causes a voltage difference across the qubit electrodes. In quantum information processing experiments, the realized qubit interacts with a single photon on average in the resonator and therefore both systems must be treated quantum mechanically, i.e. the cavity mode causes a quantum voltage $\hat{V}$. Recall the standard CPB Hamiltonian describing the qubit $\hat{H}_{CPB} = 4E_C(\hat{N} - n_g^{DC})^2 - E_J \cos\hat{\delta}$. It is coupled capacitively to the cavity via a voltage V_g, which applies a voltage βV_g across the junction, with $\beta = C_g/C_\Sigma$ the voltage division factor that expresses the ratio of the effective capacitance C_g of one side of the transmon (electrode) to the cavity to total capacitance. This voltage alters the energy of the CPB, and when coupled to a quantized cavity mode with $\hat{V} = \hat{Q}/C$, it becomes

$$V_g = V_{DC} + \hat{V}. \tag{2.52}$$

This voltage allows for both a classic charge bias and quantum state control of the observable $\hat{N}$. Since the resonator is modelled as an LC circuit, the charge operator $\hat{Q}$, see Eq. 2.14 inSection 2.2, is given by $\hat{Q} = i\sqrt{\hbar/2Z_0}(\hat{a}^\dagger - \hat{a})$ with $Z_0 = \sqrt{L/C} = \omega_c C$. Substituting it into $\hat{V} = \hat{Q}/C$ leads to the quantum gate voltage

$$\hat{V} = \sqrt{\frac{\hbar\omega_c}{2C}}(\hat{a} + \hat{a}^\dagger) = V_{rms}^0(\hat{a} + \hat{a}^\dagger),$$

where V_{rms}^0 is the root-mean-square (*rms*) voltage at the qubit position per photon of the oscillator. Having quantized the cavity, substituting the gate voltage Eq. 2.52 into the gate induced charge $n_g = -C_g V_g/2e$ from the electrostatic term in the CPB Hamiltonian and expanding the square (see details in [170, 11]), one obtains a new term describing the cavity-qubit coupling, giving the total Hamiltonian

$$\hat{H} = 4E_C(\hat{N} - n_g^{DC})^2 - E_J \cos\hat{\delta} + \hbar\omega_c \hat{a}^\dagger\hat{a} + 2e\beta V_{rms}^0(\hat{a}^\dagger + \hat{a})\hat{N}\,. \tag{2.53}$$

The first two terms correspond to the normal CPB Hamiltonian under DC bias. The third term is the resonator energy, and the fourth term represents the cavity-qubit coupling.

2.5.3 The generalized Jaynes-Cummings Hamiltonian

Rewriting this Hamiltonian in the basis of the uncoupled CPB eigenstates $|i\rangle$ from Eq. 2.30, one obtains the generalized Jaynes-Cummings Hamiltonian

$$\hat{H} = \hbar\,\omega_c\,\hat{a}^\dagger\hat{a} + \hbar\sum_{i=1}^{N-1}\omega_i|i\rangle\langle i| + \hbar\sum_{i,j} g_{ij}|i\rangle\langle j|(\hat{a}^\dagger + \hat{a})\,, \tag{2.54}$$

with coupling energies

$$\hbar g_{ij} = 2\beta e V^0_{rms}\langle i|\hat{N}|j\rangle = \hbar g^*_{ji}\,, \tag{2.55}$$

where $\hbar\omega_i$ are the N transmon energy levels, and the lowest qubit level with energy $E_0 = \hbar\omega_0$ is set to zero. In the limit with large E_J/E_C, the non-nearest-neighbour matrix elements $\langle j+k|\hat{N}|j\rangle$ are nearly zero for all $|k| > 1$, and only the nearest-neighbour matrix elements $\langle j+1|\,\hat{N}\,|j\rangle$ are finite. This is obtained by evaluating the number matrix elements [103]

$$|\langle j+1|\hat{N}|j\rangle| \approx \sqrt{\frac{j+1}{2}}\left(\frac{E_J}{8E_C}\right)^{1/4}\,, \tag{2.56}$$

$$|\langle j+k|\hat{N}|j\rangle| \to 0 \qquad \text{for}|k| > 1. \tag{2.57}$$

The only relevant coupling in the transmon limit is the therefore the nearest-neighbour coupling $g_{i,i+1}$ which is proportional to E_J/E_C. It is the only coupling not suppressed by the shunting capacitance. In the regime where $g_{i,i+1} \ll \omega_i, \omega_c$ and the detunings $\Delta_i = |\omega_{i,i+1} - \omega_c| \ll \omega_{i,i+1} + \omega_c$, with $\omega_{i,j} = \omega_j - \omega_i$ being the transition frequency between energy levels i and j, we use the rotating wave approximation to obtain the significantly simplified generalized Hamiltonian

$$\hat{H} = \hbar\,\omega_c\,\hat{a}^\dagger\hat{a} + \hbar\sum_{i=1}^{N-1}\omega_i|i\rangle\langle i| + \left(\hbar\sum_{i=0}^{N-2} g_{i,i+1}|i\rangle\langle i+1|\hat{a}^\dagger + H.c.\right)\,, \tag{2.58}$$

where the levels $|i\rangle$ and $|i+1\rangle$ are connected through the ladder operators. Two cases for the cavity-qubit interaction in Eq. 2.58 arise: the resonant case with $\omega_{01} \approx \omega_c$, and the dispersive case with large detuning $\omega_{01} - \omega_c \gg g$. As opposed to the reduced coupled two-level system Hamiltonian in (2.51), this generalized effective Hamiltonian does not have an exact analytical solution for the resonant case when considering more than the first two levels of the transmon $N > 2$. It does however for the dispersive case, as is discussed in Section 2.5.5. Nevertheless, it is useful here to first solve the resonant case with only the two-level Hamiltonian $N = 2$ to understand the cavity-qubit coupling effects in terms of hybridized energy levels.

2.5.4 Eigenstates of the two-level Jaynes-Cummings Hamiltonian

The generalized Hamiltonian Eq. 2.58 for the resonant case can be analytically solved for $N = 2$ and reads the eigenenergies [78]

$$E_{\pm}^{(n)} = n\hbar\omega_c \pm \frac{\hbar}{2}\sqrt{\Delta_0^2 + 4g_{01}^2(n)}\,, \tag{2.59}$$

$$E_0^{(0)} = -\frac{1}{2}\hbar\Delta_0\,. \tag{2.60}$$

where the corresponding eigenstates given by

$$|+, n\rangle = \cos(\theta_n)|e, n-1\rangle + \sin(\theta_n)|g, n\rangle \tag{2.61}$$

$$|-, n\rangle = -\sin(\theta_n)|e, n-1\rangle + \cos(\theta_n)|g, n\rangle\,, \tag{2.62}$$

constitute the *Jaynes-Cummings ladder* shown in Fig. 2.8a. The detuning $\Delta_0 = \omega_{01} - \omega_c$ between the qubit and cavity controls the degree of hybridization of the qubit with the cavity via

$$\tan(2\theta_n) = \left(\frac{2g_{01}\sqrt{n}}{\Delta_0}\right)\,. \tag{2.63}$$

We use the labels g, e here in order to avoid confusion with the photon number states $n = 0, 1, 2, 3, \ldots$.

Near resonance $\omega_{01} \sim \omega_c$ the qubit ground $|g\rangle$ and excited $|e\rangle$ states and the photon number state $|n\rangle$ are not eigenstates of the full Hamiltonian anymore. Indeed, the new eigenstates (called dressed states) are superpositions of qubit and cavity states $|\pm, n\rangle = (|g\rangle|n\rangle \pm |e\rangle|n-1\rangle)/\sqrt{2}$ due to the interaction term (exchange of energy quanta) lifting the degeneracy of the uncoupled states $|g, n\rangle$ and $|e, n-1\rangle$. These two new eigenstates are symmetric and antisymmetric superposition states that are maximally entangled (hybridized), meaning that the qubit and cavity can no longer be considered as individual systems, and are split in energy by $\hbar 2 g_{01}\sqrt{n}$, as shown in the level diagram in Fig. 2.8a. For one excitation $n = 1$ the splitting is called vacuum Rabi mode splitting, which in the time domain results in Rabi oscillations. The qubit initially in the ground state interacts with one photon inside the cavity if it is resonant and flips into the excited state by absorbing the photon $|g, 1\rangle \rightarrow |e, 0\rangle$. Then the resonator vacuum fluctuations cause the qubit to emit a photon and flip back into its ground state, and this absorption-emission process repeats itself at a rate $2g_{01}$ leading to *vacuum Rabi oscillations* between $|g, 1\rangle$ and $|e, 0\rangle$. If the resonator is populated with more than one photon, the process will occur at a frequency $g_{01}\sqrt{n}/\pi$, and this $\sqrt{n}$ scaling is a feature that is exclusively quantum. It has been observed directly in circuit QED [67].

For the other case where the system is in the dispersive limit with a large detuning (far off resonance), the qubit and cavity don't exchange photons anymore because the detuning is much larger than coupling, and in fact the result is not a splitting of the dressed energy levels, but only a shift in the energy levels. This regime is presented in the next section where the dispersive regime is discussed.

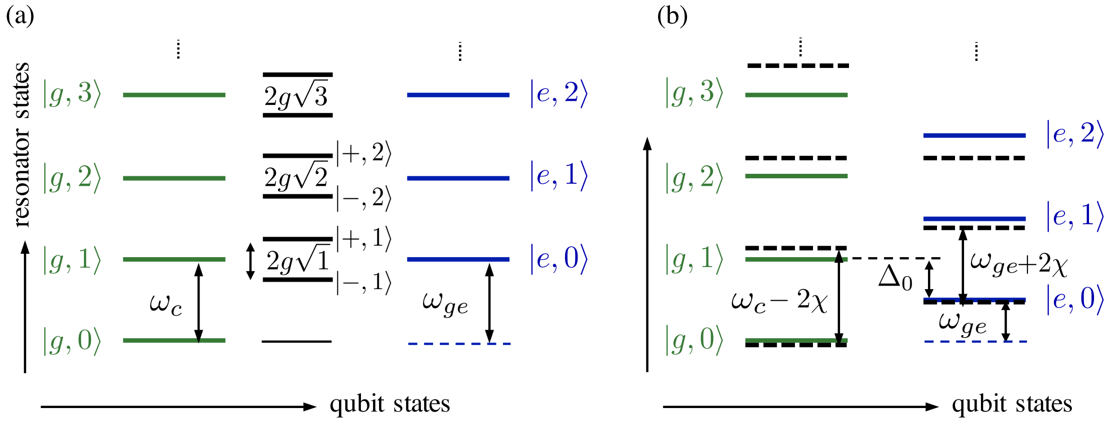

Figure 2.8: (a) Energy level diagram of the dressed Jaynes-Cummings eigenstates (black), for two transmon levels. The uncoupled energy ladder of the uncoupled cavity (green) and qubit (blue) product states $|g,n\rangle$ and $|e,n\rangle$. In the resonant case when $\Delta_0 = \omega_{eg} - \omega_c = 0$, the degeneracy of the qubit-photon states is lifted by the strong coupling g and is split in frequency by $2g\sqrt{n}$, forming new dressed states $|\pm,n\rangle$ (black levels) consisting of symmetric and antisymmetric doublets with n photons and a qubit excitation. (b) Energy level diagram in the dispersive regime $|\Delta_0| \gg g$. The coupling through the dispersive interaction manifests itself only as a shift of the energy levels.

2.5.5 Dispersive regime

The cavity resonator is used as an indirect measurement channel for Quantum Non-Demolition (QND) measurements [22], in addition to mediating the interaction between qubits. A QND measurement does collapse the transmon state, but does not subsequently interfere with the state evolution, meaning that it leaves the qubit in the pure eigenstate. The qubit with transition frequencies $\omega_{i,i+1}$ is designed to be situated in the charge-insensitive transmon regime and to operate in the *dispersive limit* where the detunings $\Delta_i = \omega_{i,i+1} - \omega_c$ between transmon and cavity are large, where $\omega_{ij} = \omega_j - \omega_i$. This means that the detunings are much greater than the couplings of the qubit transitions to the cavity resonance $\Delta_i \gg g_{i,i+1}$, in particular $|\Delta_0| \gg g_{01}$, $|\Delta_1| \gg g_{01}$. A large detuning suppresses any excitations exchanged by the qubit and the cavity, i.e. the resonator suppresses the local electromagnetic density of states at the detuned qubit frequency, thus inhibiting excited sate decay. But they still interact via the dispersive interaction which manifests itself as a shift in the coupled qubit-cavity energy levels as shown in Fig. 2.8b, which enables readout of the qubit state by measuring the influence it has on the cavity resonance [191, 18]. To understand this dispersive interaction, recall the Jaynes-Cumming Hamiltonian in Eq. 2.50 describing a superconducting cavity coupled to a transmon. Applying a unitary transformation that eliminates the direct interaction between the resonator and the transmon, as described in [104], where due to the small anharmonicity of the transmon at least three energy levels must be included in this transformation. Then expanding the Hamiltonian in powers of g/Δ gives to second order

$$\hat{H}_{disp}/\hbar = \omega_c \hat{a}^\dagger \hat{a} + \sum_{i=0}^{N-1} \omega_i |i\rangle\langle i| + \sum_{i=0}^{N-1} \chi_{i,i+1} |i+1\rangle\langle i+1| \tag{2.64}$$

$$- \chi_{01} \hat{a}^\dagger \hat{a} |0\rangle\langle 0| + \sum_{i=1}^{N-1} (\chi_{i-1,i} - \chi_{i,i+1}) \hat{a}^\dagger \hat{a} |i\rangle\langle i| \,, \tag{2.65}$$

where $\chi_{i,i+1} = g_{i,i+1}^2/\Delta_i$ are known as the “partial” dispersive energy shifts, or dispersive couplings between the resonator and the qubit. The first and second term here are simply the cavity and transmon energies. The third and fourth terms express a renormalization of the qubit respectively cavity energies, whereas the fifth term represents the state-dependent dispersive shifts.

Dispersive regime for the two-level system

We again make the two-level approximation, but keep coupling terms including the coupling to the second excited level, to obtain the dispersive Hamiltonian as

$$\hat{H}_{disp}/\hbar = \frac{1}{2}\left(\omega_{01} + \frac{g_{01}^2}{\Delta_0}\right)\hat{\sigma_z} + \left(\omega_c - \frac{g_{12}^2}{2\Delta_1} + \chi\hat{\sigma}_z\right)\hat{a}^\dagger \hat{a} \,, \tag{2.66}$$

with χ the dispersive shift. For a pure two level system the dispersive shift would simply be $\chi = \chi_{01}$, but for the transmon it is $\chi = \chi_{01} - \chi_{12}/2$ due to pairwise coupling of higher energy levels. In the transmon limit $E_J/E_C \gg 1$, the dispersive shift χ can be approximated as [103]

$$\chi \simeq -\frac{g_{01}^2 E_C}{\Delta_0(\Delta_0 - E_C)}\,. \tag{2.67}$$

The Hamiltonian Eq. 2.66 is identical to the one we would have obtained with a pure two-level system by defining the renormalized resonator frequency $\tilde{\omega}_c = \omega_c - g_{12}^2/2\Delta_1$ and renormalized qubit frequency $\tilde{\omega}_{01} = \omega_{01} + g_{01}^2/\Delta_0$. The renormalized parameters come from the fact that this Hamiltonian models the transmon as an effective two-level system (a qubit) but includes the effects on these levels introduced by the interaction with the third level. The resonator renormalization $\tilde{\omega}_c$ is induced by coupling to higher transmon energy levels, whereas the qubit transition frequency renormalization $\tilde{\omega}_{01}$, called the Lamb shift, is induced by the vacuum fluctuations in the cavity [68]. The term in Eq. 2.64 corresponding to the exchange of excitations between the transmon and the resonator has vanished in Eq. 2.66 and has been substituted by the term $\chi\hat{\sigma_z}\hat{a}^\dagger\hat{a}$. This term can be interpreted in two ways leading to two equivalent pictures by regrouping the terms to give

$$\text{cavity shifted :} \qquad \hat{H}_{disp,c}/\hbar = \frac{1}{2}\tilde{\omega}_{01}\hat{\sigma_z} + (\tilde{\omega}_c + \chi\hat{\sigma_z})\hat{a}^\dagger\hat{a}\,, \tag{2.68}$$

$$\text{or} \tag{2.69}$$

$$\text{qubit shifted :} \qquad \hat{H}_{disp,q}/\hbar = \frac{1}{2}(\tilde{\omega}_{01} + 2\chi\hat{a}^\dagger\hat{a})\hat{\sigma_z} + \tilde{\omega}_c\hat{a}^\dagger\hat{a}\,. \tag{2.70}$$

In the first picture $\hat{H}_{disp,c}$, the resonator frequency is shifted by a qubit state-dependent dispersive shift χ. In the second picture, it is the qubit frequency that is shifted by the so-called ac-Stark shift $2\chi\hat{a}^\dagger\hat{a}$ that depends on the number of photons $n = \hat{a}^\dagger\hat{a}$ in the cavity. The qubit shift picture is studied and presented in Section 6.3.

We mostly focus on the cavity shift picture for the purpose of our experiments because we are interested in using this picture for the readout scheme. When the qubit is in state $|0\rangle$ the renormalized cavity resonance is $\tilde{\omega}_c - \chi$, whereas when the qubit is in the excited state $|1\rangle$ the cavity is at $\tilde{\omega}_c + \chi$, seen in Fig. 2.9 for the transmission amplitude or phase. In other words, the two level system of the qubit is mapped onto the positive or negative shift of the resonator frequency $\tilde{\omega}_c$. For the case of transmons, both the ground and excited state peaks are moved up in frequency relative to the undressed cavity frequency ω_c, but the ground state is shifted more, by what we call $2\chi = g_{01}^2/\Delta_0$. Thus, in that case, ω_c does not have physical significance and is instead a convenient frequency with which to write the Hamiltonian. This 2χ shift, which is greater than the cavity linewidth, is precisely the effect that we exploit to perform quantum non-demolition readout of the qubit state. Measuring transmission and distinguishing between high and low transmitted amplitude infers the qubit state [191, 170]. Equivalently, the phase of the transmission is given by $\delta = \pm \tan^{-1}(2g^2/\kappa\Delta)$ and reflects the shift likewise.

Henceforth we define the dispersive shifts χ_i for qubit levels $i = 0, 1, 2, 3, 4, ...$ as the shifts from the cavity's bare resonance frequency ω_c to the qubit state dependent resonance frequency $\omega_i = \omega_c + \chi_i$, as seen in Fig. 7.9 in Section 7.6. Furthermore, we keep the definition of χ as in Eq. 2.67, and $2\chi/2\pi$ is the frequency difference between the ground state resonator $\omega_0/2\pi$ (sometimes labeled as ω_r) and excited state resonator $\omega_1/2\pi$.

Operating in the dispersive regime in order to perform readout of the qubit state does not prevent qubit control with microwave drives near resonant with the qubit frequency, as in Section 6.4.1. In the dispersive regime, even though the qubit drive frequency is strongly detuned from the resonator frequency, the resonator can still be populated with n_s drive photons which induce Rabi oscillations in the qubit at a

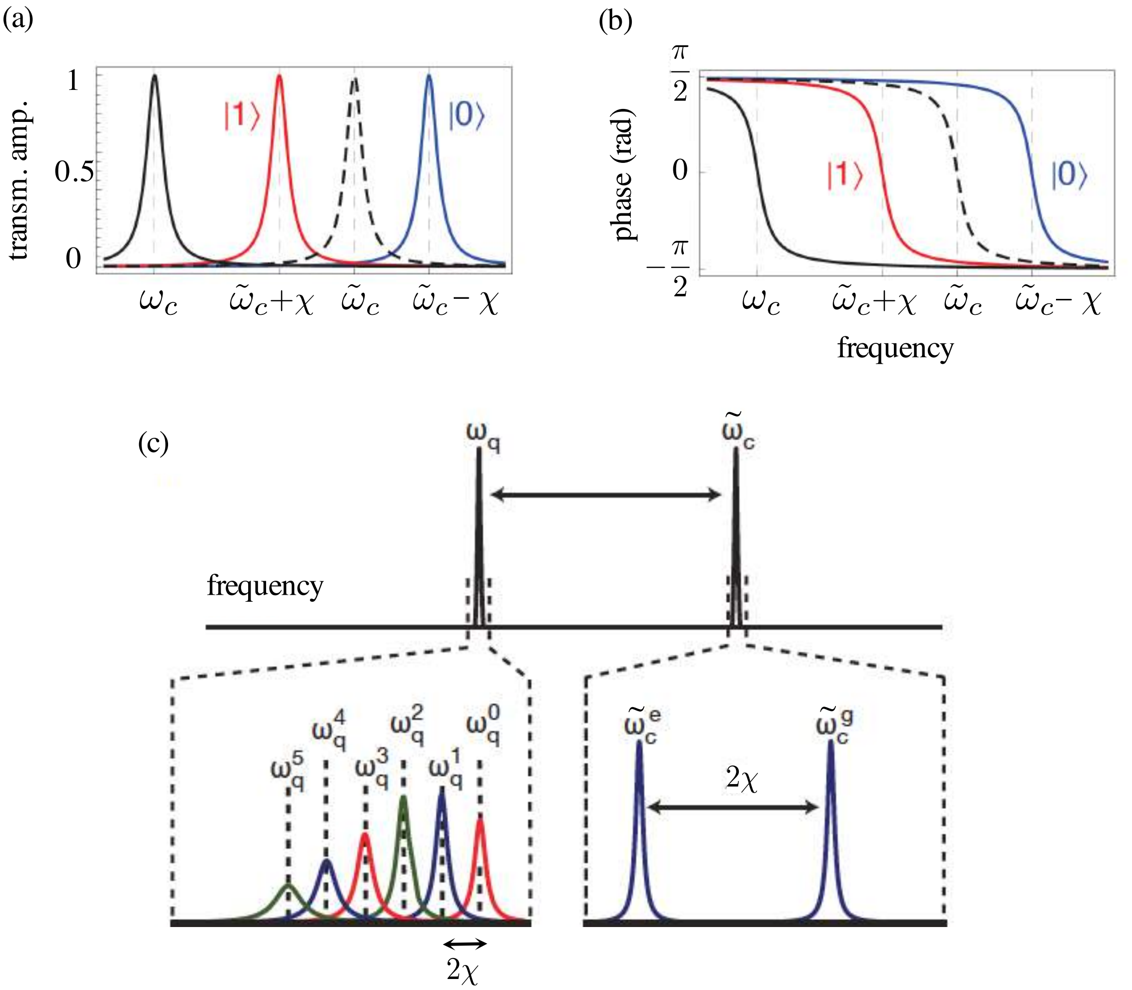

Figure 2.9: (a)(b) Transmission amplitude and phase respectively in the dispersive regime of the uncoupled resonator at its bare resonance ω_c frequency (black), and for the coupled cavity-qubit system with the renormalized frequency $\tilde{\omega}_c$ conditionally shifted by the state of the qubit to $\tilde{\omega}_c \pm \chi$ (red,blue). Figure taken from [11]. (c) In the dispersive regime, a qubit excitation results in a shift in transition frequency of the cavity and vice versa. In the qubit-shift (left box) picture the number of photons n in the cavity shifts (ac-Stark shift) the qubit frequency by $2\chi n$, this is called photon number splitting. In the cavity-shift (right box) picture the cavity splits depending on the qubit state. These number splittings allow probing of the excitation number of either the qubit or cavity mode, and can be used for readout measurements or entanglement generation. Figure taken from [170].

Rabi frequency of

$$\Omega_{Rabi} = 2\sqrt{n_s}g. \tag{2.71}$$

In contrast with the dispersive readout measurement of the qubit, a qubit drive $\omega_d = \omega_{01}$ does not measure the state of the qubit in this limit, because the transmitted signal only shows a very small difference in phase and amplitude for the two different qubit states. Hence, no unwanted entanglement between the resonator photons and qubit when controlling the state of the qubit [21].

Returning to the eigenstates Eq. 2.61 that solved the Jaynes-Cummings Hamiltonian for $N = 2$ in the resonant regime $\Delta_0 \sim 0$, we can now approximate these eigenstates in the dispersive regime $\Delta \gg g_{01}$ using $\cos\theta \sim \theta$ and $\sin\theta \sim 0$ for small θ to give

$$|+, n\rangle = |e, n-1\rangle + \frac{g_{01}}{\Delta_0}|g, n\rangle \tag{2.72}$$

$$|-, n\rangle = -\frac{g_{01}}{\Delta_0}|e, n-1\rangle + |g, n\rangle\,, \tag{2.73}$$

together with the ground state $|g, 0\rangle$. It becomes evident that in the dispersive regime the eigenstates mostly reduce to $|+, n\rangle \approx |e, n-1\rangle$ and $|-, n\rangle \approx |g, n\rangle$. Since $|e, n-1\rangle$ and $|g, n\rangle$ represent the uncoupled product states, the qubit and cavity nearly behave as individual systems, where their dispersive interaction only shifts the energy levels by a small amount g_{01}/Δ_0, illustrated in Fig. 2.8. We can therefore define a computational basis for our qubit as $|0\rangle = |-, 0\rangle = |g, 0\rangle$ and $|1\rangle = |+, 1\rangle = |e, 0\rangle$ that consists mainly of the transmon states $|g, 0\rangle$ and $|e, (n-1)\rangle$, with only a small additional photonic component of magnitude g_{01}/Δ_0.

Purcell decay in 3D cavity

This small photonic component of the resonator is a source of decay for the computational qubit state $|1\rangle$, because it allows the qubit to spontaneously de-excite by emitting a photon into the resonator at the cavity decay rate κ. This results in a new qubit decay rate [85, 84]

$$\gamma = \left(\frac{g_{01}}{\Delta_0}\right)^2 \kappa \,, \tag{2.74}$$

which is called the *Purcell effect.* In 3D circuit QED, our superconducting 3D cavities are designed with cavity decay rate κ reduced and a large detuning Δ_0 in order to guarantee qubit lifetimes are not shortened by the Purcell effect.

Chapter 3

Experimental Techniques

This chapter describes the experimental setup for our 3D circuit QED experiments and the measurement techniques used. The designing and building of the entire setup was a large part of the work performed for this thesis. We first present aspects of the cryogenic environment, then the microwave input and output lines with their chains of components are described, and finally we explain the microwave pulse generation and signal processing to control and measure the qubit.

3.1 Cryogenic microwave setup

In circuit QED experiments the transmons are typically engineered to have transition frequencies ν_{01} in the microwave range 5 GHz to 9 GHz. In order to initialise the qubits into the ground state and to prevent spontaneous thermal excitation, it is necessary to cool the devices to a temperature well below the corresponding temperature $T_q = h\nu/k_B \sim 230$ and 430 mK. Therefore, the devices are placed inside a dilution refrigerator and thermally anchored to its 10 mK base, and shielded from any thermal radiation. Cooling to this ultra-low temperature also brings our quantum electrical circuit into the superconducting state, eliminating resistive dissipation, which is one of the fundamental requirements to enable coherence of the qubit. The material of the circuit in our case is ultra-pure aluminium with a critical temperature of $T_c \approx 1.2\,\mathrm{K}$, indeed well above our fridge's base temperature. In the same manner, the 3D cavity acquires a high quality factor only when its interior walls are superconducting, because photons would dissipate rapidly in walls with a finite conductivity. In addition to the low temperature, our experiments require the interaction of the qubit with a single photon, i.e. a single quantum of energy, which in effect means controlling microwave signals to extremely low powers, on the order of less than $10^{-17}\,\mathrm{W}$. This is not a power regime that is well established in any RF or telecommunications industry (although the GHz frequency characteristic is), and therefore requires careful designing of appropriate microwave wiring and thermalisation, magnetic shielding, cryogenic filtering, low-noise amplification, up- and downconversion mixing techniques, and ultra-fast data acquisition, as illustrated in Fig. 3.3 and Fig. 3.9.

3.1.1 Cryostat

Cooling a device to roughly 1.2 K is relatively simple, by using liquid Helium (LHe) and pumping on it. Firstly, the boiling temperature of liquid Helium is 4.2 K, and so any device can be cooled to this temperature by simply immersing it in an LHe dewar, typically with a probe stick. By additionally pumping on the liquid helium, the vapour pressure is reduced and the liquid is forced to boil, thereby cooling it down further to reach 1.2 K. Reach even lower temperatures, in the mK regime, requires an Adiabatic Demagnetization Refrigerator or Dilution Refrigerator.

The cryostat used in the Leeklab is a Triton200 Cryofree Dilution Refrigerator (DR) from Oxford Instruments, shown in Fig. 3.1. It is a"dry" fridge using a mechanical Pulse-Tube Cooler for reaching roughly 4 K, as opposed to the older "wet" fridge technology which uses a LHe bath to achieve the 4 K stage. Both systems then

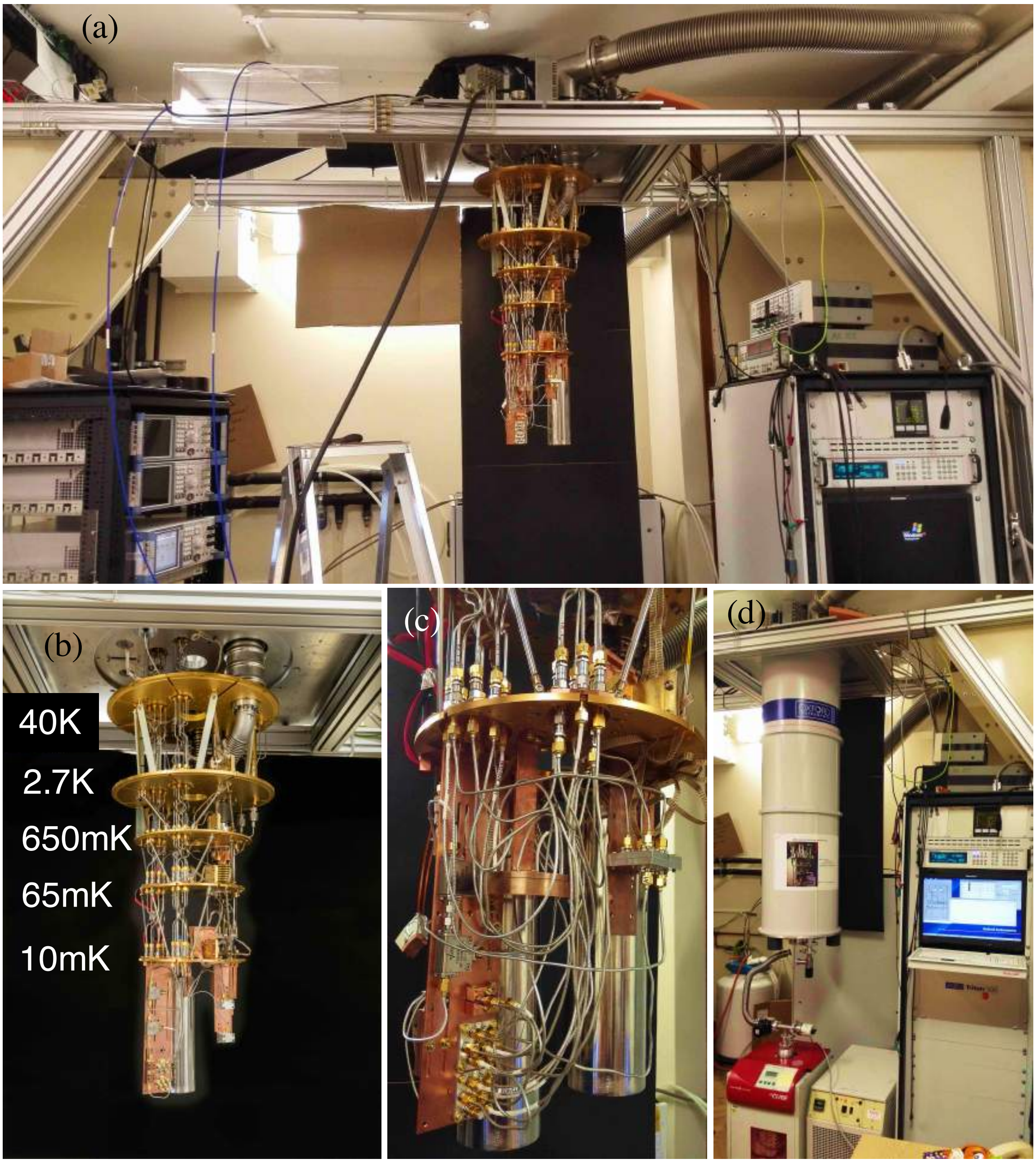

Figure 3.1: Pictures of the experimental setup. (a) The dilution refrigerator with control rack and instrument rack. (b) Close view of the open fridge showing the different temperature stages. (c) The cryogenic setup at the 10 mK stage showing magnetic shields, sample holders, switches, filters, etc. (d) The closed fridge during a cooldown.

use a closed circuit $He^3 - He^4$ mixture dilution unit to attain 10 mK. The Pulse-Tube technology is significantly cheaper since it does not require the expensive liquid helium bath to run, only electricity. This characteristic eliminates the need to refill the liquid helium manually every couple of days and typically gives the base plate more experimental space.

3.1.2 Heat flow and wiring

Our experimental devices are fixed onto the 10 mK plate of the dilution refrigerator (hereafter simply referred to as 'fridge') and are measured by sending microwave signals via coaxial microwave cables from the room-temperature electronics down all the different temperature stages of the fridge, passing through a hermetic feedthrough at the top of the fridge which is under high vacuum, see Fig. 3.1.

In circuit QED experiments, one of the key challenges is to populate the microwave cavity with a single photon on average or less. It is therefore necessary to firstly shield the cavity from higher temperature stages radiation. This is achieved by thermal anchoring the microwave coaxial cables at each temperature stage, via attenuators and feedthrough connectors. Secondly, thermal noise picked up by the propagating signal must be minimised. Indeed, classical control signals generated at room temperature are inevitably accompanied by electrical Johnson-Nyquist noise (created by the charge carriers in the conductor being thermally agitated) along the lines to the resonator. At the same time though, the signals must keep a good signal to noise ratio (SNR) throughout the experiment. The second step is to choose a large source voltage and a strong attenuation. The entire signal should be attenuated and filtered at different temperature stages by several orders of magnitude, so the noise picked up along the input route is kept low. The weak fields thereafter exiting the experiment through the output line must be strongly amplified to be detected, up to a factor of 10^8 in power. In parallel to these considerations of noise, the entire wiring must not allow for the transport of more heat than the cooling power of the cryostat can handle at each cooling stage, therefore requiring careful selection of cable materials. Calculations of heat flows for different materials and the choice of cables are presented in detail in Appendix A.1, revealing that stainless steel cables are necessary at the lower fridge stages.

3.1.3 Input lines and attenuation

Considering that the choice of material for the cables is forced upon us by the requirements on heat loads, the task is then to minimise the noise created along the input lines. Microwave control signals directed to the experimental device are generated by a microwave source at a power much higher than room temperature Johnson-Nyquist noise. Hence, the signals start off with a good signal-to-noise ratio (SNR). The RMS voltage created by a noisy resistor R is given by Planck's law of black body radiation

$$V_{noise} = \sqrt{\frac{4\hbar\omega BR}{e^{\hbar\omega/k_BT}-1}} \ , \tag{3.1}$$

where B is the bandwidth of the system, $\omega/2\pi$ is the centre frequency of the bandwidth, and R is the resistance of the noisy resistor. In the Rayleigh-Jeans approximation, for microwave frequencies in the regime 1-10 GHz with temperatures above 2 K, the condition $\hbar\omega \ll k_BT$ holds and reduces V_{noise} to

$$V_{noise} = \sqrt{4k_BTBR} \ ,$$

which gives the noise power spectral density

$$S_{v^2}(\omega) \approx 4k_BTR \ .$$

This noise power is independent of frequency and depends linearly on temperature T. The intensity of black body radiation emitted at 300 K in the range up to 40 GHz is roughly 80 times more intense than the radiation emitted at 2.7 K. We therefore mount a 20 dB attenuator (reduces input power by a factor of 100) for each microwave input line at the 2.7 K stage, and the noise from room temperature is thereby reduced below the noise generated at 2.7 K. Another two 20 dB attenuators are mounted at the 65 mK and 10 mK stage, as shown in Fig. 3.2. The attenuators also simultaneously serve the purpose of achieving the ultra-low power required to have a single photon interacting with the device.

For the purpose of our planned experiments, we built two 'tubes' of 14 cable lines in total extending down into the cryostat, as seen in Fig. 3.1c and Fig. 3.2b. Tube A has eight cable lines each with 3 × 3 dB attenuation and is intended for experiments which don't require low photon numbers. These eight cable lines allow to measure four two-port devices simultaneously. Tube B has six cable lines each with 3 × 20 dB attenuation and is used as input lines for experiments with superconducting qubits. Due to their high input attenuation, these experiments require a separate output line with amplification for acquiring the signals. The overview of the cryogenic setup is presented in Fig. 3.3.

All microwave cables have soldered SMA connectors and should present minimal reflections at each connector along the line. When microwave pulses propagate along the cable line and reflections at connectors are significant, then the percentages of the pulse's power being reflected several times will lead to constructive interferences and the original pulse will be followed by reflected smaller pulses. This is an unwanted effect for qubit control. Achieving low reflections when soldering SMA connectors is a difficult and tedious task, and it depends on several practical techniques. In short:

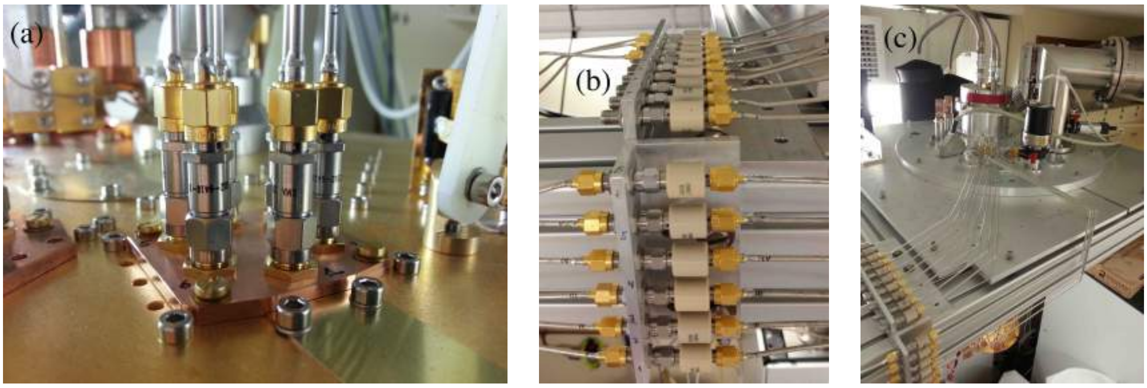

Figure 3.2: (a) Attenuators and feedthrough connectors to thermalize the input lines. (b) DC blocks isolating the fridge and protecting it from ground loops. (c) Top view of the fridge with all input and output cables.

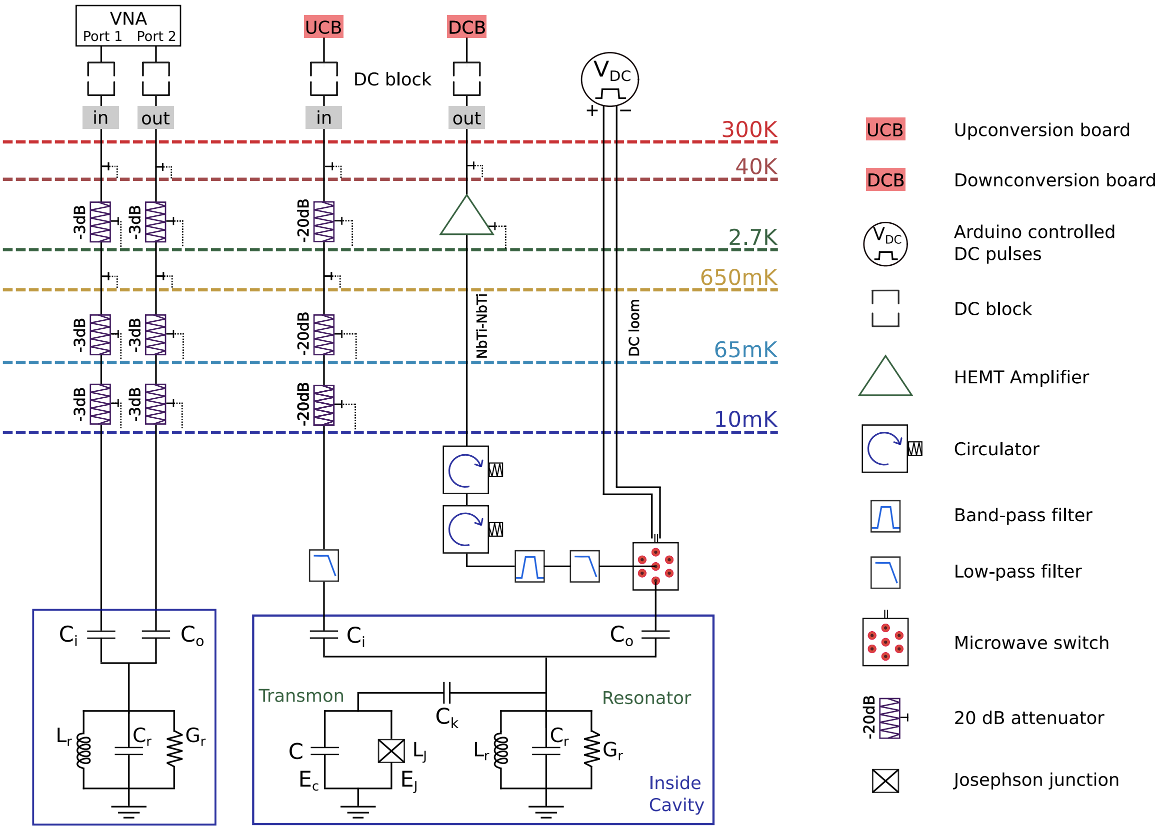

Figure 3.3: Cryogenic microwave setup.

the centre conductor must not be scratched; the centre pin should not have traces of solder on it after being soldered via the small hole onto the centre conductor; the dielectric of the coaxial cable must be prevented from expanding from the heat applied when soldering the connector onto the outer conductor. An expanded dielectric leads to an unwanted impedance mismatch, which in turn leads to strong reflections.

After soldering of each microwave cable's two connectors, its reflection coefficients were measured. These measurements are performed with a vector network analyser (VNA) from Rohde&Schwarz. The VNA measures the four S-parameters $(S_{11}, S_{21}, S_{12}, S_{22})$ as $S_{ii} = 10\log(P_{out}/P_{in})$ [dB]. The SMA connectors are commercially bought from Huber&Suhner and guarantee a maximum of approximately -19 dB reflection, if they are well assembled. The measured reflection coefficients for all our total 84 cables assembled show S_{11} to have less than -20 dB up to 15 GHz. It is possible with skill and practice to achieve less than -25 dB reflection in the range up to 20 GHz. It is even possible for the reflections to be kept beneath -20 dB in the range up to 40 GHz, even though the SMA connectors are only specified and guaranteed up to 20 GHz from the manufacturer.

3.1.3.1 Ground loops

As a side note, notice the DC blocks isolating the fridge from the microwave instruments in Fig. 3.2b and Fig. 3.1e. The installation of DC Blocks is necessary to prevent ground loops. Indeed, because there are many different instruments and cables connected to the cryostat, it can easily happen that the grounds of two instruments attached to different power supplies are both connected to the cryostat, creating a so called ground loop. Since these two grounds can be on slightly different potentials, equalising currents will flow along unpredictable paths within the cryostat. These stray currents can create unwanted induced magnetic fields, hence magnetic noise, that can negatively affect the coherence of our device. Thus the microwave lines going into the fridge are isolated with DC blocks, so that the fridge is electrically isolated and only grounded via a single conducting ground cable.

3.1.3.2 Calibration of input lines

To precisely achieve the desired low power of the control signal we measure the transmission of the entire input line. The composition of components in the cryogenic setup is shown in Fig. 3.3 and the respective attenuations and amplifications are listed in detail in Tab. A.2 in Appendix A.2. For the frequency dependant components in this table, we considered the values at 11 GHz, because that is the typical resonance frequency of our cavities. In particular, the UT85-SS/SS cables have a strong frequency dependance for their attenuation per meter, which is precisely -13.7 dB/m at 11 GHz. The UT85-SS have -5 dB/m and the UT85-TP have -2.4 dB/m. The 3 dB and 20 dB attenuators have a negligibly weak dependance on frequency, so do the vacuum feedthrough connector interfacing room and cryogenic temperatures, and the baffle plates feedthrough connectors.

Taking into consideration the frequency dependance of the different types of cables, the expected attenuation for the input lines is compared to the measured transmission at room temperature through a whole cable line in tube B from the base plate up to the top of the fridge, and shown in Fig. 3.4. The attenuation for cables in tube A is much lower, because the lines have 3 dB instead of 20 dB attenuators. These results indicate that the transmission through the cryostat at RT behaves as expected and proves that the wiring was successfully installed. When cold, the transmission of the input lines within the fridge will change slightly since the components and cables will have lower resistances and hence lower attenuation. Since we cannot directly measure the transmission of an input line with the VNA when the fridge is cold (closed), we instead measure the transmission through an input line and back up through another input line, with a small coaxial cable connecting the two at the base plate. Half of this transmission will correspond to the transmission through one input line. This technique only works for the low-attenuation lines in Tube A, since in the highly-attenuated lines of Tube B the total attenuation through an input line and return would be so strong (>140dB) that the VNA could not measure the signal anymore. Nevertheless, combining a "through" measurement on the Tube A lines with a measurement of an input line on Tube B returning on an amplified line allows us to extract the input transmission of the highly-attenuated line.

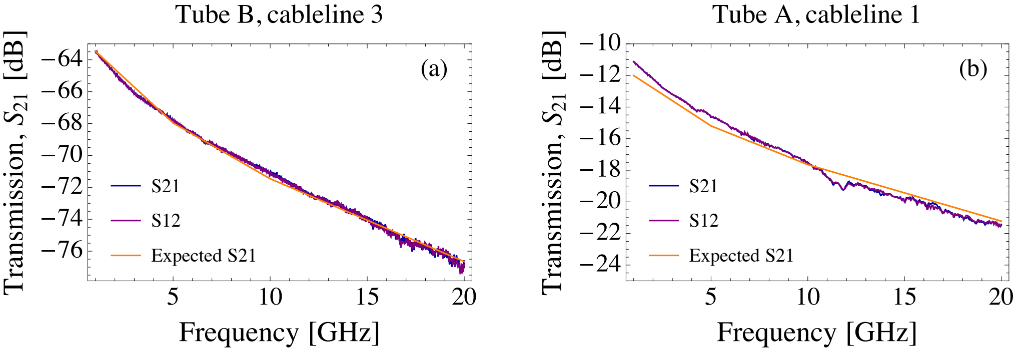

Figure 3.4: (a) Transmission measurement of the highly attenuated input cable lines in Tube B with 3 x 20 dB attenuators. The expected attenuation from summing the attenuations of all components along the lines is overlaid (orange) and fits well with the measured data (blue) (b) Attenuation of the input lines in Tube A with 3x 3 dB attenuators.

3.1.3.3 Sample thermalisation

Thermalising the sample to the 10 mK stage is accomplished by bolting the sample tightly onto a OFHC copper plate, and then fixing the copper plate against the 10 mK stage plate, as depicted in Fig. 3.1d and Fig. 3.5d. The copper plate serves as a "cold finger". Depending on the setup, there may be the need for several copper plates to be contacted in series. Optimising the thermal anchoring requires specific considerations on heat conduction across Solid/Solid interfaces. The heat flow across a pressed contact is insensitive to changes in contact area for a given total force pressing the two surfaces together. Indeed, the thermal conductance increases approximately linearly with pressure, as has been observed experimentally [64]. The opposite occurs for solder and glued joints. Hence, a good thermal connection between two solid interfaces requires a strong force, not a large area. Therefore, the two most important requirements for all our thermal anchoring of components are to minimise the number of thermal interfaces and to maximise the force of bolting. In particular, this implies that one should only use screws of minimum size M3, as smaller screw threads get destroyed with strong tightening due to the fact that oxygen free copper is a soft material.

3.1.3.4 Magnetic shielding

Performing experiments with qubits requires full protection from magnetic fields to avoid dephasing and imperfections in state preparation. Therefore, as visible in Fig. 3.5a)d), the entire cavity-qubit system is placed inside two concentric cylindrical magnetic shields, closed at the bottom and open-ended at the top. These shields are 1.0 mm thick Amumetal 4K, obtained from Amuneal Manufacturing Corporation. They are made of sheets of the special alloy Amumetal that is specifically annealed in dry Hydrogen atmosphere for optimum magnetic permeability at cryogenic temperatures.

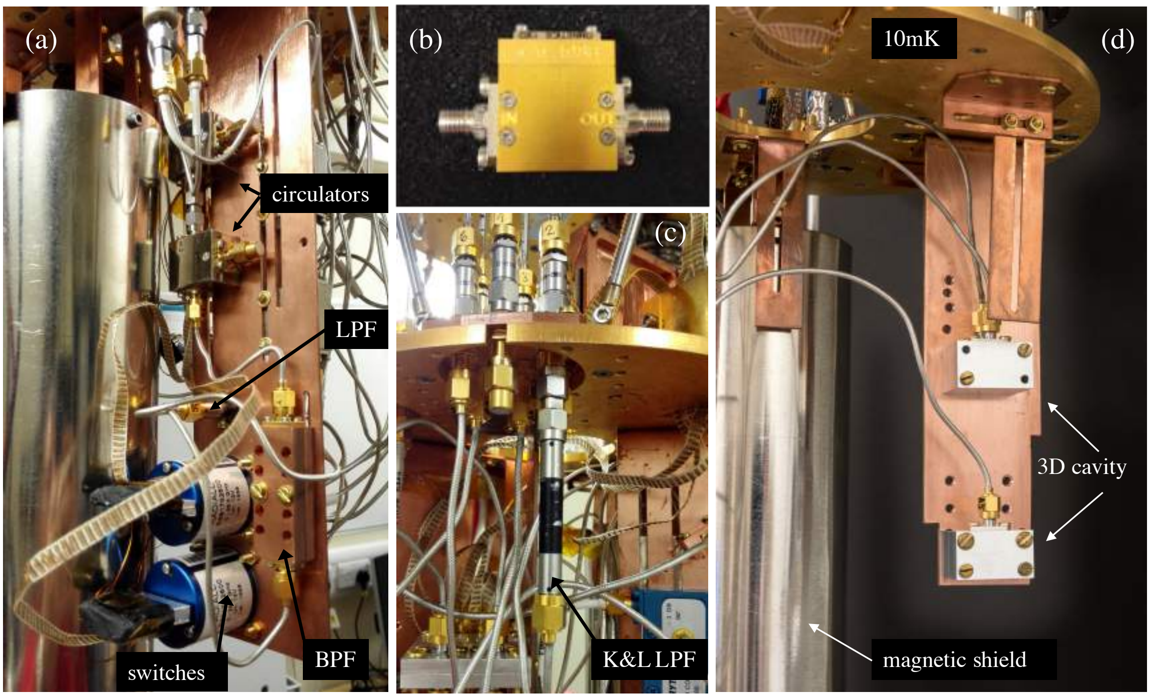

Figure 3.5: (a) Picture of the physical cryogenic microwave setup at the 10 mK stage, showing the microwave switches, bandpass filter, low-pass filter, and circulators. (b) A picture of the ultra low noise HEMT amplifier, which is placed at the 2.7 K stage on the output lines. (c) Low-pass K&L filter on the input line to the cavity. (d) Picture of two 3D cavities thermally fixed to a cold plate. The magnetic shield gets attached around the cold plate.

3.1.4 Cryogenic amplification chain

3.1.4.1 Microwave switches

It is extremely time-saving to introduce microwave switches into the cryogenic measurement setup, because they allow us to measure many samples (cavity-qubit systems) in the same fridge cooldown. Without switches, one needs an entire amplification chain (very expensive) to measure just one sample. Instead a microwave switch will allow the user to use the same input and output microwave lines to measure multiple devices. While the switch may only select one sample at a time, it can be used to switch between samples without warming up and opening the fridge, and thus saves a lot of time. Moreover, it saves space at the base plate. The switches we install are SP6T (6 output lines) electromechanical coaxial subminiature switches from Radiall that operate in the range 0 - 26.5 GHz, depicted in Fig. 3.6a. Other groups perform minor modifications to the switch for low temperature usage, but we have not found this to be necessary. The switch operates resistive copper coils at 12Vdc to create the magnetic field for the actual switching, which inevitably heats the fridge slightly from 10 mK up to 30 mK, requiring a waiting time of 5 - 10 min to re-cool (hardly an inconvenience). The switch switches under a DC pulse that is controlled by an Arduino setup, as seen in Fig. 3.6b.

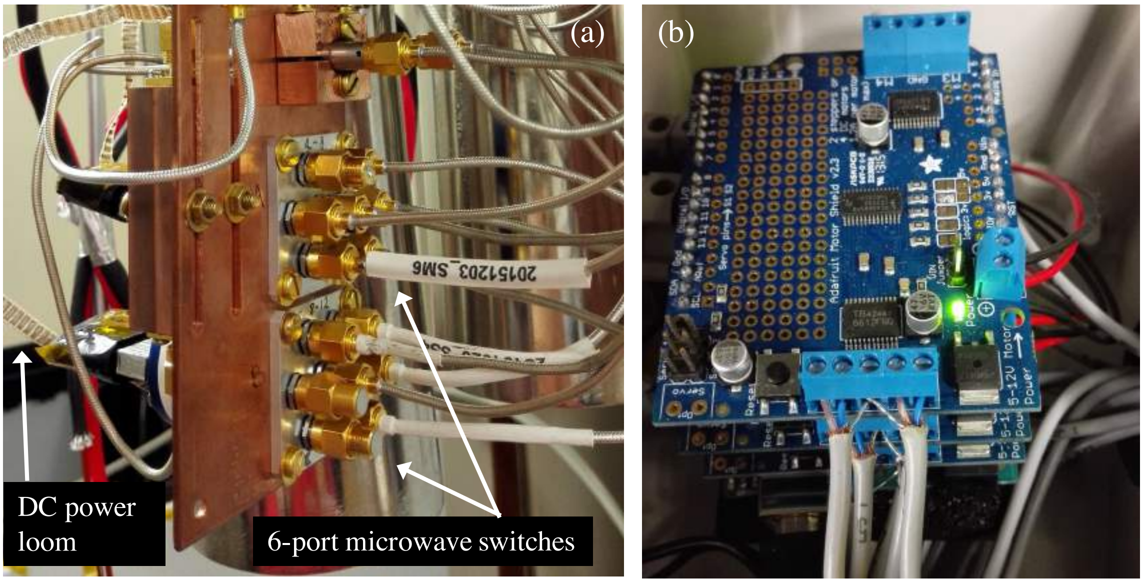

Figure 3.6: (a) Radiall 6-port electromechanical microwave switches. (b) Arduino setup to DC power the switches.

3.1.4.2 Amplification chain

The qubit readout signals that probe the cavity have powers corresponding to less than a single microwave photon energy $\bar{n} \approx 1$ per mean cavity photon lifetime. Our cavities with qubit chip inside typically reach an internal quality factor of 200000, and setting the coupling pin to have $Q_{ext} = 10^4$ gives a resonator linewidth of $\kappa/2\pi \approx 7.25$ MHz. With a resonance frequency around 10.5 GHz, the power leaking out of the cavity with a few-photon population is of the order of $P = \hbar\omega_r\bar{n}\kappa \approx 5 \times 10^{-17}W \approx -133\,\mathrm{dBm}$. In order to measure these signals with room-temperature microwave electronics, the signal must be amplified by at least 10^8 times to attain $V_{rms} = 0.5\,\mathrm{mV}$ to be detected by the ADC (Analog-to-Digital Converter). Thermal photons and amplifier noise are larger than the signal itself, and so along the output line any additional losses of the signal power between the sample and the first amplifier would require significantly more averaging to detect the signal. For instance, a mere loss of 3 dB demands 2 times more averaging to achieve the same signal-to-noise ratio (SNR), see [154]. A special type of superconducting cable with inner and outer conductor made of NbTi (low thermal conductivity but high electrical conductivity) is therefore installed to carry the weak signal without losses up to the first amplifier placed at the 2.7 K stage. Here we use an ultra low noise HEMT (High Electron Mobility Transistor) amplifier from Low Noise Factory designed to operate at cryogenic temperatures, see a picture of it in Fig. 3.5b. The HEMT amplifies the signal by a gain $G = 39\,\mathrm{dB}$ simultaneously keeping a good noise level. The reason for thermally anchoring the HEMT amplifier at the 2.7 K stage instead of the base plate is that it dissipates 15 mW which is too much for the cooling power of the fridge to handle at the base plate. The output port of the amplifier blocks any Johnson-Nyquist noise descending from cables at room temperature. When the output signal travels into room temperature cables, it is further amplified and band-pass filtered before being down-converted to an intermediate frequency, low-pass filtered, and amplified again in order for the FPGA to detect its quadratures, see Fig. 3.9. The details are presented in Tab. A.2 in Appendix A.2, and in Tab. A.3 and Tab. A.4 in Appendix A.2.

We first calculate the noise output of the HEMT. The noise power generated by a lossy component with equivalent noise temperature T^e and a bandwidth B is given by

$$N = k_B B T^e \,. \tag{3.2}$$

A component with a gain G then amplifies (or attenuates when the gain is less than unity, giving loss factor $L = 1/G > 1$) the input noise power N_{in} and also amplifies its intrinsic noise power N_a coming from the noise generated by the component itself. The output noise power N_{out} is then given by

$$N_{out} = GN_{int} + GN_a = G(k_B B_{in} T^e_{in} + k_B B_a T^e_a) \,. \tag{3.3}$$

Our HEMT has a bandwidth B_a of 1 - 12 GHz, as tests show in Fig. 3.7a, wherein the noise temperature is specified to be between $T^e_a = 5.5\,\mathrm{K}$, see Tab. A.4. The input noise source of the amplifier is the noise generated by the coaxial superconducting cable over a bandwidth of $B_{in} = 20\,\mathrm{GHz}$ thermalized at $T^e_{in} = 2.7\,\mathrm{K}$. Inserting these values into Eq. 3.3 with a gain of $G_1 = +39\,\mathrm{dB}$ we obtain a total output noise at the output of the HEMT amplifier of $N^{HEMT}_{out} = -49\,\mathrm{dBm}$. This noise travels further up the fridge output line and propagates through room temperature cables into the room temperature amplification chain shown in Fig. 3.9. We now calculate the noise amplification through this chain in order to make sure the various amplifiers do not get saturated by the noise, i.e. that the amplified input noise for each amplifier does not reach its 1 dB compression point. In a cascaded system (chain), the total SNR is principally governed by the noise added by the first amplifier when its gain G_1 is large according to Frii's law [154]

$$T_a = T_{a,1} + \frac{T_{a,2}}{G_1} + \frac{T_{a,3}}{G_1 G_2} + \dots \,, \tag{3.4}$$

with G_i representing the gain of each individual amplifier and $T_{a,i}$ the noise temperature of the i's amplifier. The noise temperature $T_{a,i}$ of each component is obtained from its specified noise figure $F_i = 1 + T_{a,i}/T_0$, where $T_0 = 290\,\mathrm{K}$ is the room temperature. The noise figure F_i is commonly expressed in dB as $NF_i = 10\log(1 + T_{a,i}/T_0)$. Inserting the values for the noise figures, gains, and bandwidths of our room temperature components (BPF - LNA - 3dB attenuator - BPF - LNA) gives us a resulting equivalent overall noise temperature $T^{RT} = 360\,\mathrm{K}$ for the cascade, as if it were a single component. The overall gain of the room temperature cascade is $G^{RT} = G_{BPF}G_{LNA}G_{3dBattn}G_{BPF}G_{LNA} = +50\,\mathrm{dBm}$. Therefore, the total output noise produced by the room temperature cascade system itself is $N^{RT} = G^{RT}k_B B T^{RT} = -27\,\mathrm{dBm}$. To this we add the room temperature amplification of the noise output from the cryogenic HEMT stage $G^{RT}N^{HEMT}_{out} \to +50\,\mathrm{dB} + -49\,\mathrm{dBm} = 1\,\mathrm{dBm}$. Together, we obtain from the sum of the two an overall noise output for our entire amplification chain (cryogenic and room temperature) of $N^{tot} \simeq 1\,\mathrm{dBm}$, since N^{RT} is negligible compared to $G^{RT}N^{HEMT}_{out}$. This calculation shows that the initial noise amplification of the HEMT is the dominant noise source, which confirms the importance of limiting the noise generated between the cavity and the HEMT in the fridge by using superconducting cables and filters.

The total attenuation of the input lines is approximatively -85 dB at the cavity input, when 0 dBm are generated at the source, see Tab. A.2. The signal generator can send signal at powers up to +20 dBm and as low as -130 dBm. This flexibility allows us to adjust the source power such as to obtain the desired average single microwave photon energy in the cavity, depending on its linewidth. The total amplification chain from the cavity to the FPGA sums to a total of +82 dB. Therefore the signal leaving the cavity at -133 dBm should arrive at the FPGA with a power of -51 dBm, which corresponds to $8 \times 10^{-9}\,\mathrm{W}$, i.e. $V_{rms} = 0.8\,\mathrm{mV}$, which is detectable.

3.1.4.3 Circulators

The thermal noise reflected from the HEMT amplifier input back down the cables to the sample is directed through two circulators from Raditek thermalised at base temperature, shown in Fig. 3.5a. These circulators are passive non-reciprocal three-port devices, which redirect microwaves entering any port i to port $i+1$, but never to $i-1$. We place 50 Ω termination loads on port 3 and use port 1 as input and port 2 as output. So the noise traveling back down the line from the amplifier enters the circulator at port 2 and is redirected into the absorbing load at port 3, providing an isolation of > 25 dB. On the other hand, the signal coming from the cavity traveling up the cryostat to be amplified and detected passes through the circulators with a minimal attenuation of < 0.5 dB. We placed two such circulators in a series to maximise the effect. The circulators used have a limiting bandwidth of either 4 - 8 GHz or 8 - 12 GHz and were tested for performance of S_{21} and S_{12} at room temperature and 4 K, one of which is displayed in Fig. 3.7b.

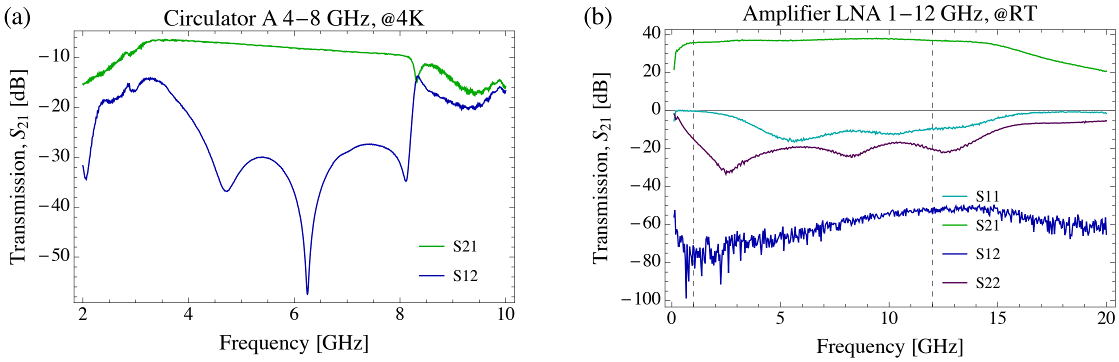

Figure 3.7: (a) Test of a circulator at 4 K, with -20 dB input power. (b) Test of an LNA HEMT amplifier at room temperature, with -60 dB input power.

3.2 Microwave signal generation and data acquisition

Time resolved experiments with superconducting qubits require two essential microwave pulse schemes. First, the qubit state is manipulated with qubit control pulses typically generated and sent at or near the qubit transition frequency $\omega_{qb} \approx 5-7\,\mathrm{GHz}$. The second is generating and measuring the transmission through the cavity of a readout pulse in order to detect the state of the qubit. Both these schemes require precise control over the amplitude, phase, and frequency of the signals with nanosecond timescale. This is accomplished by using Arbitrary Waveform Generators (AWG) and IQ mixers for modulating and upconverting the signals. The readout also requires an IQ mixer to downconvert the signal to an intermediate frequency which an ADC card can digitize.

3.2.1 Continuous wave control signals

In general, a continuous wave $S = A\cos(\omega t + \phi)$ is represented as a vector (A, ϕ) in polar coordinates. However, controlling the phase directly at GHz and above frequencies with microwave electronics is unpractical and imprecise. Therefore we use the orthogonal *in-phase* (I) and *quadrature* (Q) components in cartesian coordinates to generate the wave. Using the identity $\cos(\alpha \pm \beta) = \cos\alpha\cos\beta \mp \sin\alpha\sin\beta$, the wave becomes

$$\begin{aligned}
S &= A\cos(\omega t + \phi) \\
&= A\cos\phi\cos(\omega t) - A\sin\phi\sin(\omega t) \\
&= I\cos(\omega t) - Q\sin(\omega t) \qquad (3.5) \\
&= I\cos(\omega t) + Q\cos(\omega t + \frac{\pi}{2})\,. \qquad (3.6)
\end{aligned}$$

The amplitudes $I = A\cos\phi$ and $Q = A\sin\phi$ are just DC voltages with no frequency. The continuous wave (A, ϕ) can thus be generated simply by controlling amplitudes instead of phases via

$$A = \sqrt{I^2 + Q^2} \qquad \text{and} \qquad \phi = \arctan(Q/I)\,. \tag{3.7}$$

In practice, this *quadrature upconversion* is realized with an IQ-mixer from *Marki*, see Fig. 3.8 and Tab. A.3. The IQ-mixer has three inputs and one output port. A microwave carrier signal $S_{LO} = A_{LO}\cos(\omega_{LO}t)$, called Local Oscillator (LO), is generated by the SMF100A signal generator from *Rohde&Schwarz* (for specifications see Tab. A.3) with a frequency ω_{LO} of up to 20 GHz and is fed into the IQ-mixer's *LO* input port at a power of 13 dBm, as shown in Fig. 3.8a, where it is split into two signals. The first signal gets directly multiplied with the voltage $S_I = I$ produced by the AWG that is applied to the input port I, and it is *in-phase* with the initial carrier signal. The second one then first undergoes a $\pi/2$ phase shift, hence *quadrature*, and multiplied with the voltage $S_Q = Q$ applied to the input port Q. The resulting signals are combined and the final continuous wave output signal $S_{RF} = I\cos(\omega_{LO}t) - Q\sin(\omega_{LO}t)$ then propagates down the fridge to the cavity-qubit system. This quadrature upconversion is used for both continuous qubit drives and continuous readout signals. The length of these continuous wave signals is controlled by applying the S_I and S_Q voltages as square pulses of the desired length.

3.2.2 Pulsed control signals

Qubit control signals require arbitrary waveform amplitude modulation in order to have optimal pulse shapes, e.g. Gaussian, DRAG [39], etc. This is achieved with the AWG directly generating and applying AC voltages $S_I = A_I\cos(\omega_{IF}t + \alpha_I)$ and $S_Q = A_Q\cos(\omega_{IF}t + \alpha_Q + \phi)$ with intermediate frequency ω_{IF} to the IQ-mixer. Our

AWG has a limited bandwidth allowing it to create arbitrary waves with frequency up to $\omega_{IF} = 500\,\mathrm{MHz}$. The resulting upconverted output RF signal is

$$S_{RF} = \frac{A_{LO}}{\sqrt{2}}[\cos(\omega_{LO}t) \cdot S_I + \cos(\omega_{LO}t + \frac{\pi}{2}) \cdot S_Q]\,. \tag{3.8}$$

Setting $\alpha_I \equiv \alpha_Q \equiv \alpha_{IQ}$ and using trigonometry we obtain three different cases

$$\begin{aligned}&\phi = 0 : \\ &S_{RF} = \frac{A_{LO}A_IA_Q}{2}\{\cos[(\omega_{LO} + \omega_{IF})t + \alpha_{IQ} - \frac{3\pi}{4}] + \cos[(\omega_{LO} - \omega_{IF})t - \alpha_{IQ} - \frac{3\pi}{4}]\}\end{aligned} \tag{3.9}$$

$$\phi = +\frac{\pi}{2} : \quad S_{RF} = \frac{A_{LO}A_IA_Q}{\sqrt{2}}\cos[(\omega_{LO} + \omega_{IF})t + \alpha_{IQ} \tag{3.10}$$

$$\phi = -\frac{\pi}{2} : \quad S_{RF} = \frac{A_{LO}A_IA_Q}{\sqrt{2}}\cos[(\omega_{LO} - \omega_{IF})t - \alpha_{IQ} \tag{3.11}$$

For the case where the free adjustable parameter $\phi = 0$ and $A_I = A_Q$, the resulting upconverted signal consists of only two sideband signals with frequencies $\omega_{LO} \pm \omega_{IF}$, called the right and left sidebands, shown in Fig. 3.8d. Their amplitudes and phases can be controlled with $A_I = A_I(t)$ and $A_Q = A_Q(t)$ and $\alpha_{IQ} = \alpha_{IQ}(t)$ which are time-dependent and thus can generate any envelope to create the desired pulse shape. However, if A_I and A_Q are not identical then the signal at the carrier frequency ω_{LO} is not entirely suppressed. By setting the parameter $\phi = \pm\pi/2$ and $A_I = A_Q$, the left of right sideband is canceled, and the result is a single frequency output signal, which is what we need to drive the qubit. The mixer has imperfections in the form of amplitude imbalance and phase imbalance, which lead to imperfect suppression of the undesired sideband, and must thus be calibrated. Furthermore, the mixer has small DC offset errors at the IQ ports that lead to carrier leakage from the LO to the RF port. This means that if we send qubit drives upconverted using DC mixing as described in Eq. 3.7 they have the same frequency as the LO carrier leakage, leading to a small continuous qubit drive even when no voltage is applied to the I and Q ports. This is the reason why we drive the qubit with sideband mixing instead, where the carrier leakage is detuned by typically 62.5 MHz from the qubit frequency. A schematic of the pulse generation for qubit drive and readout signal is presented in Fig. 3.8.

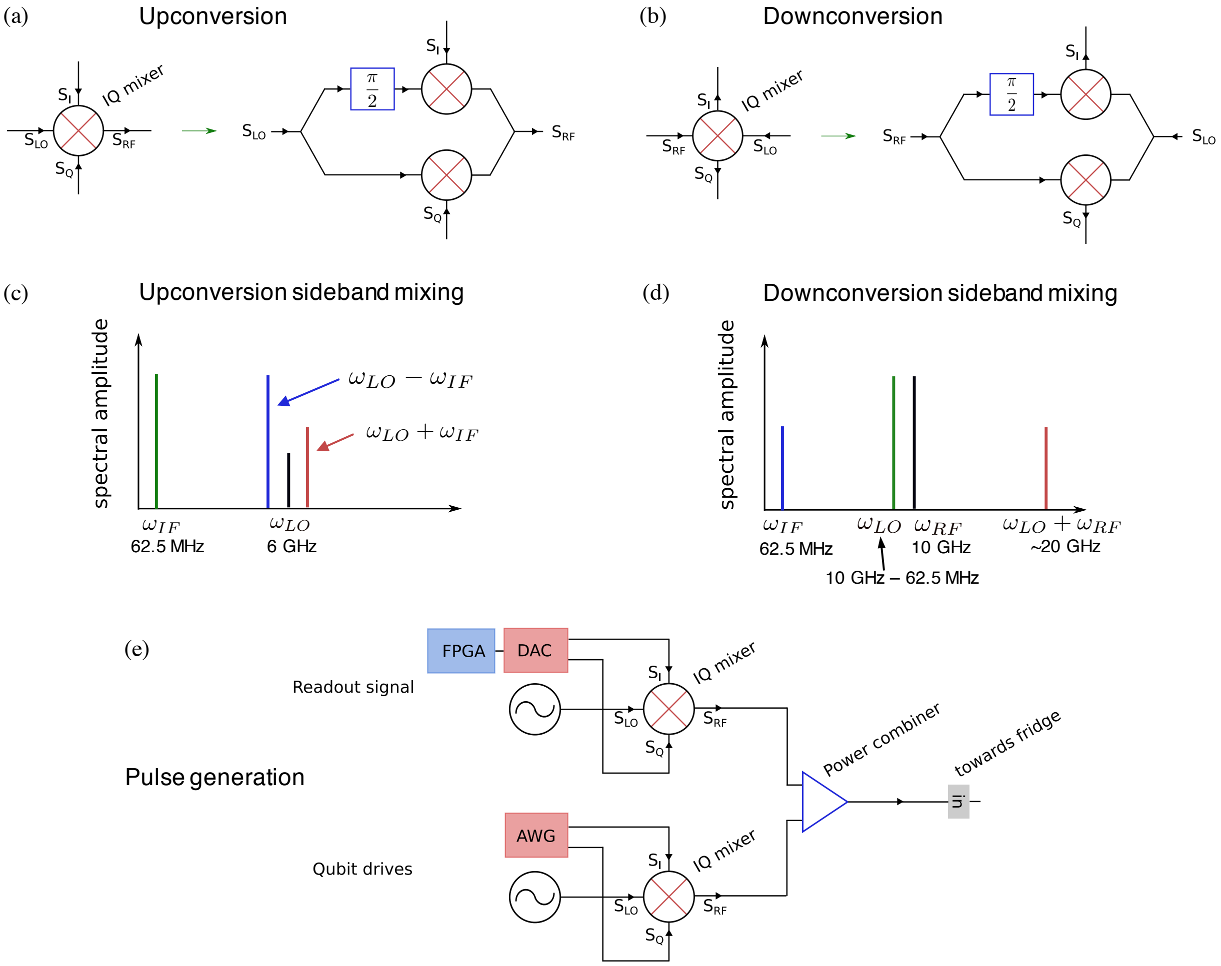

Figure 3.8: (a) Schematic of an IQ mixer used for upconversion. (b) IQ mixer used for downconversion. (c) Spectral result of sideband mixing with an IQ mixer for upconversion. (d) Spectral result of sideband mixing with an IQ mixer for downconversion. (e) Schematic of upconversion in our setup to generate the readout signal pulses and the qubit drive pulses.

3.2.3 Down conversion and signal processing

The readout of the qubit state is performed by probing the cavity on resonance with a continuous wave readout pulse, allowing us to infer the state of the qubit based on the transmission amplitude of the cavity response. The RF readout pulses are generated with quadrature upconversion, analogous to the qubit drive pulses, by a signal generator for the carrier signal and the DAC board featured on the FPGA for the I and Q input quadratures (where the DAC acts as an AWG). As described in 3.1.4.2, the transmitted readout signal exits the cavity at an extremely low power and gets amplified by the HEMT before reaching room temperature, where it passes through two pairs of bandpass filters and low noise amplifiers before reaching the downconversion setup, shown in Fig. 3.9. Many repetitions of the experiment are required to average out the amplified noise that dominates over the transmission signal of interest. The RF signal $A(t)\cos(\omega_{RF}t + \alpha_{RF})$ has a frequency in the range $\omega_r \approx 7 - 11\,\mathrm{GHz}$ and thus too high to be acquired and digitized by the ADC card featured on the FPGA, which has a sampling rate of 250 MS/s. As a result, the RF must be mixed down to an intermediate frequency $\omega_{IF} = 62.5\,\mathrm{MHz}$ that can then be acquired (the choice of 62.5 MHz comes from the need for at least 4 points per period). A fast oscilloscope could be used for acquisition without the need for downconversion, but oscilloscopes do not average efficiently. This quadrature downconversion, analogous to the upconversion as shown in Fig. 3.8, is achieved by mixing the incoming RF signal at ω_{RF} with a local oscillator signal ω_{LO} in the IQ-mixer. The resulting $S_I(t)$ and $S_Q(t)$ quadratures exiting the mixer each have two components, one with the difference of the frequencies $\omega_{RF} - \omega_{LO}$, and one with the sum $\omega_{RF} + \omega_{LO}$. The quadratures components with the sum of frequencies then get filtered out through a low-pass filter. The LO frequency is set to be detuned from the RF frequency by the desired intermediate frequency $\omega_{LO} = \omega_{RF} - \omega_{IF}$. The result is downconverted IQ quadratures at $\omega_{IF} = 62.5\,\mathrm{MHz}$ (heterodyne detection), which get further amplified and then each pass through a band-pass filter centred around ω_{IF}, and finally get acquired by the ADC card. The incoming quadratures $S_I(t) = A(t)\cos(\omega_{IF}t + \alpha_{RF})$ and $S_Q(t) = A(t)\sin(\omega_{IF}t + \alpha_{RF})$ are digitized over a time period of $4\,\mu$s and contain the information about the state of the qubit, which is extracted by a further digital downconversion to DC (digital homodyne), performed by the FPGA by multiplying the digitized quadratures with ideal cosine and sine waves

$$\begin{pmatrix} I(t) \\ Q(t) \end{pmatrix} = \begin{pmatrix} \cos(\omega_{IF}t) & \sin(\omega_{IF}t) \\ -\sin(\omega_{IF}t) & \cos(\omega_{IF}t) \end{pmatrix} \begin{pmatrix} S_I(t) \\ S_Q(t) \end{pmatrix} \tag{3.12}$$

After this multiplication both traces are averaged over thousands of experiments to enhance the signal-to-noise ratio. Then the resulting averaged $I(t)$ and $Q(t)$ traces are integrated over each period of 16 ns and the result is the digital downconverted DC envelope trace for each one. They are then combined to obtain the amplitude time trace of the original signal via $A(t) = \sqrt{I(t)^2 + Q(t)^2}$ and phase via $\alpha = \arctan\left(Q(t)/I(t)\right)$. Finally, the amplitude trace is integrated over time and divided by the number of points to obtain the average of the time-resolved response. This single final amplitude (phase) point represents the cavity response for the transmitted signal at that frequency ω_{RF}, and it is this amplitude (phase) that gives us the information about the state of the qubit.

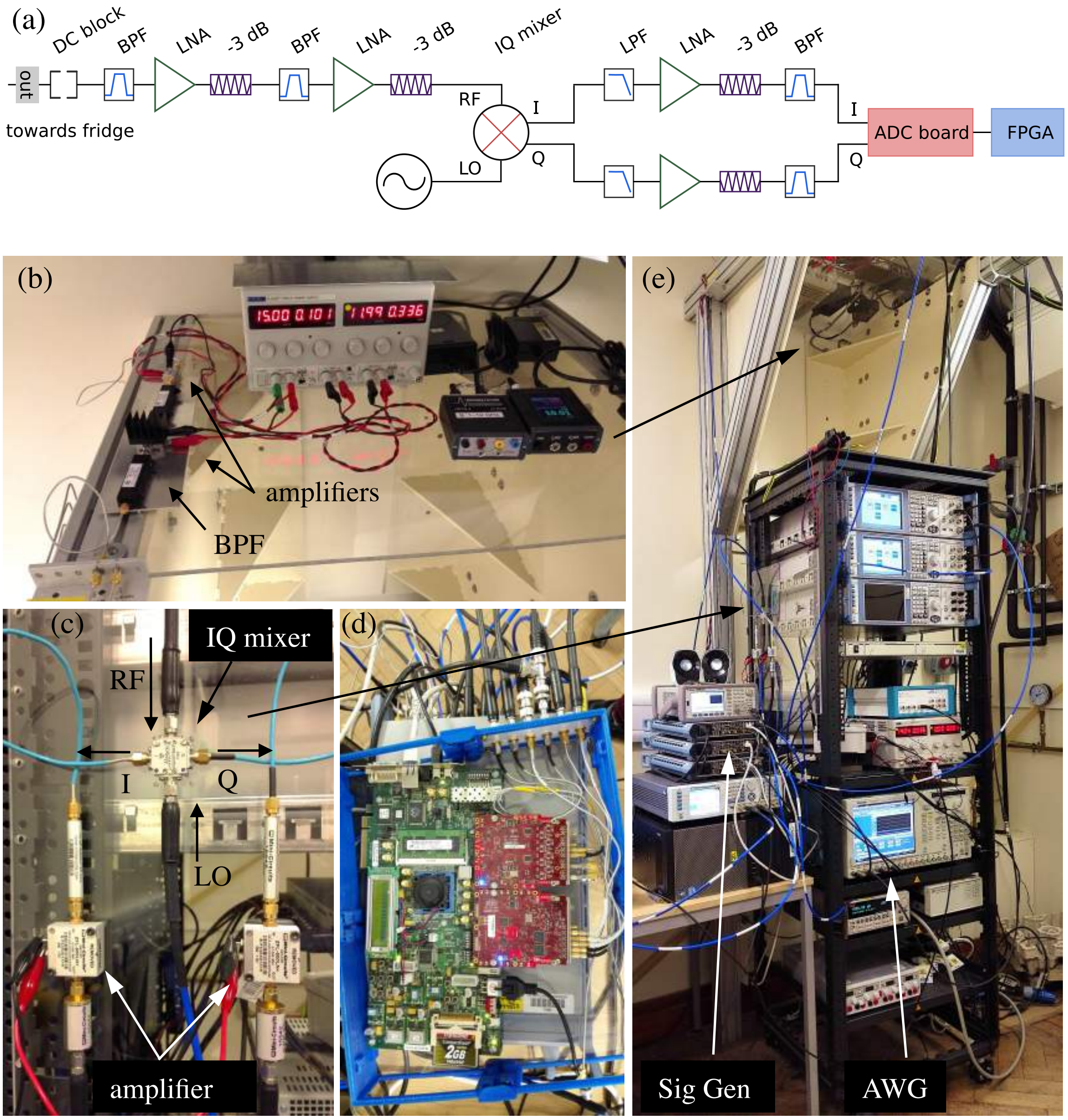

Figure 3.9: (a) Schematic of the RT amplification, downconversion, and data acquisition chain. (b) Picture of the RT amplifier setup on the output line. (c) Downconversion setup showing the IQ mixer. It takes the RF signal coming (b), and mixes it with the LO provided at a frequency detuned by 62.5 MHz. The downconverted output signals $S_I(t)$ and $S_Q(t)$ each get filtered and amplified again, and then enter the ADC card on the FPGA shown in (d). (d) FPGA (green board) with the built-in ADC card (red board) used for data acquisition, and the DAC card (2nd red board) used as an AWG to generate IF signals to upconvert readout pulses. (e) Picture of the microwave instruments setup showing the signal generators and the AWG. All instruments are synchronised by a 10 MHz reference clock via the dual distribution amplifier. A trigger source is connected to the instruments to set the repetition rate and enable averaging over many identical experiments.

Chapter 4

Fabrication of Josephson junctions and transmon devices

This chapter presents the techniques and procedures for fabrication of nano-scale Josephson junctions and superconducting qubits. The development, implementation and optimisation of micro- and nanofabrication processes were a central effort for the scope of this thesis. Electron beam lithography and angle shadow evaporation are the two main processes developed for the realisation of qubit devices. It is a crucial part of circuit QED to precisely engineer defined properties of the devices to enable quantum information processing, and this chapter illustrates how to achieve them.

4.1 Josephson junction fabrication process

The basic general lithographic procedure is presented in Fig. 4.1: first, a substrate surface is coated with a radiation-sensitive polymer film (resist) and exposed to radiation in some desired pattern; following exposure, a development step removes the exposed resist, thereby leaving the pattern in relief on the substrate surface; the substrate itself can then be patterned by depositing a metal into the open areas of the resist relief pattern; finally, the resist is removed in the lift-off step and the result is the desired device.

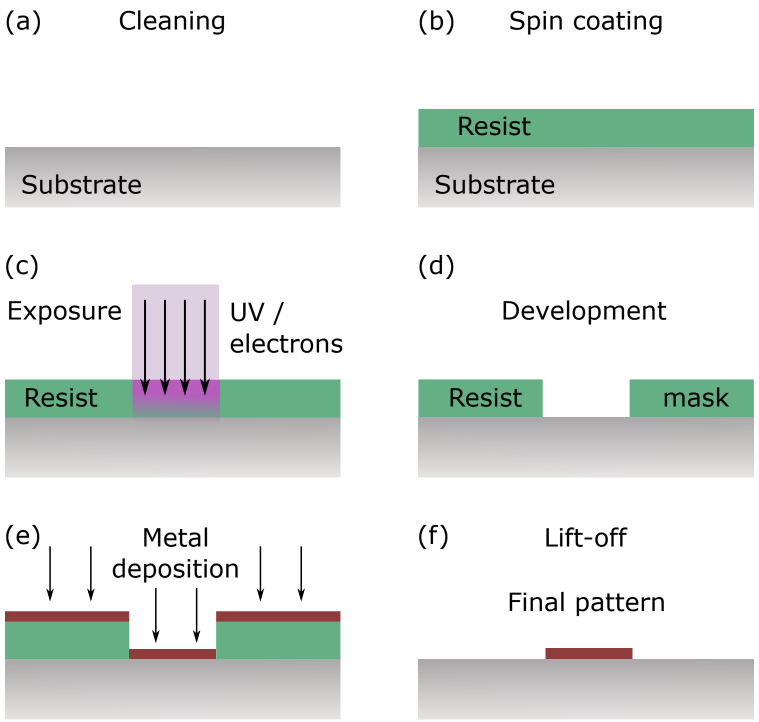

Figure 4.1: General lithography fabrication procedure. (a) Clean the substrate. (b) Spin coat a layer of resist. (c) Expose the chip to UV light in the case of photolithography or to an electron-beam in the case of electron-beam lithography. (d) Remove the exposed area of the resist by placing the chip in a developer, thereby creating the resist mask. (e) Deposit a thin film of metal. (f) Place the chip in a lift-off solution that dissolves the resist, thereby leaving only the desired pattern of metal.

The substrate used for our devices is pure C-plane sapphire from *CrysTec* bought in the form of 3" wafers of thickness 0.5 mm. Sapphire has the chemical composition Al_2O_3 and is a perfect insulator with a very low dielectric loss tangent $< 10^{-4}$. Since dielectric loss is one of the main sources of decoherence for qubits, sapphire is the natural choice. Circuit QED groups have tested many alternative substrates to try to improve coherences, but to date the sapphire remains the most common choice.

4.1.1 Cleaning and dicing

Fabrication of nano-scale Josephson junctions requires very clean and precise procedures in order to achieve the long coherence times for the qubit. Any residues or"dirt" underneath, above, or in vicinity of the junction will limit the coherence.

Therefore the chip must be first extremely well cleaned. Before cleaning though, the wafer must be diced into small chips of 5x5 mm. Since sapphire is an extremely hard material, it must be cut in a dicing machine with special blades made of diamond. For actual qubits, we use sapphire chips that are double-side epi-polished and are pre-diced by the firm SurfaceNet GmbH. The firm pre-dices them in 5.0 x 5.0 mm to a precision of ±0.01 mm. The only inconvenience of the double-side polishing is that the chips are more difficult to see during fabrication.

The cleaning of the individual 5x5 mm chips requires the removal of all dirt and organic residues. An O_2-plasma etcher can be used to achieve this, but this strong etching can alter the surface structure of the chip [155, 87], which is potentially a non-desirable outcome. Indeed, the critical current of the junction can be influenced by the surface roughness of the substrate. We instead perform the cleaning of the chip by placing it first in warm Acetone in an Ultrasonic bath and subsequently in Dimethyl Sulfoxide (DMSO) at 80 °C. The DMSO specifically removes all the organic “residues”.

4.1.2 Lithography

Standard fabrication techniques involve different steps depending on the type of device produced. Two key differences are the use of photolithography or electron beam lithography (e-beam lithography), and the use of a single or double resist layer. For devices with features down to roughly 1 μm it is typical to use photolithography, because it is much faster and cheaper. Indeed, an entire 3” wafer of devices can be produced in one session. For features of resolution smaller than the wavelength of UV light, i.e. features of characteristic size smaller than 1 μm, it is necessary to use an electron beam lithography system, which is expensive, technically more difficult to use, and can only pattern small areas at once. For most simple devices, a single layer of resist suffices, but making Josephson junctions requires a double layer (Dolan bridge technique) and the use of e-beam lithography due to the small nano-scale features involved.

4.1.3 Electron-beam lithography

Josephson junctions require electron-beam lithography that allows patterning of features down to roughly 5 - 10 nm. The e-beam lithography system focuses a beam of electrons directly onto the polymer resist on the chip, resulting in photo scission of the exposed polymer. In other words, the chemical bonds in the resist are broken up, introducing a different solubility of the exposed vs unexposed regions of the resist in certain solvents, therefore allowing the removal of the desired exposed pattern in the chosen solvent to form a shadow mask. Therefore, the critical feature of an e-beam system is its acceleration voltage. During the development of Josephson junctions in this thesis, we first used a Raith system with an acceleration voltage of 10 kV, photographed in Fig. 4.6a. After several months of fabrication development, it was discovered that 10 kV is too low for Josephson junction fabrication (due to excessively strong backscattering at such low voltages), and we then used permanently a JEOL JBX-5500 series ZC system with a voltage of 50 kV.

The standard technique to fabricate Josephson junctions (Dolan bridge technique) uses a free standing resist bridge with a double angle shadow evaporation, as shown in Fig. 4.2. The bridge is achieved using a bilayer of resist and harnessing the undercut created by the backscattering of the electrons in the lower resist (due to its higher exposure sensitivity). Depositing the aluminium film at two different angles with an oxidation step in between creates the junction, as illustrated in Fig. 4.2e. The detailed fabrication recipe is presented in Tab. B.1 in Appendix B.1.

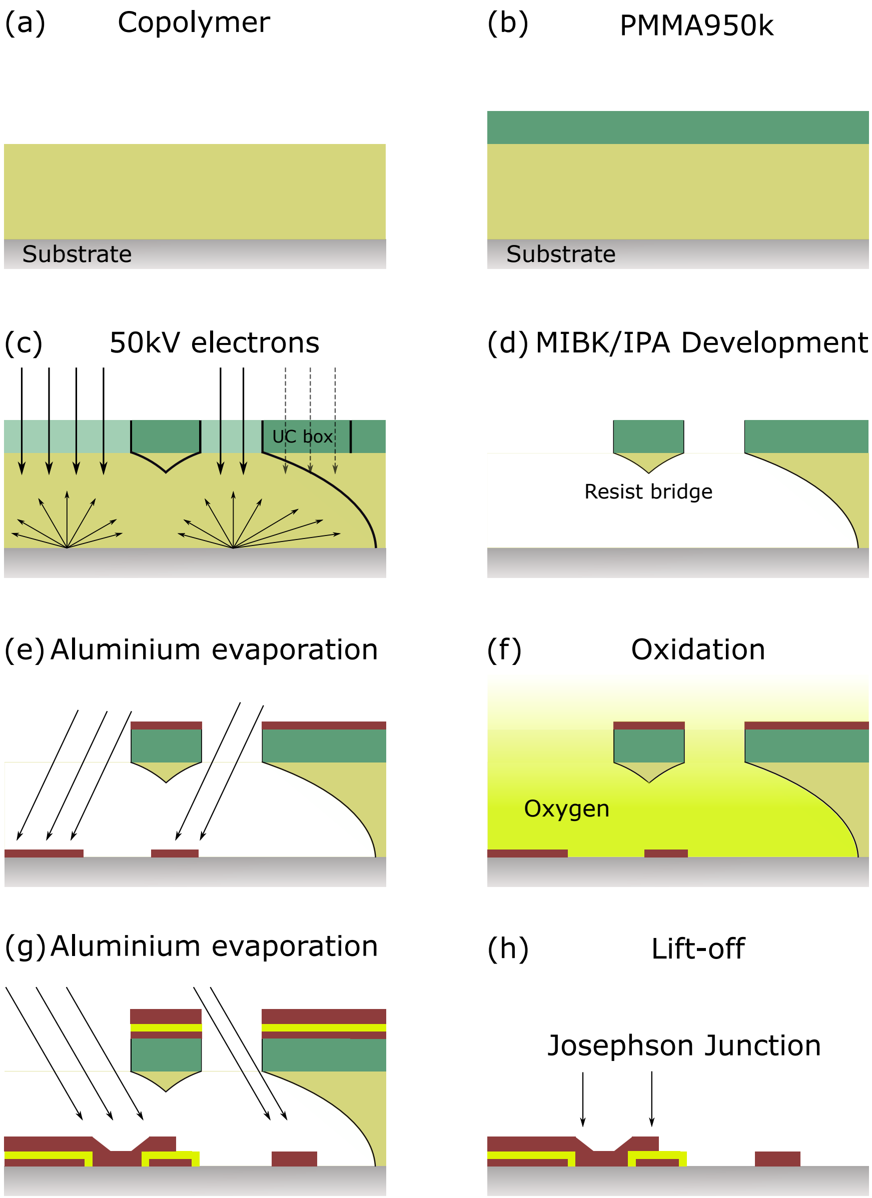

Figure 4.2: Josephson junction fabrication. (a) A layer of copolymer of thickness 600 nm is spun on the clean sapphire chip and then baked. (b) A second layer of PMMA of thickness 250 nm is spun on top of the copolymer layer and again baked. (c) The desired junction pattern is exposed with 50 kV electron-beam lithography. (d) The exposed resist is developed away with MIBK-Isopropanol mixture, leading to a free standing Dolan bridge. (e) Evaporation of a thin film of aluminium of thickness 30 nm at a growth rate of 0.5 nm/s at an angle from the vertical direction of typically 0° to - 40°. (f) Aluminium oxidation with a gas mixture of 85% Ar and 15% O_2 for several minutes at a few mbar. (g) Shadow evaporation of aluminium of thickness 70 nm at an angle of 20° to 45°. (h) Resist lift-off in acetone for 15 min at 50 °C.

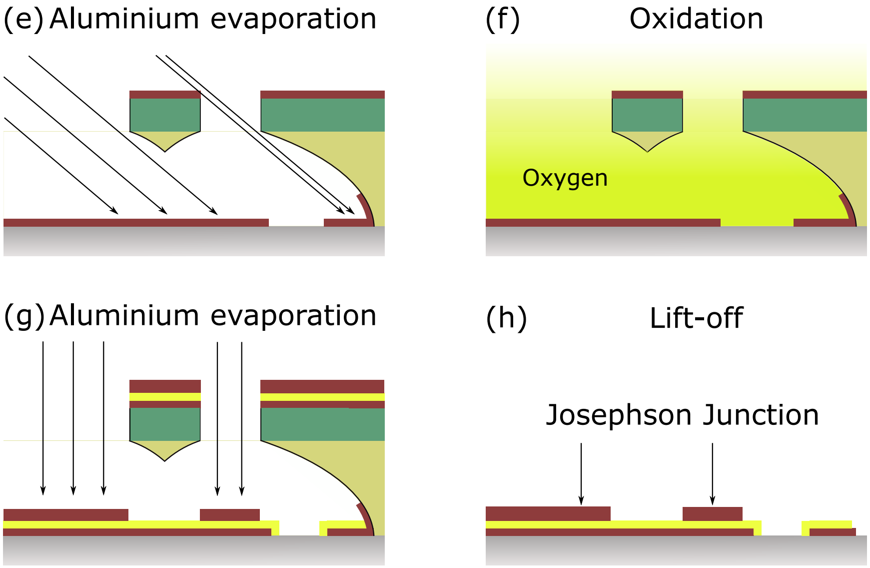

Figure 4.3: Josephson junction fabrication with the “T”-technique and large angle. (a)(b)(c)(d) Identical to Fig. 4.2. (e) Evaporation of a thin film of aluminium of effective thickness 30 nm (reading of the thickness monitor 60 nm) at a growth rate of 0.5 nm/s at an angle from the vertical direction of 60°. At this angle, the shadow pattern is deposited entirely onto the side wall. (f) Aluminium oxidation. (g) Evaporation of aluminium of thickness 70 nm at an angle of 0°. (h) Resist lift-off. The side wall deposition is entirely removed, leaving no shadow arm.

Resist deposition

The resist bridge is achieved using a bilayer of resist, which is spun onto the chip directly after cleaning. The 5x5 mm chips, however, are first dehydrated by baking them at 180 °C for 2 min in order to remove any water molecules from the humidity in cleanroom atmosphere. The spin coating is done by depositing a single droplet of resist onto the chip with a precise pipette, making sure that the droplet does not float over the edge of the chip. Any resist reaching the underside of the chip will prevent the chip from laying flat in the e-beam lithography system later. The first layer of resist spun onto the chip with the spin coater is a pure Copolymer of methyl methacrylate (MMA) and methacrylic acid (MAA), which 3-4 times more sensitive than a pure poly methyl methacrylate (PMMA). It is very sensitive to the direct, secondary and backscattered electrons from the beam during lithography. It basically serves as a spacer between the substrate and the second resist layer allowing for a large undercut of up to 700 nm to be realised, see Fig. 4.2d. It is this undercut that allows for the creation of the free standing bridge, called Dolan bridge [59]. The spin coating is done at 3000 rpm for 45 s with a very quick ramp up time. This spinning speed creates a layer of thickness of roughly 600 nm. The chip is baked at 180 °C for 5 min on the hotplate shown in Fig. 4.4b. The second layer is a pure low sensitivity, but high resolution ploymethyl methacrylate PMMA950k (a large molecular weight) that is spun directly thereafter at 2500 rpm for 45 s creating a thickness of approx. 250 nm, followed by baking again at 180 °C for 5 min. The slower spinning speeds create edge beads that can be up to 1000 μm in size. Spinning tests showed that 3000 rpm and 2500 rpm, respectively, are the lowest speeds at which the edge beads do not become too large. Furthermore, it is important to note that the temperature in the cleanroom should be at least 19 °C for spin coating, below which the resist does not stick well to the substrate anymore.

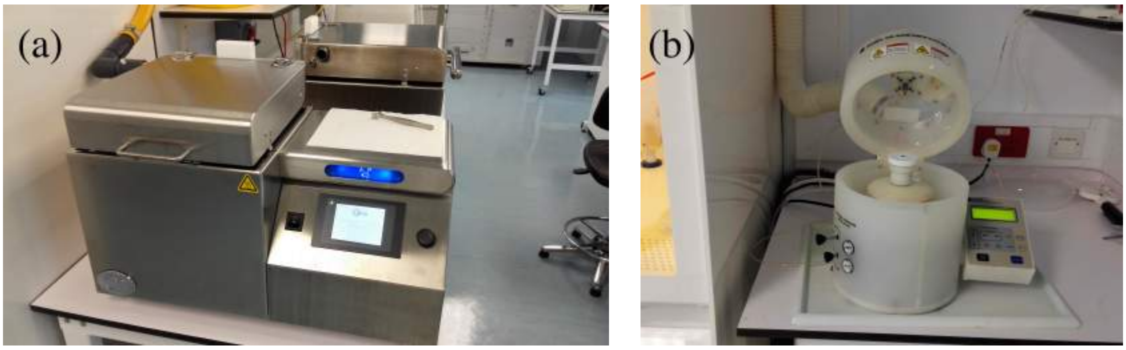

Figure 4.4: (a) Picture of the hotplate used for dehydration and baking the chips. (b) Spin coater.

The resist datasheets indicate that the copolymer should have thickness of 500 nm at 4000 rpm and the PMMA a thickness of 230 nm at 4000 rpm. We tested these using a surface profiler that uses a scanning tip to measure the height profile starting on the chip where we scratched the resist away, and then advancing onto the resist.

The profiles are shown for each resist individually in Fig. 4.5, and the result is quite consistent with the datasheets up to ±20 nm. However, when surface profiling a chip with the bilayer Copolymer/PMMA, the total height was only 630 nm. This suggests that the PMMA does not stick as well to the Copolymer than directly onto the sapphire. For this reason, we decided make the PMMA thicker by spinning it at a lower speed, 2500 rpm instead of 4000 rpm, thereby increasing the robustness of the bridge. In addition, we decided to spin the Copolymer at 3000 rpm to increase the height for angle evaporation design purposes. From actual angle evaporations, trigonometry, and a measurement with the SEM of the angle evaporated shift, see Section 4.1.5, we were able to determine the total thickness of the bilayer to be 850 nm ±30 nm. Since the Copolymer datasheet reliably predicts thicknesses, we know that the Copolymer at 3000 rpm is 600 nm thick. Therefore the PMMA at 2500 rpm has a thickness of approx. 250 nm.

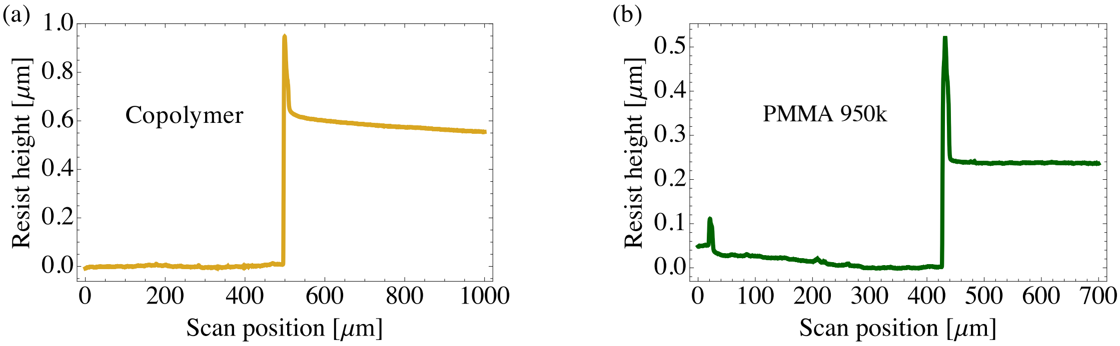

Figure 4.5: Resist profiling. (a) Resist profile of a sapphire chip with a layer of copolymer spun at 4000 rpm. (b) Resist profile of a sapphire chip with a double layer copolymer/PMMA950k spun at 4000 rpm. The profiling was done by scratching away a part of the resist.

Charge layer

The high energy electrons from beam need to be able to escape the exposed surface area during the lithography. Since sapphire is an insulating material, the inability to escape leads to an accumulation of electrostatic charge on the chip, which in turn leads to deflections and shifts of the e-beam. The solution is to add a thin charge dissipation layer - which is transparent to the 50 kV electrons - on top of the bilayer to facilitate the discharge. Several types of discharge layers are possible. Initially, we deposited a 10 nm layer of aluminium, which worked well for the charge dissipation. The problem with the aluminium is that it is not easy to selectively remove after the exposure. Some groups successfully remove it with an aluminium etchant consisting of sodium hydroxide NaOH solved in water 10%. Unfortunately, this etchant also affects our PMMA layer underneath and cracks it. Instead, we sputter a 10 nm layer of gold as the charge layer, using the sputterer depicted in Fig. 4.9. The gold is subsequently removed in a selective gold etchant solution KI/I_2 (potassium iodide / iodine) for 10 s. It is important to sputter the gold instead of depositing it with an e-beam evaporator, because the electron beam actually exposes the chip during the deposition. More recently, we have moved from using gold to using a thin layered conductive plastic *Electra* as the charge layer, which can be spun onto the chip, and can be easily removed by dipping it into DI water for just 10 s. When placing the prepared chip into the e-beam system, it is important to contact the chip, i.e. the charge layer, to the sample holder of the e-beam lithography system to assure firm contact to ground.

Junction design and file preparations

The e-beam can write in scan steps down to 1 nm onto a writefield area of up to 1000 x 1000 μm. Larger areas need to be exposed by patching together adjacent writefields (“stitching”). The patterns are drawn in AutoCAD software and then directly given to the e-beam system software in a “.dxf” file format. The pattern file may contain different layers, where each layer can then be assigned a different

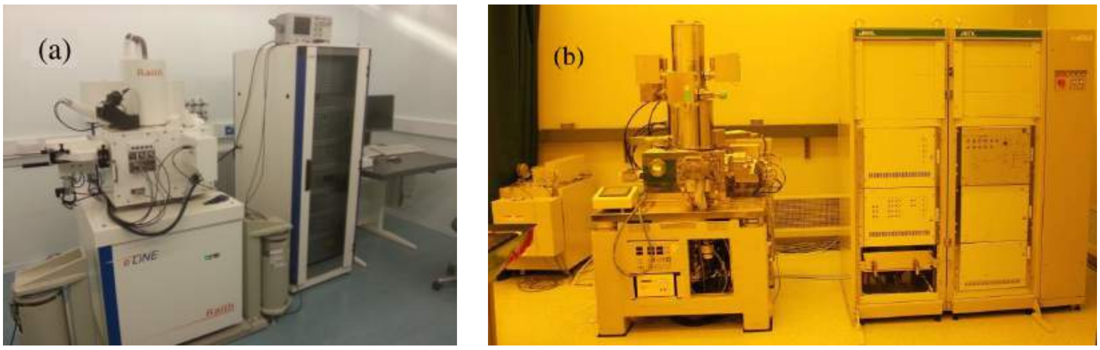

Figure 4.6: (a) The Raith 25 kV e-beam lithography system. The maximum operating acceleration voltage 10 kV used initially is too low to fabricate free standing bridges. (b) The JEOL 50 kV e-beam system used to fabricate the qubits in this thesis.

exposure dose. The pattern for our Josephson junction design is shown in Fig. 4.7. The blue pattern is the main pattern, and the purple is the undercut box. The design leads to a free standing bridge of 300 nm width and 1200 nm in length. The"T"-shape design, developed in [100] allows the bridge to have a standard length which is independent of the finger width. Our first batches of junctions had a design without the T-shape, as seen in Fig. 4.8 and Fig. 4.12, but the bridges were not reliable whenever we changed the finger width. The T-shape is believed to act as a stress-relief for the bridge and renders the bridges more reliable. Dimensions with height and width of the junction area have been reliably tested for values between 150 nm to 500 nm. The specific widths of fingers designed, typically 200 nm, end up being consistently wider by roughly 50 nm after the fabrication procedure, mainly due to the proximity effect.

Electron-beam exposure and dose tests

Once the chip is under vacuum inside the e-beam system, aligned, the built-in SEM beam is focused, the stigmatism is corrected, and the beam current is calibrated, the system automatically executes the designed pattern with the given doses. Small features in the pattern are exposed using Aperture 2 with beam current 1 nA (high

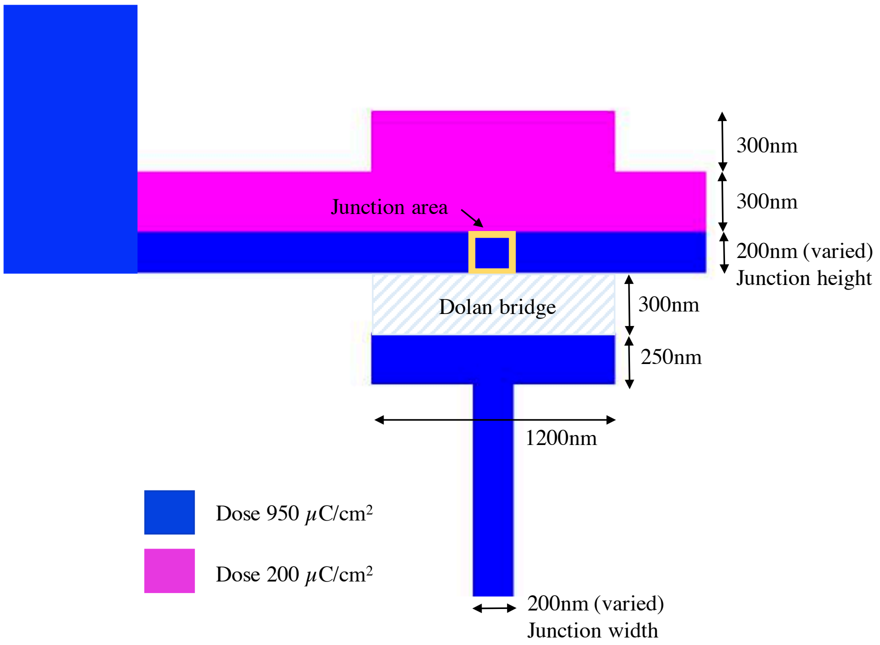

Figure 4.7: AutoCAD design of the Josephson junction exposure pattern. The blue area is the junction pattern exposed at the main dose of $950\mu C/cm^2$, and the magenta regions are the undercut boxes exposed at $200\mu C/cm^2$ used to create the desired undercuts in the resist.

resolution, but slow), whereas large contact pads are exposed with Aperture 3 with current 10 nA (lower resolution, but faster). The exposure time T_{exp} is given by

$$T_{exp} \cdot I_e = D \cdot A, \tag{4.1}$$

where D is the exposure dose, A is the exposed area, and I_e is the electron beam current. A single rectangular contact pad of area 100 x 100 μm^2 that is exposed with Aperture 2 with beam current 1 nA and a dose of 750μC/cm^2 therefore takes a time 75 s to expose. Since our multi-junction test chips have 24 junctions with 48 contact pads, it would take 1 hour to expose a chip. Therefore it is necessary for time-saving purposes to use the Aperture 3 with 10 nA to reduce the exposure time by a factor of 10 to 6 min per chip. Dose tests have revealed that Aperture 3 exposures can be executed with the same dose as for Aperture 2.

Junction fabrication requires careful determination of the appropriate exposure dose for the main pattern and the undercut boxes. A dose test series is required for each new design. The PMMA layer defines the aluminium structures since it has a higher resolution than the Copolymer, which develops away more quickly. The Copolymer will be overexposed to allow for the large undercut needed to carve out the bridge. It is for the control of this undercut that the dose test is specifically crucial. Later in the fabrication process, aluminium will be evaporated at a strong angle, and this additionally creates the need to have a very deep undercut behind the junction finger. This deep undercut is created by exposing undercut boxes, i.e. the purple area in Fig. 4.7, at a lower dose than the main dose, thereby only affecting the Copolymer and not the PMMA. The actual dose test is performed by exposing an array of the same pattern, where each pattern is assigned a different dose, ranging from 700 to $1200\mu\mathrm{C/cm}^2$ for the main pattern, and from 100 to $400\mu\mathrm{C/cm}^2$ for the undercut boxes. Within each dose array pattern, the junction and undercut boxes designs vary in sizes. This method allows to determine which undercut box size at which dose is the ideal one.

Development

After the electron beam lithography, the exposed pattern needs to be developed away. First the Electra charge layer is removed in DI water for 10 s. Then the bilayer of resist is developed, i.e. removed, by dipping and carefully moving the chip in a mixture of MIBK:IPA (1:3) for 45 s, followed by a rinse in IPA for 15 s and then a very gentle N_2 blow dry. It is important to blow dry at a soft pressure to avoid breaking the bridges. Furthermore, it is important to note that the temperature affects the development process. Therefore we place the beaker of MIBK:IPA in hotbath at 25 °C in order to have a consistent and known temperature during development. Where both layers of resist have been removed, the substrate is now exposed; where only the bottom layer is removed, there is a region of undercut accessible through evaporation of metal with an angle. The Copolymer shows a strong undercut which has removed all the resist from underneath both sides of the bridge leaving it free standing.

We then inspect the dose test array under a Scanning Electron Microscope (SEM), see Fig. 4.9 to find the ideal dose and undercut box size. These are easily recognisable, since too low doses show an unsharp pattern and too strong doses show a collapsing top layer overhang. An example of such an ideal Dolan bridge after development is shown in Fig. 4.8, where the first one is made from the old design without the T-shape and thinner PMMA layer, and the second one is with the T-shape and thicker PMMA layer. The undercuts in the Copolymer layer are clearly visible in both cases. Note that to achieve good imaging under SEM, it is necessary to deposit a 10 nm layer of gold or palladium on top for charge dissipation, analogous to the charge layer for e-beam lithography. Without the gold layer, the image rapidly becomes all white due to charge accumulation.

The next step is then to place the chip into the e-beam evaporator for aluminium deposition. However, one can introduce an extra cleaning step first. Some groups perform UV-ozone, O_2 plasma etching [155, 87] or ion gun milling to clean out “descum”) the substrate surface in the pattern from resist residues. This cleaning can improve coherence times and ageing of junctions. We have tested these techniques as cleaning steps a several times, but have not obtained systematic and conclusive results yet concerning their compatibility and positive effects. Therefore for all devices in this thesis, there was no cleaning step performed before evaporation.

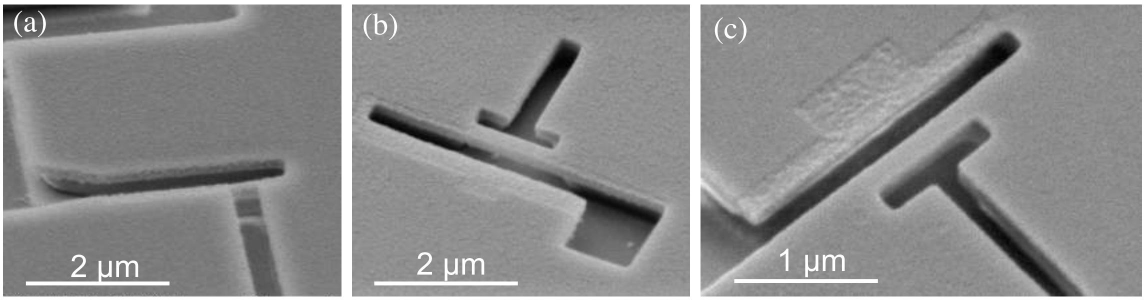

Figure 4.8: SEM pictures of the developed free standing resist bridges. (a) Resist bridge for the standard design. (b)(c) Resist bridge with the "T"-shape technique and thicker resist layers with improved robustness.

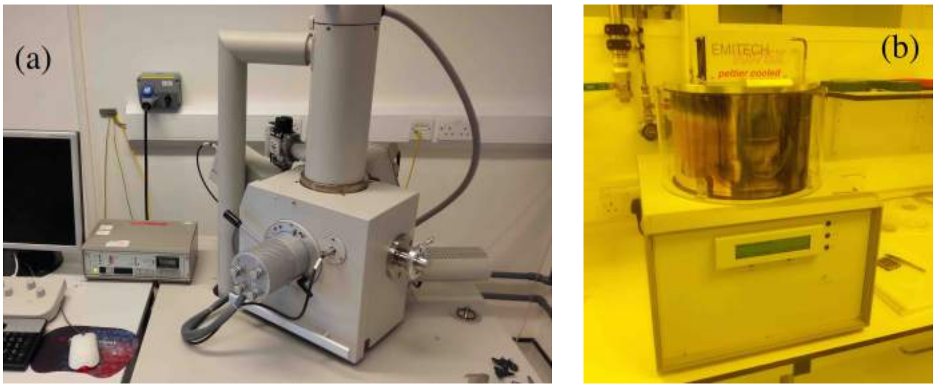

Figure 4.9: (a) Picture of the 25 kV SEM used to image the Josephson junctions. (b) Sputterer used to deposit the gold layer for charge dissipation.

4.1.4 Shadow evaporation

Shadow evaporation is the most common established technique to produce Josephson junctions [59]. It involves depositing the two layers of the Josephson junction in two different steps with two different angles, where the bridge serves as a shadow to break the contact between the two electrodes of the junction, as illustrated in Fig. 4.2 and Fig. 4.3. The main properties of an evaporator for this purpose needs is a very stable evaporation rate between 0.2 and 1 nm/ s, a stage that can rotate the sample at any angle between 0 and 180° in both directions, and an inlet for oxygen to perform the oxidation step. We use a home built electron-beam evaporator depicted in Fig. 4.10a, which was designed and built by Dr. Peter Leek in Oxford. The fully automatic control software was written and implemented by Andrew Patterson. It runs a 10 kV electron beam source and has a crucible selector holding four different materials: aluminium, gold, titanium, and palladium. The main chamber is separated by a gate valve from the load lock chamber, which allows for shorter pump down times and allows for oxidation of the sample without breaking the main chamber vacuum. The load lock has a fully rotating sample stage controlled by a motor able to rotate 360° in both directions, shown in Fig. 4.10b. A gas bottle with a mixture of 15% oxygen (O_2) and 85% argon (Ar) for the oxidation step is attached to the load lock via a double stage pressure regulator and a needle valve that allows for controlling a constant and small flow rate down to 0.1 mbar/ s.

To achieve higher vacuum, a titanium pump is first executed: titanium is evaporated during 2 min to absorb various molecules left in the chamber, in particular water and nitrogen. This typically allows our evaporator to reach roughly 8 x 10^{-8} mbar. Then a first layer of 30 nm of 5N pure aluminium is evaporated onto the rotated sampleholder under a defined angle of 60° to the substrate normal (see Fig. 4.3). The deposited aluminium layer forms the bottom electrode of the Josephson junction. The deposition rate is tracked with a built-in crystal oscillator monitor which slightly changes its mass and resonance frequency during deposition. In the subsequent oxidation step, the sample chamber is filled with the mixture of oxygen and argon until a defined pressure is reached, typically 2 mbar. Diluting the pure oxygen with argon is done to have a better control over the oxidation process, because otherwise it happens too rapidly and we would not be able to vary it to reach the desired junction parameters. The gas inlet flow rate is set to 0.2 mbar/ s. At higher speeds the final oxidation pressure is not reliably met and at even lower speeds the inlet and pump out times become a substantial fraction of the total oxidation time. The oxygen oxidises the surface of the aluminium layer, typically for a defined duration of 60 s. The result is a thin aluminium-oxide layer with a thickness on the order of a nanometer depending on the partial oxygen pressure and the oxidation time. The oxidation conditions are controlled by using the calibration results of an oxidation series of test Josephson junctions, presented in Section 4.3.3. The pressure·time of the oxidation is chosen in order to achieve a critical current and room-temperature resistance of the junction corresponding to the desired Josephson energy for the qubit. Having finished the oxidation, the gas is pumped out of the sample chamber and the sampleholder is rotated to a second position at 0° relative to the substrate normal, and a second layer of 70 nm aluminium is evaporated. In this way, the upper aluminium layer which overlaps the lower aluminium layer forms the top electrode of the Josephson junction. With this technique, a sub-micron scale Josephson junction, consisting of an aluminium bottom electrode, a very thin tunnel barrier of aluminium-oxide, and an aluminium top electrode can be created in the evaporator process chamber without breaking the vacuum. This is crucial since the thickness as well as the quality of the oxide layer sensitively determines Josephson and charging energies of the tunnel junction. The final step is to perform a post-oxidation of the sample before venting it to atmospheric pressure. This is done by venting the chamber again with the oxygen mixture at 20 mbar for 2 min (the pressure·time here is irrelevant, as long as it is high enough to saturate the oxidation). The idea is to have the top of the junction neatly oxidised with a uniformly distributed layer of clean aluminum-oxide before exposing it to the dirty atmospheric pressure.

The final step after the shadow evaporation is to strip the resist bilayer (and the thin film of aluminium now on top of it) from the sapphire substrate in a process called “lift-off”. This is done by placing the chip in hot Acetone at 50 °C for 10-

15 min. The aluminium thin film should lift-off in a single sheet piece, which we gently blow off with the use of a clean pipette. After dipping in IPA and N_2 blow drying, the chip can be inspected under an optical microscope to check if the junction is actually there and the lift-off worked neatly. An example of a junction with the SEM is seen in Fig. 4.12. If the lift-off does not work properly, the reason is usually a wrong exposure dose. In the future, some tests need to be performed on additional resist residues cleaning of the chip in order to improve coherence times and obtain less ageing of the junctions. For example, after the lift-off in Acetone, the chip could be placed in hot DMSO for 15 min to remove the rest of the residues on and around the junction. Many groups perform the lift-off in NMP for several hours [100], which it seems really leaves the junctions clean and also prevents them from ageing.

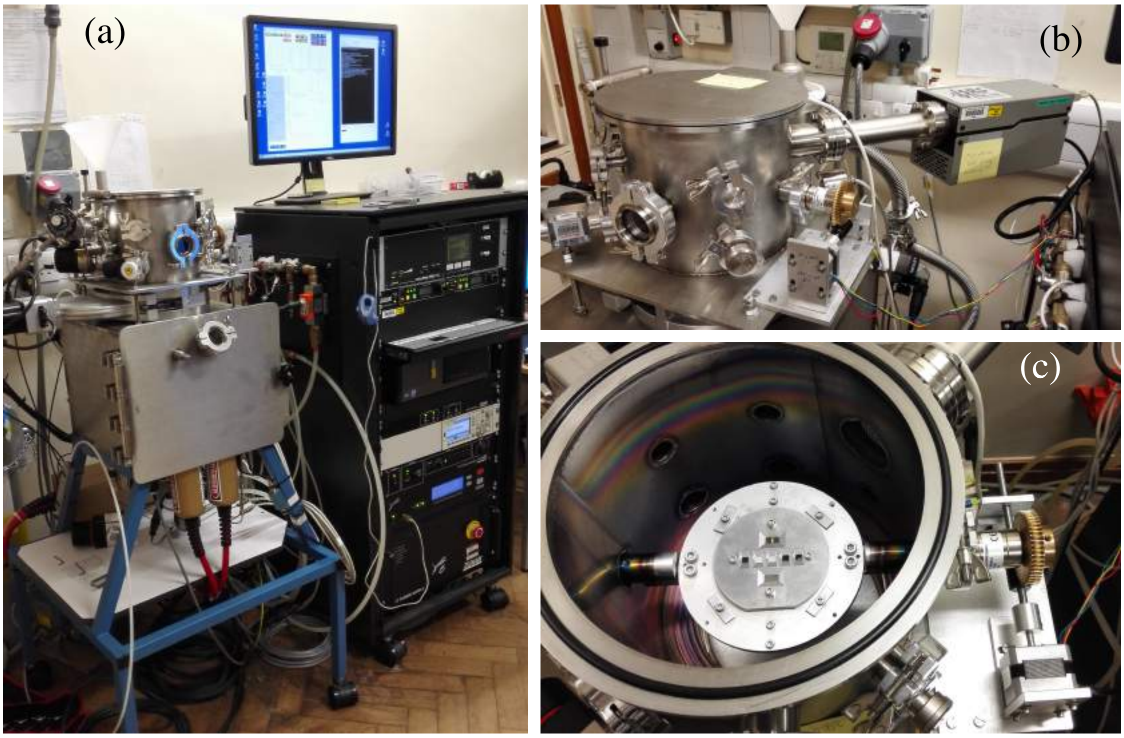

Figure 4.10: evaporator

4.1.5 Junction thickness and evaporation angle

The reason for choosing the first layer (30 nm) substantially thinner than the second (70 nm) is that this way the top layer thickness does not substantially vary at the transition from substrate to aluminium overlap. Furthermore, the layer must be at least 10 to 15 nm, because the superconducting gap energy is expected to be modified for such thin films, enabling the undesired presence of quasi-particle traps [136]. When depositing metal under a large angle, the effective thickness of the deposited layer will not be the actual tracked evaporated quantity. Since $\cos(60) = 1/2$, we end up with only half the thickness, i.e. due to the 60° angle the evaporated aluminium through the resist shadow mask is distributed over double the surface, as illustrated in Fig. 4.11. From simple trigonometry the effective thickness is determined by the surface width d_{end} of the deposited layer via

$$d_{end} = \frac{d_{evap}}{\cos(\alpha)}, \tag{4.2}$$

where d_{evap} is the opening width of the incoming evaporated particles, associated with the integrated evaporation rate as measured by the crystal monitor, and α is the evaporation angle relative to the substrate normal. For the first layer of our junctions, $\alpha = 60^\circ$ and the desired thickness is 30 nm, so we evaporate 60 nm to end up effectively with 30 nm.

The large angle of 60° is responsible for depositing the first layer“T”-pattern of the bridge onto the resist side wall in the undercut, a principle called “side wall deposition”. This way, this shadow structure is removed during lift-off. The resist profile is specifically designed with the undercut boxes for this purpose of removing the shadow structure Without the undercut boxes, the side wall deposition would rip off too close to the junction. In Fig. 4.12c, the SEM image shows the first layer

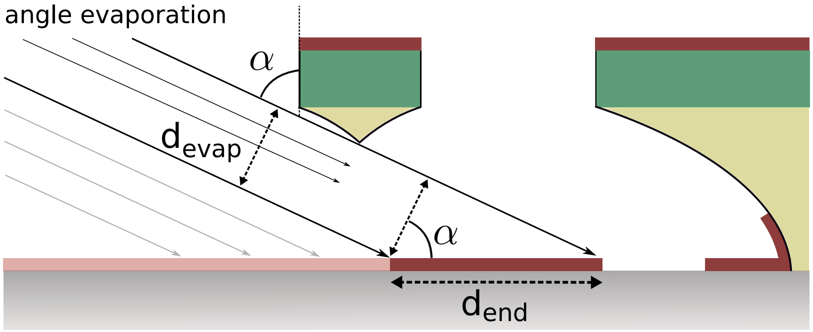

Figure 4.11: Schematic of a large angle evaporation, showing that the effective final surface width d_{end} of the evaporated thin film depends on the the angle α. At an angle of $\alpha = 60°$, the system needs to evaporate 60 nm to give a final thickness on the chip of 30 nm.

"T"-structure ripped off during liftoff leaving only the finger as the bottom electrode. The "T"-structure is obviously present in the second layer, since it is deposited with no angle and hence no side wall deposition.

Inspecting the junction after lift-off with the SEM allows to indirectly measure the height $h_{bilayer} = 850\,\mathrm{nm}$ of the bilayer resist by measuring the length of the shift l_{shift} =1500 nm between the two deposited layers and using the formula

$$h_{bilayer} = l_{shift}/\tan(60°), \tag{4.3}$$

The formula indicates that a minimum angle of 50° is necessary to achieve the required overlap of the junction fingers (relative shift of the two deposited layers).

As mentioned above, the initial design for Josephson junctions did not contain the bridge's "T"-shape in the pattern (see Fig. 4.8a), and the evaporation was done at the two respective angles 30°/30°. With these relatively low angles, the first layer shadow structure does not get deposited on the side wall, and hence is still present after the lift-off, as seen in Fig. 4.12a)b).

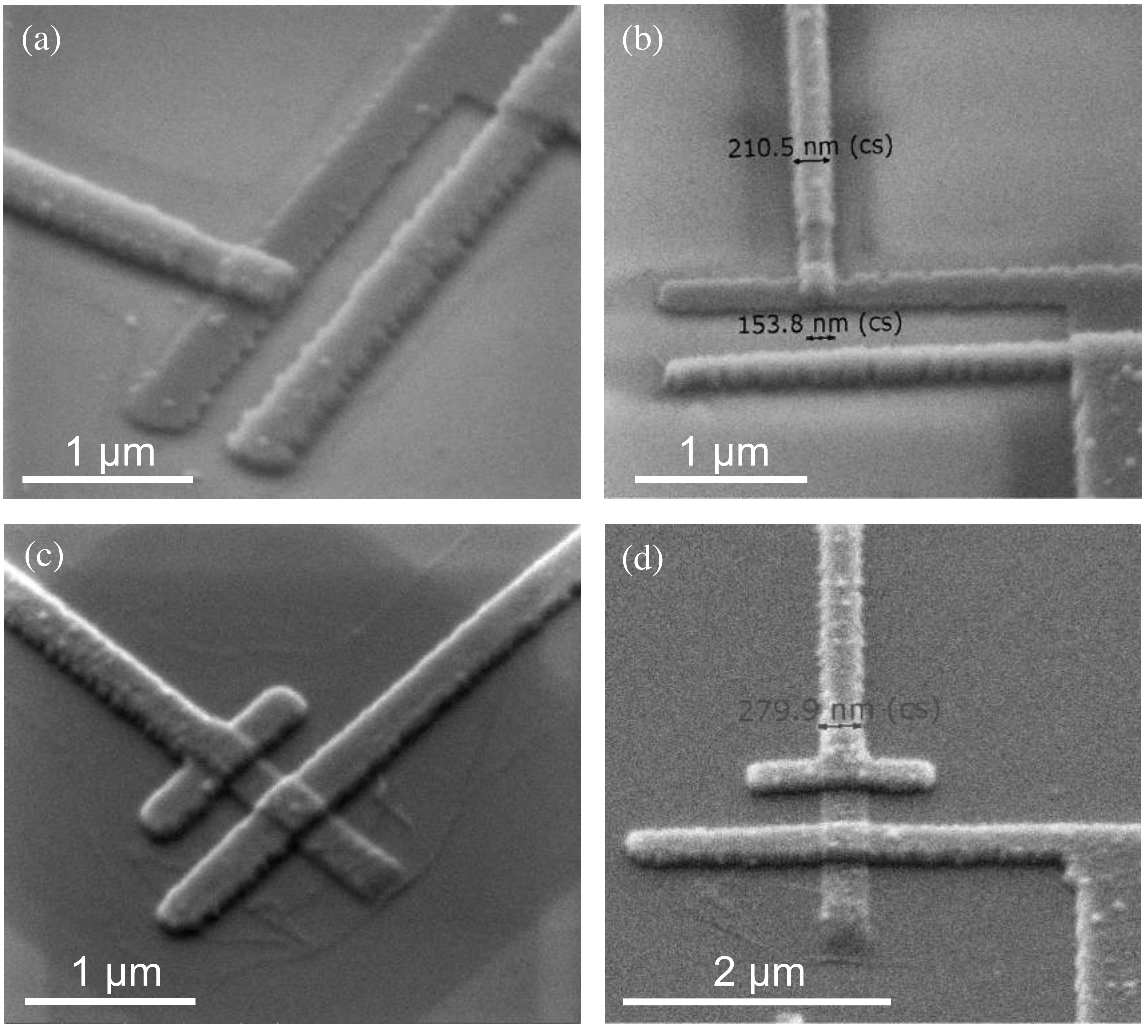

Figure 4.12: SEM images of fabricated Josephson junctions. (a)(b) Original design with the shadow arm. (c)(d) “T”-shape design.

4.2 3D transmon design

The design for the entire 3D transmon is shown in Fig. 4.13, where the large green pads are the shunting capacitor electrodes, and the inset is a zoom on the Josephson junction area. The dimensions of the pads are designed in order to obtain the desired charging energy $E_C \sim 1/C_\Sigma$ to place the transmon into the regime with a good E_J/E_C ratio of a approximately 100. Varying the geometry of the capacitor pads can have a significant effect on the transmon's coherence times due to dielectric surface

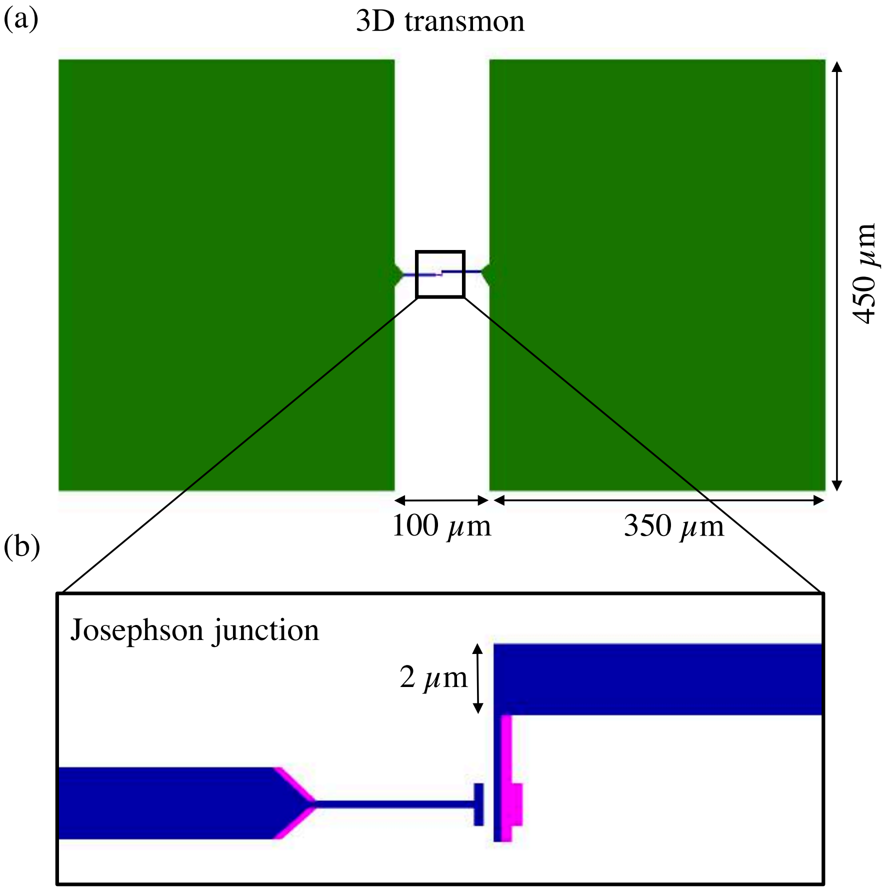

Figure 4.13: AutoCAD design pattern of 3D transmon qubit for e-beam lithography exposure. (a) Design of the entire qubit with the large shunting capacitor pads in green. (b) Zoom on the Josephson junction area.

participation ratios leading to more or less dielectric losses [192].

4.3 DC measurements of Josephson junctions

4.3.1 Junction parameters

Superconducting qubits for circuit QED experiments require two precisely engineered parameters of the Josephson junction in order to achieve the Transmon regime and a strong cavity-qubit coupling strength g: the Josephson energy E_J and the charging energy E_C. These two fundamental energies are defined by (see Section 2.3.2)

$$E_J = \frac{\Phi_0 I_c}{2\pi} \qquad\qquad E_C = \frac{e^2}{2C}\,, \tag{4.4}$$

where I_c is the critical current of the junction, $\Phi_0 = h/2e$ the flux quantum, and C is the total capacitance between the two superconducting islands on either side of the junction. The critical current is a measure of how strongly the two phases are coupled through the tunnel junction. It is therefore proportional to the junction area A and must also be dependant on the tunnel barrier thickness d. Defining the critical current density j_c which scales exponentially with the barrier thickness allows us to express the critical current as

$$I_c = j_c A \tag{4.5}$$

$$j_c = -\frac{q_s\,\hbar\,\kappa_s}{2\,\mathrm{m}_s}\sqrt{n_{s1}n_{s2}}e^{-\kappa_s\,d} \tag{4.6}$$

$$C_J = \epsilon_0\epsilon_r\frac{A}{d}\,, \tag{4.7}$$

with n_{s1}, n_{s2} the magnitudes of the wave function at the boundaries $\pm d/2$ of the junction, and κ_s the characteristic decay constant, see [73] for a detailed derivation. The energies can therefore be directly controlled by designing the height and width of the junction fingers for the e-beam lithography to achieve the desired junction area A. The junctions fabricated for qubits in this thesis are designed to be 200 x 200 nm, but effectively end up being between 150 x 150 nm and 250 x 250 nm due to variations in the resist thickness and the development step. The second control parameter, the grown barrier thickness d, is proportional to the product $p_{ox} \cdot t_{ox}$ of the oxygen pressure and oxidation time, which allows us to control it using the calibration graphs in Fig. 4.18. In reality, we do not directly measure d, rather the room temperature tunnel resistance R_n of the junction (the junctions electrical resistance in its normal state), which then gives us the critical current with help of the Ambegaokar-Baratoff relation [4]

$$I_c = \frac{\pi\Delta(T)}{2eR_n}\,\tanh(\frac{\Delta(T)}{2k_BT})\,. \tag{4.8}$$

The $\Delta(T)$ represents the superconductor's energy gap and k_B is the Boltzmann constant. When $T \to 0$, as is effectively the case for our junctions when we cool the qubits down to 10 mK, then (4.9) simplifies to

$$I_c = \frac{\pi\Delta(0)}{2eR_n}. \tag{4.9}$$

Replacing this critical current into (4.4) gives us the Josephson energy E_J directly as a function of the tunnel resistance R_n

$$E_J = \frac{\Phi_0}{2\pi}\frac{\pi\Delta(0)}{2eR_n}\,. \tag{4.10}$$

According to BCS theory [89], the superconducting energy gap $2\Delta(0)$ is related to the critical temperature of the superconductor as $2\Delta(0) = 3.50\,k_BT_c$. Four-point measurements at 10 mK of 50 nm aluminium thin films fabricated in our home-built evaporator in Oxford revealed a critical temperature of $T_c = 1.26\,\mathrm{K}$ and a superconducting energy gap of $\Delta(0) = 0.191\,\mathrm{meV}$ for our aluminium films. A plot of (4.11) using these values is shown in Fig. 4.14a. The panel b) shows the plot for the transition frequency of the qubit using the relation

$$f_{01} = \sqrt{8E_JE_C}/h. \tag{4.11}$$

4.3.2 DC measurement setup

We built a four-point DC measurement setup to measure the room-temperature resistance of the junctions and the I-V curve at 10 mK. However, the Josephson junctions kept blowing up as shown in the SEM images in Fig. 4.15. We suspect that some electric discharges form the operational amplifiers contained in the circuit were

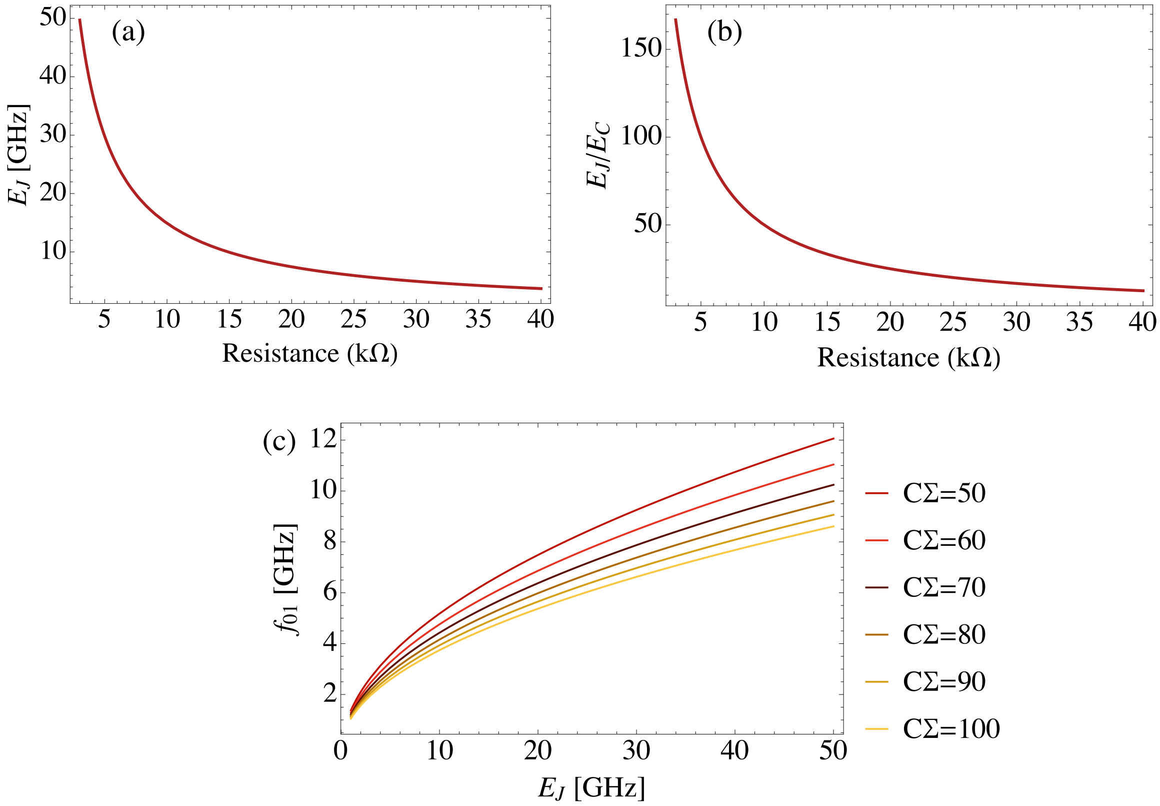

Figure 4.14: (a) Josephson energy E_J as a function of the normal junction resistance R_n, with $\Delta = 0.191\,\mathrm{meV}$. (b) The ratio E_J/E_C vs junction resistance R_n with a fixed E_C, allowing us to choose the target resistance to obtain a good transmon regime $E_J/E_C \gg 1$. (c) The transmon transition frequency f_{01} vs Josephson energy E_J for various values of charging energy $E_C \sim 1/C_\Sigma$. This allows us to choose the right capacitance for the transmon design to target a desired qubit frequency.

causing the blows. Therefore, we instead measured the room-temperature resistance of the junctions with a DC probe station from the firm Semiprobe (Lab Assistant model) and a Keithley 2450 Sourcemeter depicted in Fig. 4.17. The prober can carefully contact its very fine probe needles to the small aluminium contact pads of 100 x 100 μm fabricated on each side of every Josephson junction, as seen in the optical microscope image Fig. 4.16. Accordingly, we could fabricate chips containing 20 to 40 junctions that could then be easily DC probed via their contact pads to measure the resistances with the Sourcemeter, without ever blowing up the junctions. Indeed, the Sourcemeter is a sophisticated electronic instrument that can apply very small

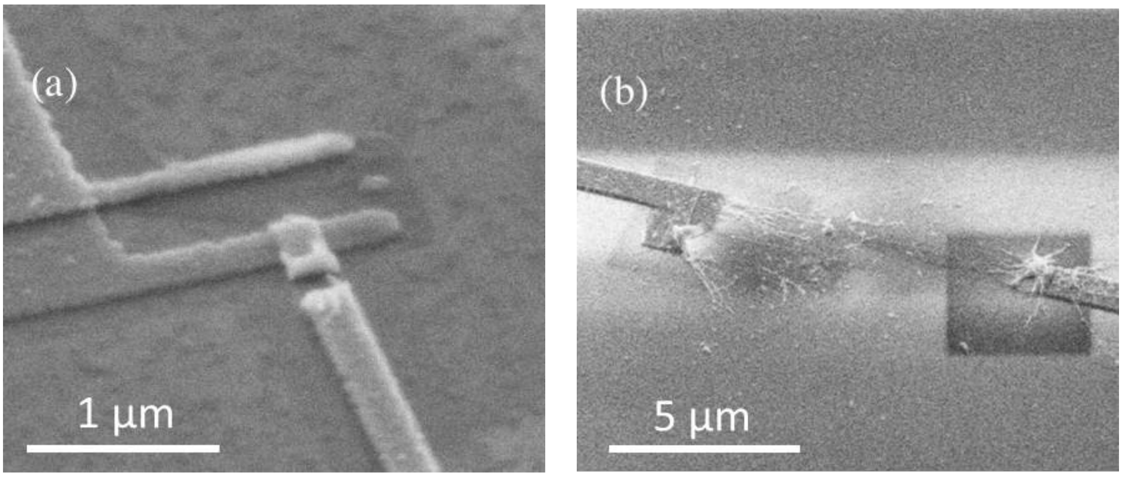

Figure 4.15: SEM images of blown Josephson junctions. (a) A junction torn in the thin junction area. (b) A junction fully blown apart as a result of an electric DC discharge.

voltages - down to nanovolts - and is internally well designed and protected to prevent any electrical discharges that would destroy the junctions. We apply a voltage of 0.1 mV with the Sourcemeter across the Josephson junction, it measures the resulting current and displays the corresponding resistance. Our junctions typically display a room temperature resistance of a few kΩ to tens of kΩ. We subtract a resistance of roughly 30 Ω from the part that is not due to the junctions by measuring a junction that is deliberately fabricated to be shorted.

4.3.3 Junction oxidation, resistances, and ageing

When Josephson junctions are exposed to air, they undergo a phenomenon known as “ageing”, where the normal state resistance increases over time. Two mechanisms are known to provoke the ageing. The first effect is the continuing oxidation of the junction barrier in air, which happens mostly near the circumference of the junction. The second is believed to originate from the fact that the AlO_x barrier that is formed during fabrication is rich of oxygen and only slowly relaxes to the stable $\mathrm{Al_2O_3}$ by a diffusive mass transport from the oxygen rich surface to the underlying aluminium

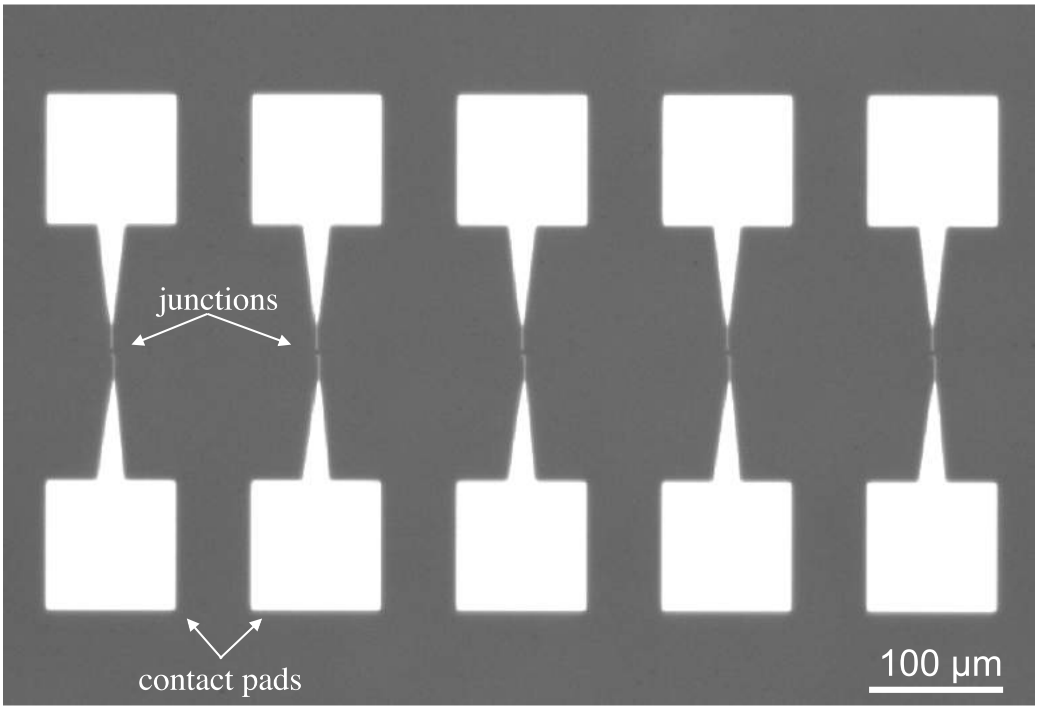

Figure 4.16: Optical microscope image of an array of Josephson junctions with contact pads for DC measurements of the junctions on the probe station at room temperature.

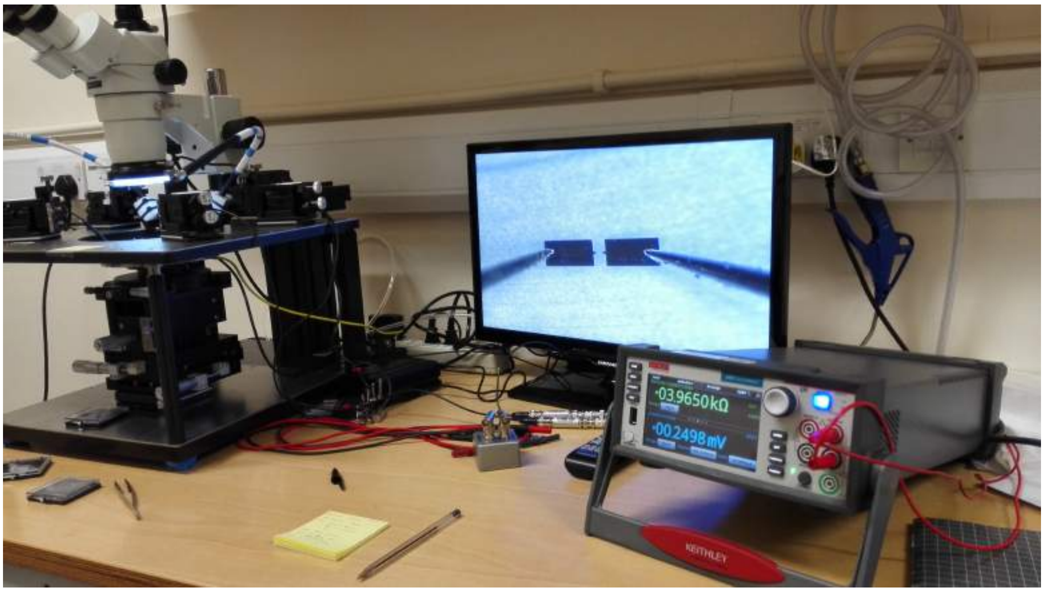

Figure 4.17: Picture of the DC measurement setup with the probe station and the Sourcemeter used to measure the normal resistance of a Josephson junction. In fact, this very picture shows the successful probing of our first transmon qubit, displaying a junction resistance of $R_n = 3.965\,\mathrm{k}\Omega$.

[106]. Some groups [100] have found that the ion mill removing organic residue before deposition is likely to play a significant role in preventing the ageing, and that the long lift-off (several hours) in hot solvent "anneals" the junction and prevents subsequent ageing.

We measured the room temperature normal resistances of a series of junctions fabricated under varying oxygen pressure and oxidation times, i.e. varying $p_{ox} \cdot t_{ox}$. The consistency across many identical junctions on a single chip is shown in Fig. 4.18 for various chips. The junctions on chip5 were oxidised at 2 mbar for 60 s and displayed a normal resistance $R_n = 5.4 \pm 1\,\mathrm{k\Omega}$ directly after liftoff (Days 0) with a standard deviation of $0.6\,\mathrm{k\Omega}$, which is a maximum of 10% difference. The ageing of the junctions on chip1 over the period of several days is shown in Fig. 4.19. Each point represents the average resistance over all measured junctions on a given day. The ageing curve is fitted to a non-linear equation

$$R_n = R_0 + \alpha \log(t), \tag{4.12}$$

where t is the time exposed to air after lift-off, R_0 is the initial resistance after lift-off, and α is the ageing factor. The particular chip in Fig. 4.19 fits to the values $R_0 = 20.4\,\mathrm{k\Omega}$ and $\alpha = 2.17$. Our junction evaporation and oxidation process is subject to fluctuations in the resulting tunnel resistances from one chip to another, and therefore such reference graphs are only of limited use. We postulate that the likely reasons for the fluctuations are the imperfect vacuum in the loadlock chamber, excess water vapour in the chamber, and the imperfect stability in the evaporation rate of the aluminium in our home-built evaporator. Furthermore, it should be noted that the resistance decreases slightly when the chip is cooled to 10 mK.

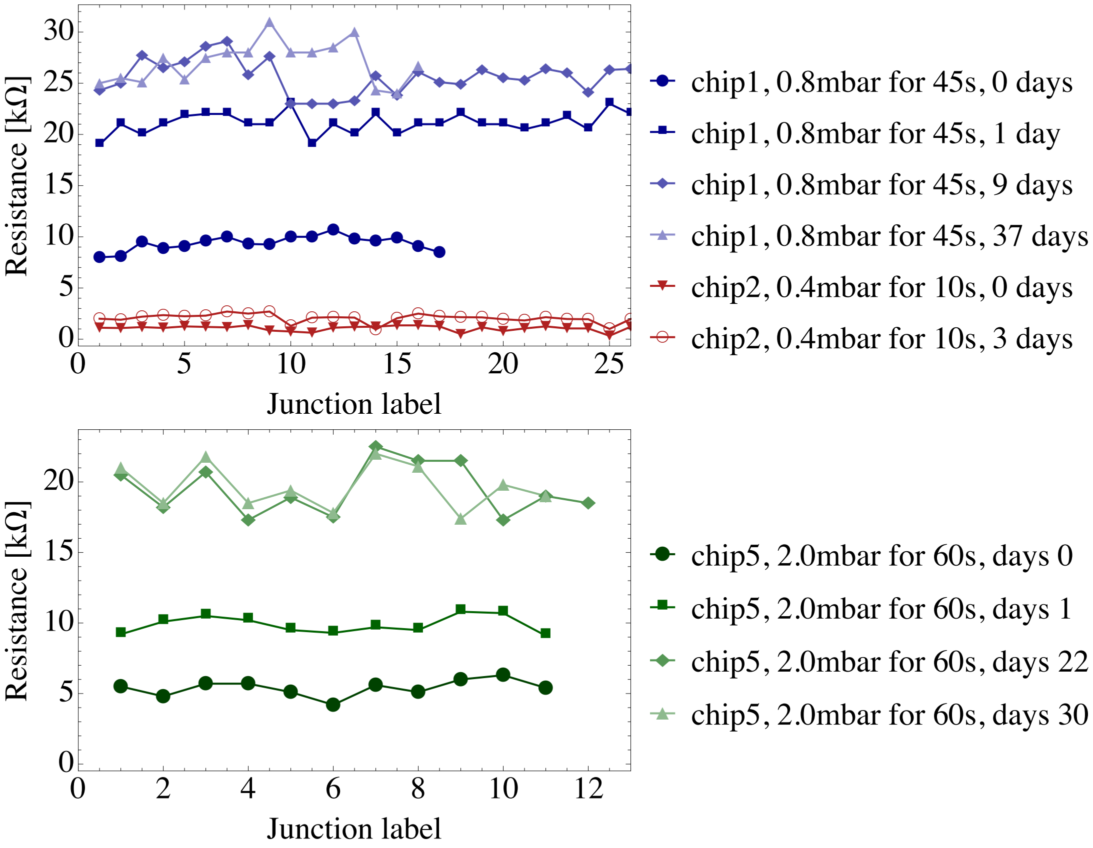

Figure 4.18: Room temperature normal resistances for many identical Josephson junctions fabricated on the same chip. The blue traces are chip1 results, the red are chip2, and the green are chip5. The various traces are results for varying amounts of days after the liftoff, showing the ageing.

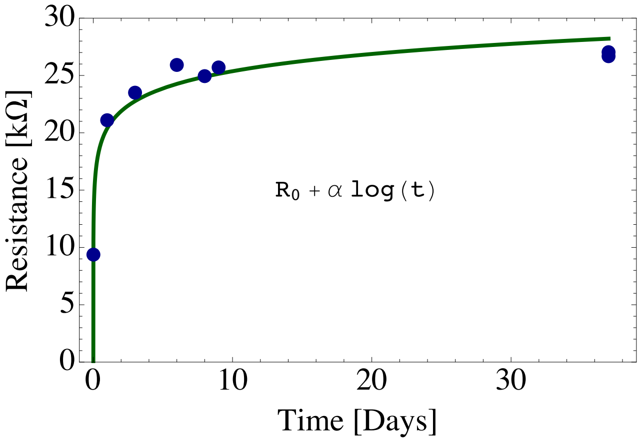

Figure 4.19: Average normal resistance of the junctions on the chip1 over time, showing the ageing of the junctions. The green line is the non-linear fit of the ageing.

4.3.4 Investigation of junction oxidation rates

We investigate the fluctuations in the junction oxidation process resulting in the spread of resistances from chip to chip with the use of a residual gas analyser (RGA). The RGA is attached to the loadlock chamber. The RGA is a mass spectrometer that analyses the pressure in the chamber and displays the precise content in the form of pressure contribution of each atomic mass unit (amu). The RGA analysis for the water content during the aluminium evaporation is shown in Fig. 4.20b. The water content slowly decreases during the short pump phase, and then first drops when the electron beam source is turned on and starts to heat up. It drops again once the aluminium evaporation occurs, reaching as low as $3.5 \cdot 10^{-8}$ mbar in the case of chip5. Five chips were evaporated while monitoring the water content with the RGA and then oxidised with identical oxygen pressure 2 mbar for 60 s. In order to achieve different water contents before the aluminium evaporation of the first junction layer, we altered the procedure for pumpdown, such as introducing a Ti pump or not, pumping for a longer or shorter time. The mean resistance across many junctions on each chip was measured and plotted in Fig. 4.20a. We predicted that water in the chamber during the junction oxidation would act as catalyst to the oxidation, but in this experiment the results show no correlation between the water content and the resistance of the junctions. We postulate that the reason for this is that the experiment has too many uncontrollable parameters such as evaporation rate, presence of other gases in the chamber, liftoff and fabrication variations from chip to chip. The current upgrade of the evaporation to a cryopump will likely improve the vacuum in the chamber and thereby help to slow down the oxidation rate in order to better control the junction resistances.

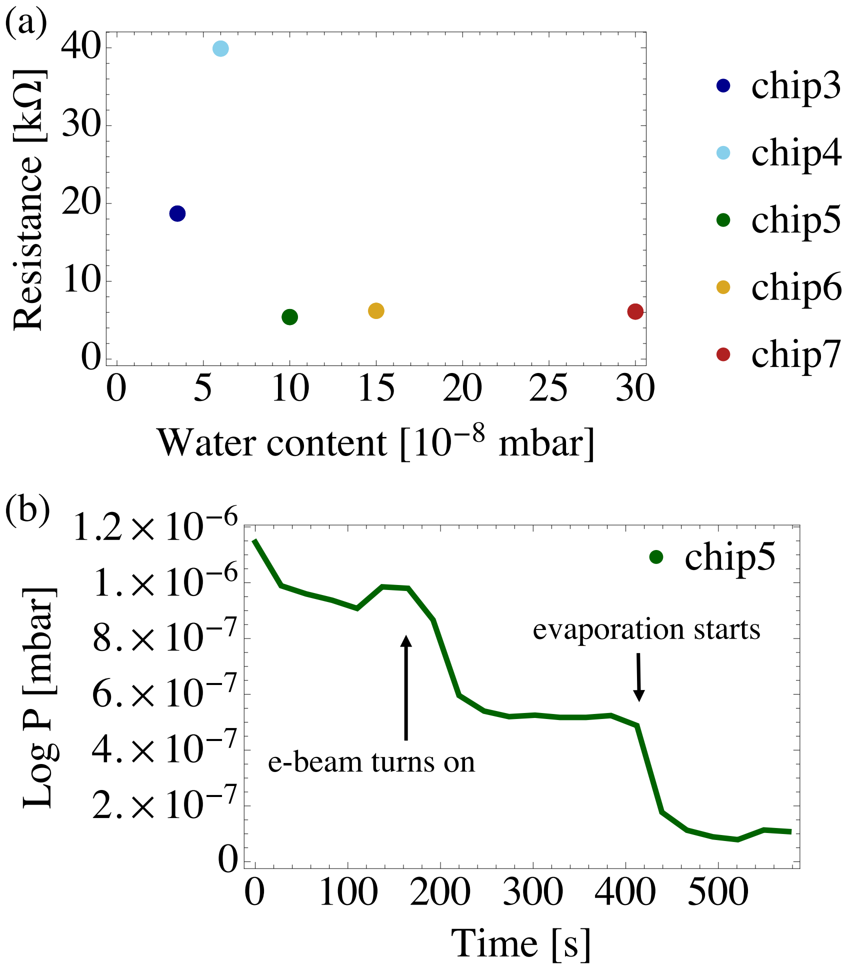

Figure 4.20: (a) Average resistance of junctions on a chip for various chips evaporated under different water content pressures. (b) Time evolution of the total pressure P in the chamber during an aluminium evaporation, here of chip5. The pump down was only a short 10 min and there was no Ti pump performed.

Chapter 5

Resonators and 3D cavities

The superconducting transmon qubit is embedded in a three dimensional aluminium cavity which acts like a coupled resonator. The theory on rectangular cavities, their quality factors, and the LCR resonator model are presented in this chapter. We present measurements of high quality factors of cavities that underwent an aluminium etching process.

5.1 Rectangular cavities

In this section we present the 3D cavities that we use for circuit QED as shown in Fig. 5.1. The cavities have a chipslot drilled to place the sapphire chip that has the transmon qubit embedded. The cavities have a port hole on one side to enable an SMA pin to enter the cavity for external coupling in order to let signals inside. The chipslot is 0.55 mm deep. We first present the bare cavity with no chip slot and no chip.

Solving Maxwell's equations with boundary conditions in a rectangular cavity describes the electric field modes that can build up inside. Considering a cavity formed by a perfect conductor, the boundary conditions are $E_{\parallel} = 0$ and $H_{\perp} = 0$.

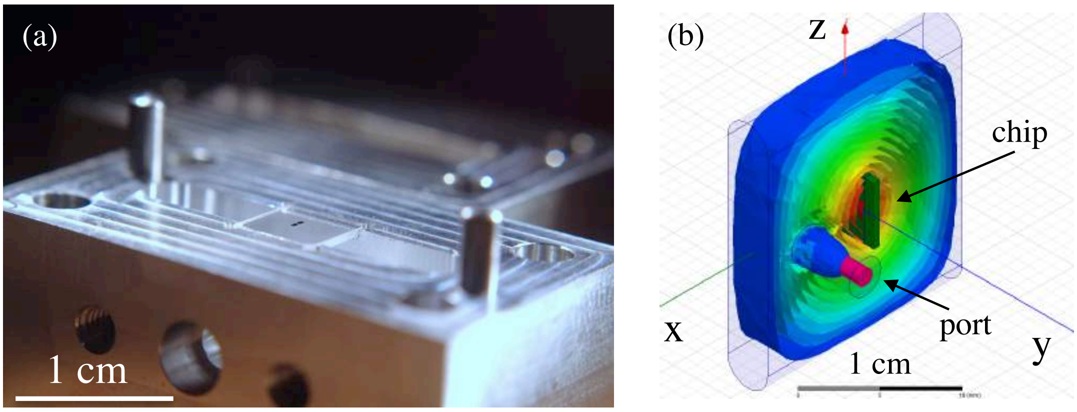

Figure 5.1: (a) Picture of a 3D aluminium cavity with a sapphire chip embedded. (b) Simulation of the electric field strength and distribution of the first TE101 mode in a one port 3D cavity with a sapphire chip embedded. Simulation performed with HFSS software.

This means $E_x = E_z = 0$ on the end walls at $y = 0, b$ with

$$\begin{aligned} E_x &= E_0 \cos\left(\frac{m\pi x}{a}\right) \sin\left(\frac{n\pi y}{b}\right) \sin\left(\frac{p\pi z}{d}\right) \\ E_y &= E_0 \cos\left(\frac{m\pi x}{a}\right) \sin\left(\frac{n\pi y}{b}\right) \cos\left(\frac{p\pi z}{d}\right) \\ E_z &= E_0 \sin\left(\frac{m\pi x}{a}\right) \sin\left(\frac{n\pi y}{b}\right) \cos\left(\frac{p\pi z}{d}\right), \end{aligned} \tag{5.1}$$

where a, b, and d are the cavity dimensions along x, y, and z axes, respectively, as shown in Fig. 5.2, and m, n, and p are positive integers representing the mode indices.

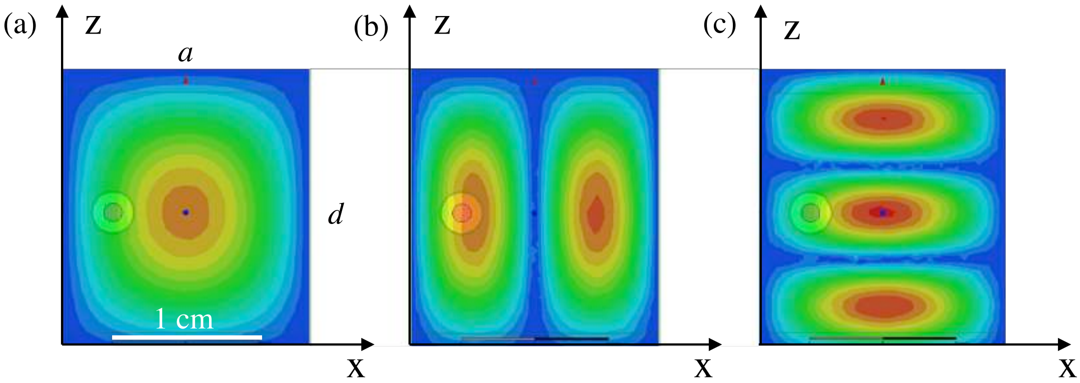

Figure 5.2: Electric field strength and distribution of the lowest three TE eigenmodes in a 3D cavity. (a) TE101. (b) TE201. (c) TE103.

The resonance frequencies of the cavity are given by [90]

$$\nu_r = \frac{c}{2\pi\sqrt{\mu_r\epsilon_r}}\sqrt{\left(\frac{n\pi}{a}\right)^2+\left(\frac{m\pi}{b}\right)^2+\left(\frac{p\pi}{d}\right)^2}. \tag{5.2}$$

It is clear from Eq. 5.1 that the lowest non-vanishing mode is one with maximum one index equal to zero, since two indices with value zero would in all cases make all the E fields vanish. For cavities with $b < a, d$, the lowest mode is TE_{101}, where (m,n,p)=(1,0,1) which has only one electric field component

$$E_y = E_0 \cos\frac{m\pi x}{a}\cos\frac{p\pi z}{d}, \tag{5.3}$$

with a resonance frequency at

$$\nu_r = \frac{c}{2\pi\sqrt{\mu_r\epsilon_r}}\sqrt{\left(\frac{\pi}{a}\right)^2+\left(\frac{\pi}{d}\right)^2}. \tag{5.4}$$

A visualisation of this mode is shown in Fig. 5.2, making clear that the field strength is independent of the dimension b in the y axis.

5.2 Energy storage, dissipation, and Q-factors

As derived in [90], resonant cavities possess a set of discrete frequency modes. When exciting a particular mode by an external source, its electric field can only build up in the cavity if it is exactly at its resonance frequency. In reality, dissipation in the cavity walls leads to a smearing out of the sharp resonance frequency, allowing a narrow band of frequencies around the eigenfrequency to enter. The quality factor Q of a cavity is a measure of the sharpness of response of the cavity to an external excitation, and is defined as 2π times the ratio of the time-averaged energy stored in the cavity to the energy loss per cycle

$$Q = \omega_0\frac{\text{Stored energy}}{\text{Power loss}}, \tag{5.5}$$

where ω_0 is the resonance frequency assuming no losses. The power dissipated in ohmic losses must be equal to the negative of the time rate of change of stored energy U due to conservation of energy. Thus the total energy stored $U(t)$ as a function of time is given by

$$\begin{aligned} \frac{dU}{dt} &= -\frac{\omega_0}{Q}U \\ U(t) &= U_0 e^{-\omega_0 t/Q}, \end{aligned} \tag{5.6}$$

where the second identity is the solution to the time derivative equation. This means that an initial amount of energy U_0 stored in the cavity decays away exponentially with a decay constant inversely proportional to Q. Oscillations of the electric fields in the cavity are consequently also exponentially damped as

$$E(t) = E_0 e^{-\omega_0 t/2Q}\, e^{-i\omega_0 t}. \tag{5.7}$$

Damped oscillations do not have a pure frequency such as the above, but rather have a superposition of frequencies around $\omega = \omega_0$,

$$E(t) = \frac{1}{\sqrt{2\pi}} \int_{-\infty}^{\infty} E(\omega) e^{-i\omega_0 t}\, \mathrm{d}\omega \tag{5.8}$$

$$E(\omega) = \frac{1}{\sqrt{2\pi}} \int_{0}^{\infty} E_0 e^{-\omega_0 t/2Q}\, e^{-i(\omega-\omega_0)t}\, \mathrm{d}t\,. \tag{5.9}$$

Performing this elementary integral leads to a frequency distribution for the energy in the cavity in the shape of a Lorentzian

$$|E(\omega)|^2 \propto \frac{1}{(\omega_0/2Q)^2 + (\omega-\omega_0)^2}\,. \tag{5.10}$$

The energy $|E(\omega)|^2$ is maximum at resonance frequency $\omega = \omega_0$. It has a full width at half-maximum $\delta\omega = \omega_0/Q$. The width $\delta\omega$ is the frequency separation between the half-power points, i.e. the bandwidth at -3 dB, or half the amplitude as shown in Fig. 5.3, and the quality factor is

$$Q = \frac{\omega_0}{\delta\omega} = \omega_0 \tau = 2\pi\frac{\nu_0}{\kappa}, \tag{5.11}$$

which relates to the lifetime τ and linewidth κ of the resonator.

The energy loss of a cavity is composed of two main parts. The first part is the internal power dissipation due to lossy dielectric of the finite conducting walls $P_{int,c}$ and of the dielectric filling the cavity $P_{int,d}$ (as is the case when placing a sapphire chip inside the cavity in 3D circuit QED). For an empty cavity filled with high vacuum the $P_{int,d}$ is dropped. The second part is the external loss P_{ext} through the coupled microwave ports. The total quality factor for a cavity as defined in Eq. 5.5 is then

$$Q_{tot} = \omega_0 \frac{U}{(P_{int,c} + P_{int,d}) + P_{ext}} . \tag{5.12}$$

Defining $Q_{int} = \omega_0\, U/(P_{int,c} + P_{int,d})$ and $Q_{ext} = \omega_0\, U/P_{ext}$ then splits the total quality factor into

$$\frac{1}{Q_{tot}} = \frac{1}{Q_{int}} + \frac{1}{Q_{ext}} . \tag{5.13}$$

The Q_{int} is called the *unloaded* Q, since it is characteristic of the resonant circuit itself in the absence of any load from external circuitry, whereas the Q_{tot} is called the *loaded* Q. Defining in addition the coupling coefficient $g = P_{ext}/P_{int} = Q_{int}/Q_{ext}$ gives

$$Q_{tot} = \frac{Q_{int}}{1+g} . \tag{5.14}$$

The case $g = 1$ is referred to as critical coupling, $g < 1$ undercoupling, and $g > 1$ overcoupling.

The internal quality factor $Q_{int,c}$ for a rectangular cavity of dimensions (a, b, d) with lossy conducting walls can be directly calculated from the conductivity of the cavity walls σ_c [154]. The formula is obtained by integrating the stored energy and the power loss in Eq. 5.5 using Eq. 5.1:

$$Q_{int,c} = \frac{\omega_0 U}{P_{int,c}} = \frac{\sqrt{\pi \nu_0 \mu_0 \sigma_c}(a^2 + b^2)abd}{2d(a^3 + b^3) + ab(a^2 + b^2)} . \tag{5.15}$$

This will be used in 5.4.4 to determine the conductivity of our cavities by inserting experimental obtained values of Q_{int}. Similarly, the internal quality factor $Q_{int,d}$ for a rectangular cavity with a lossy dielectric filling with loss tangent $\tan\delta$, but with perfectly conducting walls, can be found to be

$$Q_{int,d} = \frac{\omega_0 U}{P_{int,d}} = \frac{1}{\tan\delta}\,. \tag{5.16}$$

A cavity with both lossy conducting walls and a lossy dielectric filling then has a combined $Q_{int} = (1/Q_{int,c} + 1/Q_{int,d})^{-1}$.

5.3 Parallel LCR circuit resonator

A 3D waveguide cavity can be fully represented by a parallel LCR circuit with resistance R, capacitance C, and inductance L, as shown in Fig. 5.3a.

Considering the voltage and current across a resonator as complex numbers, then its impedance is defined as $Z = V/I$. Following [154], the impedance of a parallel

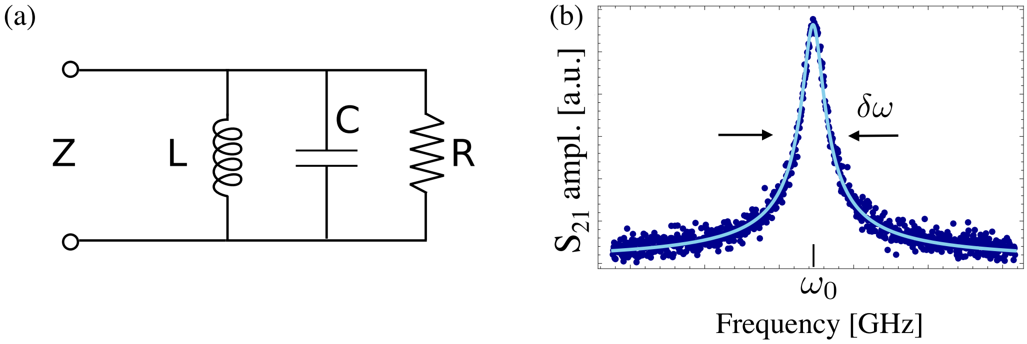

Figure 5.3: (a) Circuit diagram of a parallel LCR circuit. (b) Transmission spectrum of a GHz resonator (3D cavity) with resonance at ω_0 fitted to a Lorentizian function. The full width at half maximum $\delta\omega$ determines the quality factor.

LCR resonant circuit takes the form

$$\frac{1}{Z} = \frac{1}{Z_R} + \frac{1}{Z_C} + \frac{1}{Z_L} \tag{5.17}$$

$$Z = \left(\frac{1}{R} + i\omega C + \frac{1}{i\omega L}\right)^{-1} . \tag{5.18}$$

Consider now the Q_{int} of the resonator. According to Eq. 5.5 and Eq. 5.13, and only considering the internal power loss P_{int}, we can split the average energy stored into the electrical U_{el} and magnetic U_{mag} component to obtain

$$Q_{tot} = \omega\,\frac{U_{el} + U_{mag}}{P_{loss}}\,, \tag{5.19}$$

where we have relabelled $P_{int} \equiv P_{loss}$ for clarity. The power dissipated by the resistor is given by

$$P_{loss} = \frac{1}{2}\frac{|V|^2}{R}\,, \tag{5.20}$$

the average electric energy stored in the capacitor and average magnetic energy stored in the inductor respectively is

$$U_{el} = \frac{1}{4}|V|^2 C \tag{5.21}$$

$$U_{mag} = \frac{1}{4}|I_L|^2 L = \frac{1}{4}|V|^2\frac{1}{\omega^2 L} . \tag{5.22}$$

The circuit is in resonance when the average electric and magnetic stored energies are equal $U_{el} = U_{mag}$, implying that the resonant frequency is defined as

$$\omega_0 = \frac{1}{\sqrt{LC}} . \tag{5.23}$$

Evaluated at resonance the internal Q becomes

$$Q_{int} = \omega_0\frac{2U_{mag}}{P_{loss}} = \frac{R}{\omega_0 L} \tag{5.24}$$

$$= \omega_0 RC\,. \tag{5.25}$$

We can now express the impedance as a function of the quality factor by defining $\omega = \omega_0 + \Delta\omega_0$ and rewriting Eq. 5.17 as

$$Z = \left[\frac{1}{R} + i\omega C\left(\frac{\omega^2 - \omega_0^2}{\omega^2}\right)\right]^{-1} \simeq \left(\frac{1}{R} + 2iC\Delta\omega\right)^{-1} \tag{5.26}$$

$$= \frac{R}{1 + 2i\Delta\omega RC} = \frac{R}{1 + 2iQ_{int}\Delta\omega/\omega_0}\,. \tag{5.27}$$

This relation demonstrates that the resonance for the parallel LCR circuit indeed appears at the frequency ω_0 and that the Q_{int} relates to its bandwidth.

Considering now that our cavity is coupled to microwave ports, let Z_0 represent this external load impedance on the circuit, and the external quality factor Q_{ext} can then be expressed similarly as

$$Q_{ext} = \frac{Z_0}{\omega_0 L}\,, \tag{5.28}$$

Finally, we obtain the coupling constant for the LCR circuit as

$$g = \frac{Q_{int}}{Q_{ext}} = \frac{R}{Z_0}\,. \tag{5.29}$$

5.3.1 Two-port transmission measurement

We are interested in the transmission and reflection of a cavity coupled to two microwave ports. The ’S-matrix’ formulation is useful to describe the two-port network analysis of circuit. The four coefficients S_{ij} of the S-matrix are the four S-parameters: $S_{11}, S_{21}, S_{12}, S_{22}$. Each element S_{ij} represents the ratio of the amplitude of an outgoing wave on port i to the amplitude of the incoming wave on port j. From [154] the transmission coefficient S_{21} is given by

$$S_{21} = \frac{Z}{Z + Z_0}\,, \tag{5.30}$$

for a resonator with impedance Z coupled to an external transmission line with impedance Z_0. Using Eq. 5.26, this gives us

$$\begin{aligned} S_{21} &= \frac{R}{R + Z_0 + 2iZ_0 Q_{int}\Delta\omega/\omega_0} \\ |S_{21}|^2 &= \frac{R^2}{(R+Z_0)^2 + (2Z_0 Q_{int}\Delta\omega/\omega_0)^2}\,, \end{aligned} \tag{5.31}$$

where the second relation represents the transmission amplitude and visibly has the form of a Lorentzian peak. More generally, the Lorentzian distribution function describing the resonance line shape of a cavity mode has the form

$$F(\omega) = A_0 \frac{1}{1 + \left(\dfrac{\omega - \omega_0}{\delta\omega/2}\right)^2}, \tag{5.32}$$

where A_0 is the maximum amplitude of the peak at the resonance frequency ω_0 and $\delta\omega$ is the full-width at half-maximum FWHM, see Fig. 5.3b. Equating Eq. 5.31 with Eq. 5.32 gives us

$$\delta\omega = \frac{\omega_0(R+Z_0)}{Z_0 Q_{int}} \qquad \text{with} \qquad A_0 = \frac{R^2}{(R+Z_0)^2}\,, \tag{5.33}$$

which allows us now to express the total Q from Eq. 5.11 for the cavity using the results from Eq. 5.28 and Eq. 5.29 as follows

$$\frac{1}{Q_{tot}} = \frac{\delta\omega}{\omega_0} = \frac{R+Z_0}{Z_0 Q_{int}} \tag{5.34}$$

$$= \frac{1+g}{Q_{int}} \tag{5.35}$$

$$= \frac{1}{Q_{int}} + \frac{1}{Q_{ext}}\,. \tag{5.36}$$

Measuring the FWHM of a cavity resonance allows us directly to obtain the Q_{tot}, but it does not allow direct extraction of the internal or external quality factors Q_{int} and Q_{ext}. The solution is to additionally extract the *insertion loss* IL from the measured resonance. Since the transmission is usually measured with a VNA (Vector

Network Analyzer) in logarithmic units as $S_{ij} = 10\log(P_{out,j}/P_{in,i})$ [dB], the insertion loss IL is defined in dB as the difference between 0 dB and the maximum transmission, as shown in Fig. 5.3b. Converting the IL from dB units into an amplitude (voltage) via $l_0 = 10^{-\mathrm{IL}/20}$, the insertion loss becomes the deviation of the peak transmission from unity at resonance frequency ω_0 of the Lorentzian line shape, which corresponds to the amplitude in Eq. 5.31 ($l_0 = \sqrt{A_0}$) such that

$$A_0 = \left(\frac{R}{R+Z_0}\right)^2 = \left(\frac{g}{g+1}\right)^2 = \left(\frac{Q_{int}}{Q_{int}+Q_{ext}}\right)^2 . \tag{5.37}$$

Substituting Eq. 5.13 into Eq. 5.37, we can obtain the internal quality factor directly from measuring the insertion loss IL and loaded Q_{tot} via

$$Q_{int} = \frac{Q_{tot}}{1-\sqrt{A_0}} = \frac{Q_{tot}}{1-10^{-\mathrm{IL}/20}} . \tag{5.38}$$

Finally, we also obtain the following relation in dB units

$$\mathrm{IL} = -20\log\left(\frac{g}{g+1}\right)\ \mathrm{dB}, \tag{5.39}$$

which is useful to analyse over- and undercoupling regimes. For instance, it directly shows that a strongly overcoupled resonator $g \gg 1$ has near unit transmission IL $\simeq 0$.

5.3.2 Reflection measurement

For measurements in reflection from a single coupling port, the reflection coefficient S_{11} is given by

$$\begin{aligned} S_{11} &= \frac{Z-Z_0}{Z+Z_0} && (5.40)\\ &= \frac{R-Z_0(1+2iQ_{int}\Delta\omega/\omega_0)}{R+Z_0(1+2iQ_{int}\Delta\omega/\omega_0)} && (5.41)\\ &= \frac{Q_{int}-Q_{ext}(1+2iQ_{int}\Delta\omega/\omega_0)}{Q_{int}-Q_{ext}(1+2iQ_{int}\Delta\omega/\omega_0)} , && (5.42) \end{aligned}$$

where we have used Eq. 5.26 and Eq. 5.29. This reflection function expresses a dip in power at the resonance frequency, seen in Fig. 5.4a, as opposed to a peak in transmission for S_{21}. In the reflection measurement, the loaded Q is not related to the width of the dip anymore. However, both Q_{int} and Q_{ext} are present in Eq. 5.40 and therefore they are directly obtained from fitting the function to the data in the complex plane, see Fig. 5.4c. The reflection measurement is only useful for overcoupled or slightly undercoupled cavities with $g \simeq 1$, because with strong undercoupling the reflected signal is swamped by the background trace due to the impossibility to calibrate out the lines down the fridge.

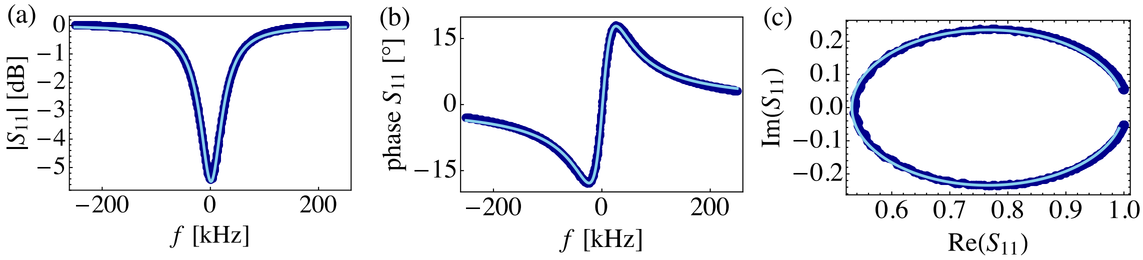

Figure 5.4: Reflection measurement S_{11} and fit of the 3D cavity with a sapphire chip embedded. (a) Amplitude of S_{11}. (b) Phase of S_{11}. (c) Smith chart, plot and fitting in the complex plane. The extracted quality factors are $Q_{int} = 195000$ and $Q_{ext} = 250000$.

5.4 Measurements of 3D cavities

5.4.1 Cavity design

The geometry for our cavity is engineered in order to optimise the mode structure for minimising qubit leakage into higher cavity modes. Our standard cavity with dimensions 17 x 3.5 x 20 mm has resonance frequencies of the TE_{101}, TE_{102}, and TE_{201} modes at 11.58 GHz, 17.40 GHz, and 19.17 GHz respectively. We used such a design because the second and third TE mode are further away from the first in frequency by more than 5 GHz, simultaneously though still keeping the mode non-degeneracy between TE_{201} and TE_{102}. The cavities are machined of Aluminium T6061, and etched cavities are made of ultra pure Aluminium 5N5 with 99.9995% purity.

5.4.2 Aluminium etching

Obtaining extremely high Q cavities requires etching the inner surfaces of the cavity walls. The aluminium etchant used for this purpose is ANPE 80/5/5/10 in VLSI quality (normal purity), a liquid mixture from Microchemicals GmbH, which is made of phosphoric acid, nitric acid, acidic acid, and water, with the concentrations shown in Tab. 5.1.

Mixture	H_3PO_4	: HNO_3	: CH_3COOH	: H_2O
Concentration [w/w]	73 %	: 3.1 %	: 3.3 %	: 20.6 %

Table 5.1: Concentrations in the aluminium etchant.

The nitric acid is responsible for oxidising the aluminium to form Al_2O_3 at the surface where the phosphoric acid then dissolves the Al_2O_3. The acetic acid is mixed for the purpose of wetting and buffering, whereas the water is to control the etch rate for given temperatures. The etchant's specification sheet indicates the temperature dependance of the etching rate in angstrom per minute. For a temperature of 50°C and 60°C we get an etch rate of 21 μm/hour and 33 μm/hour respectively. The results from cavity etchings in [156] indicate that etching more than 100 μm does not improve the quality of the cavity. To remove a 100 μm layer we must therefore etch the cavity for three hours at 60°C.

The mixture needs to be refreshed upon saturation, which is apparent when no etching bubbling is visible anymore and the mixture has turned very dark green. A red fume starts emanating when the mixture is heated too much, above 70°. The first pair of 5N5 Aluminium half-cavities that were etched in 500mL of acid showed us that the etching process will not keep the surfaces flat at a mm scale, as clearly visible in Fig. 5.5a. It was expected that by stirring the mixture during the process with a magnetic stirrer at a rate of 350 rpm the mixture would be constant and homogeneously active. A second test with no stirring showed that the surface flatness after the etching did not significantly improve. The best approach is to use very fine sandpaper to polish the top half-cavity surface to make it flat again after the etching, such that when closing the cavity with the second half the two surfaces match tightly with no leaks for light. An alternative is to machining the top surface flat again, but because the ultra pure aluminium 5N5 is so soft, this inevitably creates large burrs which deter the quality factor. Furthermore, when taking the first test cavities out of the etching mixture, they were rinsed in a distilled water beaker and then blown dry with nitrogen, and subsequently placed in an ultrasound cleaner with distilled water for several hours. This cleaning procedure has revealed itself to be particularly faulty because the test cavity continued to etch at several spots during the time it was sitting in the DI water in the ultrasound. Many small craters of the order of 1-2mm appear, as seen in Fig. 5.5b, presumably because the acid mixture was not well rinsed in these spots and was not neutralised when placed in the DI water. In fact, placing the cavities in DI water for a longer period of time precisely enabled the left over acid to continue etching, because it needs to be in an aqueous environment to act. Indeed, this problem had not occurred with first etching tests of 6061 Aluminium when the cavities were not placed in DI water for a longer time. The definite solution is to dip the cavities in an Arrhenius base, methanol H_3COH, for a minute after rinsing with DI water. The OH^- from the methanol will neutralise the acid H_3O^+ molecules

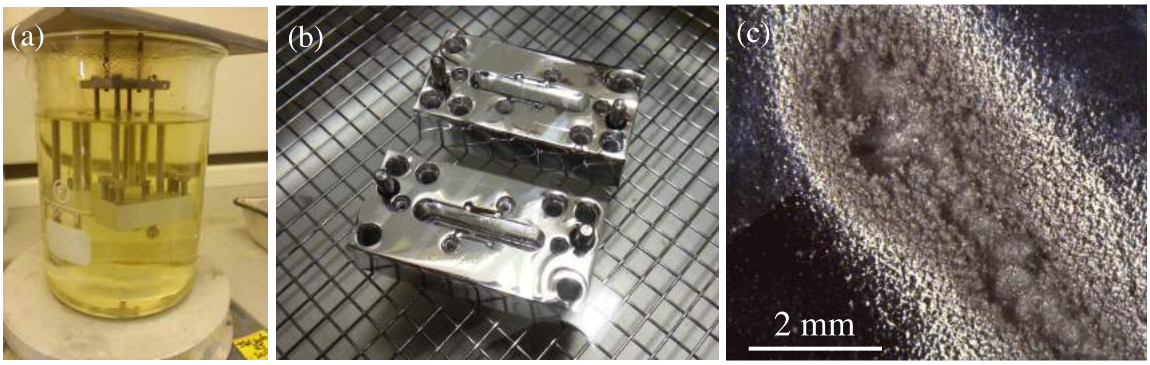

Figure 5.5: (a) A picture of the aluminium etching setup. (b) The smooth, but uneven, etched surfaces of a 5N5 pure aluminium cavity. (c) Example of spots were the acid was not properly neutralised and continued the etching.

from the phosphoric acid. A subsequent test etching has shown that this procedure of neutralisation is effective.

In order to save on acid mixture, a test was performed on a sample of 5N5 Aluminium with a tape protection of the outside walls of the cavity, in the hope that the tape prevents the covered surface of being etched. In addition, a special laquer, which is usually used in electropolishing procedures, was painted onto one surface in the hope that it would protect it as well. It turns out the laquer gets dissolved by the acid and the tape gets partly released, rendering these efforts unsuccessful in protecting the outside walls during the etching process.

The results from Tab. 5.2 show that the etching has significantly improved the internal quality factor of the one-port aluminium cavities, bringing them typically above 5 million.

5.4.3 Measurements and extraction of quality factors

The transmission spectrum of a cavity shows resonance peaks at the cavity modes TE_{101}, TE_{102}, and TE_{201}. These modes are observed in Fig. 5.6, which shows the niobium cavity measured at room temperature (red) and at 4 K (blue) with a probe stick in a helium dewar. When the cavity enters its superconducting state, the internal Q of the cavity suddenly jumps to a high value and therefore the insertion loss IL jumps to nearly zero. The data is calibrated for the attenuation of the microwave cable lines down the probe. The niobium cavity was also measured at 10 mK and revealed a $Q_{int} = 4.6 \cdot 10^6$, see Tab. 5.2.

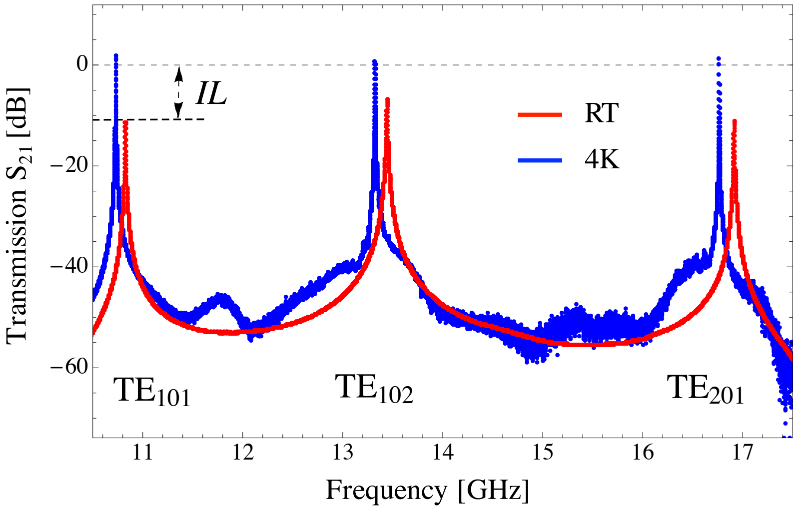

Figure 5.6: Transmission data S_{21} of the three lowest Niobium cavity modes measured at RT (red) and 4 K (blue). The insertion loss IL indicated jumps to zero when the cavity becomes superconducting below 9 K. Note that the slight offset of the measurements above zero results from the inability to calibrate the microwave cables inside the helium dewar.

In circuit QED the readout mechanism of the qubit consists of probing the cavity with a constant microwave tone at the resonance frequency. To extract the information about the qubit from the cavity at an optimum rate, the external Q should be low, at the order of 2000 -10000. If the cavity on the contrary is used as a photon storage, then the Q_{ext} should be very large, at the order of 10^7 to 10^8. As a result, it is necessary to understand and control the behaviour of the external Q, which mainly depends on the pin length of the SMA port connectors entering the cavity, i.e. the distance between the interior cavity wall to the end of the pin. The pin distance x_p is defined such that when it is positive the pin extends into the cavity, at value 0 it is exactly at the height of the wall, and when it is negative it is retracted from the cavity. The further back the pin, the higher the Q_{ext}. For two-port transmission measurements, when the Q_{int} is very high, the insertion loss becomes too small and can only be measured with a large error. Therefore it is a useful method to set the coupling pins back in order to get $Q_{ext} \gg Q_{int}$. Then the measurable loaded quality factor becomes $Q_{tot} \simeq Q_{int}$, and therefore the internal Q is directly obtainable from measuring the FWHM of the resonance peak, without having to use the erroneous IL. Fig. 5.7a shows the non-linear fit of the loaded Q as a function of coupling pin distance for the niobium cavity at 4 K.

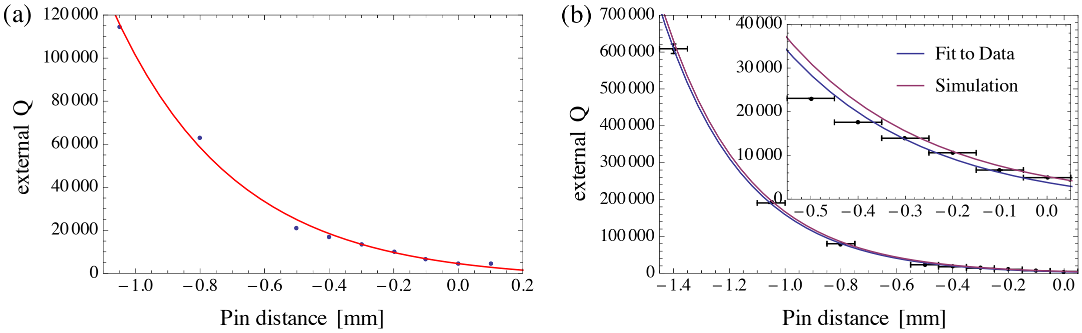

Figure 5.7: (a) The measured external quality factor Q_{ext}, which is approximatively equal to the loaded Q, as a function of pin distance in the Nb cavity at 4 K. The red line is a best fit to the data, as a guide to the eye. (b) The measured Q_{ext}'s for a set of different pin lengths Nb cavity at 4 K compared to simulation. The blue line is a best fit to the data, as a guide to the eye.

The highest internal Q is obtained with the Nb cavity at 10 mK. It was measured to be 3.85M when the temperature of the cryostat had been 22 mK for a day. Two days later, it was measured to be 4.6M at 22 mK. This indicates that the cavity is not perfectly thermalised and that only time brought the bulk of the cavity to the actual 22 mK. The thermalisation was done with a copper braid. A second round of measurements on the Nb cavity was performed, where base temperature of the cryostat was 10 mK, and a tin-platted copper braid was used. Tin is a superconductor below

Cavity	Type	T [K]	ω_r [GHz]	Q_{int}	Q_{ext}
2-port cavities 15 × 8 × 32.7 mm					
Nb	Niobium	RT	10.827	2110	
		4K	10.792	$288{\cdot}10^3$	
		10 mK	10.852	$4.6{\cdot}10^6$	
B1	Al 6061	10 mK	10.983	$1.45{\cdot}10^6$	
2-port cavities 17 × 3.5 × 20 mm					
S1	Al 6061 wcs	RT	11.7889	2000	
		10 mK	11.8434	$366{\cdot}10^3$	
S2	Al 5N5 wcs	RT	11.7882	2100	
		10 mK	18.0614	$607{\cdot}10^3$	
S2	Al 5N5(e) wcs	RT	11.6887	1600	
		10 mK	11.7448	$2.27{\cdot}10^6$	
Rect1	Al 5N5(e)	10 mK	11.0936	$2.7 \cdot 10^6$	$1.3 \cdot 10^8$
1-port cavities 17 × 3.5 × 20 mm					
Rect2	Al 5N5(e)	10 mK	11.130	$5.4 \cdot 10^6$	$2.2 \cdot 10^6$
Rect3	Al 5N5(e) wcs	10 mK	11.817	$5.2 \cdot 10^6$	$1.1 \cdot 10^6$
Rect4	Al 5N5(e) wcs	10 mK	11.817	$5.8 \cdot 10^6$	$6.3 \cdot 10^6$

Table 5.2: Measured quality factors of various cavities. “wcs” stands for “with chip slot”. The 5N5(e) are etched cavities. The Q_{int} were fitted in [110].

3.7 K. For this reason, the braid could perform very badly as a thermal conductor. Indeed the same Nb cavity was measured now to have only 2.65M internal Q, the cryostat being at base temperature since 3 days. This is a hint that the cavity was in fact badly thermalised by this braid. The cavity S1 Al 6061 was also thermally anchored with the tin-plated copper braid, with a Q_{int} of only 366000. Compared to the cavity B1 Al6061 which had a value of 1.45M, this is another hint that the braid is responsible for the low Q. Al5N5 cavities were measured with copper braid.

5.4.4 Surface conductivities

We now use Eq. 5.15 for the surface conductivity of the different materials and compare theoretical values σ_c to values obtained experimentally via the extracted Q_{int}'s. The resulting values being close to the theoretically predicted ones [1] indicates that our measurements and extraction methods of Q_{int} are reliable.

	Cavities $15 \times 8 \times 32.7$ mm				
Cavity	Al 6061 RT	Cu RT	Nb RT	Al 6061 10 mK	Nb 10 mK
σ_c exp. [S/m]	$22.8\cdot10^{6}$	$58.3\cdot10^{6}$	$7.4\cdot10^{6}$	$3.0\cdot10^{12}$	$24.5\cdot10^{12}$
σ_c theo. [S/m]	$24.6\cdot10^{6}$	$58.0\cdot10^{6}$	$6.7\cdot10^{6}$	-	-
	Cavities $17 \times 3.5 \times 20$ mm				
Cavity	Al 6061 RT	Al 6061 10 mK	Al 5N5 RT	Al 5N5 10 mK	
σ_c exp. [S/m]	$30\cdot10^{6}$	$10\cdot10^{12}$	$21\cdot10^{6}$	$40\cdot10^{12}$	
σ_c theo. [S/m]	$24.6\cdot10^{6}$	-	$38.0\cdot10^{6}$	-	

Table 5.3: Comparison of theoretical surface conductivities and measured conductivities obtained from the measured internal quality factors.

5.4.5 Adding a sapphire chip to the cavity

Typical 3D Circuit QED experiments have a sapphire chip placed in the centre of the cavity on which the superconducting qubit is fabricated, as shown in the simulation of our current cavities in Fig. 5.1. This lossy dielectric significantly reduces the internal quality factor of the cavity. We have measured cavities with a chip with a $Q_{int} \simeq 200000$. From reviewing the literature, it is evident that no group has yet achieved Q_{int} higher than roughly 500000. The extreme high quality factors are only achieved in empty cavities. An experiment at Yale University [156] has demonstrated the highest quality factors in etched cylindrical cavities using the TE011 mode reaching $Q_{int} = 740 \cdot 10^6$, and in etched rectangular cavities reaching $Q_{int} = 69 \cdot 10^6$. It is worth noting that the etching process is tedious and time-consuming, and that our unetched cavities have sufficiently high quality factors for our current 3D circuit QED experiments.

Chapter 6

3D Circuit QED

This chapter presents 3D circuit QED experiments through the characterisation of a transmon qubit embedded in a 3D cavity. First, we describe resonator and qubit spectroscopy, followed by Rabi oscillations experiments. Then we present the experiments to characterise the decay and coherence times of the qubit.

Our single-junction superconducting transmon qubit is embedded in an aluminium 3D cavity, depicted in Fig. 6.1, with a bare fundamental mode $\omega_c/2\pi = 10.47\,\text{GHz}$. The cavity is thermally anchored, inside a magnetic shield, at the base temperature 10 mK inside the dilution refrigerator. Two SMA coupled ports allow microwave signals in and out of the cavity at a rate of $\kappa/2\pi \approx 480\,\text{kHz}$, limited by a coupling quality factor $Q_{ext} = 25000$. The internal quality factor reaches $Q_{int} = 190000$ and $5\,\text{x}\,10^6$ with and without the sapphire chip inside, respectively.

The photograph in Fig. 6.1a)b) shows the first working transmon qubit we embedded in a nano-machined aluminium cavity. We have subsequently fabricated several qubits and characterised them in both two-port and one-port cavities. In this chapter we present in detail the characterisation of a transmon we name Transmon-J, which we embedded in a two-port 6061-aluminium cavity machined in the Clarendon Laboratory workshop. Through characterisation of the Transmon-J this chapter presents how experimental 3D circuit QED is performed with a single qubit.

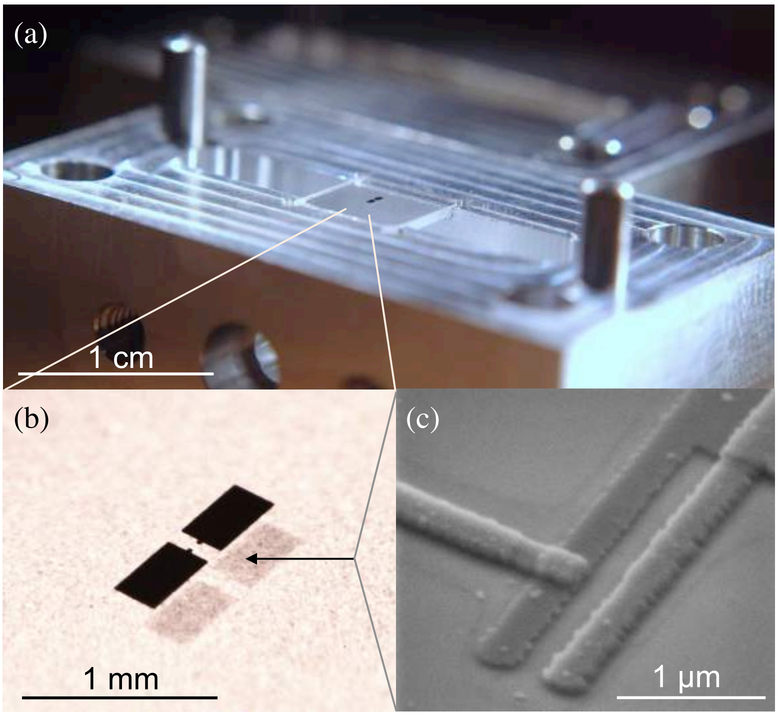

Figure 6.1: (a) Photograph of the open 3D aluminium nano-machined cavity with the qubit on the sapphire chip embedded at the centre. Courtesy of Arjan van Loo. (b) Photograph of the superconducting qubit Transmon-1st. The two capacitive electrodes have dimensions 250 x 450 μm each and are separated by 100 μm. (c) SEM image of the Josephson Junction.

6.1 Resonator spectroscopy

In circuit QED, the first and most basic measurement that is always performed is finding the resonance frequency of the cavity, which at the same time serves the purpose of verifying that the experimental setup works correctly (in particular, it checks that the powered cold amplifier works and that the FPGA acquires and digitizes the transmitted signal properly). At low applied power (where the resonator population is on the order of a few photons), the quantum effects of the dispersive regime discussed in Section 2.5.5 dominate and the resonator frequency undergoes a shift conditioned on the state of the qubit. At high powers though, the system behaves classically and the transmission profile is centred about the “bare” cavity frequency [148]. To perform the resonator sweep, we send coherent readout microwaves of frequency $\omega_{\mu\mathrm{w}}$ (called the RF signal) through the resonator at a chosen detuning $\Delta_{\mu\mathrm{w}} = \omega_{\mu\mathrm{w}} - \omega_c$ from the bare cavity resonance ω_c, and measure the averaged voltage amplitude of the transmission coefficient S_{21} (or reflection coefficient S_{11} for one-port cavities) of the signal over many experiments. Through our heterodyne detection scheme (Section 3.2.3), the voltage amplitude of the transmission signal at $\omega_{\mu\mathrm{w}}$ is recorded by the FPGA. More precisely, the down-converted I and Q voltage quadratures of the transmitted signal are individually sampled at a rate of one sample per 4 ns for 10 μs, and then combined to form the voltage transmission amplitude $T = \sqrt{I^2 + Q^2}$, resulting in the time resolved cavity response trace shown in Fig. 6.7a. This trace is integrated over the 10 μs to give one data point. The experiment is repeated on the order of 10^4 times, meaning that each data point gets averaged 10^4 times, and as a result we obtain the resonator trace plotted in Fig. 6.2c.

This measurement allows us to directly extract the state populations of the qubit. As described in Section 5.3, the cavity can be described by a parallel LCR resonator and therefore has a response that takes the form of a Lorentzian peak

$$S_{21}^{i}(\omega_{\mu\mathrm{w}}) = \frac{p_i}{1 + 2\,\mathrm{i}\,Q_t(\omega_{\mu\mathrm{w}} - \omega_i)/\omega_i}\,, \tag{6.1}$$

or dip for the one-port case, centred around the qubit state-dependent frequency ω_i, with qubit states $i = 0, 1, 2, ...$, with magnitude p_i representing the state population, and Q_t the total quality factor. When the total population p is distributed over several states $|i\rangle$, the transmission becomes

$$S_{21}(\omega_{\mu\mathrm{w}}) = \sum_i S_{21}^{i}(\omega_{\mu\mathrm{w}})\,. \tag{6.2}$$

This population distribution is visible in a resonator spectroscopy of our 3D cavity coupled to the Transmon-J shown in Fig. 6.2c, where we clearly observe the resonator

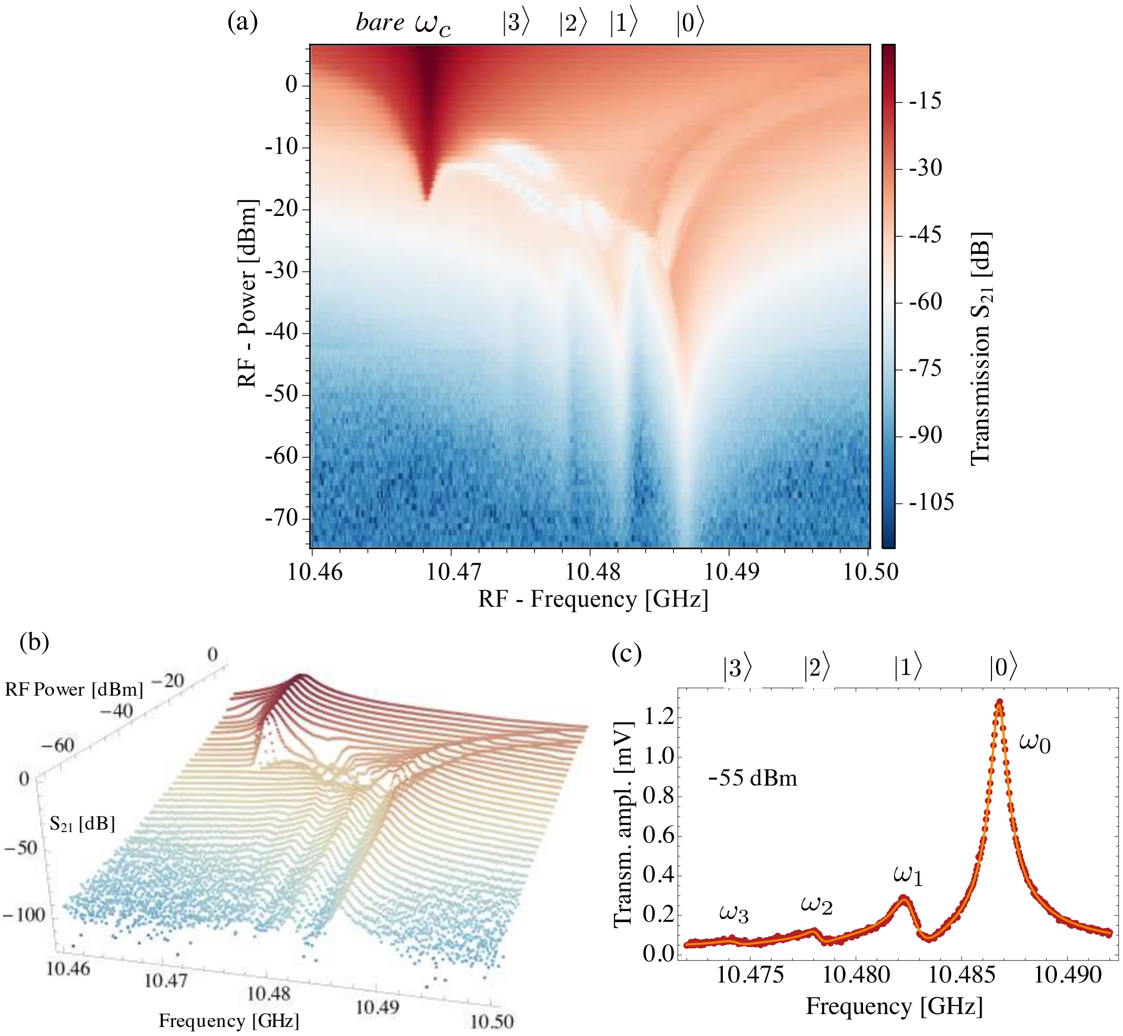

Figure 6.2: (a) Resonator spectroscopy as a function of RF input powers in dBm. At low input powers, < -50 dBm, the cavity resonance undergoes a dispersive shift due to the presence of the qubit via the dispersive interaction, and it behaves linearly. At high incident power, the dispersive shift of the cavity is neutralised and the mode of the cavity appears at it's bare resonance frequency ω_c. (b) 3D plot of the data in (a). (c) Transmission trace at the input power -55 dBm, fitted to a multi-peak Lorentzian function. The resonator peak shifts in frequency ω_i depending on the state of the qubit $|i\rangle$ for $i = 0, 1, 2, 3$.

dispersively shifting for qubit states $i = 0, 1, 2, 3$. The qubit indeed has residual thermal population in the excited and higher levels due to the fact that the cavity is not perfectly cold, and therefore these populations accordingly shift the resonator. The Eq. 6.2 is fitted to the data and allows to extract the thermal populations of the qubit p_i, see Section 6.3.1.

A transmission measurement sweeping RF frequencies for a range of RF input powers is shown in Fig. 6.2. Detailed values for the Transmon-J are presented in Tab. 6.1, albeit for a different cooldown than the one shown in Fig. 6.2, meaning that the values are slightly different due to ageing of the transmon. At low input powers, the cavity experiences the dispersive shift $\chi_0/2\pi = 15.1\,\mathrm{MHz}$ from its bare resonance frequency ω_c to ω_0 (ω_0 is now the resonator frequency when the qubit is in the ground state $|0\rangle$) due to the qubit-cavity coupling $g/2\pi = 327\,\mathrm{MHz}$. In this low power regime, less than -50 dBm, the cavity is linear, meaning that the cavity response (i.e. amplitude of oscillation) as a function of input power (i.e. number of photons) is linear. This low-power linear and well-behaved response regime is what we use for performing readout because we can be confident that the cavity does not jump or switch due to bistability or some other non-linear effect. One such low power resonator spectroscopy trace is shown in Fig. 6.2c for an RF input power of -55 dBm. For higher incident power, the Kerr non-linearity kicks in [20], the dispersive approximation breaks down, and the cavity response becomes non-linear. A dip in transmission appears, most likely due to interference between two bistable solutions of the cavity, and follows the cavity down in frequency with increasing power and disappears again at the cavity's bare frequency ω_c. This regime is used to study bistability effects, switching, squeezing, and is used for Josephson parametric amplifiers [173, 31, 25, 127, 30, 120, 20, 186, 145]. Eventually, at a high power above $-20\,\mathrm{dBm}$, the dispersive couplings reduce to zero and the cavity jumps to its bare resonance frequency ω_c where transmission rapidly rises to near unity to the so-called bright state. In this strongly driven dispersive regime of the superconducting cavity coupled to the transmon qubit, it has been shown [159] that the unexpected onset of the high-transmission "bright" state at a critical power depends sensitively on the initial qubit state. Exploiting this Jaynes-Cummings nonlinearity allows to perform a single shot high-fidelity *high-power readout* scheme, which we use in Section 7.9 in Chapter 7. The experiments in this chapter, however, are performed exclusively using the low power state-dependent dispersive readout scheme to infer the qubit-state by measuring transmission.

6.2 Qubit spectroscopy

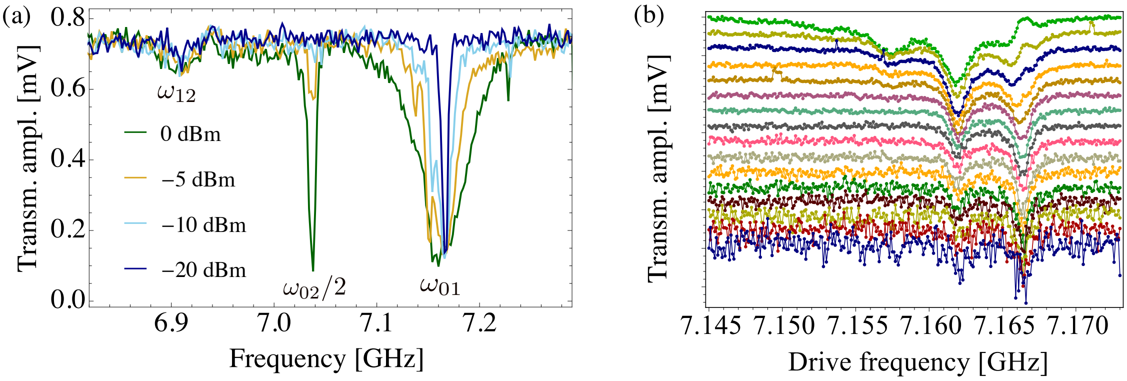

Figure 6.3: (a) Pulsed qubit spectroscopy for varying qubit drive powers. The ω_{12} transition and the two-photon transition $\omega_{02}/2$ appear at higher drive powers. (b) Photon number splitting traces as a result of the AC stark shift shown for continuous RF powers in the range -50 dBm to -80 dBm.

To measure the transition frequency of the qubit, we apply two microwave signals: a qubit microwave pulse at some frequency followed by a qubit readout pulse at the resonator frequency. In detail, a first pulsed microwave sinusoidal signal referred to as the qubit drive is applied to the cavity, which is capacitively coupled to the transmon, and its frequency ω_{spec} is swept over a range which is far detuned from the resonator. The qubit pulse is turned off prior to a subsequent pulsed microwave readout tone is turned on and is applied through the cavity at exactly its ground state resonance frequency ω_0, and a high transmission is recorded. When the drive frequency approaches ω_{01}, then the qubit transition gets driven and acquires a population towards its excited state and therefore shifts the resonator frequency by the dispersive shift 2χ. The qubit pulse is a long saturation tone, much longer than its coherence time, so that it drives some equilibrium incoherent population of the qubit, to a classical mixed state of being in state $|0\rangle$ half the time or state $|1\rangle$ half the time, which avoids the need to carefully tune the π-pulse power. The resonator is fully shifted to the excited frequency ω_1 when the qubit is in $|1\rangle$, but it appears with half its height in both ground frequency ω_0 and excited frequency ω_1 when the qubit is in the mixed state. As a result, the readout tone which is applied at ω_0 now has a decreased transmission amplitude to about half the value that it has when the qubit is entirely in $|0\rangle$. A saturation pulsed spectroscopy for various powers is shown in Fig. 6.3a. The drive frequency at the maximum drop in transmission is the qubit frequency ω_{01}.

Initially, to find the qubit frequency we perform a qubit spectroscopy with high qubit drive power over a wide frequency range. Once we have located the qubit frequency, here at $\omega_{01}/2\pi = 7.1663\,\mathrm{GHz}$, we can repeat spectroscopy for lower or higher drive powers in order to indentify the various qubit transitions. The spectroscopy trace for drive power 0 dBm in Fig. 6.3a shows several dips in addition to ω_{01}: the two-photon transition $\omega_{02}/2 = (\omega_{01} + \omega_{12})/2 = 2\pi \times 7.039\,\mathrm{GHz}$ where the ground state gets excited directly into the second excited state $|0\rangle \rightarrow |2\rangle$; and the transition $\omega_{12}/2\pi = 6.915\,\mathrm{GHz}$ from the first to the second excited state of the qubit. These transitions are used to directly extract the values for the transmon anharmonicity α and charge energy $\alpha/2\pi = (\omega_{01} - \omega_{12})/2\pi = -E_C = 256\,\mathrm{MHz}$. Knowing ω_{01} and E_C, the Josephson energy E_J can then directly be obtained from $E_J \simeq (\omega_{01}/2\pi)^2/8E_C = 24.6\,\mathrm{GHz}$. Consequently, we obtain $E_J/E_C = 96$, which clearly places our qubit in the transmon regime. For lower qubit drive powers these additional transitions gradually disappear one after the other as they are not sufficiently driven anymore. Fig. 6.4 shows the qubit spectroscopy focused on the fundamental qubit transition ω_{01} as a function of drive power, displaying two horizontal traces at powers -12 dBm and -24 dBm in the second panel. The qubit linewidth experiences power broadening for increasing drive powers, according to the expected power dependence given by $\delta\omega_{HWHM} = \sqrt{1/T_2^2 + 4\Omega^2 T_1/T_2}$, with T_1 and T_2 the qubit lifetime and dephasing time, and Ω the Rabi drive rate of the corresponding transition [171]. The drive induces stimulated emission of the qubit and therefore reduces its lifetime, thereby broadening its linewidth. Notice furthermore the photon number splitting of the qubit frequency that becomes apparent at low powers below -30 dBm. This number splitting phenomenon is presented in the next section.

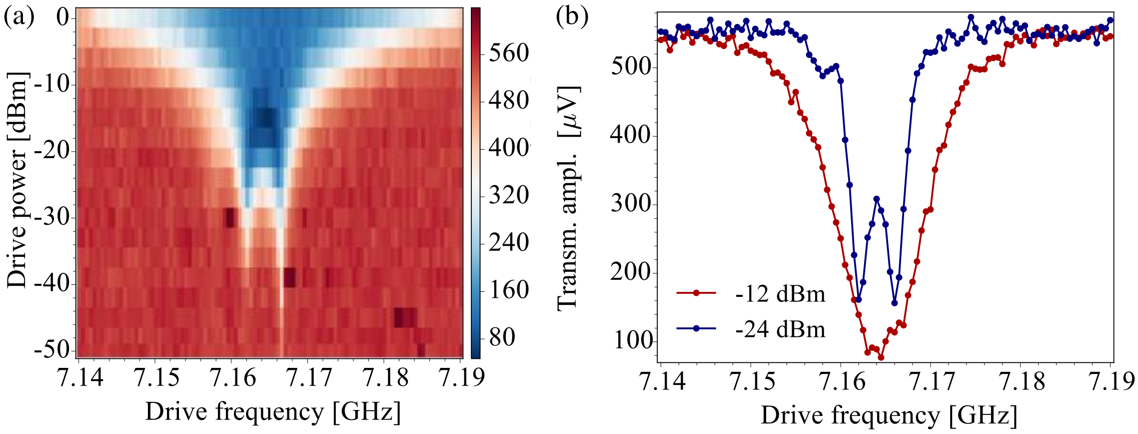

Figure 6.4: (a) Qubit spectroscopy for varying qubit drive powers (power at the RT upconversion), showing the power broadening of the qubit linewidth. (b) Qubit spectroscopy traces from (a) at the drive powers -12 dBm and -24 dBm.

6.3 Photon number splitting

We now turn to the second picture in Eq. 2.68 where the qubit frequency depends on the number of photons in the cavity. The Hamiltonian term for the qubit in $\hat{H}_{disp,q}/\hbar$ is now $(\tilde{\omega}_{01}+2\chi\hat{a}^{\dagger}\hat{a})\hat{\sigma_z}/2$. This picture expresses a photon-number dependent AC-Stark shift $2\chi\hat{a}^{\dagger}\hat{a}$ on the renormalized qubit frequency $\tilde{\omega}_{01}$. This is fully equivalent to the other picture where instead the Hamiltonian is interpreted as having the cavity undergo a qubit state-dependent shift χ. The qubit frequency is shifted to $\tilde{\omega}_{01}+2\chi$ if the cavity contains one photon, to $\tilde{\omega}_{01}+4\chi$ if it contains two photons, to $\tilde{\omega}_{01}+6\chi$ if it contains three photons, and so on. Since our cavity is in some non-zero thermal state, it contains a superposition of photon number states and therefore the qubit frequency is split into many peaks. This number splitting [170] can be used to entangle the qubit with the number state of the cavity if the number peaks are sufficiently resolved [113, 93]. Furthermore, as long as we are in the low power regime below a critical number of photons $\hat{n} \leq \hat{n}_{crit} = \Delta^2/4g^2$ [170], then the number-split qubit frequencies are stable.

A measurement of the well-resolved number splitting of our transmon is shown in Fig. 6.4b. The experiment is performed by probing the cavity with a continuous (as opposed to pulsed) RF signal in order to have the cavity constantly populated with photons while we drive the qubit frequency. Decreasing the power of the RF signal reduces the number of photons in the cavity and therefore shows a decreasing number of qubit number splittings. When the dip in transmission of the zero photon frequency relative to the one photon frequency stays constant for further decreasing RF power, then it indicates the point at which the cavity is solely populated by the thermal background population, and not the RF tone anymore. In Fig. 6.3b, the RF power at which this dip ratio between photon number states $n = 0$ and $n = 1$ happens is -68 dBm (light gray trace). At this point, the ratio is roughly half, which indicates that the average thermal photon population in the cavity is roughly $\bar{n} = 0.5$. From the Bose-Einstein statistics of the photon population at thermodynamic equilibrium

$$\bar{n} = \frac{1}{e^{\hbar\omega_c/k_B T_c} - 1} ,$$

we obtain a cavity temperature $T_c \simeq 450\,\mathrm{mK}$, which is very high. Furthermore, the dip corresponding to one intra-resonator photon $\bar{n} = 1$ on average is most prominent for the corresponding input RF power -52 dBm. This is roughly the maximum RF power we use in order to perform the qubit readout in our experiments with a single photon on average. In conclusion, the number splitting experiment serves as a calibration method for optimal readout power.

6.3.1 Thermal photon population

The residual excitation of the transmon, i.e. thermal excitation, is given approximately by the ratio of the qubit ground state population p_g to the excited state population p_e as

$$\frac{p_e}{p_g} = e^{-\frac{\hbar\omega_{ge}}{k_B T_q}} . \tag{6.3}$$

This comes from statistical mechanics, where in thermal equilibrium the Boltzmann distribution is the probability distribution that gives the probability that a system will be in a certain state as a function of that state's energy and the temperature of the system [107]. Taking the normalized ratio of the resonator transmission amplitude $p_e/p_g = 0.2$ corresponding to both states gives us the qubit temperature $T_q = 210\,\mathrm{mK}$. A more precise method to measure the qubit temperature involves comparing Rabi oscillation amplitudes between the first and second transitions [92, 140], but it is only reliable when the second state $|2\rangle$ population is nearly zero, which is clearly not our case as seen in Fig. 6.2c.

6.4 Driving the qubit

The Jaynes-Cummings Hamiltonian Eq. 2.50 describes in one of its terms the energy of the qubit as $\hbar\omega_{01}\sigma_z/2$ with its transition frequency ω_{01}. For the sake of quantum computing, one needs a channel to read out the state of the qubit and at the same time a channel to control it. Thus it is of advantage to use an external gate line to drive the qubit, and use the resonator as readout channel. In traditional 2D circuit QED, this external drive is implemented by sending a microwave signal through an additional transmission line capacitively coupled to the transmon. In a 3D circuit QED setup however, the external qubit drive is applied through the same input channel (the cavity coupling port) as the readout.

6.4.1 External drive

Just as a single isolated spin reacts to an applied external magnetic field, the state of the superconducting qubit reacts to an external EM field that can drive transitions of the two-level system from ground to excited state. For a given oscillating voltage $V_d = \mathcal{A}\cos(\omega_d t + \phi)$, with frequency ω_d, phase ϕ, and amplitude $\mathcal{A}$, the CPB Hamiltonian in Section 2.4.1 is modified by replacing the gate voltage by

$$V_g = V_g^{DC} + V_d\,, \tag{6.4}$$

where the subscript d stands for "drive". Expanding the squares and restricting ourselves again to the first two levels only, the Hamiltonian of the whole system in the laboratory frame then reads

$$H = -\frac{1}{2}(\epsilon\hat{\sigma}_z + E_J\hat{\sigma}_x) + \frac{\hbar\Omega_{Rabi}}{2}\cos(\omega_d t + \phi)\hat{\sigma}_x\,, \tag{6.5}$$

where $\Omega_{Rabi} = 4E_C C_g \mathcal{A}/\hbar e$ is the so-called Rabi frequency (the meaning will become clear later). The drive term is time dependant and has a high frequency ω in the order of GHz. The purpose of changing to the rotating frame is for visualization, in order to better understand the physics. So after changing to the qubit frame, we additionally applying the rotating wave approximation (RWA) to move to the rotating frame. This neglects terms with fast oscillating frequency $2\omega_d$. Although, for it to be valid, the detuning $\omega_{01} - \omega_d$ and the amplitude Ω_{Rabi} must be small. The driven Hamiltonian then reads

$$\tilde{H} = \frac{\hbar}{2}\Delta\hat{\sigma}_z + \frac{\hbar\Omega_{Rabi}}{2}\left(\cos\phi\hat{\sigma}_x + \sin\phi\hat{\sigma}_y\right), \tag{6.6}$$

with $\Delta = \omega_{01} - \omega_d$ the detuning of the qubit drive to the qubit transition frequency. Note that the time-dependance has been removed through the rotating frame and RWA. Since $\Omega_{Rabi} \propto \mathcal{A}$, the driving term now clearly shows that the amplitude $\mathcal{A}$ or phase ϕ of the applied microwave drive give us the possibility to rotate the state of the qubit about any arbitrary axis on the equatorial plane of the Bloch sphere, see Fig. 2.1c. This two-level Hamiltonian is therefore now again analogous to the one of a spin-$\frac{1}{2}$ in a static magnetic field

$$H = \frac{1}{2}\hbar\vec{B}\cdot\vec{\sigma}, \tag{6.7}$$

with $\vec{B} = (B_x, B_y, B_z) = (\Omega_{Rabi}\cos\phi\,,\ \Omega_{Rabi}\sin\phi\,,\ \Delta)$.

This analogy allows us to represent the evolution of the qubit in the Bloch sphere Fig. 2.1 picture of the $|g\rangle$,$|e\rangle$ subspace. Indeed, Eq. 6.6 shows that the detuning induces rotations around the z-axis, whereas the two quadratures of the drive induce rotations around the x- and y-axes that continuously oscillate the qubit state between the ground and excited state, a process called Rabi oscillations, which is used to create bit-flips. In a real experiment, the microwave generators used to produce the qubit drive are phase locked to a common reference sinusoidal signal with an arbitrary but extremely stable absolute phase ϕ. This arbitrary value is defined as the zero phase

$\phi = 0$ at $t = 0$. Hence, when the first qubit drive at $t = 0$ is sent to the qubit, this pulse implicitly defines the x-axis on the Bloch sphere. The phase of all subsequent microwave pulses will be with respect to that initial phase reference.

In principle the qubit is found in the ground state as long as no drive is applied. The quantum gates of most interest for this thesis are the $\pi/2$-pulse and the π-pulse that excite the qubit from the ground state $|g\rangle$ into the equal superposition state $(|0\rangle + |1\rangle)/\sqrt{2}$ and into the excited state $|e\rangle$ respectively. This corresponds to performing a rotation of $\theta = \pi/2 = 45°$ and $\theta = \pi = 90°$ around one of the equatorial axes. With a zero detuning $\omega_{01} - \omega_d = 0$ drive and phase set to zero, the driving Hamiltonian becomes $\hat{H} = \frac{1}{2}\hbar\Omega_{Rabi}\hat{\sigma}_x$ which states that the Bloch vector starts to precess with frequency Ω_{Rabi} around the $x-$axis. The microwave drive amplitude $\mathcal{A}$ only determines the value of the Rabi frequency $\Omega_{Rabi} \propto \mathcal{A}$. The total angle θ of the qubit state rotation however is determined by the area under the microwave pulse $\int_0^{t_0} \Omega_{Rabi}\cos(\omega_d t)\mathrm{d}t$. For a given drive amplitude, the condition $\Omega_{Rabi} t = \theta$ therefore determines how long the drive must be applied for in order for the state vector to stop precessing exactly at the the desired rotated angle θ. It is important to understand that in this way we can control the state of the qubit either by changing the microwave pulse amplitude or the pulse length. Single qubit gates are then given by the pulse length t_0:

$$\text{Hadamard gate :} \qquad |g\rangle \rightarrow \frac{|g\rangle + |e\rangle}{\sqrt{2}} \qquad \pi/2\,\text{pulse} \qquad t_0 = \frac{\pi}{2\Omega_{Rabi}} \tag{6.8}$$

$$\text{X gate :} \qquad |g\rangle \rightarrow |e\rangle \qquad \pi\,\text{pulse} \qquad t_0 = \frac{\pi}{\Omega_{Rabi}}. \tag{6.9}$$

6.4.2 Rabi oscillations

When the external drive, given by the drive Hamiltonian in Eq. 6.6, is on resonance with the qubit frequency $\omega_d = \omega_{01}$, the microwave field induces transition between the qubit states $|0\rangle$ and $|1\rangle$ around the x-axis (defining the phase to be zero). After a microwave pulse length τ the probability that the qubit initially in the ground state is in state $|1\rangle$ is given by $|p_1|^2 = \sin^2(\Omega_{Rabi}\,\tau/2)$. The state vector on the Bloch sphere therefore rotates continuously around the x-axis making the probability p_1 oscillate in time with Rabi frequency Ω_{Rabi} as long as the drive is turned on.

Coherently manipulating the quantum state of the transmon to perform quantum gates first requires us to measure and analyse Rabi oscillations in order to accurately calibrate the $\pi/2$- and π-pulses needed for our experiments to characterise the energy decay and dephasing times of the qubit. Starting with the qubit in the ground state $|0\rangle$, we apply a microwave pulse at ω_{01} for varying pulse length, followed by a readout pulse. Fitting the resulting Rabi oscillations, e.g. Fig. 6.5c, between state $|0\rangle$ and $|1\rangle$ at a chosen qubit drive power, permits us to experimentally extract the π-pulse duration (π-pulse calibration) required to achieve a complete population transfer from $|0\rangle$ to $|1\rangle$ at transition frequency ω_{01}. The Rabi oscillations are fitted to a slowly decaying sine function with Ω_{01} the Rabi frequency of the first qubit transition. Performing Rabi oscillations at a given drive power for a range of varying qubit drive frequencies, plotted in Fig. 6.5a, allows to determine and calibrate the exact qubit frequency by extracting the drive frequency at which the Rabi rate is lowest.

A similar experiment with Rabi oscillations can be performed by varying the qubit drive power as shown in Fig. 6.6a. Recalling Eq. 2.71 in Section 6.4.1, the resulting fitted Rabi oscillations verify the expected linear scaling of the Rabi frequency Ω_{01} with drive pulse amplitude $\mathcal{A} \propto \sqrt{\hat{n}_s}$, see Fig. 6.6b. This experiment allows us to select drive power needed to obtain $\pi/2$- and π-pulses of the desired length.

Alternatively, one can control the Rabi oscillations by fixing the Rabi pulse length

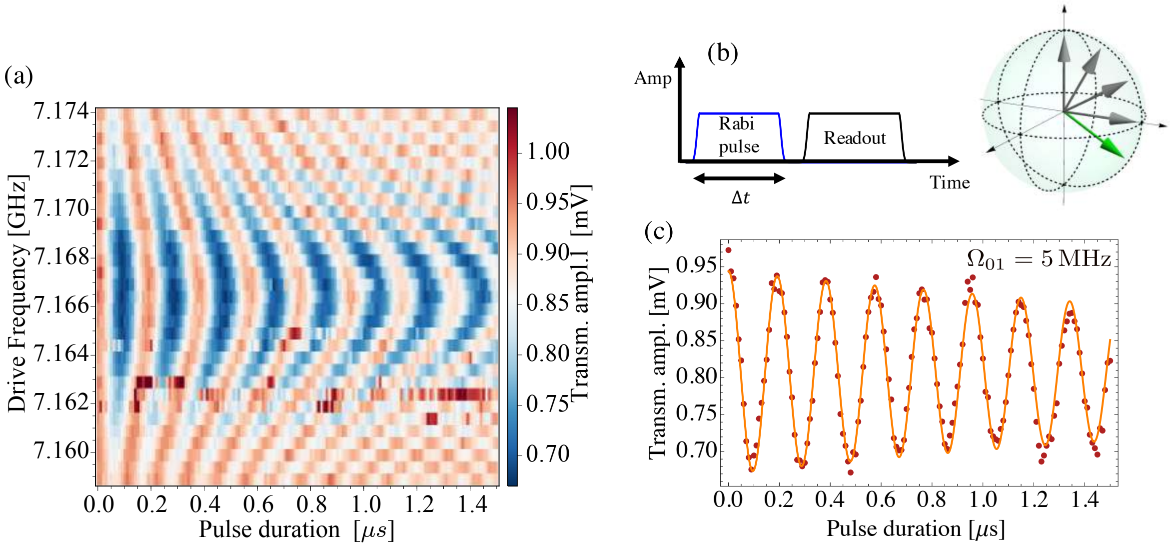

Figure 6.5: Rabi oscillations performed on the qubit in the two-port cavity. (a) Rabi oscillations for varying qubit Rabi drive frequencies, for fixed input power -10 dBm. The qubit drive frequency at which the Rabi frequency is the lowest is used as a calibration of the exact qubit transition frequency. (b) Schematic of the Rabi pulse sequence with varying pulse length and the Bloch vector rotating on the Bloch sphere under a Rabi drive. (c) Fitting of Rabi oscillations for the trace in (a) at drive frequency 7.166 GHz.

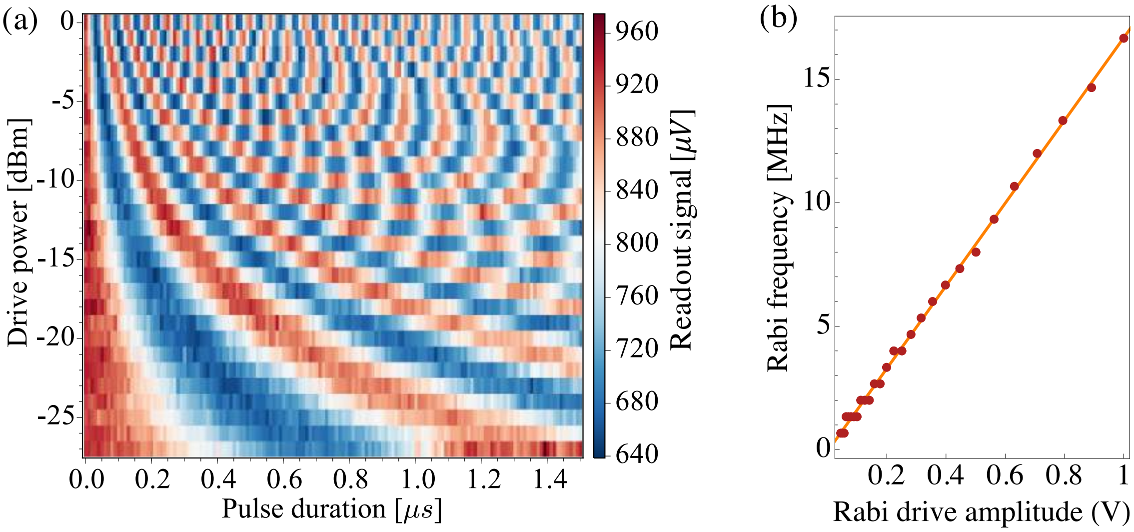

Figure 6.6: (a) Rabi oscillations for varying qubit Rabi drive powers. (b) Plot of the resulting Rabi frequencies that scale linearly as a function of the drive amplitude.

and varying the pulse amplitude. This is actually the more desirable method because the AWG operate faster when it can simply sweep the amplitude instead of having to load a new pulse shape (length) for each pulse duration step in the sweep. Furthermore, quantum algorithms need to have the shortest quantum gate time in order to optimise the number of gates that can be performed before the qubit decays. Therefore, choosing and fixing the shortest pulse length and varying the amplitude is the best gate method. There is naturally a lower limit to how short pulses can be made, since too short pulses lead to a large undesirable spread in the frequency of the pulse. Since the transmon has a weak anharmonicity, too short pulses therefore lead to large single-qubit gate errors. Techniques that employ pulse shaping to abate these errors typically involve Derivative Removal via Adiabatic Gate (DRAG) pulses [36]. In this thesis however, all Rabi pulses are done without any pulse shape optimization and are driven by varying the pulse duration. Having obtained the π-pulse calibration, the qubit can be initialised in the state $|0\rangle$ and we proceed to investigate its decay and phase coherence.

6.4.3 Qubit relaxation time

The energy relaxation time T_1 is measured by extracting the exponential decay of the qubit population. A resonant π-pulse is applied to excite the qubit to state $|1\rangle$, at which point the resonator is fully shifted to ω_1. After waiting a time Δt the population has decayed and the remaining population is measured by the usual transmission readout through the resonator. The more the qubit state has decayed, the stronger the transmission of the readout signal at ω_0 becomes. Sweeping the delay time Δt the remaining population follows a time-domain exponential decay curve, shown in Fig. 6.8b for our Transmon-J, which we fit to $p(t) = e^{-t/T_1}$ and

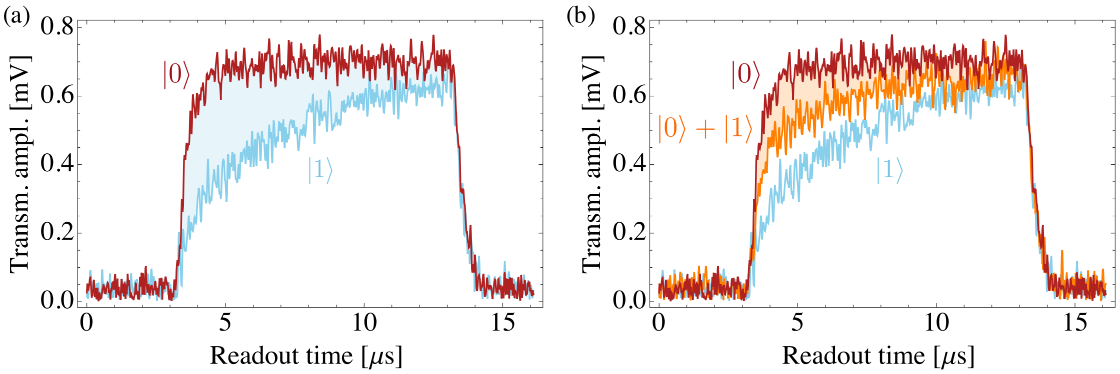

Figure 6.7: (a) Time-resolved cavity response for the qubit in the ground state $|0\rangle$ and for the qubit initially excited to state $|1\rangle$. (b) Time-resolved cavity response for various readout delays $\Delta t = 0.5\,\mu$s, $6\,\mu$s, and 18 μs after an initial π-pulse. The qubit state population is proportional to the area between the ground state trace and the trace for which the remaining population is in question.

extract the qubit relaxation time $T_1 = 7.1\,\mu$s. Inferring an excited state population is possible by comparing the time-resolved cavity response trace of this state to traces corresponding to the qubit in state $|0\rangle$ and $|1\rangle$, as shown in Fig. 6.7a. The qubit state population is proportional to the area between the ground state trace and the trace for which the remaining population is to be determined, shown in Fig. 6.7b for readout delays $\Delta t = 0.5\,\mu$s (red), $6\,\mu$s (orange), and $18\,\mu$s (blue), corresponding to the states $|0\rangle$, some incoherent mixture $|0\rangle + |1\rangle$, and $|1\rangle$, respectively.

This decay experiment can be used to calibrate the exact qubit frequency in an analogous way to the one with Rabi oscillations in Fig. 6.5b. In Fig. 6.8a the excited state decay traces are plotted for a range of different qubit drive frequencies applied, resulting in a density plot that clearly allows to determine at which frequency the decay is the slowest, in this case $\omega_d/2\pi = 7.1663\,$GHz. The reason for this is because a detuned π-pulse (off resonance) leads to an additional $\hbar\Delta\hat{\sigma}_z/2$ rotation around the z-axis during the Rabi rotation around the x-axis due to the first term in Eq. 6.6, where now $\Delta = |\omega_{01} - \omega_d| > 0$. The π-pulse on the Bloch sphere therefore ends up not at the excited state $|1\rangle$, but at a lower latitude, i.e. a state population increasingly

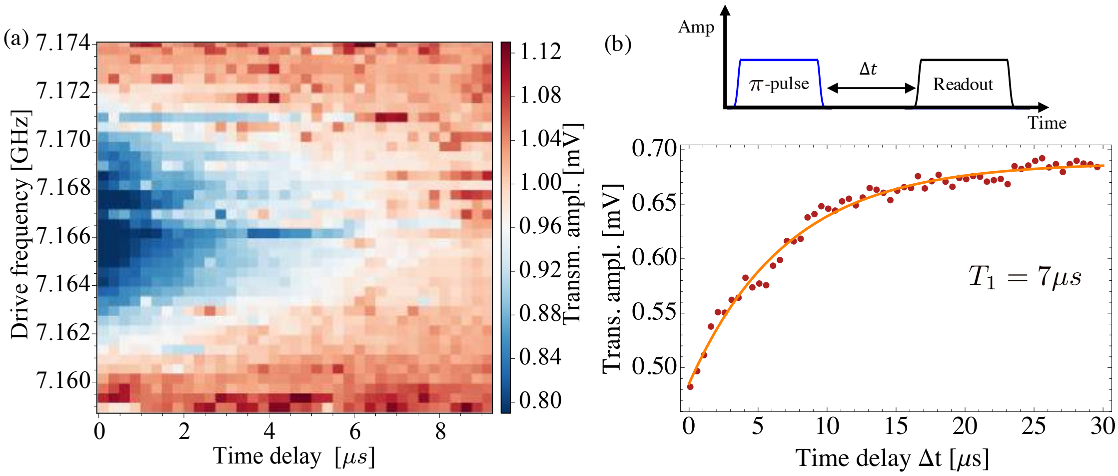

Figure 6.8: Energy relaxation for the Transmon-J qubit. (a) Qubit decay experiment for a range of qubit drive frequencies, allowing to exactly calibrate the qubit transition frequency $\omega_{01}/2\pi = 7.1663\,\text{GHz}$. (b) Schematic of the pulse sequence. (c) Exponential decay curve of the excited qubit state with characteristic decay time $T_1 = 7.1\,\mu\text{s}$.

lower than unity with increasing detuning. This then shows up as a higher initial transmission in the readout in Fig. 6.8a for detuned drive frequencies.

The qubit characterisation so far has been based on the Tranmon-J device which has a decay time $T_1 = 7.1\,\mu\text{s}$. It is worth mentioning the decay time that we obtained for our very first working transmon qubit, which we label by Transmon-1st, is $T_1 = 25\,\mu\text{s}$ and shown in Fig. 6.9b. It was measured in a one-port aluminium cavity that was produced by CNC Nano-Machining at the Rutherford Appleton Laboratory (positional accuracies down to $0.5\,\mu\text{m}$), depicted in Fig. 6.1c. The decay curve from the reflection measurement in the case of a one-port cavity shows the inverse amplitudes to a two-port cavity transmission measurement, since the resonator is a dip that gets shifted instead of a peak. The experiment performed with the Transmon-1st shown in Fig. 6.9a illustrates the technique we typically use to calibrate the π-pulse length. By measuring decay traces for varying initial excitation pulse durations we can extract the exact pulse duration that produces the highest amplitude. This one then corresponds to an exact π-pulse, and the exact $\pi/2$-pulse is then just half of it.

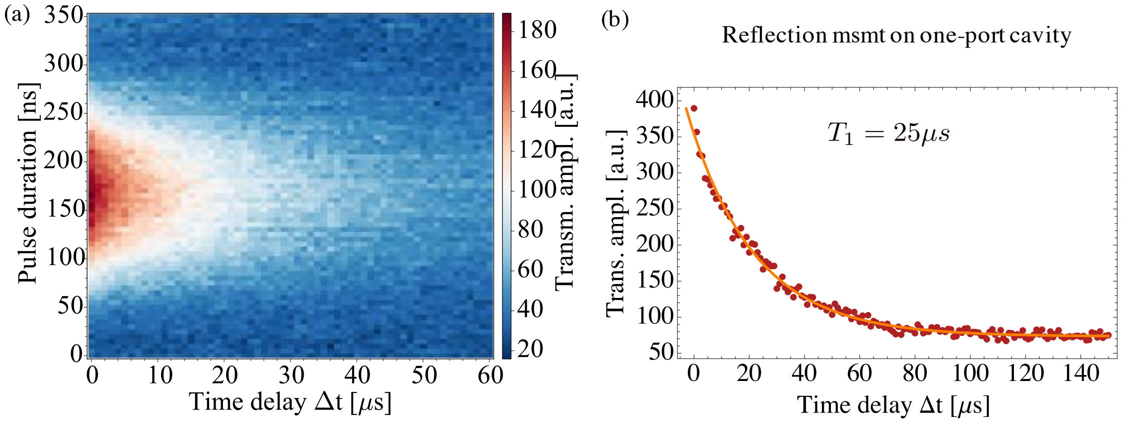

Figure 6.9: Energy relaxation for the Transmon-1st qubit. (a) Qubit decay experiment for different qubit pulse durations, allowing to exactly calibrate the pulse length that performs an exact π-pulse. (b) Energy relaxation trace showing an excited state exponential decay time of $T_1 = 25\,\mu$s.

6.4.4 Ramsey experiment and dephasing time

Whereas the previous section presented measurements of the energy relaxation of the qubit, this section presents the measurements on the phase decoherence (dephasing), which is investigated by measuring Ramsey interference fringes.

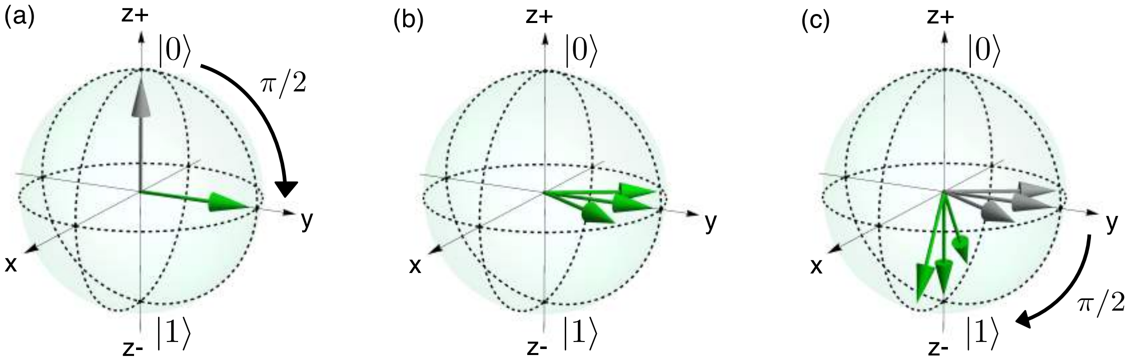

Figure 6.10: Bloch sphere representation of the Ramsey experiment pulse sequence. (a) Apply a $\pi/2$-pulse to bring the qubit state in a superposition state of $|0\rangle$ and $|1\rangle$. (b) Allow a free evolution time to pass where the Bloch vector dephases. (c) Apply a second $\pi/2$-pulse to project the state back onto the z-axis.

A Ramsey experiment consists of first applying to the qubit a short microwave $\pi/2$-pulse at the qubit transition frequency ω_{01}, with phase $\phi = 0$, and with calibrated amplitude from the previously performed Rabi measurement. This brings the qubit into an equal superposition state of $|0\rangle$ and $|1\rangle$. Then, after allowing a variable free-evolution time Δt to pass, another identical $\pi/2$-pulse is applied, as schematically depicted in Fig. 6.10a). For the Ramsey experiment the drive is purposefully detuned, $\Delta_d = \omega_{01} - \omega_d \sim$ MHz, by a few MHz from the qubit transition frequency in order to generate oscillating traces, called Ramsey interference fringes. Indeed, in the rotating frame, the qubit acquires a phase $\phi = \Delta_d \Delta t$ during the delay time by rotating around the z-axis, according to Eq. 6.6. When the second $\pi/2$-pulse is then applied, the final state has a projection on the z-axis which is dependant on the accumulated phase: the x-component of the state is either rotated towards the excited state $(+z)$ or the ground state (−z). Hence it ultimately has a sinusoidal dependance on the delay time. The whole pattern just described is repeated by sweeping the delay time. An example of such a Ramsey experiment is shown in Fig. 6.11b. The fitted exponentially decaying envelope of the oscillations gives the dephasing time $T_2 = 3.9\,\mu$s, according to the fit function

$$A = e^{-t/T_2} \cos(\omega_{01} t) \,, \tag{6.10}$$

where A represents the voltage amplitude of the oscillations. Similar to the experiment presented in Fig. 6.8a, carrying out Ramsey traces for varying detunings Δ_d around the qubit frequency allows for exact calibration of the qubit frequency from the plot in Fig. 6.11a. The Ramsey oscillations disappear when the detuning Δ_d of the pulses is exactly zero, leaving a simple exponential decay with no oscillations. Here this happens at exactly $\omega_d/2\pi = 7.1663\,$GHz again, just as for the calibration result in Fig. 6.8, thereby further confirming the qubit transition frequency of Transmon-J.

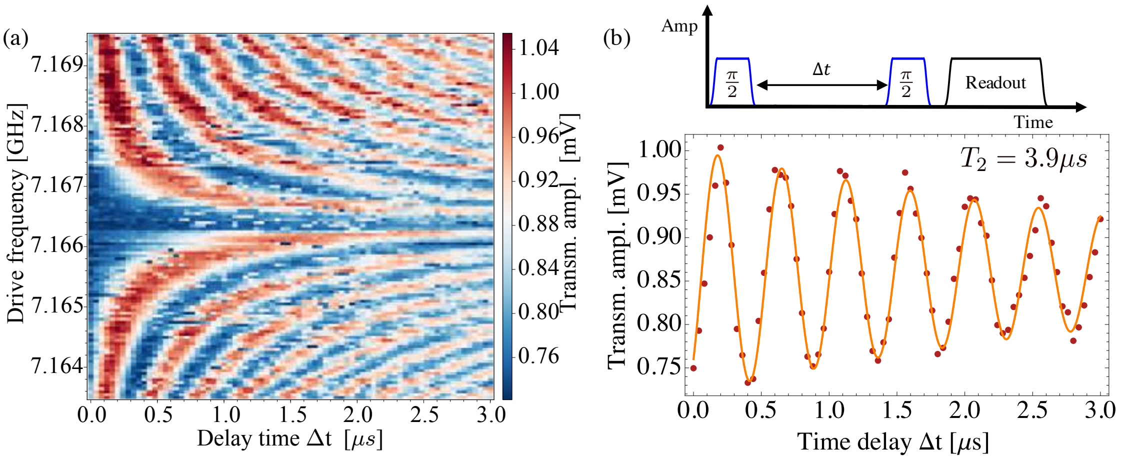

Figure 6.11: (a) Ramsey experiment for varying qubit drive frequencies, i.e. varying the detuning around the qubit transition frequency. The drive frequency at which the Ramsey oscillations disappear corresponds to the exact qubit transition frequency $\omega_{01}/2\pi = 7.1663\,\mathrm{GHz}$. (b) Schematic of the pulse sequence for the Ramsey experiment and a Ramsey interference fringes trace from the line cut in (a) at drive frequency $\omega_d/2\pi = 7.16425\,\mathrm{GHz}$, showing the characteristic dephasing time $T_2 = 3.9\,\mu\mathrm{s}$.

6.5 Conclusions

We have demonstrated successful fabrication of several superconducting transmon qubits and have fully characterised their coherence in a 3D circuit QED setup. Our first transmon shows a long lifetime of $T_1 = 25\,\mu\mathrm{s}$, which is not as long as but comparable with that of typical transmons from recently published high-profile 3D circuit QED experiments. For instance, the single-junction 3D transmon in [71] has $T_1 = 27\,\mu\mathrm{s}$ with a $T_2 = 5\,\mu\mathrm{s}$, and the two transmons in [196] have $T_1 = 60\,\mu\mathrm{s}, 18\,\mu\mathrm{s}$ with $T_2 = 9\,\mu\mathrm{s}, 10\,\mu\mathrm{s}$ respectively. Record coherence times however are still an order of magnitude higher compared to our fabricated qubits in Oxford, e.g. in [163] with $T_1 = 70\,\mu\mathrm{s}$, $T_2 = 95\,\mu\mathrm{s}$, or in [150] with $T_1 = 84\,\mu\mathrm{s}$, $T_2 = 72\,\mu\mathrm{s}$. Nonetheless, our measured phase coherence $T_2 = 3.9\,\mu\mathrm{s}$ is long compared to our fast gate times $t_{gate} < 100\,\mathrm{ns}$, enabling complex gate sequences for future experiments. At the current stage, we postulate our decay time T_1 to be primarily limited by the lack of proper cleaning steps during the junction fabrication (e.g. lack of in-situ Ar ion milling, see Chapter 4, and attribute the short T_2 coherence time to the bad thermalization of the qubit and cavity and the lack of Eccosorb filters on the input lines of the cavity at the 10 mK stage.

Device	$\omega_r/2\pi$ GHz	$\omega_{01}/2\pi$ GHz	Δ GHz	$\chi_0/2\pi$ MHz	g MHz	E_J GHz	$\alpha/2\pi\,(-E_C)$ MHz	E_J/E_C
Transmon-1st	10.6323	4.965	5.661	6.3	189	9.94	394	32
Transmon-J	10.4836	6.8460	3.623	15.1	327	24.6	256	96
Transmon-X	10.9782	4.9692	6.006	14.3	164.5	14.1	243	58
Coaxmon	9.3837	5.5465	3.837	14.3	234	29.5	123	227

Table 6.1: Results for the characterisation of the qubits measured for this thesis, with the cavity ground state resonance $\omega_r \equiv \omega_0$, the qubit transition frequency ω_{01}, the detuning Δ_0, dispersive shift χ_0, the coupling strength g_{01}, the anharmonicity and charging energy $\alpha = -E_C$, Josephson energy E_J, and the E_J/E_C ratio placing the qubit in the transmon regime. Transmon-1st is the first transmon measured. Transmon-J is the transmon used to present characterisation in this chapter, where it had a frequency $\omega_{01}/2\pi = 7.1663\,\text{GHz}$. In a second cooldown it aged to $\omega_{01}/2\pi = 6.8460\,\text{GHz}$ (thereby also changing ω_r), and we use it to measure the decay of higher energy levels in Chapter 7. Transmon-X is the qubit used at MIT, see Chapter 7. Coaxmon is the coaxial transmon measured with a coaxLC resonator architecture, see Chapter 8.

Chapter 7

Coherence and decay of higher energy levels of a superconducting transmon qubit

In this chapter we present measurements of coherence and successive decay dynamics of higher energy levels of a superconducting transmon qubit. By applying consecutive π-pulses for each sequential transition frequency, we excite the qubit from the ground state up to its fourth excited level and characterise the decay and coherence of each state. We find the decay to proceed mainly sequentially, with relaxation times in excess of $20\,\mu$s for all transitions. We also provide a direct measurement of the charge dispersion of these levels by analysing beating patterns in Ramsey fringes. The results demonstrate the feasibility of using higher levels in transmon qubits for encoding quantum information.

7.1 Introduction

The experiment in this chapter was performed with Simon Gustavsson under the supervision of William D. Oliver in the Superconducting Circuits and Quantum Computation Group at the Massachusetts Institute of Technology as part of a research visit in the context of this D.Phil work. The results presented in this chapter closely follow the original publication [150]. The work was performed in collaboration with Samuel Bader who developed and performed the numerical simulation of the transmon [7], presented in Section 7.8.

Universal quantum information processing is typically formulated with two-level systems, or qubits [141]. However, extending the dimension of the Hilbert space to a d-level system, or "qudit," can provide significant computational advantage. In particular, qudits have been shown to reduce resource requirements [135, 29], improve the efficiency of certain quantum cryptanalytic protocols [12, 35, 62, 28], simplify the implementation of quantum gates [108, 40], and have been used for simulating multi-dimensional quantum-mechanical systems [96]. The superconducting transmon qubit [103] is a quantum anharmonic LC-oscillator with the inductor replaced by a Josephson junction. The non-linearity of the Josephson inductance renders the oscillator weakly anharmonic, which allows selective addressing of the individual energy transitions and thus makes the device well-suited for investigating multi-level quantum systems. The weakness of its anharmonicity renders more energy levels accessible over a specified frequency range than those of highly anharmonic charge or flux qubits. The transmon's energy potential is shallower than the parabolic potential of an harmonic oscillator, leading to energy levels that become more closely-spaced as energy increases, see Fig. 7.6a. Although leakage to these levels can be a complication when operating the device as a two-level system [36], the existence of higher levels has proven useful for implementing certain quantum gates [55, 2]. Full quantum state tomography of a transmon operated as a three-level qutrit has also been demonstrated [19].

In this experiment, we investigate the energy decay and the phase coherence of the first five energy levels of a transmon qubit embedded in a three-dimensional cavity [148]. We find the energy decay of the excited states to be predominantly sequential, with non-sequential decay rates suppressed by two orders of magnitude. The suppression is a direct consequence of the parity of the wave functions, in analogy with the orbital selection rules governing transitions in natural atoms. We find that the sequential decay rates scale as i, where $i = 1, ..., 4$ is the initial excited state, thus confirming the radiation scaling expected for harmonic oscillators [118, 194]. The decay times remain in excess of $20\,\mu$s for all states up to $i = 4$, making them promising resources for quantum information processing applications. In addition, we characterise the quantum phase coherence of the higher levels by performing Ramsey-type interference experiments on each of the allowed transitions, and find strong beating in the resulting interference pattern, due to quasiparticle tunnelling. This experimental result provides a direct measurement of the charge dispersion of the different levels [33, 84, 166, 169, 176, 193].

7.2 Experimental setup at MIT

The superconducting transmon qubit for this experiment, which we label Transmon-MIT, consists of a single nano-fabricated Josephson junction (Al/AlO$_x$/Al) contacted between two large electrodes of sizes $600\,\mu$m x $250\,\mu$m that the form the capacitor. This circuit is fabricated on a 5 mm x 5 mm sapphire chip, which is embedded in an aluminium 3D cavity with a bare fundamental mode $f_c = 10.97537\,$GHz, thermally anchored at a base temperature of 15 mK inside a dilution refrigerator. Two SMA coupled ports allow microwave signals in and out of the cavity at a rate of $\kappa/2\pi \approx 100\,$kHz.

In our experiments, all microwave pulse sequences to control the qubit up to state $|4\rangle$ are generated via single-sideband mixing (upconversion by an I/Q mixer) from a

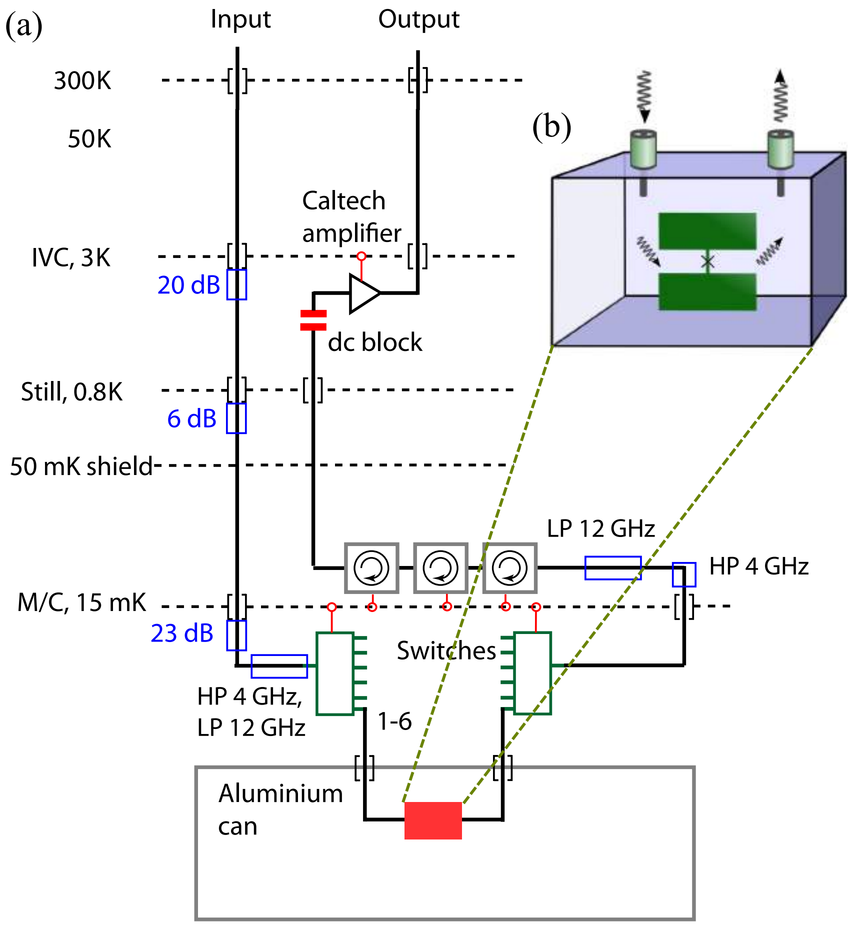

Figure 7.1: (a) Schematic of the measurement setup at MIT, showing the microwave circuitry and temperature stages of the dilution refrigerator. (b) Schematic of the transmon qubit (not to scale) embedded in the three-dimensional cavity.

12GS/s Tektronix AWG 7122 and a carrier signal of frequency 3.5 GHz from a *single* Agilent 8267D PSG vector signal generator. The AWG's analog bandwidth of 3.2 GHz is sufficiently large, and the anharmonicity of the transmon sufficiently weak, to allow the upconversion of microwave pulses into a range of frequencies large enough to access all transition frequencies from f_{01} to f_{34} without the need for numerous signal generators. From the measured transition frequencies listed in Tab. 7.1, the anharmonicities $\alpha_{ij} = f_{01} - f_{ij}$ are found to be $\alpha_{12} = 274.8\,\text{MHz}$, $\alpha_{23} = 583.7\,\text{MHz}$, and $\alpha_{34} = 941.2\,\text{MHz}$ respectively, well within the AWG's bandwidth. The single-sideband mixing requires careful calibration of the amplitude and phase imbalances of the IQ-mixer in order to achieve full cancelation of the undesired sideband. Calibration for simultaneous sideband cancelation of all four upconverted qubit transition pulses f_{01}, f_{12}, f_{23}, f_{34} is shown in Fig. 7.2.

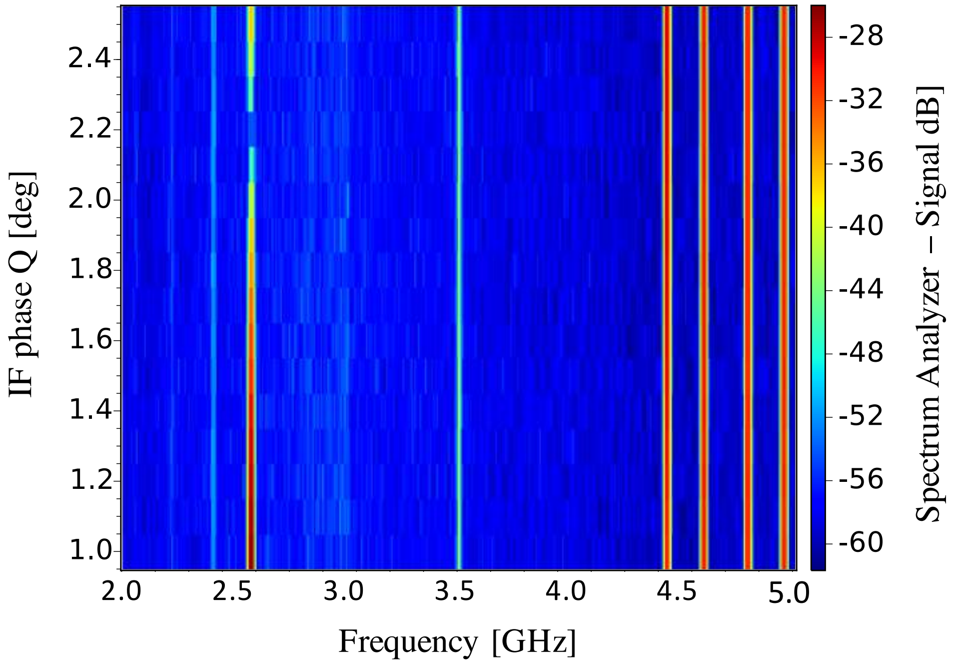

Figure 7.2: Calibration for simultaneous sideband cancelation of all four upconverted qubit transition pulses f_{01}, f_{12}, f_{23}, f_{34}. The amplitude and phase imbalances of the IQ-mixer are calibrated for each of the four IF signals mixed with the single LO pump tone.

All drive pulses have flat-top sections of variable duration and Gaussian-shaped rise and fall envelopes with fixed duration of 20 ns, chosen to prevent undesired leakage to neighbouring levels. The delay between pulses in a drive sequence is constant and set to 70 ns, which is much shorter than any of the sequential decay times.

Furthermore, in this chapter, all frequencies are given in actual frequency f instead of angular frequency ω as in the previous chapters.

7.3 Device characterisation

The Transmon-MIT is characterised by comparing the measured dispersive shifts of the resonator with the numerical simulation (see Section 7.8), we determined the Josephson energy $E_J = 14.07\,\text{GHz}$ and charging energy $E_C = 243\,\text{MHz}$ with a ratio $E_J/E_C = 58$, placing it in the charge-insensitive transmon regime, leading again to a dispersive Hamiltonian of the atom-cavity system with coupling strengths g_i of the cavity photon field to each qubit transition $|i\rangle \to |i{+}1\rangle$, with levels $i = 0, 1, 2, 3, 4$. We use the same standard state-dependent dispersive shift readout scheme as presented in the previous chapter. From the resonator and qubit spectroscopic measurements shown in Fig. 7.3, the Transmon-MIT reveals a non-tunable first transition frequency $f_{01} = 4.9692\,\text{GHz}$, a detuning from the cavity $\Delta = |f_c - f_{01}| = 6.00617\,\text{GHz}$, and a coupling strength $g_0/2\pi = 164.5\,\text{MHz}$. The measured relaxation times and dephasing times are listed in Tab. 7.1. During a different cooldown, the following additional values for the lowest transition of our transmon were measured: $T_2^* = 90 - 115\,\mu\text{s}$, and with spin echo $T_{2E} = 154\,\mu\text{s}$.

7.4 Rabi oscillations and decay for the first two qubit transitions

As presented in Section 2.5.5 and Section 6.1, the interactions between the qubit in state $|i\rangle$ and the cavity causes a dispersive shift χ_i of the cavity resonance to a new frequency $f_i = f_c + \chi_i$, see Fig. 7.9, which is exploited for the readout of the qubit state [191]. We probe the state by sending coherent readout microwaves of frequency $f_{\mu\text{w}}$ through the resonator at a chosen detuning $\Delta_{\mu\text{w}} = f_{\mu\text{w}} - f_c$ from the bare cavity resonance, and measure the averaged transmission coefficient S_{21} of the signal over many experiments. We define $f_{\mu\text{w}}$ as the "RF" signal, specifically referring

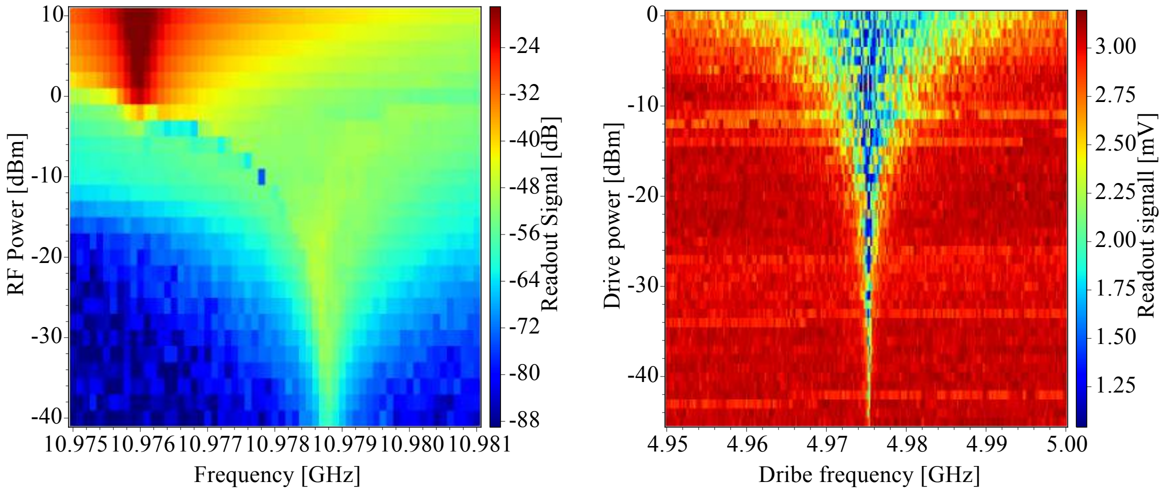

Figure 7.3: (a) Resonator spectroscopy for varying RF power, revealing the bare cavity resonance and the dispersive low-power regime. (b) Qubit spectroscopy performed for increasing drive power, showing the power broadening of the qubit linewidth. At low powers, the qubit linewidth is very narrow, revealing its long coherence times.

to the readout tone, and use this label throughout the chapter. Through a heterodyne detection scheme, the voltage amplitude of the transmission signal at $f_{\mu\mathrm{w}}$ is recorded, from which the qubit state population p_i is then directly extracted. The resonator transmission takes the form of a Lorentzian peak Eq. 6.1 that is centred around the qubit state-dependent resonator frequency f_i for $i = 0, 1, 2, 3, 4, \ldots$

Exciting the transmon to a higher level first requires us to measure and analyse Rabi oscillations between adjacent pairs of energy levels, working sequentially up the ladder of states, as depicted in Fig. 7.6a. Combined with qubit spectroscopy at each step, this protocol allows us to obtain the successive transition frequencies up to $f_{i-1,i}$ and to accurately calibrate the corresponding π-pulses. Starting with the qubit in the ground state $|0\rangle$, we apply a microwave pulse at f_{01} which drives the population between states $|0\rangle \leftrightarrow |1\rangle$, see Fig. 7.4a. As the qubit undergoes Rabi oscillations, the resonator transmission peak continuously rises and falls, oscillating between the discrete shifted resonance frequencies f_0 and f_1. Fitting the Rabi oscillations on state

$|1\rangle$ permits us to experimentally extract the π-pulse duration $\pi_{01} = 40\,\mathrm{ns}$ from the white dashed line in Fig. 7.4a, required to achieve a complete population transfer at transition frequency f_{01}. In the second step, we add a second Rabi drive tone at f_{12} promptly after the π_{01}-pulse (with a delay of $70\,\mathrm{ns}$, much shorter than the decay time Γ_{10}^{-1} from state 1 to 0), so as to perform Rabi oscillations between states $|1\rangle \leftrightarrow |2\rangle$, as shown in Fig. 7.4b, enabling the calibration of the second π-pulse of duration $\pi_{12} = 29\,\mathrm{ns}$ to reach $|2\rangle$. This process is repeated by adding a drive tone at each subsequent transition in order to calibrate the π-pulses up to the desired state. These procedures also allow us to experimentally extract the dispersive shifts χ_i. A full numerical simulation of our coupled qubit-cavity Hamiltonian, see Section 7.8, predicts all the qubit transition frequencies $f_{i-1,i}$ and the dispersive shifts χ_i, and they are in very good agreement with the experimentally obtained values, displayed in Tab. 7.1 and Tab. 7.2.

Proceeding with an initially prepared state $|2\rangle$, we observe its time-resolved population decay in Fig. 7.5a. The resulting stepwise transfer of the resonator peak from $f_2 \to f_1 \to f_0$ is a signature of the transmon's sequential decay, as observed by comparing it to the density plot in Fig. 7.5b of a multi-level sequential decay model starting from level $|2\rangle$. The sequential decay is a consequence of the symmetry of its wave functions. This feature is investigated in more detail later Section 7.6.2. The Fig. 7.5c displays three overlayed resonator traces from Fig. 7.5a for delay times $t_R = 3\,\mu\mathrm{s}$ (blue), $49\,\mu\mathrm{s}$ (orange), and $191\,\mu\mathrm{s}$ (red). The Lorentizans clearly show the remaining qubit populations in the different qubit levels over time as the resonator peak transfers back down to the ground frequency f_0 after complete energy relaxation of the qubit.

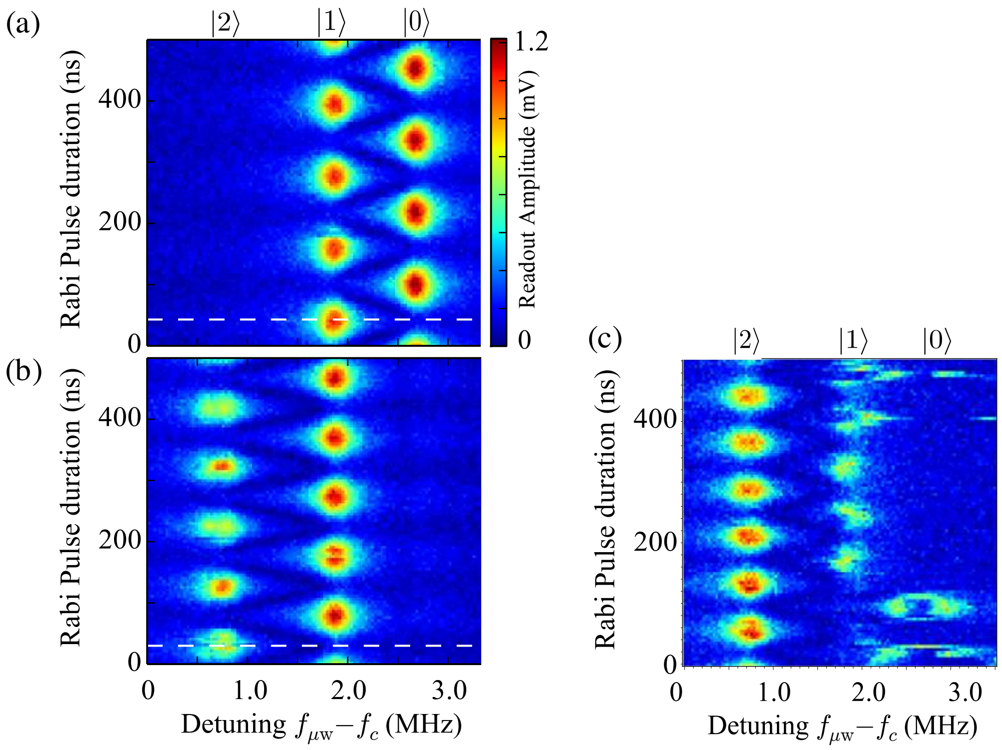

Figure 7.4: (a) Rabi oscillations between state $|0\rangle$ and $|1\rangle$ under a Rabi drive tone of varying duration at f_{01}. The white dashed line indicates the position of the first π-pulse at $\pi_{01} = 40\,\text{ns}$. (b) Rabi oscillations between $|1\rangle$ and $|2\rangle$ with $\pi_{12} = 29\,\text{ns}$, obtained by adding a Rabi drive tone at f_{12} after initialising state $|1\rangle$ by applying π_{01}-pulse. (c) Rabi oscillations between $|2\rangle$ and $|3\rangle$ obtained by adding a Rabi drive tone at f_{23} after initialising state $|2\rangle$ by applying a π_{01}-pulse followed by a π_{12}. The Resonator does not shift deterministically conditioned on the qubit state anymore, but jumps randomly between the different positions due to mixing with higher states of the transmon.

7.5 Depopulation sequence and Rabi oscillations for higher levels

When driving Rabi oscillations on the transition $|i\rangle \leftrightarrow |i+1\rangle$ for $i \geq 2$, the readout by the method presented above is not possible in this device, because state $|3\rangle$ does not appear as a conditional shift to the resonator. This is a consequence of the fact that certain states escape the dispersive regime due to their mixing with higher-excited states that have transition frequencies close to the resonator frequency, see simulation in Section 7.8. As a result, we use a modified readout protocol, which does not require

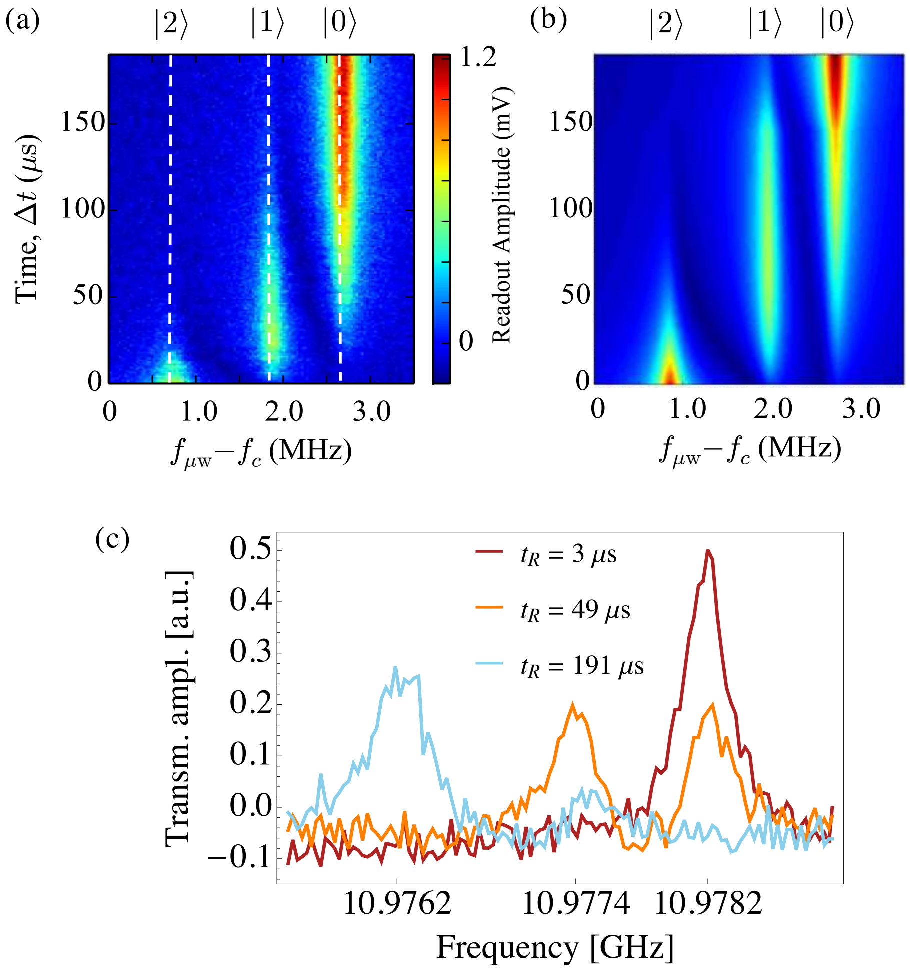

Figure 7.5: (a) Qubit population decay from level $|2\rangle$ to $|1\rangle$ to $|0\rangle$, obtained by varying the time delay Δt before readout. The frequency sweep of the readout pulse detuning reveals the temporal transition of the resonator frequency from f_2 to f_1 to f_0. (b) Density plot of a multi-level decay model starting from level $|2\rangle$, in good agreement with the experimentally observed decay. (c) Three overlayed resonator traces from (a) for delay times $t_R = 3\,\mu$s (blue), 49 μs (orange), and 191 μs (red). They show the remaining qubit populations in the different qubit levels

.

measurement pulses at the shifted resonance f_3 or f_4. After preparing the state $|i\rangle$ via the upward sequence of π-pulses $S_i^{\uparrow} = (\pi_{01}, \pi_{12}, \ldots, \pi_{i-1,i})$, we additionally apply a depopulation sequence $S_i^{\downarrow} = (\pi_{i,i-1}, \ldots, \pi_{21}, \pi_{10})$ to the qubit immediately before the readout. This maps the population p_i of state $|i\rangle$ onto that of the ground state $|0\rangle$, allowing us to measure p_i by simply probing the resonator at frequency f_0.

By incorporating the depopulation sequence we are able to drive Rabi oscillations of the transmon up to state $|4\rangle$, as shown in Fig. 7.6(c). The Rabi frequencies Ω_{ij}, extracted via a best-fit curve, are proportional to the matrix elements $\langle i|\hat{n}|j\rangle$ between the states i and j, where $\hat{n}$ denotes the number of Cooper pairs transferred between the two junction electrodes forming the capacitor (see Section 7.8). Consequently, Ω_{ij} increase as $\langle i|\hat{n}|j\rangle \propto \sqrt{j}$, as expected from the coupling between the transmon states and the resonator [103].

Having thus obtained all the transition frequencies and π-pulse calibrations, the qubit can be initialised in any state up to $|4\rangle$ with the sequence $S_4^{\uparrow}$, and we proceed to investigate the decay and phase coherence of these higher levels.

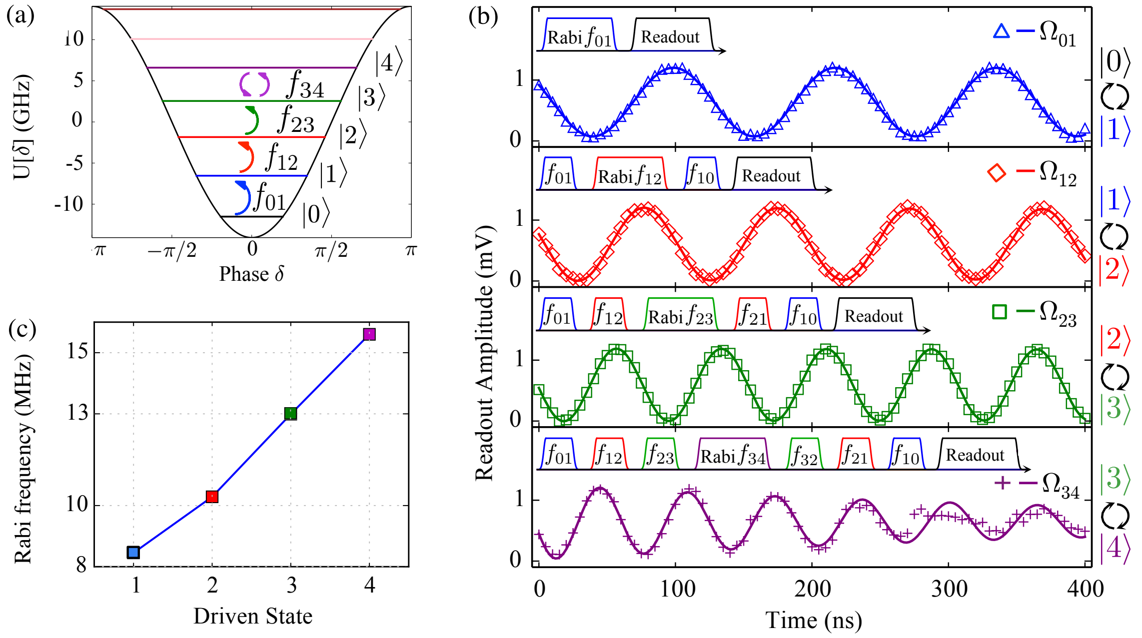

Figure 7.6: (a) Simulated energy spectrum of the transmon with parameters $E_J/E_C = 58$, where $U[\delta]$ is the Josephson potential. (b) Rabi oscillations on each successive qubit transition up to state $|4\rangle$ using the depopulation readout method. The corresponding excitation pulse sequence and respective depopulation sequence are shown for each Rabi drive. The solid lines are best-fit curves allowing the extraction of the Rabi frequencies. (c) Plot of extracted Rabi frequencies Ω_{ij} as $\Omega_{01} = 8.45\,\text{MHz}$, $\Omega_{12} = 10.3\,\text{MHz}$, $\Omega_{23} = 13.0\,\text{MHz}$, and $\Omega_{34} = 15.6\,\text{MHz}$, respectively.

7.6 Decay of higher energy levels

We start by measuring the dynamics of the state population decay by introducing a varying time delay before the readout process. The calibrated and normalised population evolutions starting from states $|1\rangle$, $|2\rangle$, and $|3\rangle$ are plotted in Fig. 7.7(a)-(c). The decay from state $|4\rangle$ has also been measured and is presented in Fig. 7.8.

7.6.1 Extraction of the state populations

In the following, we describe how the measured data of the population decays in Fig. 7.5a and Fig. 7.8 must be corrected to obtain the actual normalized populations. The data from each decay trace is the measured voltage $V_i(t)$ detected by the data acquisition card for a readout pulse at f_0. However, the data for each trace must be corrected for the overlap of the Lorentzian tails from the other populations present in frequency space at the point f_0, as seen in Fig. 7.5c and Fig. 7.9, as well as for the decay during the readout. We represent the evolution of the measured populations as $\vec{V}(t) = [V_0(t), V_1(t), V_2(t), V_3(t), V_4(t)]^\mathsf{T}$ and define here the value at f_k of an individual cavity response Lorentzian centred at f_i as

$$L_{ik} = L_i(f_k) = \frac{1}{[1 + 2\,\mathrm{i}\,Q_t(f_k - f_i)/f_i]}, \tag{7.1}$$

with Q_t the total quality factor. In our first decay experiment, the total population p is distributed over several states $|i\rangle$, and as presented in the transmission spectrum becomes $L_k(f_k) = \sum_i L_i(f_k)$. Fitting this $L_k(f_k)$ for $k = 0, 1, 2$ to the resonator decay trace from the initialized state $|2\rangle$ at delay time $t_R = 8\,\mu$s shown in Fig. 7.9 demonstrates how the Lorentzian tail overlaps need to be taken into account, and also that they must be fitted in the complex plane to take into account the phase information in order to properly fit the Lorentzians.

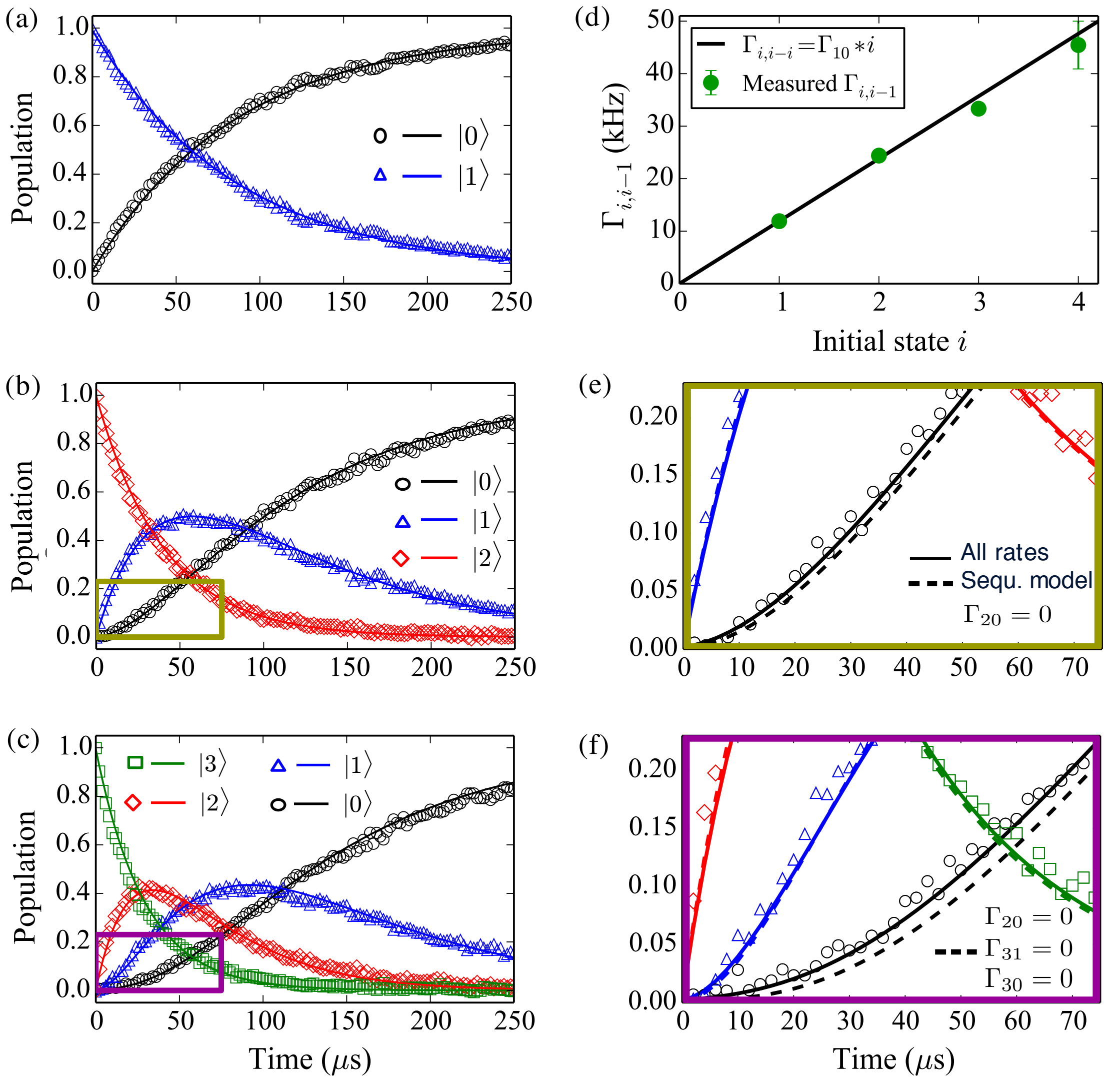

Figure 7.7: (a)-(c) Population decay traces of the qubit states up to $|3\rangle$, obtained by varying the time delay Δt before the depopulation sequence. The solid lines are state occupations from the multi-level decay model taking into account all decay channels. (d) The sequential decay rates $\Gamma_{i,i-1}$ (green dots) for increasing energy state i, showing the roughly linear dependance (solid line). (e)(f) Zoom of decay curves in panel (b) and (c) respectively, showing the model with all transition rates allowed (solid line) compared to the model with only neighbouring transitions allowed (dashed line). The extracted decay times are listed in Tab. 7.1.

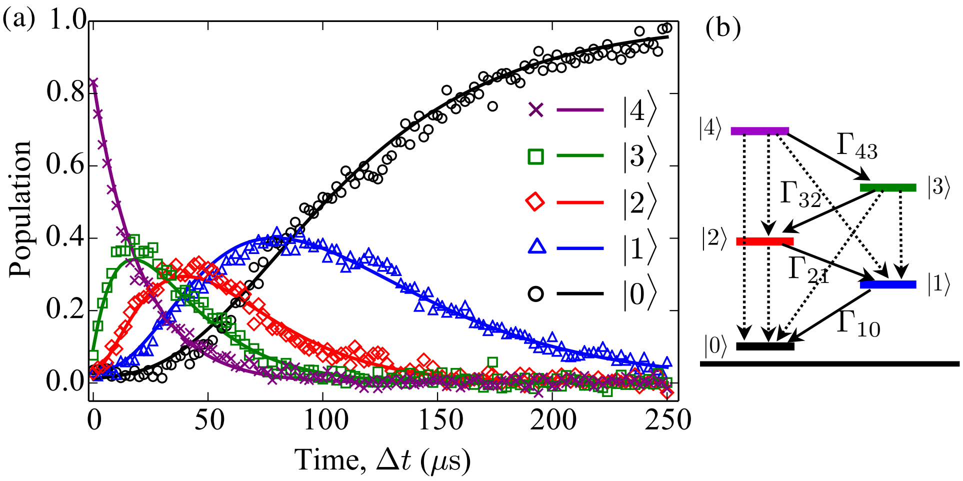

Figure 7.8: (a) Measured decays of the qubit populations up to energy state $|4\rangle$. The data represents the populations after correction for overlapping Lorentzians and relaxation during readout. The solid lines are numerical solutions to the sequential decay model. (b) Energy level scheme showing the sequential decay rates via the solid arrows.

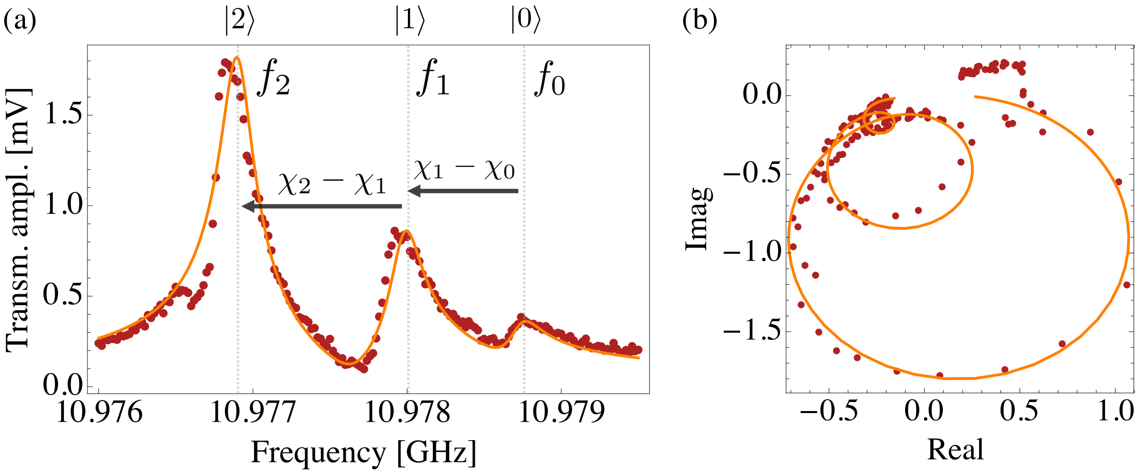

Figure 7.9: (a) Transmission spectrum of the measured trace (red dots) at readout delay $t_R = 8\,\mu$s from the population decay plot in Fig. 7.5a of an initially prepared state $|2\rangle$. The acquired signal is the averaged readout amplitude of the cavity response and is proportional to the transmission coefficient S_{21}. The best-fit (orange) is a sum of overlapping Lorentzian peaks centered at frequencies f_2,f_1, and f_0, corresponding to the qubit being in state $|2\rangle$, $|1\rangle$, and $|0\rangle$ respectively, and expressing the dispersive shifts χ_0, χ_1 and χ_2. (b) Transmission signal fitted in the complex plane in order to consider the phase in addition to the amplitude.

The corrected state populations $p_i^*(t) \in \vec{p}^*(t)$ are obtained by $\vec{p}^*(t) = L^{-1} \cdot \vec{V}(t)$, with the inversion matrix L given by

$$L = \begin{pmatrix} L_{00} & L_{10} & L_{20} & L_{30} & L_{40} \\ L_{10} & L_{00} & L_{20} & L_{30} & L_{40} \\ L_{10} & L_{20} & L_{00} & L_{30} & L_{40} \\ L_{10} & L_{20} & L_{30} & L_{00} & L_{40} \\ L_{10} & L_{20} & L_{30} & L_{40} & L_{00} \end{pmatrix}. \tag{7.2}$$

The matrix elements are obtained by fitting the Lorentzian transmission profile in the complex plane to the measured voltages, as shown in Fig. 7.9(b) for a sample trace at delay time $t_R = 8\,\mu$s.

The data $\vec{p}^*(t)$ must then be corrected for the relaxation of the qubit during the readout time of $T_{read} = 8\,\mu$s. The card averages the signal over the time of acquisition T_{read}, during which the population from the Lorentzian $p_0^*(t)$, mapped to centre f_1 after the depopulation sequence (corresponding to qubit in $|1\rangle$), relaxes by a factor

$$\bar{\Lambda} = \frac{1}{T_{read}} \int_{T_{read}} \mathrm{e}^{-\Gamma_{10} t}\, \mathrm{d}t, \tag{7.3}$$

where the rate Γ_{10} is extracted from the decay model fit. The final true populations are therefore obtained by

$$\begin{cases} p_i = p_i^* - p_0^*(1 - \bar{\Lambda}/T_{read}) & \text{for each } i = 1, 2, 3, 4 \\ p_0 = p_0^* - p_1^*(1 - \bar{\Lambda}/T_{read}) \end{cases} \tag{7.4}$$

and are plotted in Fig. 7.8 after being normalised.

When performing readout with the depopulation method, these cumbersome steps for extracting the populations can be replaced by the simpler method of directly measuring calibration values for the population of each state. This is done by pumping the population to state $|i\rangle$ and measuring the readout voltage response at f_0. Then the inversion matrix L_{cal} contains simply the calibration voltage values measured as

$$L_{cal} = \begin{pmatrix} 2.3 & 0 & 0 & 0 \\ 0.4 & 2.3 & 0 & 0 \\ 0.4 & 0.25 & 2.3 & 0 \\ 0.4 & 0.25 & 0.2 & 2.3 \end{pmatrix}. \tag{7.5}$$

The calibrated populations $p_i(t) \in \vec{p}(t)$ are thus given by

$$\vec{p}(t) = L_{cal}^{-1} \cdot \vec{V}(t). \tag{7.6}$$

This method also intrinsically calibrates for the decay during readout and is the method used to acquire the normalised population decay traces in Fig. 7.7.

7.6.2 Multi-level decay model

We model the data with a multi-level rate equation describing the evolution of the state population vector $\vec{p}$, with Γ_{ij} representing the decay rate from state i to j:

$$\frac{\mathrm{d}\vec{p}(t)}{\mathrm{d}t} = \Gamma^{\mathsf{T}} \cdot \vec{p}(t)^{\mathsf{T}} \tag{7.7}$$

$$(\Gamma)_{jj} = -\sum_{k=0}^{j-1} \Gamma_{jk}. \tag{7.8}$$

The coefficients $(\Gamma)_{jj}$ are the diagonal elements of the decay rates matrix Γ, and the Γ_{ij} for $i \neq j$ are the off-diagonal elements. The upward rates are considered to be negligible by setting $\Gamma_{ij} = 0$ for all $i < j$, as $k_B T \ll h f_{ij}$ for all i, j. Indeed, the quiescent state-$|1\rangle$ population of our transmon is measured to be less than 0.1% [92]. The state occupations of the model are plotted (solid lines) and compared to the experimental data in Fig. 7.7 for each state, whereby the rates Γ_{ij} are used as fitting parameters to extract all the system's relaxation rates. The fitting was performed iteratively, starting with the decay from $|1\rangle$, where we fit Γ_{10} and then fix it for the next decay from $|2\rangle$, where Γ_{21} and Γ_{20} are determined, and so forth.

The most prominent feature of the data is that the decay proceeds mainly sequentially, with the non-sequential decay rates suppressed by two orders of magnitude. The extracted decay times are in excess of $20\,\mu$s for all states up to $|4\rangle$, and are listed in Tab. 7.1. For the sequential rates, we find that the rates scale linearly with state i, as plotted in Fig. 7.7(d); this behaviour is consistent with decay processes

Frequency	f^*_{01}	f^*_{12}	f_{23}	f_{34}
Exp. f (GHz)	4.9692	4.6944	4.3855	4.0280
Sim. f (GHz)	4.9692*	4.6944*	4.3874	4.0475
Sequ. decay^{-1}	Γ_{10}	Γ_{21}	Γ_{32}	Γ_{43}
time (μs)	84 ± 0.24	41 ± 0.21	30 ± 0.21	22 ± 2
Non-sequ.$^{-1}$	Γ_{20}	Γ_{31}	Γ_{30}	
time (μs)	1812 ± 223	1314 ± 359	2631 ± 694	
Dephasing T_2	$T_{2\,(01)}$	$T_{2\,(12)}$	$T_{2\,(23)}$	$T_{2\,(34)}$
time (μs) ±20%	72	32	12	<2

Table 7.1: Comparison of experimental and simulated values for the transition frequencies $f_{i,i+1}$, the relaxation times Γ_{ij}^{-1} for the sequential and non-sequential rates, the dephasing times $T_{2\,(ij)}$ for the superpositions of states $|i\rangle$ and $|j\rangle$. The asterisks indicate the values that were fitted to the experiment for use as parameters in the full numerical simulation of the coupled qubit-cavity Hamiltonian.

related to fluctuations of the electric field (like Purcell or dielectric losses), for which we expect the lifetimes to be inversely proportional to $|\langle i|\hat{n}|j\rangle|^2$ (see Section 7.8 for numerical calculations of the matrix elements). Furthermore, theoretical relaxation rates between neighbouring levels due to quasiparticle tunnelling also respect this approximate dependance $\Gamma_{i,i-1} \simeq i\,\Gamma_{10}$ [32, 34]. We note that the anharmonicity of this device is sufficiently weak that its decay rates scale as those of Fock states in a harmonic oscillator [118, 194].

To illustrate the effect of the non-sequential rates, we also fitted the data to a model involving only sequential rates (dashed lines in Fig. 7.7(e)(f)). Although the deviations between the two fits are small, inclusion of the rates Γ_{20}^{-1}, Γ_{30}^{-1} and Γ_{31}^{-1} does provide somewhat better matching for the initial increase in ground state population $|0\rangle$ for $t < 70\,\mu$s where we would expect the largest impact. From numerical simulations of the qubit-resonator Hamiltonian, we expect the rates Γ_{20} and Γ_{31} to be strongly suppressed due to the parity of those states [49], whereas the matrix element

$|\langle 3|\hat{n}|0\rangle|^2$ relevant for Γ_{30} is about 100 times smaller than $|\langle 1|\hat{n}|0\rangle|^2$ (see Section 7.8). Quasiparticles also contribute to relaxation rates for non-neighbouring levels, and theory [33] predicts that they are suppressed by at least three orders of magnitude, a much stronger suppression than we extract. This suggests that the non-sequential decay rates are dominated by some non-quasiparticle process, such as dielectric loss or coupling to other cavity modes.

7.7 Coherence of higher energy levels

We now proceed to investigate the phase coherence of the higher levels by performing a Ramsey-fringe measurement, whereby we obtain the dephasing times T_2. A Ramsey experiment on state $|i\rangle$ consists of first applying π-pulses to bring the transmon to state $|i-1\rangle$, followed by a $\pi/2$-pulse at frequency $f_{i-1,i}$ to bring it into a superposition of states $|i-1\rangle$ and $|i\rangle$, then allowing a variable free-evolution time Δt to pass, and finally applying a second $\pi/2$-pulse before applying the depopulation sequence and performing the readout. The measured Ramsey fringes are shown in Fig. 7.10 for each state up to $|4\rangle$. The frequency of the $\pi/2$-pulses was purposefully detuned to generate oscillating traces.

The measured Ramsey oscillations in Fig. 7.10a directly reveal that the phase coherence for higher states become shorter. The coherence times $T_{2\,(ij)}$ for the superpositions between states $|i\rangle$ and $|j\rangle$, for $i, j = 0, 1, 2, 3, 4 \;\; (i < j$ and $j = i + 1)$, are qualitatively defined as the decay time for the amplitude of the fringes. The states $|2\rangle, |3\rangle$ and $|4\rangle$ show clear modulation in addition to the main oscillations, and leakage to lower levels causes the amplitude oscillations to drift toward zero. The power spectral density of the data, obtained via a discrete Fourier transform and plotted in Fig. 7.10b, reveals two well-defined frequency components for states $|2\rangle$ and $|3\rangle$, and

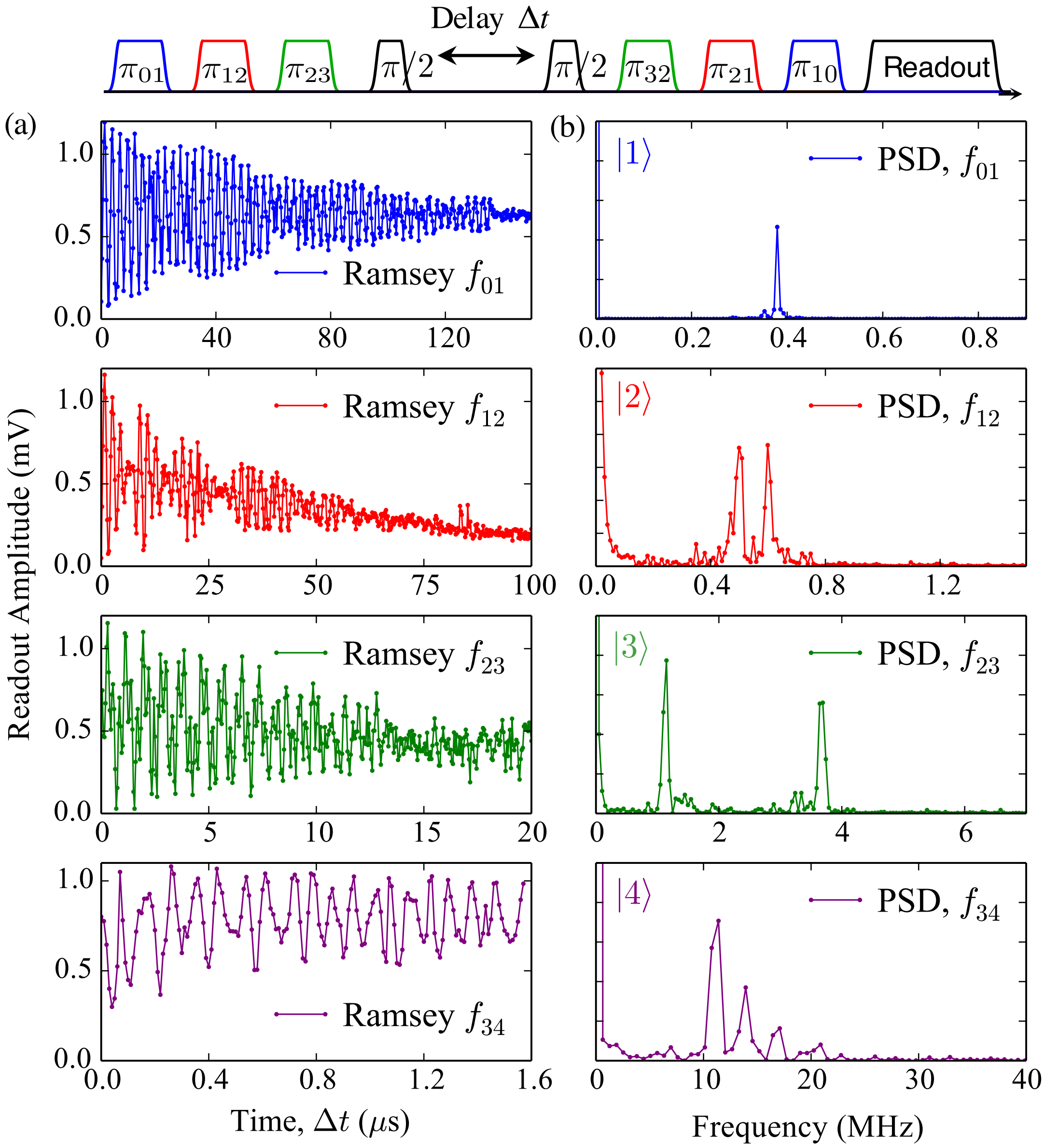

Figure 7.10: (a) Ramsey oscillations experiment on each subsequent energy transition up to state $|4\rangle$. (b) The Power Spectral Density (PSD), obtained from the discrete Fourier transforms of the corresponding Ramsey fringes. The Ramsey pulse sequence (top) corresponds to the fourth-row panel, representing a Ramsey sequence on state $|4\rangle$, with the black $\pi/2$-pulses representing the $\pi_{34}/2$-pulses performed at frequency f_{34} to bring the transmon into the superposition state $(|3\rangle + |4\rangle)/\sqrt{2}$ before allowing the free evolution time Δt.

a number of frequencies for state $|4\rangle$ (making it impossible to obtain a reasonable fit for this last state).

In order to fit the Ramsey fringes for states up to $|3\rangle$, we first subtract a smoothed background to discard the energy decay toward state $|0\rangle$. The voltage amplitude A of the oscillations is then fitted to exponentially damped double sinusoid curves

$$A = e^{-t/T_2}[\cos(2\pi f_A t) + \cos(2\pi(f_A + \Delta f)t)], \tag{7.9}$$

and displayed in Fig. 7.11. The extracted $T_{2\,(ij)}$ values are listed in Tab. 7.1, and are found to be accurate within 20%. The frequencies f_A, $f_A + \Delta f$ represent the two frequency components that fit the beating pattern in each Ramsey fringes plot, and have values $[f_A, \Delta f]_{(ij)} = [379\,\mathrm{kHz}, 0\,\mathrm{Hz}]_{(01)}, [504\,\mathrm{kHz}, 93\,\mathrm{kHz}]_{(12)}$, and $[1.1\,\mathrm{MHz}, 2.5\,\mathrm{MHz}]_{(23)}$. The fit parameter Δf represents the total charge dispersion splittings $\epsilon_{ij}(n_g) \leq \epsilon_{ij}^{(max)}$ for each transition between state i and j, as defined in Section 2.4.2 and reported in Tab. 7.2, with $j = i + 1$ and $\epsilon_{ij} = \epsilon_{ij}(n_g{=}1/2) - \epsilon_{ij}(n_g{=}0)$.

The splitting of the transition frequencies can be understood in terms of quasi-particle tunnelling between the two junction electrodes, see Section 2.4. Despite the large E_J/E_C ratio, the transmon retains some sensitivity to charge fluctuations, and the charge dispersion approximately grows in an exponentially way with increasing level number, see Fig. 2.6 in Section 2.4.2.

From our full numerical transmon-cavity simulation (see next section Section 7.8 for details), we calculate the change in level splitting $\epsilon_{ij}(n_g)$ between levels i, j as a function of the effective offset charge n_g [103], shown in Fig. 7.12. The maximum change in ϵ_{ij} due to quasi-particle tunnelling is given by $\epsilon_{ij}^{(max)} = \epsilon_{ij}(n_g = 1/2) - \epsilon_{ij}(n_g = 0)$, as marked by vertical dashed lines, but note that what we measure experimentally is the dispersion between $n_g + 1/2$ and n_g for an unknown value of n_g.

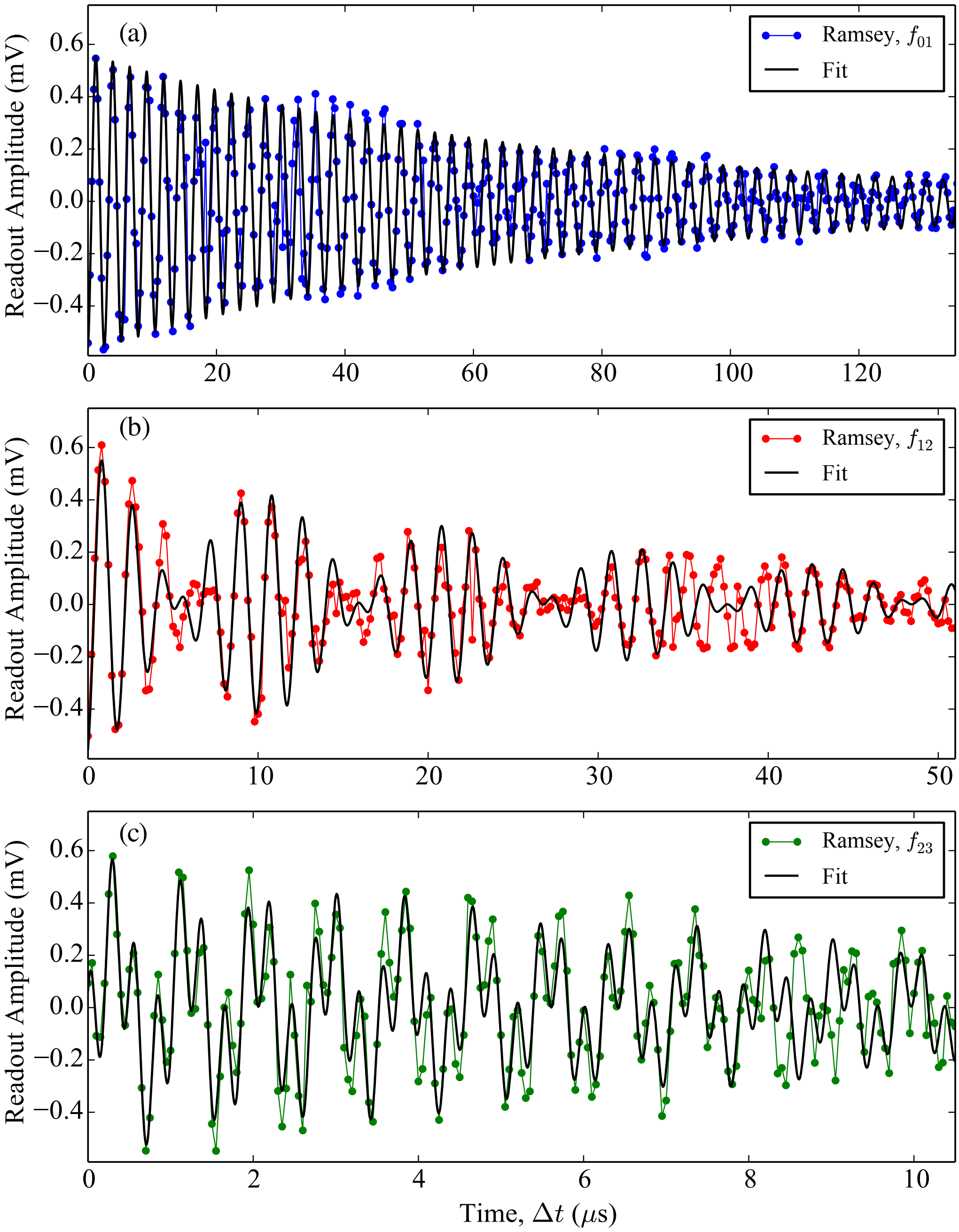

Figure 7.11: (a)(b)(c) Fits of the Ramsey oscillations on each subsequent energy transition up to state $|3\rangle$. The Ramsey traces are plotted after subtracting a smooth background to discard the energy decay towards state $|0\rangle$. The best fits reveal the dephasing times $T_{2\,(i,j)}$ for the superpositions between states $|i\rangle$ and $|j\rangle$, for $i, j = 1, 2, 3$, where each T_2 time is qualitatively defined as the decay time for the amplitude of the fringes. The measured Ramsey fringes on state $|4\rangle$ have a beating pattern containing several frequencies, making it impossible to obtain a reasonable fit.

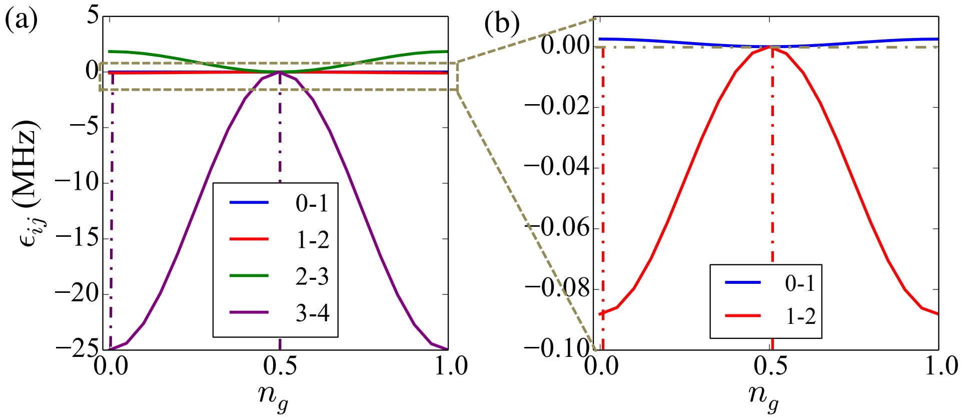

Figure 7.12: (a) Calculated change in transition frequency $\epsilon_{ij}(n_g)$ as a function of the effective offset charge n_g, expressing the charge dispersion of each transition. (b) Zoom of the lowest two transitions 0-1 and 1-2.

The measured splittings are compared to the calculated maximum splittings $\epsilon_{ij}^{(max)}$ in Tab. 7.2. State $|1\rangle$ is unresolved, in agreement with the small splitting of 2.5 kHz predicted, whereas we find that the splittings of states $|2\rangle$ and $|3\rangle$ are well predicted by the simulation. Charge traps between the substrate and the deposited metal film, or the presence of two-level fluctuators in the junction, also lead to charge fluctuations, possibly explaining the additional peaks seen in the spectrum of the state $|4\rangle$, and possibly explaining the worse agreement with the simulated splitting.

For quantum information purposes, the noise causing the beating in the Ramsey fringes can be refocused with an echo sequence by adding a temporally short π-pulse (broad frequency spectrum) to the centre of the Ramsey sequence [77].

Qubit State i	$\|0\rangle$	$\|1\rangle$	$\|2\rangle$	$\|3\rangle$	$\|4\rangle$
Exp. χ_i (MHz)	2.8	2	0.88		
Sim. χ_i (MHz)	2.8*	2	0.85		
Exp. ϵ_{ij} (MHz)		-	0.09	2.53	5-10
Sim. $\epsilon_{ij}^{(max)}$ (MHz)		0.0025	0.091	1.89	26.8

Table 7.2: Comparison of experimental and simulated values for the dispersive shifts χ_i. The measured charge dispersion splittings $\epsilon_{ij}(n_g)$ extracted from Ramsey fringes are compared to the simulated maximum splittings $\epsilon_{ij}^{(max)}$.

7.8 Numerical simulation of the coupled transmon-cavity system

The numerical simulation presented in this section follows the original simulation performed in [7] for [150]. Recall from Section 2.5.2 in Chapter 2, that the coupled transmon-cavity system is described by the effective Hamiltonian

$$\begin{aligned} H &= H_T + H_R + H_D \qquad (7.10)\\ &= 4E_C(\hat{N} - n_g)^2 - E_J \cos\hat{\delta} + \hbar 2\pi f_c(\hat{a}^\dagger\hat{a} + \frac{1}{2}) + 2e\beta V_{\text{rms}}\hat{N}(\hat{a}^\dagger + \hat{a})\,, \qquad (7.11)\end{aligned}$$

where the first term represents the transmon, the second the cavity, and the third one the coupling. Furthermore, recall that the Hamiltonian is rewritten in the basis of the uncoupled states $|i\rangle$ [103], leading to the generalized Hamiltonian which considers higher levels of the transmon

$$H = \hbar\sum_j 2\pi f_j|j\rangle\langle j| + \hbar 2\pi f_c\hat{a}^\dagger\hat{a} + \sum_{i,j} g_{ij}|i\rangle\langle j|(\hat{a}^\dagger + \hat{a})\,, \qquad (7.12)$$

where the sum contains the coupling energies

$$\hbar g_{ij} = 2e\beta V_{\text{rms}}\langle i|\hat{N}|j\rangle = \hbar g_{ij}^*\,. \qquad (7.13)$$

As presented in Section 2.4, the unperturbed Hamiltonian H_T has an analytic solution in terms of Mathieu functions, for which the energy spectrum in the phase basis $|\delta\rangle$ for several higher levels is shown in Fig. 7.6a. The lowest four wavefunctions $\langle i|\delta\rangle$ given by the lowest four transmon eigenstates $|i\rangle$ in the phase basis $|\delta\rangle$ are displayed in Fig. 7.13.

To numerically solve the coupled system, the modelling of the energies proceeds in the charge basis. Since the interaction involves $\hat{N}$, we first numerically diagonalize H_T itself in terms of the $\hat{N}$ basis kets. The relevant Hilbert space of the transmon

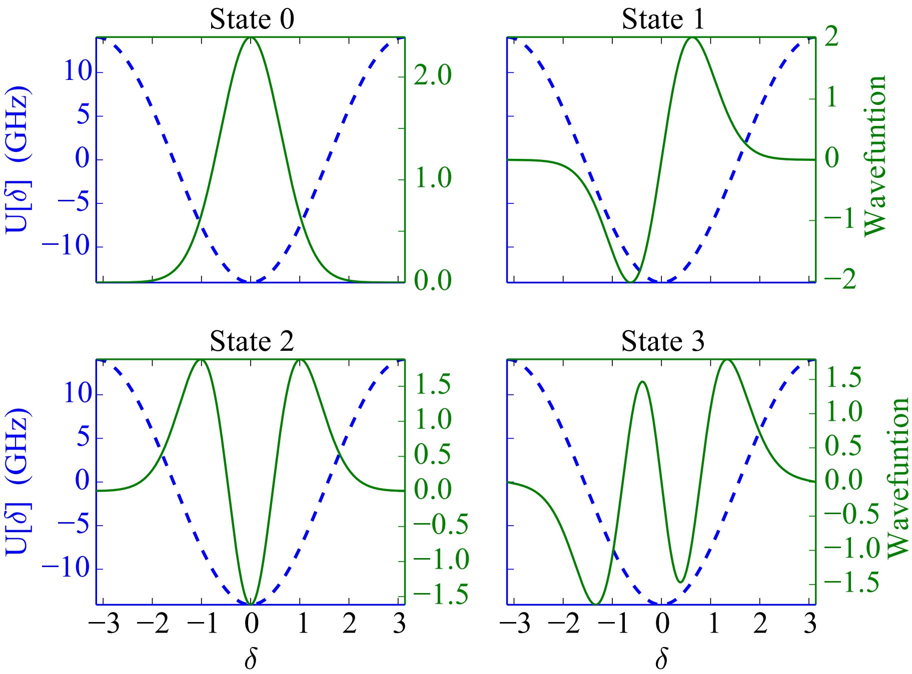

Figure 7.13: The transmon wavefunction amplitudes from simulation in δ-space, overlaid against the Josephson potential $U[\delta]$. Note that, for this figure, the Hamiltonian was solved at $n_g = 0$, which allows for a pure real energy eigenbasis.

can then be well represented for our purposes by only the lowest few eigenstates, i.e. the important lowest energy levels can be properly captured by linear combinations of a small set of charge basis states. The "effective completeness" of our restricted basis is checked in our simulation, by showing that the states $|i\rangle$ we care about have negligible projections $\langle i|N\rangle$ onto all charge basis states $|N\rangle$ beyond $|N| = 10$. For the figures and tables in this work, the highest transmon state discussed is state $|8\rangle$. However, the lowest twenty states $|N| = 10$ were used in simulation, which provides an energy margin of approximately seven times the cavity frequency.

For the resonator Hilbert space, we restrict our attention as well to only the lowest twenty states. Then, representing the coupled Hamiltonian H in Eq. 7.12 on the Kronecker basis of the lowest H_T and H_R eigenstates, we re-diagonalize the entire Hamiltonian and read off the energies.

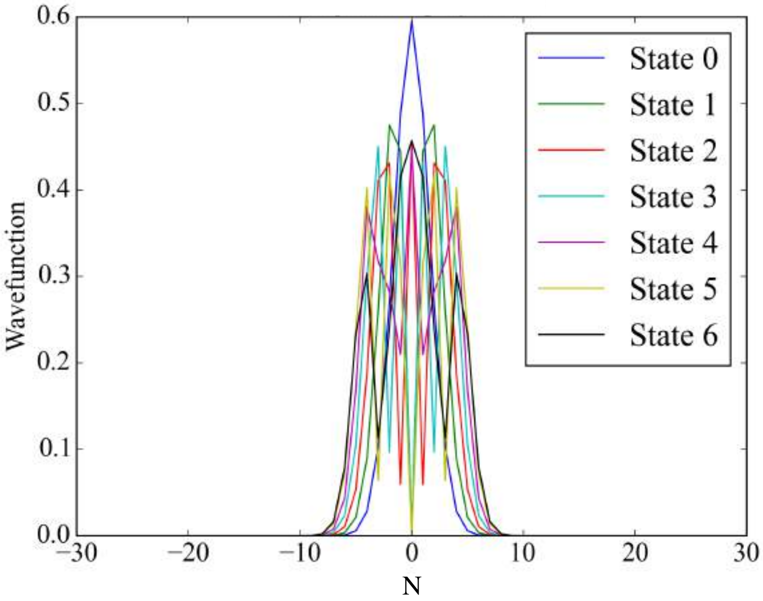

Figure 7.14: Projections $\langle i|N\rangle$ of the relevant qubit states $i = 0, 1, 2, 3, 4, 5, 6$ onto the charge basis states $|N = n\rangle$ to check for completeness of the restricted charge basis.

Of course, this requires knowledge of the various constants in the Hamiltonian: E_J, E_C, and g. To quickly obtain starting guesses for the energy scales from the frequencies, one can use the approximate relations already presented in Section 2.4.2

$$h(f_{01} - f_{12}) \approx E_C\,, \qquad hf_{01} \approx \sqrt{8E_JE_C} - E_C\,, \tag{7.14}$$

which can be derived from perturbation theory [103]. Those constants can be refined by fitting to the first two frequencies in the transmon and the dispersive shift of the first level. Thereafter the model will be able to predict the other frequencies, as well as the other dispersive shifts, displayed in Tab. 7.1 and Tab. 7.2. Once the model is fitted, we can examine the properties of our system.

This simulation provides valuable insight into the aforementioned difficulty of experimentally probing states $|i\rangle$, for $i > 2$. The dispersive readout method assumes that the transmon transitions are in the "dispersive regime," i.e. the detuning of any transmon frequency from the resonator is far greater than the coupling strength, so

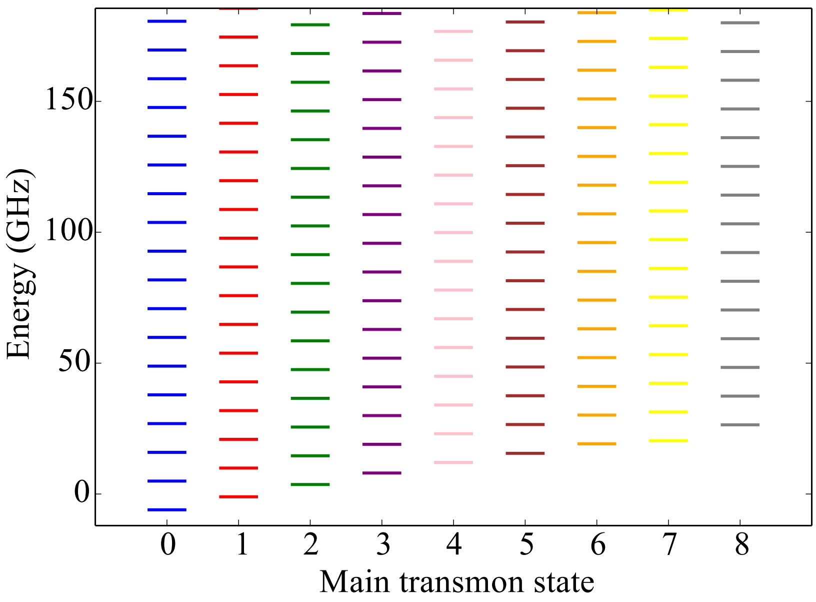

Figure 7.15: Level scheme for the coupled transmon system up to state $|8\rangle$. We can group the eigenstates of the total system by which transmon state each projects onto the most when the resonator is traced out. We see that, corresponding to each transmon eigenstate, there is a ladder of total eigenstates, separated by a regular frequency.

the resonator only provides a small effective frequency shift to the barely intermixed transmon states [22]. The opposite situation, where the resonator frequency is close to a transition frequency, leads to heavy mixing between transmon states, and is known as the "resonant regime" [103].

To examine this distinction in practice, we can cluster our diagonalized total eigenstates into different "ladders" based on which pure transmon state they most project onto, as in Fig. 7.15. That is to say, "Ladder 0" is the set of total energy eigenstates which, when the resonator is traced out, project mostly onto pure transmon state $|0\rangle$.

Explicitly, if ψ_T^k and ψ_R^l represent the transmon and resonator eigenstates respectively, then the projection of a total state Ψ_{TR} onto the pure transmon state k is

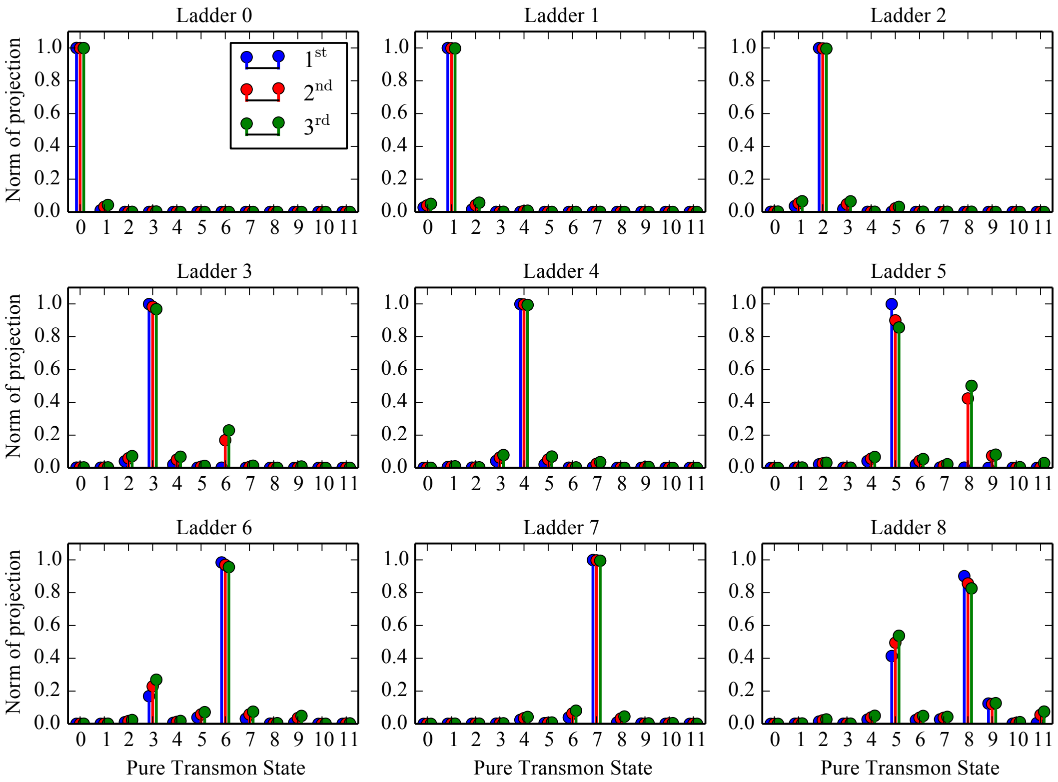

Figure 7.16: Projections of the first, second, and third states of each ladder onto the pure transmon states with the resonator traced out, per (7.15). We see that the first ladder of states are almost *entirely* transmon state $|0\rangle$. For instance, if the system were in the lowest eigenstate of Ladder 0 and the experimenter directly measured the state, the experimenter would almost always find 0. Dissimilarly, states from Ladder 3 have significant projections onto both state $|3\rangle$ and state $|6\rangle$, because the 3-6 transition is resonant with the cavity frequency. The same can be said of 5-8.

given by

$$\mathrm{Proj}(\Psi_{\mathrm{TR}}, k) = \sum_l \langle \psi_T^k | \langle \psi_R^l | \Psi_{\mathrm{TR}} \rangle \tag{7.15}$$

and an eigenstate Ψ_{TR} is in "Ladder i" if $|\mathrm{Proj}(\Psi_{\mathrm{TR}}, k)|$ is maximized by $k = i$. The values of $|\mathrm{Proj}(\Psi_{\mathrm{TR}}, k)|$ for the first three states in each ladder are shown in Fig. 7.16.

If we are in the dispersive regime, we expect to find, for each pure transmon eigenstate i, a ladder of total eigenstates separated by some regular frequency $f_c + \chi_i$. And each total eigenstate in a given ladder should project almost *entirely* onto the same pure transmon state when the resonator is traced out. Referencing the projections of each total eigenstate, given in Fig. 7.16, we find this to be the case for the “well-behaved” transmon states $|0\rangle, |1\rangle, |2\rangle, |4\rangle$, and $|7\rangle$. And the spacing of the eigenstates in these ladders is highly regular (only varying on the kHz range in simulation). However, when we examine Ladder 3 in Fig. 7.16, we see that these states also have a significant projection onto pure transmon state $|6\rangle$, and vice-versa. The same mixing occurs for Ladders 5 and 8. This suggests that these transitions are not well described by the dispersive regime. Indeed, the simulation predicts that the 3-6 transition is a mere 187 MHz detuned from the resonator, and 5-8 is only 91 MHz detuned.

A transition i-j is in the dispersive regime only if the ratio $|\Delta_{ij}|/g_{ij} \gg 1$, that is, the cavity-transition detuning dominates over the coupling strength. This condition prevents states i and j from mixing. These ratios are tabulated in Tab. 7.3 for each significant transition, and we see that the ratio is lowest specifically for the noted troublesome transitions.

State	0	1	2	3	4	5	6	7	8
0		36.5		561.5					
1	36.5		27.8		181.1				
2		27.8		24.6		45.5			
3	561.5		24.6		23.5		5.8		
4		181.1		23.5		24.1		40.7	
5			45.5		24.1		25.3		2.2
6				5.8		25.3		25.7	
7					40.7		25.7		33.5
8						2.2		33.5	

Table 7.3: Compilation of $|\Delta_{ij}|/g_{ij}$ ratios for each transmon transition in the system. Infrequent transitions for which this ratio is much greater than 1000 (such as parity-forbidden or far off-diagonal jumps) have been omitted for ease of viewing. We see quantitatively that the 3-6 transition and the 5-8 transition are of order unity, and not safely within the dispersive regime.

These low values are of order 1, so these transitions are neither resonant nor dispersive, and our intuition from either regime is sure to break down. In fact, the eigenstates of Ladder 3 are *not* evenly separated; the spacing varies on the MHz scale (that is, three orders of magnitude more variation than for properly dispersive Ladders in simulation). Consequently, attempted dispersive measurements on transmon state $|3\rangle$ will not find a stable dispersive shift to associate with the state, but rather a complex, noisy profile representing the interactions of the state $|3\rangle$ and state $|6\rangle$ with the resonator.

However, the experiment was able to circumvent this difficulty and probe state $|3\rangle$ by using a readout scheme with a depopulation sequence which renders it only dependent on the dispersion of states $|0\rangle$ and $|1\rangle$. In general, future qudit schemes on transmon systems may have to plan around these "accidental resonances" which are bound to arise as more transitions come into play.

Conclusions

In conclusion, we have demonstrated the preparation and control of the five-lowest states of an artificial atom in a three-dimensional cavity. We observed predominantly sequential energy relaxation, with non-sequential rates suppressed by two orders of magnitude. In addition, our direct measurement of the charge dispersion at higher levels agrees well with theory and facilitates further studies of the crucially important dephasing characteristics of quantum circuits. The measured qubit lifetimes in excess of $20\,\mu$s at all energy states up to $|4\rangle$ expands the practicability of transmons for quantum information applications and simulations using multi-level systems.

7.9 Higher energy levels of the qubit in Oxford

We reproduced the experiment on higher energy levels of a transmon presented above (the prior part of this chapter) with the Transmon-J qubit, fabricated and measured in our Lab in Oxford and characterised in Chapter 6. We again investigate the decay and coherence of the higher levels and draw conclusions in comparison to the Transmon-X qubit from MIT.

7.9.1 High-power readout

The qubit is measured using single-shot high-power readout (introduced in Section 6.1), performed by probing the cavity with a readout pulse at the bare resonance frequency $f_c = 10.4685\,\mathrm{GHz}$ of the cavity with a high-power of -1 dBm. At this power, the high-transmission "bright" state is maximally sensitive to the initial qubit state. A frequency sweep of the readout transmission around the cavity resonance at -1 dBm input power is shown in Fig. 7.17 for the qubit initially in the ground state $|0\rangle$ and for the qubit initially in the first excited state $|1\rangle$. The large jump in transmission amplitude depending on the qubit state allows us to clearly distinguish between the two qubit states in a single shot.

7.9.2 Decay of higher levels

We measure the energy relaxation of the Transmon-J from an initial excitation state $|3\rangle$ by varying the time delay before the readout process which includes the depopulation pulses. The decay traces are shown in Fig. 7.18, where we plotted the data as 1 - Signal (mV) for the sake of presenting the data in the same exponential decay form as in Fig. 7.7. The pulse sequences used here for populating the qubit into its higher levels are analogous to the ones used in the previous part of this chapter in

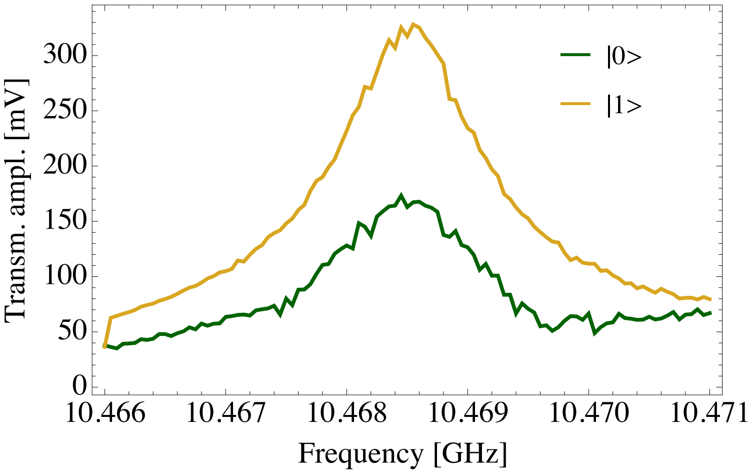

Figure 7.17: High-power frequency sweep of the resonator at its bare frequency for the qubit initially in the ground state $|0\rangle$ and in the first excited state $|1\rangle$. The state-dependent transmission amplitude allows to perform single shot readout of the qubit state.

Section 7.5, Section 7.6, and Section 7.7 for the Transmon-X at MIT. Furthermore, note that we plot the raw data here and have not corrected the traces with calibration values of the populations of each state as we had done for the Transmon-X using Eq. 7.5 to obtain Fig. 7.7.

An immediate observation is that the initial and end populations of the traces of the states are high, even after the qubit is back in its ground state. This can be explained if we include the finite temperature of the qubit, which is much higher here than in the previous case. For this reason we build a multi-level decay model including thermal distributions, and for simplicity we neglect non-sequential decays since we showed in Tab. 7.1 that they are suppressed by more than two orders of magnitude. We modify our decay model in Eq. 7.7 to express the thermal excitations as stimulated absorption by including non-zero sequential upward rates $\Gamma_{i,i+i}$ in the equations. These had been neglected in Eq. 7.7 due to the extremely low effective temperature of the Transmon-X qubit [92]. The downward rates have a spontaneous emission $\Gamma^{(sp)}_{i+i,i}$ and a (thermal) stimulated emission $\Gamma^{(st)}_{i+i,i}$ component, giving one decay rate $\Gamma_{i+i,i} = \Gamma^{(sp)}_{i+i,i} + \Gamma^{(st)}_{i+i,i}$.

Following the principle of detailed balance, the multi-level decay model for the evolution of the state occupations for $p_i(t)$ for $i = 0, 1, 2, 3$ is then given by the set of equations

$$\begin{aligned}
\frac{\mathrm{d}p_0(t)}{\mathrm{d}t} &= -\Gamma_{01}p_0(t) + \Gamma_{10}p_1(t) \\
\frac{\mathrm{d}p_1(t)}{\mathrm{d}t} &= \Gamma_{01}p_0(t) - \Gamma_{10}p_1(t) - \Gamma_{12}p_1(t) + \Gamma_{21}p_2(t) \\
\frac{\mathrm{d}p_2(t)}{\mathrm{d}t} &= \Gamma_{12}p_1(t) - \Gamma_{21}p_2(t) - \Gamma_{23}p_2(t) + \Gamma_{32}p_3(t) \\
\frac{\mathrm{d}p_3(t)}{\mathrm{d}t} &= \Gamma_{23}p_2(t) - \Gamma_{32}p_3(t)\ .
\end{aligned} \tag{7.16}$$

We are chiefly interested in extracting the three decay rates $\Gamma_{i+1,i}$ for $i = 0, 1, 2$ by fitting to the data. The upward rates $\Gamma_{i,i+1}$ can be eliminated as fitting parameters by calculating them from the steady state solutions (thermal equilibrium) of the equation system. They are obtained by solving the equations for $\mathrm{d}p_i(t)/\mathrm{d}t = 0$ for all $i = 0, 1, 2, 3$. The solution to the resulting equations gives the upward rates $\Gamma_{i,i+1}$ as a function of the downward rates $\Gamma_{i+1,i}$ and the ratio of the corresponding populations

$$\Gamma_{i,i+1} = \Gamma_{i+1,i}\,\frac{p_{i+1}}{p_i} \qquad \text{for } i = 0, 1, 2 \tag{7.17}$$

In statistical mechanics, the Boltzmann distribution is a probability distribution that gives the probability in thermal equilibrium that a system will be in a certain state as a function of that state's energy and the temperature of the system [107]. It is given as

$$p_i = \frac{e^{-\epsilon_i/k_B T}}{\sum_i^N e^{-\epsilon_i/k_B T}} \qquad \text{for } i = 0, 1, 2, 3 \tag{7.18}$$

where p_i is the probability of state i to be occupied, ϵ_i the energy of state i, T_q the temperature of the system, and N the total number of states accessible to the system. Applied to our system, the p_i is the population of state i, the energy of state i is $\epsilon_i = \hbar\omega_{0i}$, with ω_{0i} the transition frequency between the ground state $|0\rangle$ and excited state $|i\rangle$, $T = T_q$ is the temperature of the qubit, and $N = 3$ is the number of qubit states under consideration. The ratio of neighbouring populations in Eq. 7.17 can then be calculated given the single parameter T_q, and the upward rates become

$$\Gamma_{i,i+1} = \Gamma_{i+1,i} \frac{p_{i+1}}{p_i} = \Gamma_{i+1,i} \frac{e^{-\hbar\omega_{0,i+1}/k_B T_q}}{e^{-\hbar\omega_{0i}/k_B T_q}} \,. \tag{7.19}$$

Replacing these upward rates in the decay model Eq. 7.16 now gives us a simple model with only four parameters $\Gamma_{32}, \Gamma_{21}, \Gamma_{10}, T_q$ to fit. The initial populations $p_i(t)$ at time $t = 0$ could be estimated by transferring the thermal equilibrium occupations given by Eq. 7.18 with the π-pulse sequence. Due to our π-pulse imperfections however, these initial populations cannot be predicted precisely, and we therefore set them in the model to the initial values in the data.

In contrast to the Transmon-X which had very long T_1 times relatively to the readout time $T_{read} = 8\,\mu$s, our relaxation times are comparable to our readout time of $T_{read} = 4\,\mu$s. The model must therefore also account for the decay during the readout time of the data acquisition by adding the corrections to the model populations using Eq. 7.3 and Eq. 7.4. This indeed brings the model traces to the correct population distribution that matches the data at time $t = 15\,\mu$s.

From an independent T_1-measurement of the first excited state of the qubit we extract $\Gamma_{10}^{-1} = 6.2\,\mu$s which we fix as the first parameter. Varying the parameter T_q and the remaining two rates Γ_{32}, Γ_{21} iteratively we then fit the calibrated model to the data in Fig. 7.18, and the values of the best obtained fit are reported in Tab. 7.4. The extracted decay rates again show that the sequential rates scale approximately linearly. This thermal multi-level decay model fits well with our data and thereby strongly indicates that significant sequential upward rates $\Gamma_{i,i+1}$ due to the finite qubit temperature (qubit placed at 10 mK but not well thermalized) explain the high state occupations at the start and end of the evolution of the qubit states.

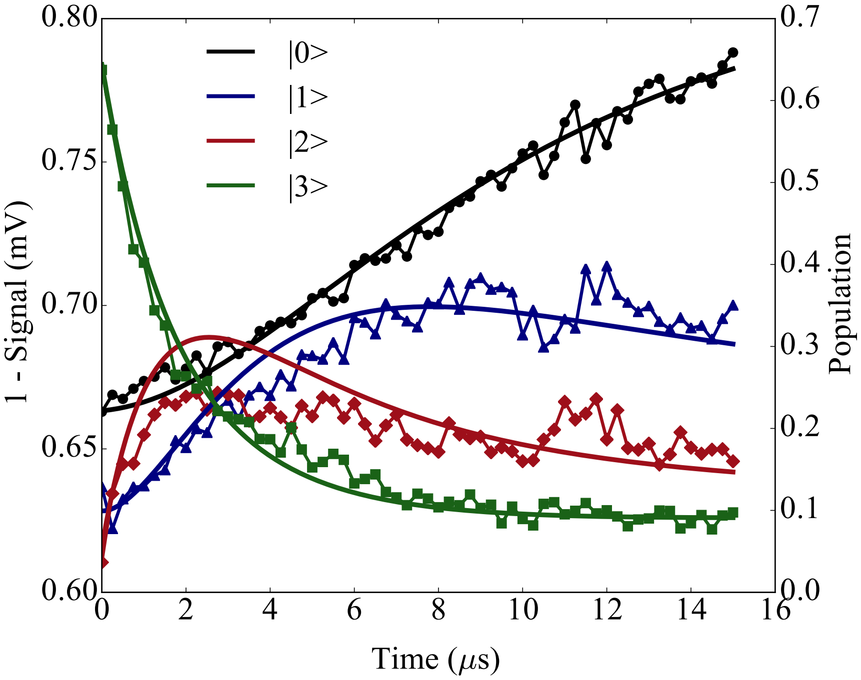

Figure 7.18: Population decay traces of the qubit states up to $|3\rangle$, obtained by varying the time delay Δt before the depopulation sequence. The solid lines are state occupations from the sequential multi-level decay model taking into account upward rates that express thermal excitations. The model traces are calibrated for the decay during the readout time and are then best fit to the data by adjusting the qubit temperature and sequential decay rates.

Frequency Exp. f (GHz)	f_{01} 6.848	f_{12} 6.589	f_{23} 6.307
Sequ. decay^{-1} time (μs)	Γ_{10} 6.2 ± 0.3	Γ_{21} 3.1 ± 0.2	Γ_{32} 2.0 ± 0.1
Dephasing T_2 time (μs) ±20%	$T_{2\,(01)}$ 5.3	$T_{2\,(12)}$ 3.2	$T_{2\,(23)}$ 2.3

Table 7.4: Experimental values for the Transmon-J qubit measured in Oxford for the transition frequencies $f_{i,i+1}$, the relaxation times Γ_{ij}^{-1} for the sequential and non-sequential rates, the dephasing times $T_{2\,(ij)}$ for the superpositions of states $|i\rangle$ and $|j\rangle$. Errors on the decay rates are determined as the maximum deviation for which the model still fits the data reasonably.

7.9.3 Coherence of higher levels

The phase coherence of the higher levels is also investigated using Ramsey-type experiments up to qubit state $|3\rangle$. The dephasing traces and the corresponding power spectral densities obtained via Fourier transform are displayed in Fig. 7.19, and the coherence times $T_{2,(01)}, T_{2,(12)}, T_{2,(23)}$ are found in Tab. 7.4. As opposed to the Transmon-X which revealed two clearly distinguishable frequency components for the states $|2\rangle$ and $|3\rangle$ (see Fig. 7.10), our Transmon-J here only shows one well-defined frequency component as well as one or two less important additional components, indicated by the black arrows in Fig. 7.19. We consider two possible explanations. The first is that the charge dispersion splitting is unresolved and therefore we only see one important frequency component. This explanation is justified by the results of the numerical simulation of the Transmon-J, which predicts that the maximum splitting $\epsilon_{23}^{(max)}$ is less than 30 kHz, and $\epsilon_{12}^{(max)}$ less than 3 kHz, and $\epsilon_{01}^{(max)}$ in the order of Hz. This is mainly the result of the high ratio $E_J/E_C = 96$ of the Transmon-J which greatly flattens its levels. This is in contrast to the Transmon-X, where the much lower ratio $E_J/E_C = 58$ showed larger charge dispersion (see Tab. 7.2) that allowed the Ramsey experiment to resolve the frequency splitting. The second explanation would be that the splitting revealed between the smaller indicated peak together with the major one (the two black arrows in Fig. 7.19) indeed represents the charge dispersion. That would then mean that the observed transition frequency splitting of 3.19 MHz on state $|2\rangle$ and of 8.21 MHz on state $|3\rangle$ is mainly induced by quasi-particle tunnelling between the two junction electrodes, charge traps between the substrate and the deposited metal film, or the presence of two-level fluctuators in the junction, as already mentioned in Section 7.7. These are likely dominant effects in our qubit causing the large splitting which in turn strongly limits our coherence times.

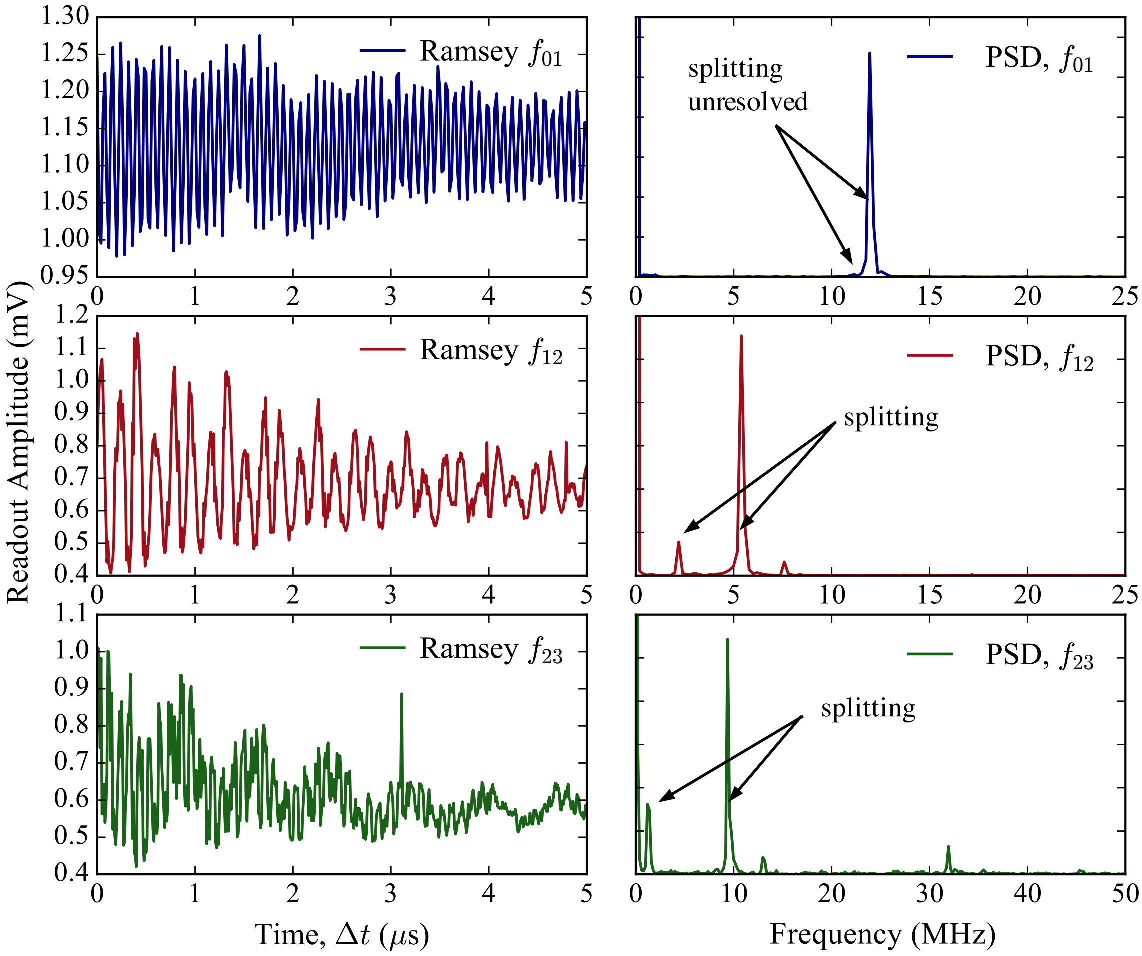

Figure 7.19: (a) Ramsey oscillations experiment on each subsequent energy transition up to state $|3\rangle$ with the Transmon-J in Oxford. The horizontal axis represents the pulse duration, and all traces are taken at identical input power. (b) The Power Spectral Density (PSD), obtained from the discrete Fourier transforms of the corresponding Ramsey fringes.

Chapter 8

A coaxial circuit QED architecture

This chapter presents a novel qubit architecture based on coaxial geometries for the qubit and resonator, that we call the coaxmon architecture. It allows for scaling up by using the 3rd dimension for readout resonators and input/output control, thereby allowing for scalable grids of qubits.

8.1 Motivation for coaxial circuit QED

We introduce a novel coaxial circuit QED architecture that consists of a coaxial LC resonator (which we call *coaxLC*) on one side of a chip coupled to a coaxial transmon (which we name the *coaxmon*) fabricated on the back of the chip, see Fig. 8.9. The similar geometry of the two allows for strong coupling across the dielectric of the sapphire chip. Coaxial readout and control coupling ports are placed inline in the 3rd dimension. This architecture allows the coaxial microwave cables to be directly coupled to the resonator with no physical contact or additional on chip circuit structures (no bonding). We demonstrate in Section 8.2 that we can fabricate and measure high-Q coaxial LC resonators by controlling the length of a spiral inductor between the inner and outer rings of the coaxLC. Then we show that replacing the spiral inductor by a Josephson junction on the back side of the chip creates a circuit QED system. We demonstrate qubit spectroscopy and Rabi oscillations in Section 8.2.3.1, proving the coherence of the system. This lumped element resonator only has a single resonant mode as opposed to the many modes in a 3D cavity due to its physical size, although for much higher frequencies higher modes will also appear. This is an important property of the coaxLC since it avoids leakage from the coupling of the qubit to higher modes of the resonator. This architecture is a significant departure from current circuit QED implementations in a number of ways. First, the qubit has a concentric coaxial topology which naturally suppresses spontaneous radiation due to radial symmetry. Second, the qubit is fabricated on the back side of the chip where the resonator is fabricated. Third, the input/output control lines as well as the readout resonator are inline in 3rd dimension, which allows to create a grid of qubits without presence of resonators in the grid. These characteristics make it a highly promising architecture for scaling up to the many-qubit grids necessary for quantum computing.

8.2 Coaxial LC resonators

8.2.1 CoaxLC design and simulation

Designing a two port lumped element coaxial parallel LC resonator (coaxLC), geometry shown in Fig. 8.3 and Fig. 8.1, requires finite elements simulations with HFSS to find the correct parameter range for the resonance frequency ω_r, capacitance C_r, and inductance L_r of the circuit given by

$$\omega_r = \frac{1}{\sqrt{L_r C_r}} \tag{8.1}$$

The purpose of the coaxLC is to serve as a readout resonator for the coaxial transmon (coaxmon) in a circuit QED setup. Since both circuits need to have a similar geometry and size in order to achieve coupling, measuring a coaxLC will serve as a basis for

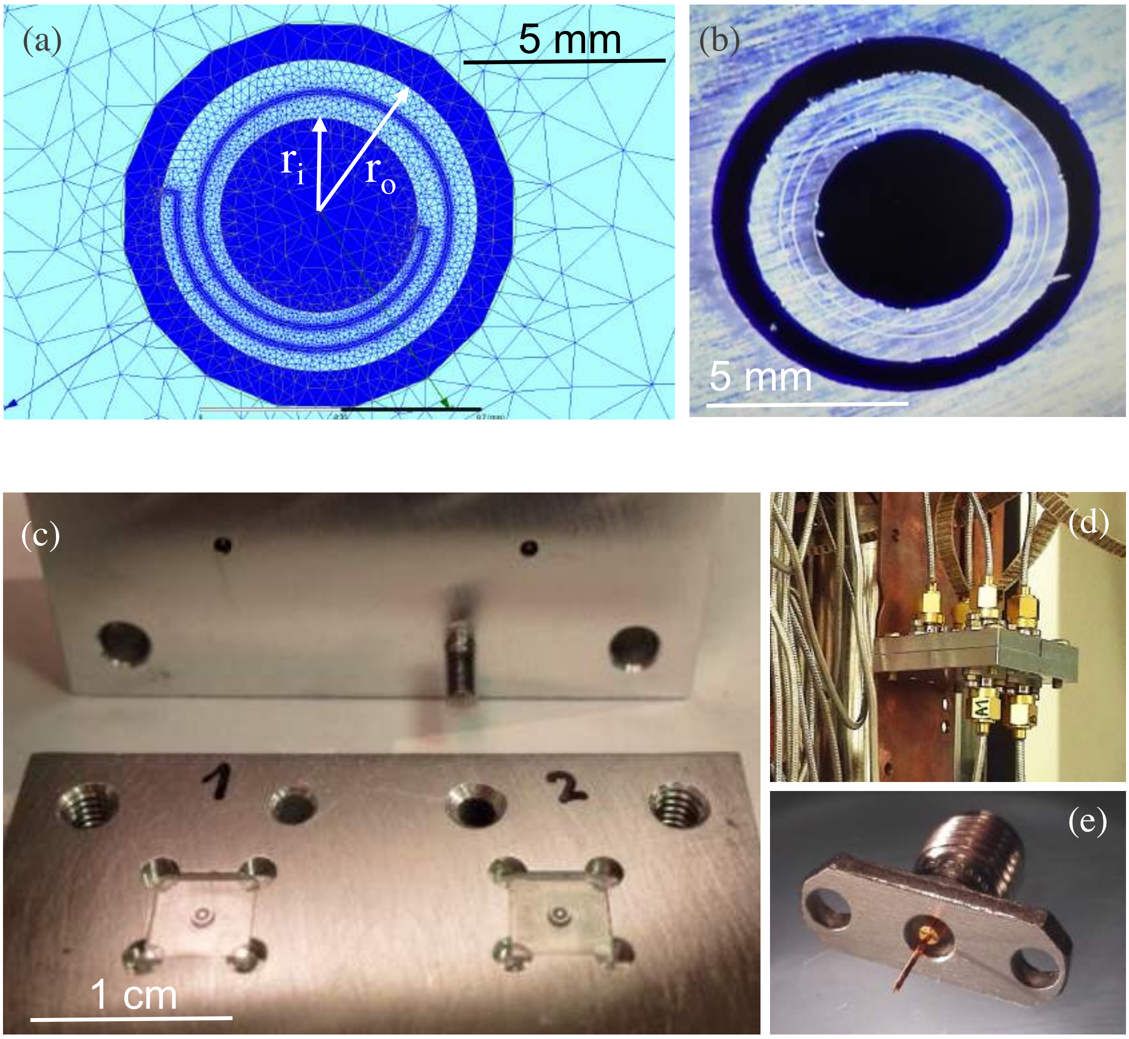

Figure 8.1: (a) HFSS simulation model of the coaxLC with the refined mesh. The coaxial capacitor geometry is defined by the radius of the inner disk $r_i = 0.25\,\mathrm{mm}$ and the inner radius of the outer ring $r_o = 0.4\,\mathrm{mm}$. (b) Optical picture of a coaxLC with bad liftoff on the capacitor ring edges. (c) Picture of the coaxLC1 and coaxLC2 chips placed in the aluminium sample holder. The small coupling port holes are visible on the inner surface of the sample holder lid. (d) Picture of the closed sample holder connected to the input/output lines and thermally attached to a copper plate fixed to the 10 mK plate. (e) Picture of the coupling pin SMA connector. The 0.4 mm thin copper wire is inserted into the connector's inner stud and then soldered in place.

designing the coaxmon's structure, and this means it is subject to several requirements which are not easily fulfilled simultaneously. The inductance of the coaxmon will be given by the engineered Josephson junction resistance as presented in Eq. 4.11. The capacitance $C = C_\Sigma$ determining the charging energy via $E_C = e^2/(2C_\Sigma)$, however, is

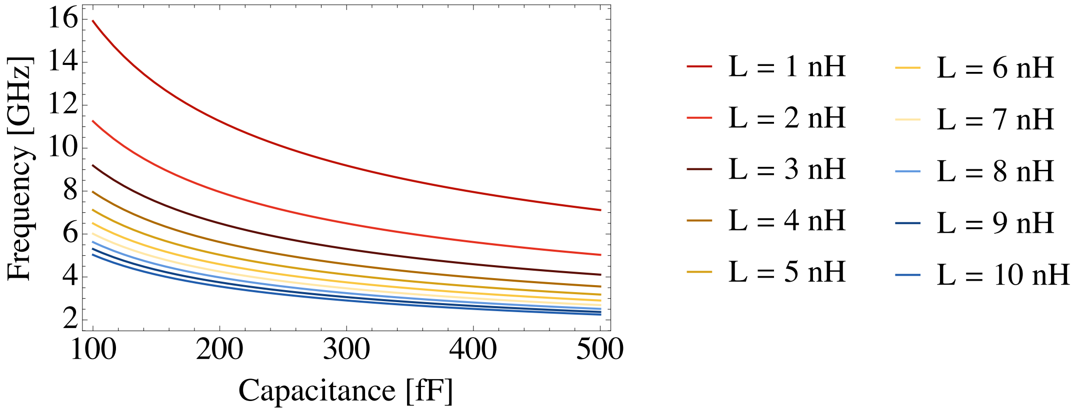

Figure 8.2: Plot of the resonance frequency of the coaxLC as a function of the capacitance for a range of inductance values via $\omega_r = 1/2\sqrt{LC}$.

difficult to calculate directly. It must be extracted by simulation, which delivers the resonance frequency for a fixed inductance, resulting in the capacitance then obtained via Eq. 8.1. A plot of the relation Eq. 8.1 for various values of the inductance is shown in Fig. 8.2 and serves as reference when fabricating the normal resistance of the Josephson junction to reach the desired qubit frequency.

The first constraint is a resonance frequency for the coaxLC in the range $\omega_r \sim 6-12\,\mathrm{GHz}$, i.e. a few GHz above the transition frequency of the coaxmon. The second constraint is that we want a capacitance C_r and inductance L_r similar to those of a transmon in the dispersive regime with $E_J/E_C \sim 50 - 100$, which corresponds to a capacitance on the order of $C \sim 100\,\mathrm{fF}$ and inductance $L_r \sim 1 - 10\,\mathrm{nH}$ for junction resistances of $R_n \sim 5 - 10\,\mathrm{k}\Omega$.

A third constraint arises from the long length needed for the wire that physically realizes the inductor. The self-inductance of a wire is given by [189]

$$L_{self}(l, w, t) = 2l \cdot (\ln \frac{2l}{w+t} + 0.5 + 0.2235\frac{w+t}{l}) \cdot 10^{-7}\,H\,, \tag{8.2}$$

where l is the length, $w = 1\,\mu\mathrm{m}$ the width, and $t = 80\,\mathrm{nm}$ the thickness. To achieve an inductance of $L_{r,self} \sim 2.5\,\mathrm{nH}$ requires a length of $l = 1.5\,\mathrm{mm}$, which can only physically fit conveniently between the two narrow concentric capacitor rings of the coaxLC if it is in the form of a spiral, as seen in Fig. 8.1a)b). The formula for self inductance Eq. 8.2 was first tested by measuring capacitively two-port coupled lumped element parallel LC oscillators with the inductor in the form of a meander line between two non concentric capacitor plates. Fitting the measured transmission spectrum with an ABCD matrix model [154] confirmed good agreement of the Eq. 8.2 with the extracted inductance of the device, showing that the mutual inductance is negligible.

The HFSS simulation of the coaxLC consisted mainly in varying the radius of the inner disk r_i and inner radius of the outer ring r_o, see Fig. 8.3 and Fig. 8.1a, with fixed inductor length l (fix inductance L_r) to simulate the resonance frequency that corresponds to the desired capacitance. The plot in Fig. 8.2 serves as rough guidance to fix the inductance in the simulation. Furthermore, the gap distance d_{gap} between the sapphire chip (coaxLC) and the tip of the centre pin of the coupling port is also varied in the simulation in order to estimate the external quality factor required to achieve a visible transmission resonance. The simulation results indicated that appropriate dimensions are $r_i = 0.25\,\mathrm{mm}$, $r_o = 0.4\,\mathrm{mm}$ with $d_{gap} = 0.25\,\mathrm{mm}$.

8.2.2 CoaxLC measurements

The fabrication of the first coaxLC1 and coaxLC2 was initially done using a single layer of PMMA950k resist, which led to a bad liftoff of the edges of the capacitor inner disk and outer ring, clearly visible in Fig. 8.1b. Subsequent resonators were made with a bi-layer, thereby solving the liftoff issues. The coaxial resonators are pure 80 nm thick aluminium thin films fabricated in the e-beam evaporator, and embedded in

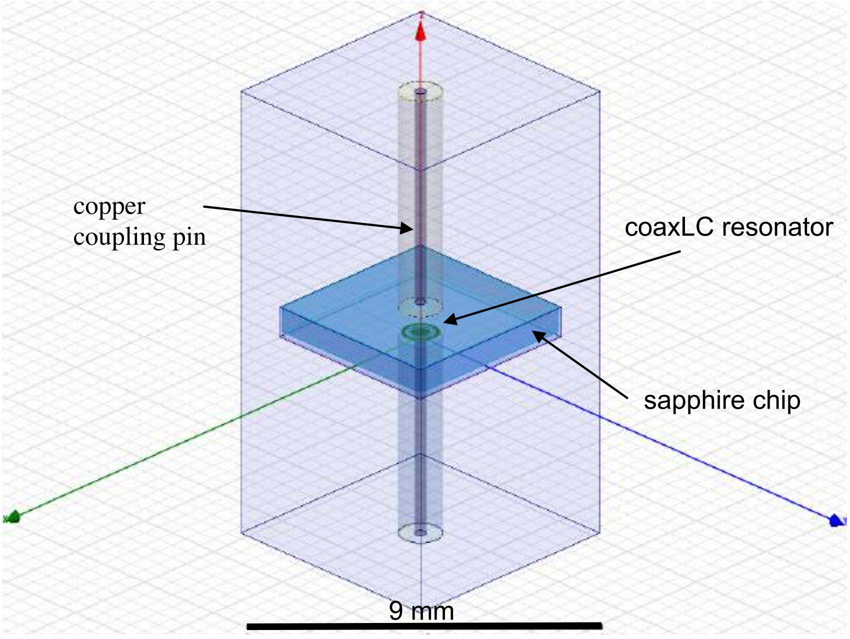

Figure 8.3: HFSS simulation model of the coaxLC resonator on a sapphire chip placed inside a sampleholder with the two coaxial coupling ports.

a carefully designed sample holder shown in Fig. 8.1c which is thermally fixed to the base plate of the dilution refrigerator at 10 mK, see Fig. 8.1d. The coupling pins pictured in Fig. 8.1e consist of a 0.4 mm diameter copper wire soldered into the center pin of an SMA connector. The two ports are connected to two input/output lines that are not highly attenuated, see Fig. 3.3 in Chapter 3, and the devices were measured with the VNA.

The measured transmission spectrum for both devices at 10 mK is shown in Fig. 8.4. CoaxLC1 has an inductor length $l = 3\,\mathrm{mm}$, leading to a resonance frequency $\omega_{r,1} = 6.78\,\mathrm{GHz}$, and fitted quality factors $Q_{int} = 850$ and $Q_{ext} = 1800$. The coaxLC2 has $l = 1.5\,\mathrm{mm}$ with $\omega_{r,2} = 9.70\,\mathrm{GHz}$ and quality factors $Q_{int} = 2230$ and $Q_{ext} = 670$. The low internal quality factor is due to the bad liftoff. The corrsponding HFSS simulation spectrums are overlaid (black) and show reasonably good agreement with the measurements, see compared values in Tab. 8.1. In order to obtain good

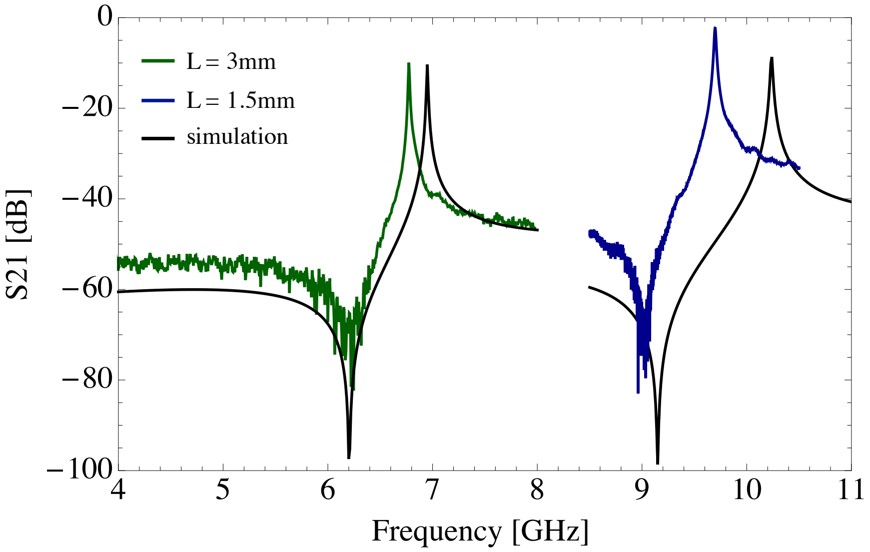

Figure 8.4: Transmission measurements of the coaxLC1 (green) and coaxLC2 (blue). The solid black lines are the respective HFSS simulation results. The data is corrected for the attenuation of the input and output microwave lines.

simulation results for the coaxLC with HFSS, it is important to refine the mesh in and around the inductor spiral to a size smaller than its width of 1 μm, as shown in Fig. 8.1a. The gap distance for both devices was chosen as small as physically possible by filling down the coupling pin $d_{gap} = 0.2 \pm 0.1$ mm. The additional resonance in the form of a dip comes from the fact that the parallel LC is in reality a capacitively coupled LC resonator with coupling capacitances C_k in series (the coupling ports) that lead to two resonances, one dip and one peak. It is the peak resonance that relates to the internal quality factor of the coaxLC though.

Subsequently we fabricated a coaxLC3 using a double layer resist of Copolymer/PMMA950k to solve the liftoff issue. The measured transmission spectrum at 10 mK is shown in Fig. 8.5. The second resonance (dip) is not visible for this device because the coupling pins were pulled further back to $d_{gap} = 0.6$ mm with $Q_{ext} = 85000$, to the point where the coupling capacitances C_k become negligible compared to the internal C_r of the coaxLC itself, and the capacitively coupled LC circuit reduces to a

CoaxLC	$l = 3\,\mathrm{mm}$	$l = 1.5\,\mathrm{mm}$
L_{self} [nH]	5.61	2.65
exp. $\omega_r/2\pi$ [GHz]	6.78	9.70
sim. $\omega_r/2\pi$ [GHz]	6.95	10.28
$\omega_r/2\pi$ % difference	2.5	6
exp. C_r [fF]	98.4	101.5
sim. C_r [fF]	93.6	90.4
C_r % difference	5.5	11.3

Table 8.1: Experimental and simulated values obtained for the two first coaxLC's. The L_{self} is the theoretical value calculated in Eq. 8.2. This values are for $r_i = 0.25\,\mathrm{mm}$ and $r_o = 0.4\,\mathrm{mm}$

simple parallel LC resonator.

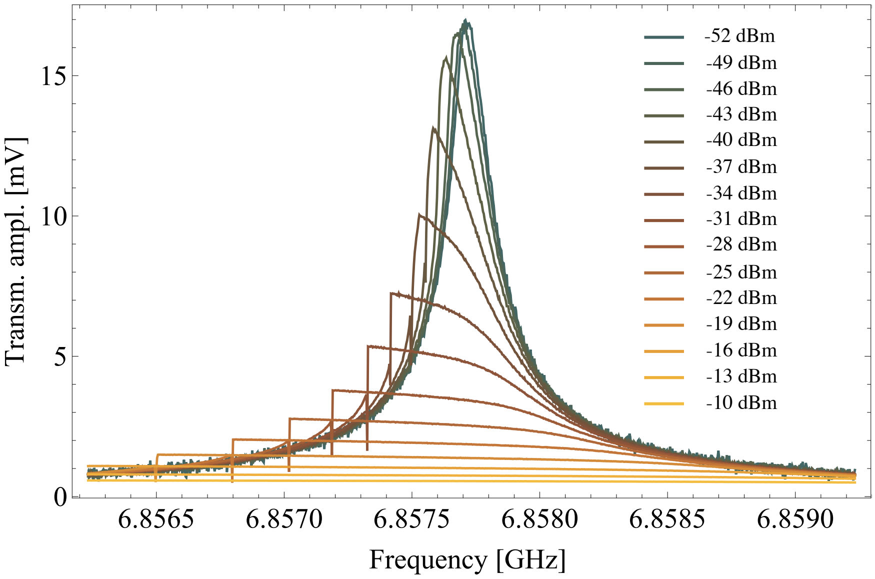

Figure 8.5: Power dependance of the CoaxLC3 device measured with a VNA at increasing input powers from -52 dB to -10 dB, with 3500 averages, $L_{ind} = 3\,\mathrm{mm}$, $f_r = 6.86979\,\mathrm{GHz}$, $Q_{int} = 110000$, and $Q_{ext} = 85000$.

The coaxLC undergoes non-linear effects (bifurcation) for high input powers where it looses its Lorentzian shape, as shown in Fig. 8.5 for the power range -52 dBm to -10 dBm. This is the evidence that indeed the resonance is that of an LC oscillator that behaves like a Duffing oscillator [58] at high power. In Fig. 8.5, the traces are referenced to the different input powers of the VNA, which is the reason that the peaks decrease in amplitude with increasing input power. We keep this visualisation, keeping the same base line, since the purpose of the plot is only to show the evidence of the non-linear effects.

The quality factors for the coaxLC3 are extracted from the measured transmission and reflection spectrum shown in Fig. 8.6 by fitting the reflection dip in the complex plane in order to take into account the magnitude and phase. It shows a high quality factor $Q_{int} = 110000$, which is two orders of magnitude larger than the first resonators that had a bad liftoff. The measured trace is corrected for the attenuation of the input and output microwave lines. This calibration was done by measuring the transmission spectrum of through the input and output line in a separate fridge cooldown by connecting them with a short "rough"-cable at the 10 mK stage, and then subtracting this attenuation calibration data from the measured coaxLC trace.

8.2.3 Coaxial circuit QED architecture: coupled coaxmon - coaxLC system

The successful design and measurement of coaxLCs prepared the grounds to fabricate a coupled coaxial qubit-cavity system for cQED. We use the coaxLC with a 1.5 mm inductor line, giving an inductance of approx 3 nH, and resonance at $\omega_r/2\pi \approx 10\,\mathrm{GHz}$ as the cavity, fabricated on the top side of a 0.5 mm thick sapphire chip. Since the coaxLC resonator geometry consists of concentric capacitor rings of dimensions $r_i = 0.25\,\mathrm{mm}$ and $r_o = 0.4\,\mathrm{mm}$ resulting in a capacitance $C_r \approx 100\,\mathrm{fF}$, we use the exact same geometry for fabricating the coaxmon. So the coaxmon is simply a coaxLC with the spiral inductor replaced by a Josephson junction fabricated on the other side of the sapphire chip (developed by Joseph Rahamim). The simulation design in Fig. 8.9 depicts this system, showing the devices and the coupling ports on

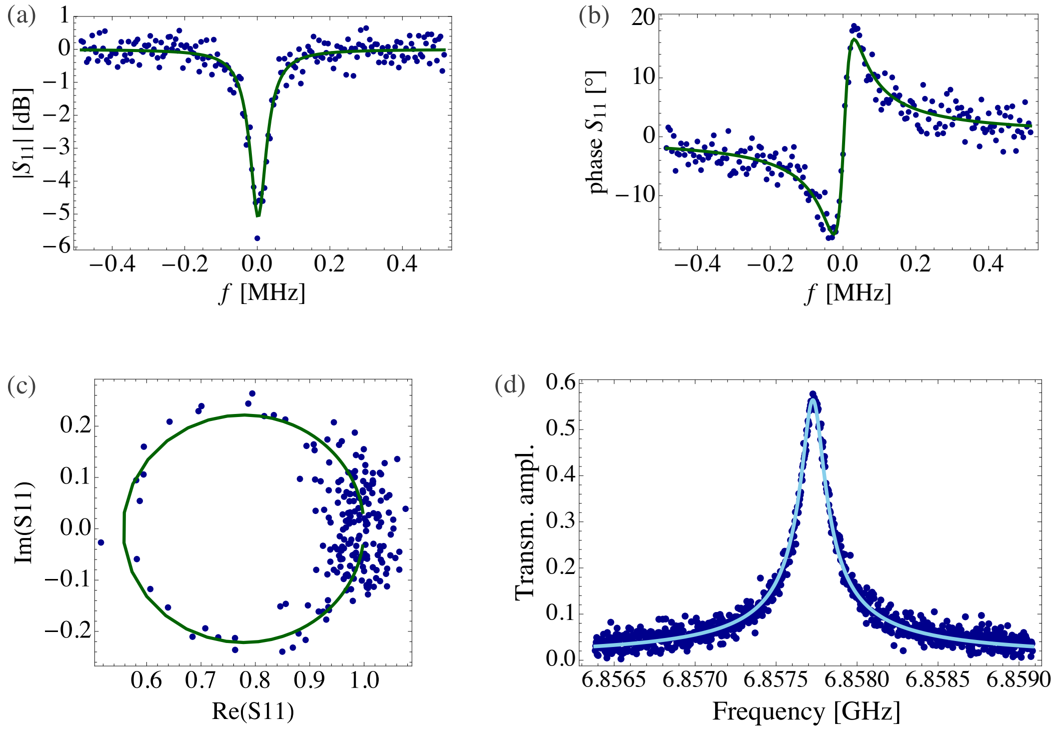

Figure 8.6: CoaxLC3 device with $L_{ind} = 3\,\text{mm}$, $f_r = 6.869\,\text{GHz}$, $Q_{int} = 110000$, and $Q_{ext} = 85000$. (a)(b)(c) Plot and fit of reflection measurement showing the amplitude, phase, and complex representation respectively. (d) Transmission measurement, corrected for the attenuation of input and output lines (5-7). Measured at low power -64 dBm.

both sides. Note, however, that in this figure the radius of the inner disk of the coaxmon is the optimal one $r_i = 0.125\,\text{mm}$ as devised in Section 8.2.3.2. The inner radius of the coaxmon fabricated and measured here is the exact same $r_i = 0.25\,\text{mm}$ as the coaxLC one. The double sided coaxmon-coaxLC chip is then placed in the aluminium sample holder, as seen in Fig. 8.1a, with an additional 0.2 mm deep pocket milled out on the side of the coaxmon to give it a vacuum buffer with the sample holder. The sample holder is again thermally fixed to the 10 mK stage of the fridge and the two coupling ports are connected to the same input and output lines used to measure the 3D transmons in Chapter 7, i.e. a highly attenuated input line and the amplification output line with the down-conversion and FPGA acquisition setup, see Fig. 3.3.

8.2.3.1 Coaxial circuit QED results

First, spectroscopic resonator measurements (see Section 6.1) of our coaxmon-coaxLC system in Fig. 8.7 for varying input powers show the dispersive coupling, with a dispersive shift $\chi_0/2\pi = 14.3\,\mathrm{MHz}$. The coaxLC's bare resonance frequency $\omega_c/2\pi = 9.3694\,\mathrm{GHz}$ at high input powers is shifted in the dispersive regime at low powers to its ground resonance frequency $\omega_r/2\pi = 9.3837\,\mathrm{GHz}$ corresponding to the qubit in the ground state $|0\rangle$. The resonance stays linear in the dispersive regime up to an input power of -45 dBm. We observe only one resonance peak at the low powers which corresponds to the qubit in the ground state $|0\rangle$. As opposed to our 3D transmon in Chapter 6, we do not see any resonance peak at the frequency corresponding to the qubit in state $|1\rangle$, which indicates that the coaxmon is very cold.

Performing the standard qubit spectroscopy measurements (see Section 6.2 for procedure details) with readout on the coaxLC ground resonance and sweeping the frequency of a qubit drive, we observe the qubit (coaxmon) transition frequency at $\omega_{01}/2\pi = 5.5465\,\mathrm{GHz}$ in Fig. 8.8a. The qubit drive is applied with a power of -20 dBm, and the readout signal is at -50 dBm. The high qubit drive power reveals the additional transitions of the qubit at $\omega_{12}/2\pi = 5.4237\,\mathrm{GHz}$ and $\omega_{02}/2 = 2\pi \cdot 5.482\,\mathrm{GHz}$. This allows us to extract the anharmonicity and charging energy of the coaxmon $\alpha/2\pi = -E_C = 123\,\mathrm{MHz}$, resulting in a Josephson energy $E_J = 29.5\,\mathrm{GHz}$, ratio $E_J/E_C = 227$, and coupling $g/2\pi = 234\,\mathrm{MHz}$, see Tab. 8.2. The conclusion from these results is that the capacitance C_Σ of the coaxmon needs to be decreased by decreasing the inner radius r_i, which is done by simulation in Section 8.2.3.2, so that the E_C increases sufficiently to obtain a larger anharmonicity and smaller E_J/E_C ratio.

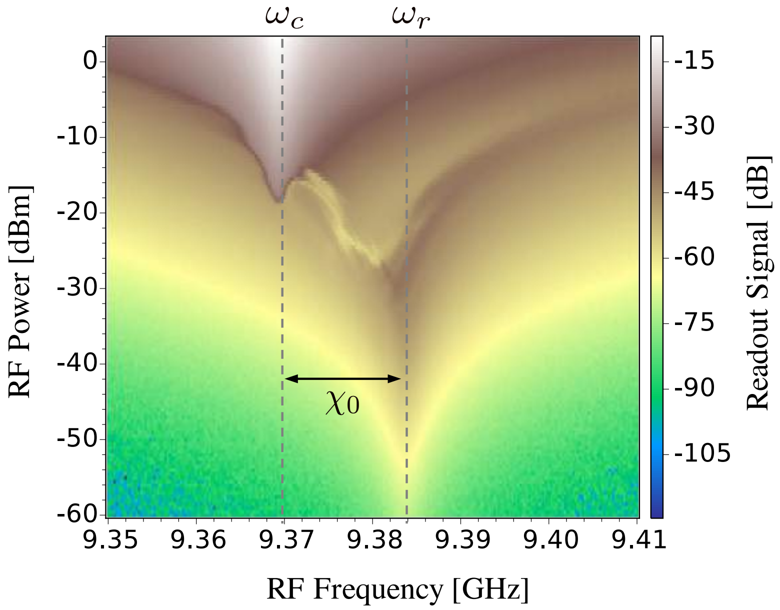

Figure 8.7: Resonator spectroscopy of the coupled coaxmon-coaxLC system for RF input powers ranging from 0 dBm to -60 dBm. The coaxLC resonance is shifted by $\chi_0/2\pi = 14.3\,\text{MHz}$ to $\omega_r/2\pi = 9.384\,\text{GHz}$ due to the dispersive interaction with the qubit at low input powers. For high powers, the dispersive shift neutralises and the coaxLC resonance appears at its bare resonance frequency $\omega_c/2\pi = 9.37\,\text{GHz}$.

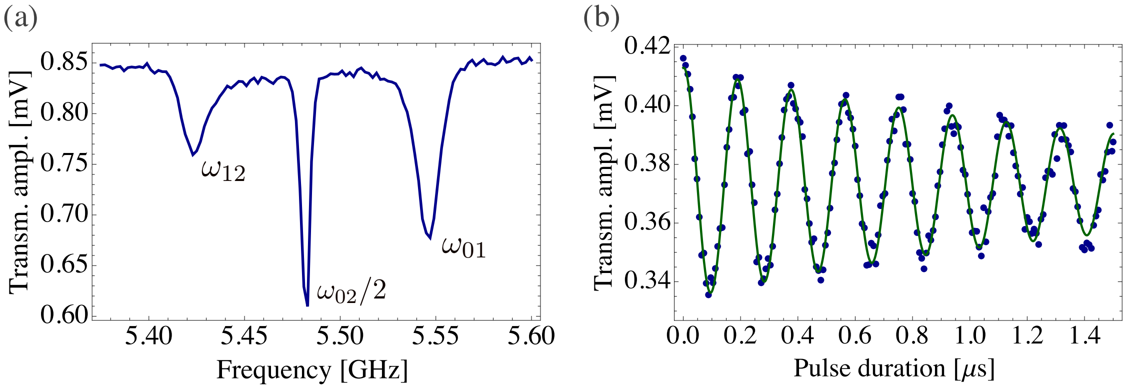

Figure 8.8: (a) Qubit spectroscopy at high drive power revealing the qubit transition frequencies $\omega_{01}/2\pi = 5.5465\,\text{GHz}$, $\omega_{12}/2\pi = 5.4237\,\text{GHz}$ and the two-photon transition $\omega_{02}/2 = 2\pi \cdot 5.482\,\text{GHz}$. (b) Rabi oscillations on the coaxmon transition ω_{01}, with fitted Rabi frequency $\omega_{Rabi}/2\pi = 5.33\,\text{MHz}$ and a relaxation time of $7\,\mu\text{s}$.

$\omega_r/2\pi$ GHz	$\omega_{01}/2\pi$ GHz	Δ GHz	$\chi_0/2\pi$ MHz	g MHz	E_J GHz	$\alpha/2\pi\,(-E_C)$ MHz	E_J/E_C
9.3837	5.5465	3.8372	14.3	234	29.5	123	227

Table 8.2: Parameters of the experimentally measured coaxmon.

In a final step we perform a Rabi experiment to prove that our coaxmon indeed is a qubit displaying coherence. Using the standard protocol presented in Section 6.4.2, we apply Rabi pulses of increasing length to obtain Rabi oscillations of the coaxmon, plotted and fitted in Fig. 8.8b.

8.2.3.2 Black Box Quantization simulation

The results obtained for the first measured coaxmon show that precise simulations for the capacitance are necessary in order to optimize the coaxmon's parameters, in particular α, E_J/E_C, to make them more similar to typical values for transmon circuit QED systems. We use the Black Box Quantization (BBQ) method [143] developed in Yale to fully simulate a 3D circuit QED system with HFSS. First, we performed BBQ simulation and compared the results to experimental data for a 3D transmon in order to prove that the BBQ simulation is consistent with experiments, which turned out to be the case. Detailed results of these simulations are presented in [174]. Then, our coupled coaxmon-coaxLC model shown Fig. 8.9 was simulated for a range of values of the inner radius r_i of the coaxmon, for various sapphire chip thicknesses, and varying the pin gap distance d_{gap}. The main result is a good set of design parameters for the geometry of the device for use as a circuit QED architecture. The key dimensions are: chip thickness 0.5 mm, coaxLC inner radius $r_i^{(res)} = 0.25\,\mathrm{mm}$, coaxmon inner radius $r_i^{(qubit)} = 0.125\,\mathrm{mm}$, coupling pin gap distance $d_{gap} = 0.25\,\mathrm{mm}$. These dimensions lead to the system parameters presented in Tab. 8.3. With these dimensions we therefore obtain a reasonable ratio $E_J/E_C \approx 100$ and sufficient anharmonicity $\alpha/2\pi \approx 200$.

The top view of the model in Fig. 8.9 shows the relative dimensions of the coaxLC and coaxmon. For this geometry, the simulations of the Purcell limiting lifetime $T_{Purcell}$ for varying values of d_{gap} reveal that for a coupling pin distance of minimum $d_{gap} = 0.2\,\text{mm}$ the coaxmon has $T_{Purcell} > 100\,\mu\text{s}$, which means that our system is far from being Purcell limited.

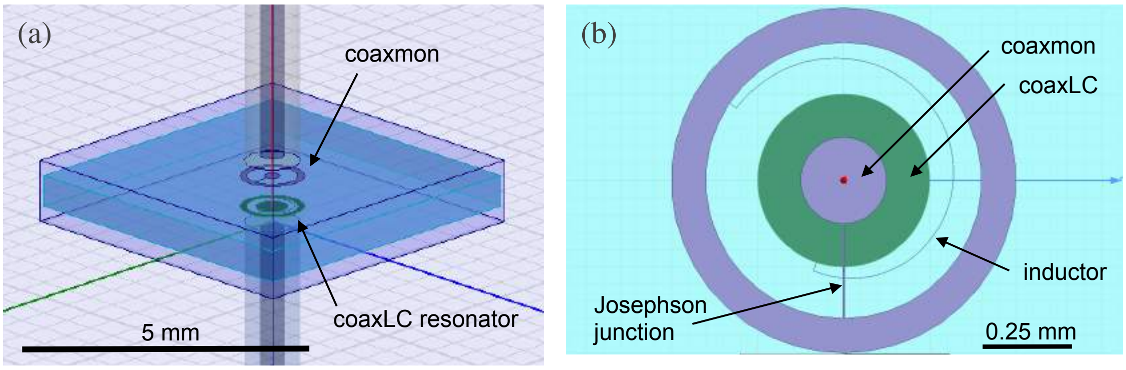

Figure 8.9: (a) HFSS simulation model of the coupled coaxmon - coaxLC system. The coaxmon (purple) is on the top face of the sapphire chip and the coaxLC (green) is on the backside of the chip. (b) Top view of the coupled system showing the relative geometries of the two devices.

	$\omega_r/2\pi$	$\omega_{01}/2\pi$	Δ	$\chi_0/2\pi$	g	E_J	$\alpha/2\pi\,(-E_C)$	E_J/E_C	$T_{purcell}$
	GHz	GHz	GHz	MHz	MHz	GHz	MHz		μs
sim BBQ	10.61	6.01	4.52	3.62	234	90	19.6	84	101
% error	3	13	7	11	4	-	13	20	-

Table 8.3: Parameters of simulations for optimal coaxmon with BBQ. Errors are calculated from comparison of experimental data and BBQ simulation of a 3D transmon.

Chapter 9

Conclusions and Outlook

9.1 Conclusions

The experimental work in this thesis consisted of three main accomplishments. The first part was designing and building a 3D circuit QED setup from scratch in a new lab which involved the following main steps: producing high quality factor cavities; designing, building and installing the cryogenic microwave setup as well as the room temperature amplification chains and data acquisition circuitry, successfully developing a recipe and fabricating Josephson junctions in Oxford, as well as measuring and controlling their normal resistances; and controlling, measuring, and fully characterising 3D transmons at 10 mK.

The second part consisted of demonstrating preparation and control of the five-lowest states of a transmon qubit in a 3D cavity and investigating the coherence and decay dynamics of these higher energy levels. The predominant energy relaxation was observed to be sequential, with non-sequential rates suppressed by two orders of magnitude. The direct measurement of the charge dispersion at higher levels agrees well with theory and facilitates further studies of decoherence characteristics of transmons. The measured qubit lifetimes in excess of $20\,\mu$s at energy states up to $|4\rangle$ expands the practicability of transmons for quantum information applications and simulations using multi-level systems. This experiment on higher levels was reproduced on a transmon fabricated and measured in Oxford, and a multi-level decay model including thermal populations was used to describe the relaxation dynamics.

The third accomplishment consisted in the demonstration of a novel coaxial transmon (coaxmon) architecture with a coaxial LC readout resonator and input/output coupling ports placed inline along the third dimension. This coaxial circuit QED architecture holds great promise for scaling up to the many-qubit grids necessary for building a quantum computer.

9.2 Outlook

This thesis has presented the development of single qubit 3D circuit QED experiments in Oxford, but that is only the first step in achieving a quantum computing building block. Indeed, this requires demonstrating the coupling and entanglement of two qubits as a next important step, in addition to implementing high fidelity two-qubit gates. The immediate next step is to fabricate a second transmon on the same or a second sapphire chip in our 3D cavity at a slightly different transition frequency and measure the two-qubit coupling. This does not require major design changes in the setup. Complete new designs are required when coupling two separate cavities as in [101]. Moreover, several important steps need to be taken to increase the lifetime and coherence of our transmons from the current typical values range $T_1 = 5 - 10\,\mu$s and $T_2 = 2 - 5\,\mu$s to state of the art values $T_1 = 20 - 90\,\mu$s and $T_2 = 15 - 100\,\mu$s. In order to achieve that, firstly the fabrication recipe needs to include a proper residual resist cleaning step before the aluminium evaporation. Most research labs use an in-situ ion gun mill to achieve this, which is not available to us, but this could be substituted by using carefully calibrated plasma etching or ashing. The current upgrading to a cryopumped chamber on our home-built e-beam evaporator may already improve lifetimes. A post lift-off cleaning step also needs to be tested and added to the fabrication recipe. Secondly, as shown in Chapter 6, the cavity and qubit are not cold enough at the base plate (over 200 mK) and therefore the presence of thermal photons in the cavity causes decoherence of the qubit state. This can be improved by better thermalizing the cavity to the 10 mK plate and adding better filters on the input and output lines to remove any radiation from reaching the cavity. A third improvement would be to optimize the dielectric surface participation ratio [192] of our 3D transmon geometry. Nevertheless, it is important to note that these improvements can be undertaken in parallel to performing new single and two-qubit experiments in one or two coupled cavities with the qubits and cavities that we currently have, because our coherence times are sufficiently good to apply sequences of many gates before decoherence becomes problematic.

The outlook described here not only applies to the 3D transmons but also to our coaxmons, since the Josephson junction is the same in both cases. Improving the fabrication of the Josephson junction will increase the lifetime of the coaxmon as well. Similarly, to prove the viability of the coaxmon architecture, the coupling of two coaxmon - coaxLC systems needs to be demonstrated. Simulations of different ways of coupling the two systems are underway and measurements are expected in the near future. These results will indicate how well two side by side coaxmons can be isolated, and simultaneously how well they can be entangled for quantum computing purposes. It is possible that some form of resonator bus will be needed to connect two coaxmons, analogous to the connecting resonators in current state of the art planar circuit QED systems that are realizing grids of qubits for quantum error correction [45].

Building a practical fault-tolerant scalable quantum computer will require applying quantum error correction codes, such as the surface code or repetition code, on thousands or millions of qubits in a 2D array to protect logical qubits [53] from errors induced by decoherence. Then operations on single logical qubits followed by quantum algorithms on several logical qubits need to be demonstrated before achieving a fault tolerant quantum computer. The current state-of-the-art has implemented the repetition code on a one-dimensional array of nine qubits [99]. It is clear that many inventions and engineering feats still lie ahead to create large reliable qubit-resonator grid structures to form the first logical qubit, and our hope is that perhaps our innovative coaxmon architecture will play a role in this great quantum endeavour.

Appendices

Appendix A

Aspects of the experimental setup

A.1 Microwave cables and heat loads

Our pulse tube cooled cryostat has a cooling power of less than 0.5 W at the 2.7 K. A single coaxial copper cable connecting the room temperature stage 300 K to the 2.7 K stage would have a heat load greater than 1 W, which would inevitably warm up the fridge. Cables with stainless steel (SS) are therefore the forced choice, as they have a low thermal conductivity. The trade-off though is that the stainless steel cables also have a significantly lower electrical conductivity than the copper ones. As shown in Fig. A.1 and Tab. A.2, we installed semi-rigid coaxial cables UT85-SS/SS made of 304 SS inner and outer conductor from base 10 mK to the 2.7 K stage, cables UT85-SS made of SPCW inner conductor and SS outer conductor from 2.7 K to 300 K, and cables UT85-TP made of tin plated copper inner and outer conductor from the fridge output to the microwave equipment. The label "UT-85" represents the standard radial size of the cables in the GHz range, and the frequency dependance of the intrinsic attenuation of the three different types of cables is plotted in Fig. A.1a. The cables are thermally anchored through oxygen-free-high-conductivity-copper (OFHC) baffle plates and feedthrough connectors at each temperature stage plate, as depicted in Fig. 3.2. These feedthrough connectors ensure that the cables have their outer conductor well thermalised. In addition, inserting attenuators onto the feedthrough connectors helps to thermalise the inner conductor of the cables, since attenuators have a finite resistance between the coaxial outer and inner conductor.

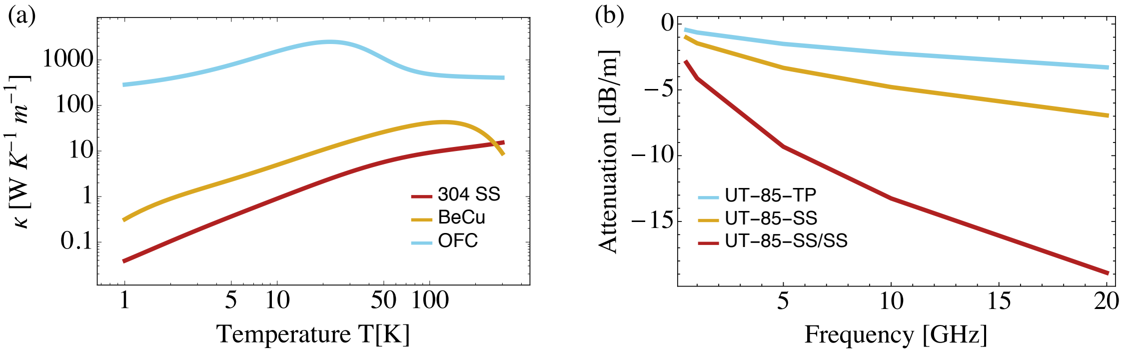

Figure A.1: (a) Temperature dependance of thermal conductivity for Stainless Steel (SS), Beryllium Copper (BeCu), and Oxygen Free Copper (OFC). (b) Frequency dependance of the attenuation of UT-85 coaxial cables made of different materials.

For determining the effective heat load at each stage in our Triton200 fridge, we consider the heat flow in a coaxial cable across a temperature difference ΔT given by

$$\dot{Q} = -\kappa A \frac{dT}{dx} \approx -\kappa A \frac{\Delta T}{L},$$

where A is the cross-section, L the length of the cable with ends at temperatures T_1 and T_2, and κ is the temperature-dependant thermal conductivity of the material. The temperature dependancies of the thermal conductivities $\kappa(T)$ of three common materials, stainless steel, beryllium-copper, and oxygen-free copper, are taken from the Cryogencis Materials Properties Database from the NIST Cryogenics Group [123] and are plotted in Fig. A.1b.

For large temperature differences though, as is the case in our fridge, the heat conduction should be calculated with thermal conductivity integrals $\Theta_{T_1}^{T_2}$,

$$\dot{Q} = \frac{A}{L} \int_{T_1}^{T_2} \kappa(T) \mathrm{d}T = \frac{A}{L}\, \Theta_{T_1}^{T_2}(\kappa)$$

Integrating the above thermal conductivities for the various temperature differences across the fridge stages gives us the results for the $\Theta_{T_1}^{T_2}$ tabulated in Tab. A.1.

Temperature		UT85	$\Theta[Wm^{-1}]$	Heat-flow [W]	Heat-flow [W]	Local
from	to	material	1 cable	1 cable	14 cables	cooling power
300 K	40 K	SS/SPCW	2943.12 / 130914	0.22 W	3.05 W	4 W
40 K	2.7 K	SS/SPCW	88.0 / 71478.7	0.1 W	1.2 W	0.5 W
2.7 K	0.65 K	SS/SS	17×10^{-2}	3.01 μW	42 μW	10 mW
0.65 K	65 mK	SS/SS	6.8×10^{-3}	6.69×10^{-8} W	9.36×10^{-7} W	200 μW
65 mK	10 mK	SS/SS	3.47×10^{-7}	4.77×10^{-12} W	6.68×10^{-11} W	4 μW

Table A.1: Heat loads in the Triton200 setup for 14 built-in cable lines.

The surface area of the semi-rigid UT85 cables includes the outer shield, the dielectric and the inner conductor. The dielectric is PTFE (teflon), which is an insulator, and has a very bad thermal conductivity to the point that it may be neglected. The surface area of the inner and outer conductor sums to $1.79\times10^{-6}\mathrm{m}^{-2}$. The centre conductor is not well thermalised, but it only represents 11% of the outer shield's area contribution. Taking the total length of the input line cables results in the total heat flows per stage in the fridge. The heat flow at the two higher temperature stages seems quite large compared to the local cooling power. These results however must be regarded with caution. In fact, the top two stages have UT85-SS/SPCW cables, which have a silver-plated copperweld (SPCW) as center conductor, which is copper-clad steel (CSS), a bi-metallic product that combines the high mechanical resistance of steel with the conductivity and resistance to corrosion of copper. Therefore, it has significantly lower thermal conductivity than the OFHC. However, we use OFHC values for the calculations of heat flows, acting as an upper bound, because there is no data available for the SPCW thermal conductivity. The last two columns in Tab. A.1 show that at each temperature stage, the local cooling power is greater than the combined heat flows of all cable lines.

A.2 Microwave components and instruments

	Input line		Output line	
Temp.	Component	Attn. [dB]	Component	Attn. [dB]
RT	Source	0 dBm	ADC	
	UT85-TP	-2.4	UT85-TP	-2.4
	IQ Upconverter	-7	BPF 55-67 MHz	-1.5
	Combiner	-3	LN Amplifier	+24
	UT85-TP	-4.8	LPF 300 MHz	-0.5
			UT85-TP	-0.5
			Attenuator	-3
			IQ Downconverter	-5.5
			UT85-TP	-2.4
			Wideband LN Amplifier	+26
			K&L BPF 8-12 GHz	-1
			Attenuator	-3
			Wideband LN Amplifier	+28
			K&L BPF 8-12 GHz	-1
			UT85-TP	-4.8
	DC block	-0.5	DC block	-0.5
RT	UT85-TP	-2	UT85-TP	-2
-	UT85-SS	-1.6	UT85-SS	-1.5
2.7 K	Attenuator	-20	HEMT amplifier	+39
-	UT85-SS/SS	-3.9	UT85-NbTi	-
65 mK	Attenuator	-20		
65 mK	UT85-SS/SS	-1.8		
10 mK	Attenuator	-20	Circulator 8-12 GHz	-0.3
			Circulator 8-12 GHz	-0.3
			K&L cryo BPF 8-12 GHz	-1
			K&L cryo LPF 12 GHz	-1
			Microwave Switch	-0.5
	UT85-TP	-0.5	UT85-TP	-0.8
10 mK	Cavity		Cavity	
	Total	**-85.5**	**Total**	**+82**

Table A.2: A detailed list of the input and output lines in the microwave measurement setup and their respective attenuations and amplifications.

Table A.3: Detailed list of components and instruments used for microwave pulse generation. Abbreviations used: Insertion Loss IL, Noise Figure NF, Isolation I, Gain G. The numbers in the first column refer to the labels in the various photos.

no.	component	manufacturer / model	specifications
1	Vector Network Analyzer (VNA)	Rohde & Schwarz ZVA50	10 MHz to 50 MHz, 2-port
2	Rb frequency standard	Stanford Research Systems FS725	20 outputs of 10 MHz sine phase noise $<$ -130 dBc/Hz at 10 Hz
3	Dual distribution amplifier	Stanford Research Systems FS735	10 MHz, 2 inputs each with 7 outputs
4	Analogue signal generator	Rohde & Schwarz SMF100A	100 kHz-22 GHz, power -130 to +30 dBm
5	Arbitrary waveform generator (AWG)	Textronix 5014C	4 channels, sample rate 1.2 GS/s, ±2.25 Vp
6	Upconversion IQ mixer	Marki-Microwave IQ-4509	LO and RF 4.5-9.0 GHz, IF DC-500 MHz $\mathrm{IL} \leq 7\,\mathrm{dB}$
7	Power combiner/splitter	Mini-Circuits ZX10-2-98+	4.75-9.8 GHz, 2 Way-0° $\mathrm{IL} = 3 + 0.3\,\mathrm{dB}$, $\mathrm{I} = 10\,\mathrm{to}\,23\,\mathrm{dB}$
8	DC Block	Aeroflex Inmet 8039	$\mathrm{IL} \leq 0.5\,\mathrm{dB}$
9	Attenuator	Mini-Circuits BW-S20-2W263+	attn 20 dB, DC-26 GHz

Table A.4: Detailed list of components used for amplification and downconversion chain. Abbreviations used: Insertion Loss IL, Noise Figure NF, Isolation I, Gain G, Low Noise LN. The numbers in the first column refer to the labels in the various photos.

no.	component	manufacturer / model	specifications
1	Microwave switch	Radiall SP6T Coaxial Subminiature	model R591762600, DC-26.5 GHz 12 Vdc, 6 positions, solder pins
2	Cryogenic low-pass filter	K&L coaxial filters 6L250-00089	12 GHz, IL $\leq$ 1 dB from 16-26 GHz IL $\geq$ 50 dB
3	Cryogenic band-pass filter	Keenlion KBF-8/12-2S OFHC	8-12 GHz, IL $\leq$ 1 dB, outside band IL $\geq$ 20 dB
4	Circulator	Raditek 8-12-Cryo with magnetic shield	8-12 GHz IL $\leq$ 0.6 dB, I $\geq$ 17 dB
5	Superconducting cable	Keycom NbTi/NbTi 085 coaxial cable	50mm, SMA connectorized
6	HEMT cryogenic amplifier	Low Noise Factory LNF-LNC1-12A	1-12 GHz, G = +39 dB, Noise = 5.5 K
7	Band-pass filter	Keenlion KBF-8/12-Q7S aluminium	8-12 GHz, IL $\leq$ 1 dB, outside band IL $\geq$ 20 dB
8	Wideband LN amplifier	Mini-Circuits ZX60-183A+	6-18 GHz, G = +28 dB, NF = 5 ± 0.2 dB
9	Wideband LN amplifier	Mini-Circuits ZVA-183+	700 MHz-18 GHz, G = +26 dB NF = 3.0 dB, NF_{max} = 5.5 dB
10	Downconversion IQ mixer	Marki-Microwave IQ-0618	LO and RF 6.0-18.0 GHz, IF DC-500 MHz IL $\leq$ 9 dB
11	Low-pass filter	Mini-Circuits VLFX-300	from DC-300 MHz IL $\leq$ 1 dB from 900 MHz-20 GHz IL $\geq$ 40 dB
12	LN amplifier	Mini-Circuits ZFL-500LN+	0.1 MHz-500 MHz, G = +24 dB, NF = 2.9 dB
13	Band-pass filter	Mini-Circuits SBP-60+	55-67 MHz IL $\leq$ 1.5 dB, outside band IL $\geq$ 30 dB
14	FPGA	Xilinx Virtex-6 FPGA with ML605 board	ADC card: model 4DSP FMC104 4-channel, 250 MS/s, 14-bit
15	DC power supply	Aim TTi EL302RT Triple Power Supply	triple outputs, 30V/2A

Appendix B

Fabrication

B.1 Fabrication recipe for qubits with electron-beam lithography

Step	Description	Equipment used	Precision
1	Cleaning	Acetone	Ultrasonic bath 50 °C 5 min
		Acetone	Again Ultrasonic bath 50 °C 5 min
			Rinse in IPA 15 s
		DMSO	80 °C 15 min
			Rinse in warm water twice
2	Dehydration	Hotplate	Bake 180 °C 2 min
			Let cool down 2 min
3	Resist coating	AR-P 617.08 (Copolymer)	Spin 45 s at 3000 rpm
4	Baking	Hotplate	Bake 180 °C 5 min
5	Resist coating	AR-P 672.045 (PMMA950k)	Spin 45 s at 2500 rpm
6	Baking	Hotplate	Bake 180 °C 5 min
7	Dissipation coating	Electra	Spin 30 s at 3000 rpm
8	E-beam lithography	Jeol JBX-5500 series ZC	Acceleration voltage 50kV
			Aperture 2
			Beam current 1 nA
			Large areas dose 750 μC/cm^2
			Junction area dose 950 μC/cm^2
			Undercut boxes dose 200 μC/cm^2
9	Dissipation removal		15 s in DI Water
10	Development	Hotplate, 1:3 MIBK:IPA	45 s at 25 °C
			Rinse in IPA 15 s
			N_2 blow dry, very low pressure
11	Cleaning (optional)	UV Ozone cleaner	10 min
12	Al deposition	Leek Evaporator	60 nm at 0.5 nm $\cdot$ s^{-1} and 60°
			Oxidation 2 mbar for 60 s
			70 nm at 0.5 nm $\cdot$ s^{-1} and 0°
13	Lift off	Hotplate, Acetone	10 min at 50 °C
			again 5 min at 50 °C
			Rinse in IPA 15 s
			N_2 blow dry

Table B.1: Fabrication recipe for Josephson junctions.

Bibliography

[1] WolframAlpha Knowledgebase. 2017. 120

[2] A A Abdumalikov, J M Fink, K Juliusson, M Pechal, S Berger, A Wallraff, and S Filipp. Experimental realization of non-abelian non-adiabatic geometric gates. *Nature*, 496(7446):482–485, 2013. 145

[3] Daniel S. Abrams and Seth Lloyd. Quantum algorithm providing exponential speed increase for finding eigenvalues and eigenvectors. *Phys. Rev. Lett.*, 83:5162–5165, 1999. 3

[4] V. Ambegaokar and A. Baratoff. Tunneling between superconductors. *Phys. Rev. Lett.*, 10:486, 1963. 96

[5] P. W. Anderson and J. M. Rowell. Probable observation of the josephson superconducting tunneling effect. *Phys. Rev. Lett.*, 10:230–232, 1963. 19

[6] Christopher Axline, Matthew Reagor, Reinier W. Heeres, Philip Reinhold, Chen Wang, Kevin Shain, Wolfgang Pfaff, Yiwen Chu, Luigi Frunzio, and Robert J. Schoelkopf. An architecture for integrating planar and 3D cQED devices. *Appl. Phys. Lett.*, 109(4), 2016. 8

[7] Samuel J. Bader. Higher levels of the transmon qubit. Master's thesis, Massachusetts Institute of Technology, 2014. 145, 166

[8] C. J. Ballance, T. P. Harty, N. M. Linke, M. A. Sepiol, and D. M. Lucas. High-fidelity quantum logic gates using trapped-ion hyperfine qubits. *Phys. Rev. Lett.*, 117:060504, 2016. 4

[9] R. Barends, J. Kelly, A. Megrant, A. Veitia, D. Sank, E. Jeffrey, T. C. White, J. Mutus, A. G. Fowler, B. Campbell, Y. Chen, Z. Chen, B. Chiaro, A. Dunsworth, C. Neill, P. O'Malley, P. Roushan, A. Vainsencher, J. Wenner, A. N. Korotkov, A. N. Cleland, and John M. Martinis. Superconducting

quantum circuits at the surface code threshold for fault tolerance. *Nature*, 508(7497):500–503, Apr 2014. 5, 7

[10] M. Baur, A. Fedorov, L. Steffen, S. Filipp, M. P. da Silva, and A. Wallraff. Benchmarking a quantum teleportation protocol in superconducting circuits using tomography and an entanglement witness. *Phys. Rev. Lett.*, 108:040502, 2012. 6

[11] Matthias Baur. *Realizing quantum gates and algorithms with three superconducting qubits*. PhD thesis, ETH Zurich, 2012. 39, 47

[12] Helle Bechmann-Pasquinucci and Asher Peres. Quantum cryptography with 3-state systems. *Phys. Rev. Lett.*, 85:3313–3316, 2000. 145

[13] J. Benhelm, G. Kirchmair, C. F. Roos, and R. Blatt. Experimental quantum-information processing with ca-43(+) ions. *Phys. Rev. A*, 77(6), 2008. 4

[14] Jan Benhelm, Gerhard Kirchmair, Christian F. Roos, and Rainer Blatt. Towards fault-tolerant quantum computing with trapped ions. *Nat. Phys.*, 4(6):463–466, 2008. 4

[15] J Bergli, Y M Galperin, and B L Altshuler. Decoherence in qubits due to low-frequency noise. *New J. Phys.*, 11(2):025002, 2009. 14

[16] P. Bertet, I. Chiorescu, G. Burkard, K. Semba, C. J. P. M. Harmans, D. P. DiVincenzo, and J. E. Mooij. Dephasing of a superconducting qubit induced by photon noise. *Phys. Rev. Lett.*, 95:257002, 2005. 14

[17] R. C. Bialczak, M. Ansmann, M. Hofheinz, M. Lenander, E. Lucero, M. Neeley, A. D. O'Connell, D. Sank, H. Wang, M. Weides, J. Wenner, T. Yamamoto, A. N. Cleland, and J. M. Martinis. Fast tunable coupler for superconducting qubits. *Phys. Rev. Lett.*, 106(6):060501, 2011. 7

[18] R. Bianchetti, S. Filipp, M. Baur, J. M. Fink, M. Göppl, P. J. Leek, L. Steffen, A. Blais, and A. Wallraff. Dynamics of dispersive single-qubit readout in circuit quantum electrodynamics. *Phys. Rev. A*, 80(4):043840, 2009. 6, 44

[19] R Bianchetti, S Filipp, M Baur, J M Fink, C Lang, L Steffen, M Boissonneault, A Blais, and A Wallraff. Control and tomography of a three level superconducting artificial atom. *Phys. Rev. Lett.*, 105(22):223601, 2010. 145

[20] Lev S. Bishop, Eran Ginossar, and S. M. Girvin. Response of the strongly driven jaynes-cummings oscillator. *Phys. Rev. Lett.*, 105(10):100505, 2010. 126

[21] A. Blais, J. Gambetta, A. Wallraff, D. I. , S. M. Girvin, M. H. Devoret, and R. J. Schoelkopf. Quantum-information processing with circuit quantum electrodynamics. *Phys. Rev. A*, 75(3):032329, 2007. 48

[22] A. Blais, R.-S. Huang, A. Wallraff, S. M. Girvin, and R. J. Schoelkopf. Cavity quantum electrodynamics for superconducting electrical circuits: An architecture for quantum computation. *Phys. Rev. A*, 69(6):062320, Jun 2004. 6, 34, 35, 37, 43, 169

[23] D. Booth, S. T. Rittenhouse, J. Yang, H. R. Sadeghpour, and J. P Shaffer. Production of trilobite rydberg molecule dimers with thousand-debye permanent electric dipole moments. *Science*, 348:99–102, 2015. 37

[24] V. Bouchiat, D. Vion, P. Joyez, D. Esteve, and M. H. Devoret. Quantum coherence with a single Cooper pair. *Phys. Scr.*, T76:165–170, 1998. 25

[25] N. Boulant, G. Ithier, P. Meeson, F. Nguyen, D. Vion, D. Esteve, I. Siddiqi, R. Vijay, C. Rigetti, F. Pierre, and M. Devoret. Quantum nondemolition readout using a josephson bifurcation amplifier. *Phys. Rev. B*, 76(1):014525–6, 2007. 126

[26] J Braumüller, M Sandberg, M R. Vissers, A Schneider, S Schlör, L Grünhaupt, H Rotzinger, M Marthaler, A Lukashenko, A Dieter, A V Ustinov, M Weides, and D P Pappas. Concentric transmon qubit featuring fast tunability and an anisotropic magnetic dipole moment. *Appl. Phys. Lett.*, 108(3), 2016. 9

[27] Teresa Brecht, Wolfgang Pfaff, Chen Wang, Yiwen Chu, Luigi Frunzio, Michel H Devoret, and Robert J Schoelkopf. Multilayer microwave integrated quantum circuits for scalable quantum computing. *Npj Quantum Information*, 2016. 8

[28] I Bregman, D Aharonov, M Ben-Or, and H S Eisenberg. Simple and secure quantum key distribution with biphotons. *Phys. Rev. A*, 77(5):050301, 2008. 145

[29] Stephen S Bullock, Dianne P O'Leary, and Gavin K Brennen. Asymptotically optimal quantum circuits for d-level systems. *Phys. Rev. Lett.*, 94(23):230502, 2005. 145

[30] M. A. Castellanos-Beltran, K. D. Irwin, G. C. Hilton, L. R. Vale, and K. W. Lehnert. Amplification and squeezing of quantum noise with a tunable josephson metamaterial. *Nat. Phys.*, 4:929–931, 2008. 126

[31] M. A. Castellanos-Beltran and K. W. Lehnert. Widely tunable parametric amplifier based on a superconducting quantum interference device array resonator. *Appl. Phys. Lett.*, 91(8):083509–3, 2007. 126

[32] G Catelani, J Koch, L Frunzio, R J Schoelkopf, M H Devoret, and L I Glazman. Quasiparticle relaxation of superconducting qubits in the presence of flux. *Phys. Rev. Lett.*, 106:077002, 2011. 160

[33] G Catelani, S E Nigg, S M Girvin, R J Schoelkopf, and L I Glazman. Decoherence of superconducting qubits caused by quasiparticle tunnelling. *Phys. Rev. B*, 86:184514, 2012. 14, 146, 161

[34] G Catelani, R J Schoelkopf, M H Devoret, and L I Glazman. Relaxation and frequency shifts induced by quasiparticles in superconducting qubits. *Phys. Rev. B*, 84:064517, 2011. 160

[35] Nicolas J Cerf, Mohamed Bourennane, Anders Karlsson, and Nicolas Gisin. Security of quantum key distribution using d-level systems. *Phys. Rev. Lett.*, 88(12):127902, 2002. 145

[36] J M Chow, L DiCarlo, J M Gambetta, F Motzoi, L Frunzio, S M Girvin, and R J Schoelkopf. Optimized driving of superconducting artificial atoms for improved single-qubit gates. *Phys. Rev. A*, 82(4):040305, 2010. 137, 145

[37] J. M. Chow, J. M. Gambetta, L. Tornberg, Jens Koch, Lev S. Bishop, A. A. Houck, B. R. Johnson, L. Frunzio, S. M. Girvin, and R. J. Schoelkopf. Randomized benchmarking and process tomography for gate errors in a solid-state qubit. *Phys. Rev. Lett.*, 102(9):090502, 2009. 32

[38] Jerry M. Chow, A. D. Córcoles, Jay M. Gambetta, Chad Rigetti, B. R. Johnson, John A. Smolin, J. R. Rozen, George A. Keefe, Mary B. Rothwell, Mark B. Ketchen, and M. Steffen. Simple all-microwave entangling gate for fixed-frequency superconducting qubits. *Phys. Rev. Lett.*, 107:080502, 2011. 7

[39] Jerry M. Chow, Jay M. Gambetta, A. D. Corcoles, Seth T. Merkel, John A. Smolin, Chad Rigetti, S. Poletto, George A. Keefe, Mary B. Rothwell, J. R.

Rozen, Mark B. Ketchen, and M. Steffen. Universal quantum gate set approaching fault-tolerant thresholds with superconducting qubits. *Phys. Rev. Lett.*, 109:060501, 2012. 68

[40] Jerry M Chow, Jay M Gambetta, Andrew W Cross, Seth T Merkel, Chad Rigetti, and M Steffen. Microwave-activated conditional-phase gate for superconducting qubits. *New J. Phys.*, 15:115012, 2013. 7, 145

[41] Y. Chu, C. Axline, C. Wang, T. Brecht, Y. Y. Gao, L. Frunzio, and R.J. Schoelkopf. Suspending superconducting qubits by silicon micromachining. *arXiv:1606.02822*, 2016. 8

[42] Isaac L. Chuang, Lieven M. K. Vandersypen, Xinlan Zhou, Debbie W. Leung, and Seth Lloyd. Experimental realization of a quantum algorithm. *Nature*, 393(6681):143–146, 1998. 4

[43] Isaac L. Chuang and Yoshihisa Yamamoto. Simple quantum computer. *Phys. Rev. A*, 1995. 4

[44] John Clarke and Frank K. Wilhelm. Superconducting quantum bits. *Nature*, 453(7198):1031–1042, 2008. 4, 24

[45] A.D. Córcoles, Easwar Magesan, Srikanth J. Srinivasan, Andrew W. Cross, M. Steffen, Jay M. Gambetta, and Jerry M. Chow. Demonstration of a quantum error detection code using a square lattice of four superconducting qubits. *Nat. Commun.*, 6:6979, 2015. 5, 196

[46] D. G. Cory, M. D. Price, W. Maas, E. Knill, R. Laflamme, W. H. Zurek, T. F. Havel, and S. S. Somaroo. Experimental quantum error correction. *Phys. Rev. Lett.*, 81(10):2152–2155, 1998. 4

[47] A. Cottet, D. Vion, A. Aassime, P. Joyez, D. Esteve, and M. H. Devoret. Implementation of a combined charge-phase quantum bit in a superconducting circuit. *Physica C*, 367(1-4):197–203, 2002. 26

[48] B.S. Deaver and W.M. Fairbank. Experimental evidence for quantized flux in superconducting cylinders. *Phys. Rev. Lett.*, 7:43–46, 1961. 19

[49] Frank Deppe, Matteo Mariantoni, E. P. Menzel, A. Marx, S. Saito, K. Kakuyanagi, H. Tanaka, T. Meno, K. Semba, H. Takayanagi, E. Solano, and R. Gross. Two-photon probe of the Jaynes-Cummings model and controlled

symmetry breaking in circuit QED. *Nat. Phys.*, 4(9):686–691, September 2008. 160

[50] David Deutsch. Quantum theory, the church-turing principle and the universal quantum computer. *Proceedings of the Royal Society A: Mathematical, Physical and Engineering Sciences*, 400(1818):97–117, 1985. 2

[51] David Deutsch and Richard Jozsa. Rapid solution of problems by quantum computation. *Proceedings: Mathematical and Physical Sciences*, 439(1907):553–558, 1992. 2

[52] M. H. Devoret. Quantum fluctuations in electrical circuits. In *Quantum Fluctuations: Les Houches Session LXIII*, 1997. 15

[53] M. H. Devoret and R. J. Schoelkopf. Superconducting circuits for quantum information: An outlook. *Science*, 339(6124):1169–1174, 2013. 6, 8, 38, 197

[54] Michel H. Devoret, John M. Martinis, and John Clarke. Measurements of macroscopic quantum tunnelling out of the zero-voltage state of a current-biased josephson junction. *Phys. Rev. Lett.*, 55:1908–1911, Oct 1985. 5, 19

[55] L. DiCarlo, J. M. Chow, J. M. Gambetta, Lev S. Bishop, B. R. Johnson, D. I. Schuster, J. Majer, A. Blais, L. Frunzio, S. M. Girvin, and R. J. Schoelkopf. Demonstration of two-qubit algorithms with a superconducting quantum processor. *Nature*, 460(7252):240–244, 2009. 6, 145

[56] L. DiCarlo, M. D. Reed, L. Sun, B. R. Johnson, J. M. Chow, J. M. Gambetta, L. Frunzio, S. M. Girvin, M. H. Devoret, and R. J. Schoelkopf. Preparation and measurement of three-qubit entanglement in a superconducting circuit. *Nature*, 467:574–578, 2010. 6

[57] David P DiVincenzo. Fault-tolerant architectures for superconducting qubits. *Phys. Scr.*, 2009(T137):014020, 2009. 8

[58] David P DiVincenzo and John A Smolin. Nonlinear spectroscopy of superconducting anharmonic resonators. *New J. Phys.*, 14(1):013051–, 2012. 187

[59] G. Dolan and J. Dunsmuir. Very small (20 nm) lithographic wires, dots, rings, and tunnel junctions. *Physica B*, 152:7, 1988. 80, 87

[60] R. Doll and M. Nbauer. Experimental proof of magnetic flux quantization in a superconducting ring. *Phys. Rev. Lett.*, 7:51–52, 1961. 19

[61] L.-M. Duan and C. Monroe. Colloquium: Quantum networks with trapped ions. *Rev. Mod. Phys.*, 82(2):1209–1224, Apr 2010. 4

[62] Thomas Durt, Dagomir Kaszlikowski, Jing-Ling Chen, and L Kwek. Security of quantum key distributions with entangled qudits. *Phys. Rev. A*, 69(3):032313, 2004. 145

[63] C. Eichler, D. Bozyigit, C. Lang, M. Baur, L. Steffen, J. M. Fink, S. Filipp, and A. Wallraff. Observation of two-mode squeezing in the microwave frequency domain. *Phys. Rev. Lett.*, 107:113601, Sep 2011. 6

[64] Jack W. Ekin. Experimental techniques for low-temperature measurements. *Oxford University Press*, pages 65–66, 2006. 60

[65] A. Fedorov, L. Steffen, M. Baur, M. P. da Silva, and A. Wallraff. Implementation of a toffoli gate with superconducting circuits. *Nature*, 481(7380):170–172, Jan 2012. 6

[66] R. P. Feynman. Simulating physics with computers. *Int. J. Theor. Phys.*, 21(6):467–488, June 1982. 2

[67] J. M Fink, M Goeppl, M Baur, R Bianchetti, P J Leek, A Blais, and A Wallraff. Climbing the jaynes-cummings ladder and observing its root n nonlinearity in a cavity qed system. *Nature*, 454(7202):315–318, 2008. 32, 42

[68] A. Fragner, M. Göppl, J. M. Fink, M. Baur, R. Bianchetti, P. J. Leek, A. Blais, and A. Wallraff. Resolving vacuum fluctuations in an electrical circuit by measuring the Lamb shift. *Science*, 322(5906):1357–1360, 2008. 45

[69] T. Frey, P. J. Leek, M. Beck, A. Blais, T. Ihn, K. Ensslin, and A. Wallraff. Dipole coupling of a double quantum dot to a microwave resonator. *Phys. Rev. Lett.*, 108(046807):046807, 2012. 4

[70] J. R. Friedman, V. Patel, W. Chen, S. K. Tolpygo, and J. E. Lukens. Quantum superposition of distinct macroscopic states. *Nature*, 406(6791):43–46, Jul 2000. 24

[71] M.J. Tiggelman C. Eichler L. Tornberg G. Johansson A. Wallraff R.N. Schouten G. de Lange, D. Rist and L. DiCarlo. Reversing quantum trajectories with analog feedback. *Phys. Rev. Lett.*, 112:080501, 2014. 142

[72] N. Gershenfeld and I. Chuang. Bulk spin resonance quantum computation. *Science*, 275:350–356, 1997. 4

[73] M. Göppl. *Engineering Quantum Electronic Chips - Realization and Characterization of Circuit Quantum Electrodynamics Systems.* PhD thesis, ETH Zurich, 2009. 95

[74] Lov K. Grover. *A fast quantum mechanical algorithm for database search.* ACM, Philadelphia, 1996. 3

[75] Stephan Gulde, Mark Riebe, Gavin P. T. Lancaster, Christoph Becher, Jürgen Eschner, Hartmut Häffner, Ferdinand Schmidt-Kaler, Isaac L. Chuang, and Rainer Blatt. Implementation of the Deutsch-Jozsa algorithm on an ion-trap quantum computer. *Nature*, 421(6918):48–50, Jan 2003. 4

[76] H. Häffner, W. Hänsel, C. F. Roos, J. Benhelm, D. Chek al kar, M. Chwalla, T. Körber, U. D. Rapol, M. Riebe, P. O. Schmidt, C. Becher, O. Gühne, W. Dür, and R. Blatt. Scalable multiparticle entanglement of trapped ions. *Nature*, 438(7068):643–646, dec 2005. 4

[77] E L Hahn. Spin echoes. *Phys. Rev.*, 80(4):580, 1950. 165

[78] S. Haroche. *Fundamental Systems in Quantum Optics*, chapter Cavity quantum electrodynamics, page 767. Elsevier, 1992. 41

[79] Serge Haroche and Jean-Michel Raimond. *Exploring the Quantum: Atoms, Cavities, and Photons.* OUP Oxford, 2006. 6

[80] Aram W. Harrow, Avinatan Hassidim, and Seth Lloyd. Quantum algorithm for linear systems of equations. *Phys. Rev. Lett.*, 103:150502, Oct 2009. 3

[81] T. P. Harty, D. T. C. Allcock, C. J. Ballance, L. Guidoni, H. A. Janacek, N. M. Linke, D. N. Stacey, and D. M. Lucas. High-fidelity preparation, gates, memory, and readout of a trapped-ion quantum bit. *Phys. Rev. Lett.*, 113:220501, Nov 2014. 4

[82] Max Hofheinz, E M Weig, M Ansmann, Radoslaw C Bialczak, Erik Lucero, M Neeley, A D O'Connell, H Wang, John M Martinis, and A N Cleland. Generation of Fock states in a superconducting quantum circuit. *Nature*, 454(7202):310–314, 2008. 6

[83] Io-Chun Hoi, C. M. Wilson, Gran Johansson, Tauno Palomaki, Borja Peropadre, and Per Delsing. Demonstration of a single-photon router in the microwave regime. *Phys. Rev. Lett.*, 107(7):073–601, Aug 2011. 6

[84] A A Houck, J A Schreier, B R Johnson, J M Chow, Jens Koch, J M Gambetta, D I Schuster, L Frunzio, M H Devoret, S M Girvin, and R J Schoelkopf. Controlling the spontaneous emission of a superconducting transmon qubit. *Phys. Rev. Lett.*, 101:080502, 2008. 6, 49, 146

[85] A.A. Houck, D.I. Schuster, J.M. Gambetta, J.A. Schreier, B.R. Johnson, J.M. Chow, L. Frunzio, J. Majer, M.H. Devoret, S.M. Girvin, and R.J. Schoelkopf. Generating single microwave photons in a circuit. *Nature*, 449:328–331, 2007. 6, 49

[86] Peter C. Humphreys, Benjamin J. Metcalf, Justin B. Spring, Merritt Moore, Xian-Min Jin, Marco Barbieri, W. Steven Kolthammer, and Ian A. Walmsley. Linear optical quantum computing in a single spatial mode. *Phys. Rev. Lett.*, 111:150501, Oct 2013. 4

[87] T. Crozes F. Lecocq I. Matei B. Pannetier O. Buisson I. M. Pop, T. Fournier and W. Guichard. Fabrication of stable and reproducible sub-micron tunnel junctions. *J. Vac. Sci. Technol. B*, 30:010607, 2012. 76, 86

[88] G. Ithier, E. Collin, P. Joyez, P. J. Meeson, D. Vion, D. Esteve, F. Chiarello, A. Shnirman, Y. Makhlin, J. Schriefl, and G. Schön. Decoherence in a superconducting quantum bit circuit. *Phys. Rev. B*, 72:134519, 2005. 13, 30

[89] J. Schrieffer J. Bardeen, L. Cooper. Theory of superconductivity. *Phys. Rev.*, 108:1157, 1957. 96

[90] John D. Jackson. Classical electrodynamics. *John Wiley & Sons Inc*, pages 352–374, 1999. 106

[91] E.T. Jaynes and F.W. Cummings. Comparison of quantum and semiclassical radiation theories with application to the beam maser. *Proceedings of the IEEE*, 51(1):89–109, 1963. 34, 35

[92] X.Y. Jin, A. Kamal, A.P. Sears, T. Gudmundsen, D. Hover, J. Miloshi, R. Slattery, F. Yan, J. Yoder, T.P. Orlando, S. Gustavsson, , and W.D. Oliver. Thermal and residual excited-state population in a 3D transmon qubit. *Phys. Rev. Lett.*, 114:240501, 2015. 131, 159, 174

[93] B. R. Johnson, M. D. Reed, A. A. Houck, D. I. Schuster, Lev S. Bishop, E. Ginossar, J. M. Gambetta, L. DiCarlo, L. Frunzio, S. M. Girvin, and R. J. Schoelkopf. Quantum non-demolition detection of single microwave photons in a circuit. *Nat. Phys.*, pages 663 – 667, 2010. 130

[94] B. D. Josephson. Possible new effects in superconductive tunnelling. *Physics Letters*, 1(7):251–253, July 1962. 19

[95] B. D. Josephson. The discovery of tunnelling supercurrents. *Rev. Mod. Phys.*, 46:251–254, Apr 1974. 19

[96] I. M. Pop S. Shankar L. Frunzio R. J. Schoelkopf M. Mirrahimi K. Geerlings, Z. Leghtas and M. H. Devoret. Demonstrating a driven reset protocol for a superconducting qubit. *Science*, 110:120501, 2013. 145

[97] B. E. Kane. A silicon-based nuclear spin quantum computer. *Nature*, 393(6681):133–137, May 1998. 4

[98] J. Kelly, R. Barends, A. G. Fowler, A. Megrant, E. Jeffrey, T. C. White, D. Sank, J. Y. Mutus, B. Campbell, Yu Chen, Z. Chen, B. Chiaro, A. Dunsworth, I.-C. Hoi, C. Neill, P. J. J. O'Malley, C. Quintana, P. Roushan, A. Vainsencher, J. Wenner, A. N. Cleland, and John M. Martinis. State preservation by repetitive error detection in a superconducting quantum circuit. *Nature*, 519(7541):66–69, Mar 2015. 5

[99] J. Kelly, R. Barends, A. G. Fowler, A. Megrant, E. Jeffrey, T. C. White, D. Sank, J. Y. Mutus, B. Campbell, Yu Chen, Z. Chen, B. Chiaro, A. Dunsworth, E. Lucero, M. Neeley, C. Neill, P. J. J. O'Malley, C. Quintana, P. Roushan, A. Vainsencher, J. Wenner, and John M. Martinis. Scalable *in situ* qubit calibration during repetitive error detection. *Phys. Rev. A*, 94:032321, Sep 2016. 5, 197

[100] Julian S. Kelly. *Fault-tolerant superconducting qubits.* PhD thesis, University of California Santa Barbara, 2015. 7, 83, 90, 100

[101] Gerhard Kirchmair, Brian Vlastakis, Zaki Leghtas, Simon E. Nigg, Hanhee Paik, Eran Ginossar, Mazyar Mirrahimi, Luigi Frunzio, S. M. Girvin, and R. J. Schoelkopf. Observation of quantum state collapse and revival due to the single-photon Kerr effect. *Nature*, 495(7440):205–209, Mar 2013. 195

[102] E. Knill, R. Laflamme, R. Martinez, and C. Negrevergne. Benchmarking quantum computers: The five-qubit error correcting code. *Phys. Rev. Lett.*, 86(25):5811–5814, Jun 2001. 4

[103] Jens Koch, Terri M Yu, Jay Gambetta, A A Houck, D I Schuster, J Majer, Alexandre Blais, M H Devoret, S M Girvin, and R J Schoelkopf. Charge-insensitive qubit design derived from the Cooper pair box. *Phys. Rev. A*, 76(4):042319, 2007. 6, 14, 26, 31, 32, 36, 40, 45, 145, 154, 163, 166, 168, 169

[104] Roger H. Koch, David P. DiVincenzo, and John Clarke. Model for $1/f$ flux noise in squids and qubits. *Phys. Rev. Lett.*, 98:267003, Jun 2007. 38, 44

[105] Pieter Kok, W. J. Munro, Kae Nemoto, T. C. Ralph, Jonathan P. Dowling, and G. J. Milburn. Linear optical quantum computing with photonic qubits. *Rev. Mod. Phys.*, 79(1):135–174, Jan 2007. 4

[106] F. D. Tichelaar M. E. J. L. P. H. Jeurgens, W. G. Sloof. Growth kinetics and mechanisms of aluminum-oxide films formed by thermal oxidation of aluminum. *J. Appl. Phys.*, 92:1649, 2002. 100

[107] L.D. Landau and E.M. Lifshitz. Statistical physics, 3rd ed. *Butterworth Heinemann*, 5, 1980. 131, 175

[108] Benjamin P Lanyon, Marco Barbieri, Marcelo P Almeida, Thomas Jennewein, Timothy C Ralph, Kevin J Resch, Geoff J Pryde, Jeremy L O'Brien, Alexei Gilchrist, and Andrew G White. Simplifying quantum logic using higher-dimensional hilbert spaces. *Nat.A quantu Phys.*, 5(2):134–140, 2008. 145

[109] A. Laucht, J. T. Muhonen, F. A. Mohiyaddin, R. Kalra, J. P. Dehollain, S. Freer, F. E. Hudson, M. Veldhorst, R. Rahman, G. Klimeck, K. M. Itoh, D. N. Jamieson, J. C. McCallum, A. S. Dzurak, and A. Morello. Electrically controlling single-spin qubits in a continuous microwave field. *Science Advances*, 1(3):e1500022–e1500022, Apr 2015. 4

[110] Adam Lawrence. Improving the lifetimes of 3d cavities for superconducting qubits. Master's thesis, University of Oxford, 2014. 120

[111] P. J. Leek, M. Baur, J. M. Fink, R. Bianchetti, L. Steffen, S. Filipp, and A. Wallraff. Cavity quantum electrodynamics with separate photon storage and qubit readout modes. *Phys. Rev. Lett.*, 104(10):100504, Mar 2010. 6

[112] P. J. Leek, S. Filipp, P. Maurer, M. Baur, R. Bianchetti, J. M. Fink, M. Göppl, L. Steffen, and A. Wallraff. Using sideband transitions for two-qubit operations in superconducting circuits. *Phys. Rev. B*, 79:180511, 2009. 7

[113] Z. Leghtas, G. Kirchmair, B. Vlastakis, M. H. Devoret, R. J. Schoelkopf, , and M. Mirrahimi. Deterministic protocol for mapping a qubit to coherent state superpositions in a cavity. *Phys. Rev. A*, 87:042315, 2013. 130

[114] Seth Lloyd. Universal quantum simulators. *Science*, 273(5278):1073–1078, 1996. 2

[115] Seth Lloyd, Masoud Mohseni, and Patrick Rebentrost. Quantum algorithms for supervised and unsupervised machine learning. *arXiv:1307.0411*, 2013. 3

[116] F. London. *Superfluids.* Wiley, New York, 1950. 19

[117] Daniel Loss and David P. DiVincenzo. Quantum computation with quantum dots. *Phys. Rev. A*, 57(1):120–, Jan 1998. 4

[118] Ning Lu. Effects of dissipation on photon statistics and the lifetime of a pure number state. *Phys. Rev. A*, 40:1707–1708, 1989. 146, 160

[119] J. Majer, J. M. Chow, J. M. Gambetta, J. Koch, B. R. Johnson, J. A. Schreier, L. Frunzio, D. I. Schuster, A. A. Houck, A. Wallraff, A. Blais, M. H. Devoret, S. M. Girvin, and R. J. Schoelkopf. Coupling superconducting qubits via a cavity bus. *Nature*, 449(7161):443–447, Sep 2007. 6

[120] Francois Mallet, Florian R. Ong, Agustin Palacios-Laloy, Francois Nguyen, Patrice Bertet, Denis Vion, and Daniel Esteve. Single-shot qubit readout in circuit quantum electrodynamics. *Nat. Phys.*, 5:791–795, 2009. 126

[121] Matteo Mariantoni. *New Trends in Superconducting Circuit Quantum Electrodynamics: Two Amplifiers, Two Resonators, and Two Photons.* Shaker Verlag, 2010. 37

[122] Matteo Mariantoni, H. Wang, T. Yamamoto, M. Neeley, Radoslaw C. Bialczak, Y. Chen, M. Lenander, Erik Lucero, A. D. OConnell, D. Sank, M. Weides, J. Wenner, Y. Yin, J. Zhao, A. N. Korotkov, A. N. Cleland, and John M. Martinis. Implementing the quantum von neumann architecture with superconducting circuits. *Science*, 334(6052):61–65, 2011. 6

[123] E.D. Marquardt. Cryogenics materials properties database. *11th International Cryocooler Conference, Keystone, Co*, June 20-22, 2000. 200

[124] J. M. Martinis, S. Nam, J. Aumentado, and C. Urbina. Rabi oscillations in a large Josephson-junction qubit. *Phys. Rev. Lett.*, 89(11):117901, Sep 2002. 5, 24

[125] John M. Martinis, Michel H. Devoret, and John Clarke. Energy-level quantization in the zero-voltage state of a current-biased josephson junction. *Phys. Rev. Lett.*, 55:1543–1546, Oct 1985. 5, 19

[126] A. Megrant, C. Neill, R. Barends, B. Chiaro, Yu Chen, L. Feigl, J. Kelly, Erik Lucero, Matteo Mariantoni, P. J. J. O'Malley, D. Sank, A. Vainsencher, J. Wenner, T. C. White, Y. Yin, J. Zhao, C. J. Palmstrøm, John M. Martinis, and A. N. Cleland. Planar superconducting resonators with internal quality factors above one million. *Appl. Phys. Lett.*, 100(11), 2012. 7

[127] M. Metcalfe, E. Boaknin, V. Manucharyan, R. Vijay, I. Siddiqi, C. Rigetti, L. Frunzio, R. J. Schoelkopf, and M. H. Devoret. Measuring the decoherence of a quantronium qubit with the cavity bifurcation amplifier. *Phys. Rev. B*, 76(17):174516–5, Nov 2007. 126

[128] Z. K. Minev, K. Serniak, I. M. Pop, Z. Leghtas, K. Sliwa, M. Hatridge, L. Frunzio, R. J. Schoelkopf, and M. H. Devoret. Planar multilayer circuit quantum electrodynamics. *Phys. Rev. Appl.*, 5:044021, Apr 2016. 8

[129] C. Monroe, D. M. Meekhof, B. E. King, W. M. Itano, and D. J. Wineland. Demonstration of a fundamental quantum logic gate. *Phys. Rev. Lett.*, 75:4714–4717, Dec 1995. 4

[130] Thomas Monz, Philipp Schindler, Julio T. Barreiro, Michael Chwalla, Daniel Nigg, William A. Coish, Maximilian Harlander, Wolfgang Hänsel, Markus Hennrich, and Rainer Blatt. 14-qubit entanglement: Creation and coherence. *Phys. Rev. Lett.*, 106:130506, Mar 2011. 4

[131] J E Mooij, T P Orlando, L Levitov, L Tian, C H van der Wal, and S Lloyd. Josephson persistent-current qubit. *Science*, 285(5430):1036–1039, 1999. 5

[132] John J. L. Morton. Quantum computing: Diamond wedding for spin couple. *Nat. Phys.*, 2(6):365–366, Jun 2006. 4

[133] F. Motzoi, J. M. Gambetta, P. Rebentrost, and F. K. Wilhelm. Simple pulses for elimination of leakage in weakly nonlinear qubits. *Phys. Rev. Lett.*, 103(11):110501, 2009. 32

[134] Clemens Müller, Jürgen Lisenfeld, Alexander Shnirman, and Stefano Poletto. Interacting two-level defects as sources of fluctuating high-frequency noise in superconducting circuits. *Phys. Rev. B*, 92:035442, Jul 2015. 14

[135] Ashok Muthukrishnan and C R Stroud. Multivalued logic gates for quantum computation. *Phys. Rev. A*, 62:052309, 2000. 145

[136] R. Lutchyn R. G. Clark N. A. Court, A. J. Ferguson. Quantitative study of quasiparticle traps using the single-cooper-pair transistor. *Phys. Rev. B*, 77:100501, 2008. 91

[137] Y. Nakamura, C. D. Chen, and J. S. Tsai. Spectroscopy of energy-level splitting between two macroscopic quantum states of charge coherently superposed by josephson coupling. *Phys. Rev. Lett.*, 79:2328–2331, Sep 1997. 5, 24, 25

[138] Y Nakamura, Yu A Pashkin, and J S Tsai. Coherent control of macroscopic quantum states in a single-cooper-pair box. *Nature*, 398(6730):786–788, 1999. 5, 25

[139] M. Neeley, R. C. Bialczak, M. Lenander, E. Lucero, M. Mariantoni, A. D. O'Connell, D. Sank, H. Wang, M. Weides, J. Wenner, Y. Yin, T. Yamamoto, A. N. Cleland, and J. M. Martinis. Generation of three-qubit entangled states using superconducting phase qubits. *Nature*, 467:570–573, 2010. 6

[140] Matthew Neeley, Markus Ansmann, Radoslaw C Bialczak, Max Hofheinz, Erik Lucero, Aaron D O'Connell, Daniel Sank, Haohua Wang, James Wenner, Andrew N Cleland, Michael R Geller, and John M Martinis. Emulation of a quantum spin with a superconducting phase qudit. *Science*, 325(5941):722–725, 2009. 131

[141] Michael A. Nielsen and Isaac L. Chuang. *Quantum Computation and Quantum Information.* Cambridge University Press, 2000. 4, 12, 145

[142] D. Nigg, M. Muller, E. A. Martinez, P. Schindler, M. Hennrich, T. Monz, M. A. Martin-Delgado, and R. Blatt. Quantum computations on a topologically encoded qubit. *Science*, 345(6194):302–305, Jun 2014. 4

[143] S.E. Nigg, H. Paik, B. Vlastakis, G. Kirchmair, S. Shankar, L. Frunzio, M. Devoret, R. Schoelkopf, and S. Girvin. Black-box superconducting circuit quantization. *Phys. Rev. Lett.*, 108:240502, 2012. 192

[144] Nissim Ofek, Andrei Petrenko, Reinier Heeres, Philip Reinhold, Zaki Leghtas, Brian Vlastakis, Yehan Liu, Luigi Frunzio, S. M. Girvin, Liang Jiang, Mazyar Mirrahimi, M. H. Devoret, and R. J. Schoelkopf. Extending the lifetime of a quantum bit with error correction in superconducting circuits. *Nature*, 536:441–445, 2016. 5

[145] F. R. Ong, M. Boissonneault, F. Mallet, A. Palacios-Laloy, A. Dewes, A. C. Doherty, A. Blais, P. Bertet, D. Vion, and D. Esteve. Circuit qed with a nonlinear resonator: ac-stark shift and dephasing. *Phys. Rev. Lett.*, 106:167002, Apr 2011. 126

[146] T. P. Orlando, J. E. Mooij, Lin Tian, Caspar H. van der Wal, L. S. Levitov, Seth Lloyd, and J. J. Mazo. Superconducting persistent-current qubit. *Phys. Rev. B*, 60(22):15398, Dec 1999. 5

[147] H. Paik, A. Mezzacapo, M. Sandberg, D. T. McClure, B. Abdo, A. D. Corcoles, O.Dial, D. F. Bogorin, B. L. T. Plourde, M. Steffen, A. W. Cross, J. M. Gambetta, and Jerry M. Chow. Experimental demonstration of a resonator-induced phase gate in a multiqubit circuit QED system. *Phys. Rev. Lett.*, 2016. 7

[148] Hanhee Paik, D I Schuster, Lev S Bishop, G Kirchmair, G Catelani, A P Sears, B R Johnson, M J Reagor, L Frunzio, L I Glazman, S M Girvin, M H Devoret, and R J Schoelkopf. Observation of high coherence in josephson junction qubits measured in a three-dimensional circuit QED architecture. *Phys. Rev. Lett.*, 107(24):240501, 2011. 7, 38, 123, 146

[149] M. Pechal, J.-C. Besse, M. Mondal, M. Oppliger, S. Gasparinetti, and A. Wallraff. Superconducting switch for fast on-chip routing of quantum microwave fields. *Phys. Rev. Applied*, 6:024009, Aug 2016. 6

[150] Michael J. Peterer, Samuel J. Bader, Xiaoyue Jin, Fei Yan, Archana Kamal, Theodore J. Gudmundsen, Peter J. Leek, Terry P. Orlando, William D. Oliver, and Simon Gustavsson. Coherence and decay of higher energy levels of a superconducting transmon qubit. *Phys. Rev. Lett.*, 114:010501, Jan 2015. 7, 142, 145, 166

[151] K. D. Petersson, L. W. McFaul, M. D. Schroer, M. Jung, J. M. Taylor, A. A. Houck, and J. R. Petta. Circuit quantum electrodynamics with a spin qubit. *Nature*, 490(7420):380–383, Oct 2012. 4

[152] Jarryd J. Pla, Kuan Y. Tan, Juan P. Dehollain, Wee H. Lim, John J. L. Morton, Floris A. Zwanenburg, David N. Jamieson, Andrew S. Dzurak, and Andrea Morello. High-fidelity readout and control of a nuclear spin qubit in silicon. *Nature*, 496(7445):334–338, Apr 2013. 4

[153] S. Poletto, Jay M. Gambetta, Seth T. Merkel, John A. Smolin, Jerry M. Chow, A. D. Córcoles, George A. Keefe, Mary B. Rothwell, J. R. Rozen, D. W. Abraham, Chad Rigetti, and M. Steffen. Entanglement of two superconducting qubits in a waveguide cavity via monochromatic two-photon excitation. *Phys. Rev. Lett.*, 109:240505, Dec 2012. 7

[154] D. M. Pozar. Microwave engineering. *Addison-Wesley Publishing Company*, 1993. 63, 64, 108, 109, 111, 184

[155] C.M. Quintana. Characterization and reduction of microfabrication-induced decoherence in superconducting quantum circuits. *App. Phys. Lett.*, 105:062601, 2014. 76, 86

[156] M Reagor, H Paik, G Catelani, L Sun, C Axline, E Holland, I M Pop, N A Masluk, T Brecht, L Frunzio, M H Devoret, L Glazman, and R J Schoelkopf. Reaching 10ms single photon lifetimes for superconducting aluminum cavities. *Appl. Phys. Lett.*, 102(19):192604, 2013. 115, 121

[157] Matthew Reagor, Wolfgang Pfaff, Christopher Axline, Reinier W. Heeres, Nissim Ofek, Katrina Sliwa, Eric Holland, Chen Wang, Jacob Blumoff, Kevin Chou, Michael J. Hatridge, Luigi Frunzio, Michel H. Devoret, Liang Jiang, and Robert J. Schoelkopf. Quantum memory with millisecond coherence in circuit QED. *Phys. Rev. B*, 94:014506, Jul 2016. 8

[158] M. D. Reed, L. DiCarlo, B. R. Johnson, L. Sun, D. I. Schuster, L. Frunzio, and R. J. Schoelkopf. High-fidelity readout in circuit quantum electrodynamics using the jaynes-cummings nonlinearity. *Phys. Rev. Lett.*, 105:173601, Oct 2010. 6

[159] M. D. Reed, L. DiCarlo, B. R. Johnson, L. Sun, D. I. Schuster, L. Frunzio, and R. J. Schoelkopf. High-fidelity readout in circuit quantum electrodynamics using the jaynes-cummings nonlinearity. *Phys. Rev. Lett.*, 105(17):173601, Oct 2010. 126

[160] M. D. Reed, L. DiCarlo, S. E. Nigg, L. Sun, L. Frunzio, S. M. Girvin, and R. J. Schoelkopf. Realization of three-qubit quantum error correction with superconducting circuits. *Nature*, 482:382–385, Feb 2012. 5, 6

[161] Matthew Reed. *Entanglement and Quantum Error Correction with Superconducting Qubits.* PhD thesis, Yale University, 2013. 33

[162] Yarema Reshitnyk, Markus Jerger, and Arkady Fedorov. 3D microwave cavity with magnetic flux control and enhanced quality factor. *EPJ Quantum Technol.*, 3:13, 2016. 33

[163] Chad Rigetti, Jay M. Gambetta, Stefano Poletto, B. L. T. Plourde, Jerry M. Chow, A. D. Córcoles, John A. Smolin, Seth T. Merkel, J. R. Rozen, George A. Keefe, Mary B. Rothwell, Mark B. Ketchen, and M. Steffen. Superconducting qubit in a waveguide cavity with a coherence time approaching 0.1 ms. *Phys. Rev. B*, 86:100506, Sep 2012. 7, 38, 142

[164] D. Ristè and L. DiCarlo. Digital feedback in superconducting quantum circuits. *arXiv:1508.01385*, 2015. 5

[165] D. Ristè, S. Poletto, M.-Z. Huang, A. Bruno, V. Vesterinen, O.-P. Saira, and L. DiCarlo. Detecting bit-flip errors in a logical qubit using stabilizer measurements. *Nat. Commun.*, 6:6983, Apr 2015. 5

[166] Diego Ristè, C C Bultink, M J Tiggelman, R N Schouten, K W Lehnert, and L DiCarlo. Millisecond charge-parity fluctuations and induced decoherence in a superconducting transmon qubit. *Nat. Commun.*, 4(1913), 2013. 146

[167] C A Ryan, M Laforest, and R Laflamme. Randomized benchmarking of single- and multi-qubit control in liquid-state NMR quantum information processing. *New J. Phys.*, 11(1):013034, Jan 2009. 4

[168] K. Saeedi, S. Simmons, J. Z. Salvail, P. Dluhy, H. Riemann, N. V. Abrosimov, P. Becker, H.-J. Pohl, J. J. L. Morton, and M. L. W. Thewalt. Room-temperature quantum bit storage exceeding 39 minutes using ionized donors in silicon-28. *Science*, 342(6160):830–833, Nov 2013. 4

[169] J A Schreier, A A Houck, Jens Koch, D I Schuster, B R Johnson, J M Chow, J M Gambetta, J Majer, L Frunzio, M H Devoret, S M Girvin, and R J Schoelkopf. Suppressing charge noise decoherence in superconducting charge qubits. *Phys. Rev. B*, 77(18):180502, 2008. 14, 146

[170] D. I. Schuster. *Circuit Quantum Electrodynamics*. PhD thesis, Yale University, 2007. 33, 37, 39, 46, 47, 130

[171] D. I. Schuster, A. Wallraff, A. Blais, L. Frunzio, R.-S. Huang, J. Majer, S. M. Girvin, and R. J. Schoelkopf. AC Stark shift and dephasing of a superconducting qubit strongly coupled to a cavity field. *Phys. Rev. Lett.*, 94(12):123602, Apr 2005. 129

[172] P. W. Shor. Algorithms for quantum computation: Discrete logarithms and factoring. In *Proceedings, 35th Annual Symposium on Foundations of Computer Science, Santa Fe*, page 124. IEEE Computer Society Press, 1994. 2

[173] I. Siddiqi, R. Vijay, F. Pierre, C. M. Wilson, M. Metcalfe, C. Rigetti, L. Frunzio, and M. H. Devoret. RF-driven Josephson bifurcation amplifier for quantum measurement. *Phys. Rev. Lett.*, 93(20):207002–4, Nov 2004. 126

[174] Peter Spring. Superconducting coaxmon qubit simulations. Master's thesis, University of Oxford, 2016. 192

[175] L. Steffen, Y. Salathe, M. Oppliger, P. Kurpiers, M. Baur, C. Lang, C. Eichler, G. Puebla-Hellmann, A. Fedorov, and A. Wallraff. Deterministic quantum teleportation with feed-forward in a solid state system. *Nature*, 500(7462):319–322, Aug 2013. 6

[176] L Sun, L DiCarlo, M D Reed, G Catelani, Lev S Bishop, D I Schuster, B R Johnson, Ge A Yang, L Frunzio, L Glazman, M H Devoret, and R J Schoelkopf. Measurements of quasiparticle tunneling dynamics in a band-gap-engineered transmon qubit. *Phys. Rev. Lett.*, 108:230509, 2012. 14, 146

[177] Shigeki Takeuchi. Experimental demonstration of a three-qubit quantum computation algorithm using a single photon and linear optics. *Phys. Rev. A*, 62(3):032301, Aug 2000. 4

[178] B N Taylor, W H Parker, D N Langenberg, and A Denenstein. On the use of the ac josephson effect to maintain standards of electromotive force. *Metrologia*, 3(4):89, 1967. 21

[179] M. Tinkham. *Introduction to Superconductivity.* McGraw-Hill International Editions, 1996. 18

[180] A. M. Turing. On computable numbers, with an application to the entscheidungsproblem. *Proceedings of the London Mathematical Society*, s2-42(1):230–265, 1937. 2

[181] Thomas Unden, Priya Balasubramanian, Daniel Louzon, Yuval Vinkler, Martin B. Plenio, Matthew Markham, Daniel Twitchen, Alastair Stacey, Igor Lovchinsky, Alexander O. Sushkov, Mikhail D. Lukin, Alex Retzker, Boris Naydenov, Liam P. McGuinness, and Fedor Jelezko. Quantum metrology enhanced by repetitive quantum error correction. *Phys. Rev. Lett.*, 116:230502, Jun 2016. 4

[182] C. H. van der Wal, A. C. J. ter Haar, F. K. Wilhelm, R. N. Schouten, C. J. P. M. Harmans, T. P. Orlando, S. Lloyd, and J. E. Mooij. Quantum superposition of macroscopic persistent-current states. *Science*, 290(5492):773–777, October 2000. 24

[183] A. F. van Loo, A. Fedorov, K. Lalumiere, B. C. Sanders, A. Blais, and A. Wallraff. Photon-mediated interactions between distant artificial atoms. *Science*, 342(6165):1494–1496, Nov 2013. 6

[184] L. M. K. Vandersypen and I. L. Chuang. NMR techniques for quantum control and computation. *Rev. Mod. Phys.*, 76:1037, 2004. 4

[185] Lieven M. K. Vandersypen, Matthias Steffen, Gregory Breyta, Costantino S. Yannoni, Mark H. Sherwood, and Isaac L. Chuang. Experimental realization of Shor's quantum factoring algorithm using nuclear magnetic resonance. *Nature*, 414:883, 2001. 4

[186] R. Vijay, D. H. Slichter, and I. Siddiqi. Observation of quantum jumps in a superconducting artificial atom. *Phys. Rev. Lett.*, 106(11):110502, Mar 2011. 126

[187] D. Vion, A. Aassime, A. Cottet, P. Joyez, H. Pothier, C. Urbina, D. Esteve, and M. H. Devoret. Manipulating the quantum state of an electrical circuit. *Science*, 296:886–889, 2002. 5, 25, 30

[188] R. F. Voss and R. A. Webb. Macroscopic quantum tunneling in 1-μm Nb Josephson junctions. *Phys. Rev. Lett.*, 47:265, 1981. 5, 19

[189] B. C. Wadell. *Transmission Line Design Handbook.* Artech House, Inc, 1991. 183

[190] A. Wallraff, D. I. Schuster, A. Blais, L. Frunzio, R.-S. Huang, J. Majer, S. Kumar, S. M. Girvin, and R. J. Schoelkopf. Strong coupling of a single photon to a superconducting qubit using circuit quantum electrodynamics. *Nature*, 431:162–167, 2004. 6, 35, 37

[191] A Wallraff, D I Schuster, A Blais, L Frunzio, J Majer, M H Devoret, S M Girvin, and R J Schoelkopf. Approaching unit visibility for control of a superconducting qubit with dispersive readout. *Phys. Rev. Lett.*, 95:060501, 2005. 44, 46, 149

[192] C. Wang, C. Axline, Y. Y. Gao, T. Brecht, Y. Chu, L. Frunzio, M. H. Devoret, and R. J. Schoelkopf. Surface participation and dielectric loss in superconducting qubits. *Appl. Phys. Lett.*, 107(16), 2015. 7, 94, 196

[193] Chen Wang, Yvonne Y. Gao, Ioan M. Pop, Uri Vool, Chris Axline, Teresa Brecht, Reinier W. Heeres, Luigi Frunzio, Michel H. Devoret, Gianluigi Catelani, Leonid I. Glazman, and Robert J. Schoelkopf. Measurement and control of quasiparticle dynamics in a superconducting qubit. *Nat. Commun.*, 5, 2014. 14, 146

[194] H Wang, M Hofheinz, M Ansmann, R Bialczak, E Lucero, M Neeley, A D O'connell, D Sank, J Wenner, A Cleland, and John M Martinis. Measurement of the decay of Fock states in a superconducting quantum circuit. *Phys. Rev. Lett.*, 101(24):240401, 2008. 146, 160

[195] G. Wendin and V.S. Shumeiko. Superconducting quantum circuits, qubits and computing. *arXiv:cond-mat/0508729*, 2005. 25

[196] N. Ofek M. Hatridge A. Narla K.M. Sliwa L. Frunzio R.J. Schoelkopf Y. Liu, S. Shankar and M.H. Devoret. Comparing and combining measurement-based and driven-dissipative entanglement stabilization. *Phys. Rev. X*, 6:011022, 2016. 5, 142

[197] N.Y. Yao, L. Jiang, A.V. Gorshkov, P.C. Maurer, G. Giedke, J.I. Cirac, and M.D. Lukin. Scalable architecture for a room temperature solid-state quantum information processor. *Nat. Commun.*, 3:800, Apr 2012. 4